# CATCHMENT WATER BALANCE IN DATA-SCARCE ENVIRONMENTS– WHAT INSIGHTS DOES THE BUDYKO FRAMEWORK PROVIDE?

## MODEL-AND DATA-BASED CONSIDERATIONS TO ASSESS WATER BALANCES ON THE WESTERN SLOPES OF THE PERUVIAN ANDES AND THEIR RELATIONSHIP TO THE BUDYKO CURVE

Zur Erlangung des akademischen Grades eines

DOKTORS DER NATURWISSENSCHAFTEN
(Dr. rer. nat.)

von der KIT-Fakultät für
Bauingenieur-, Geo- und Umweltwissenschaften

des Karlsruher Instituts für Technologie (KIT)
genehmigte

DISSERTATION

von
Jan Bondy
aus München

Tag der mündlichen Prüfung:
15. Mai 2023

REFERENT: Prof. Dr. Erwin Zehe
KORREFERENT: Dr. habil. Laurent Pfister

Karlsruhe 2023

Dedicated to my dear family and friends,
without whom I wouldn't know what to do,
nor why to do it.

# CONTENTS


Abstract ix

Zusammenfassung xii

Acknowledgments xv

Nomenclature, abbreviations and acronyms xvii

1 Introduction 1
- 1.1 Water and data scarcity in the Global South . . . . . 1
- 1.2 Hydrological predictions and assessments in data-scarce environments . . . . . 3
- 1.3 Mean annual water balance and Budyko curve . . . . . 5
- 1.4 Objectives and outline . . . . . 7

2 Catchment water balance and Budyko Framework 9
- 2.1 Water cycle and catchment water balance . . . . . 9
- 2.2 Energy balance and potential evapotranspiration . . . . 12
- 2.3 Mean annual water balance and Budyko Curve . . . . 14
  - 2.3.1 Steady state . . . . . 14
  - 2.3.2 Budyko hypothesis and equation . . . . . 15
- 2.4 Deviations from the Budyko curve . . . . . 18
  - 2.4.1 Natural second-order controls . . . . . 18
  - 2.4.2 Anthropogenic influences . . . . . 20
  - 2.4.3 Effect of estimation errors and uncertainty in the Budyko space . . . . . 23

3 Study area and data 25
- 3.1 Main study area: West Peruvian Andes . . . . . 25
  - 3.1.1 Peru's geography . . . . . 25
  - 3.1.2 Climate and meteorology . . . . . 25
  - 3.1.3 Western slopes of Andes, Chillón and Lurín basin 27
- 3.2 Data . . . . . 29
  - 3.2.1 Meteorological data . . . . . 29
  - 3.2.2 Streamflow data . . . . . 30
  - 3.2.3 Biogeophysical data . . . . . 31

4 Estimating catchment water and energy balance components in a data-scarce environment in the Peruvian Andes 34
- 4.1 CovVar model development for precipitation regionalization . . . . . 34
  - 4.1.1 Methods . . . . . 36
  - 4.1.2 Spatiotemporal rainfall patterns and statistics . 37
  - 4.1.3 The CovVar model . . . . . 40

4.1.4 Model application and validation . . . . . 42
4.1.5 Discussion of model performance . . . . . 46
4.2 Regionally calibrated Hargreaves-Samani approach for potential evapotranspiration . . . . . 48
4.2.1 Hargreaves-Samani method . . . . . 49
4.2.2 Data . . . . . 50
4.2.3 Spatiotemporal differences between reference evapotranspiration and Hargreaves-Samani . . 50
4.2.4 Calibration of Hargreaves-Samani coefficient . . 52
4.2.5 Areal potential evapotranspiration . . . . . 53

5 Paired catchment modeling approach for Lurín and Chillón River 55
5.1 Introduction . . . . . 55
5.2 Data and preprocessing . . . . . 56
5.3 Methods . . . . . 57
5.3.1 Mesoscale Hydrological Model (mHM) . . . . . 57
5.3.2 Modeling and parameter transfer . . . . . 62
5.4 Comparative catchment analysis . . . . . 67
5.5 Results . . . . . 82
5.5.1 Calibration and validation of Chillón river model 82
5.5.2 Parameter transfer and modeling of Lurín river 89
5.6 Discussion . . . . . 94
5.6.1 Relation between headwater and main catchment streamflow . . . . . 94
5.6.2 Mean water balance and relation to Budyko curve 97
5.6.3 Interannual variability of the water balance . . . 99
5.6.4 Similarity in intra-annual dynamics . . . . . 101

6 Water balance similarity and Budyko offsets of catchments on the Western slopes of the Peruvian Andes 106
6.1 Methods . . . . . 107
6.2 Results . . . . . 111
6.2.1 Characteristics of selected catchments . . . . . 111
6.2.2 Budyko offsets and correlation analysis . . . . . 114
6.3 Discussion . . . . . 117
6.3.1 Spatial heterogeneity and scale . . . . . 119
6.3.2 Snowiness . . . . . 122
6.3.3 Catchment storage and anthropogenic influences 124
6.3.4 Dataset-external controls: seasonality . . . . . 127

7 Exploring the role of soil storage capacity for explaining deviations from the Budyko curve using a simple water balance model 128
7.1 Introduction . . . . . 128
7.2 Methods, data and model . . . . . 130
7.2.1 Selection of study catchments . . . . . 130
7.2.2 Data and preprocessing . . . . . 131

7.2.3 Characteristics of selected catchments . . . . . 132
7.2.4 Hydrological modeling . . . . . 134
7.3 Results . . . . . 137
7.3.1 Water balance simulations . . . . . 137
7.3.2 Variation of total storage volume $S_{max}$ . . . . . 139
7.3.3 Variation of the capillary storage fraction $FC_{frac}$ 140
7.3.4 Simultaneous parameter variation . . . . . 142
7.4 Discussion . . . . . 143
7.4.1 Water balance modeling . . . . . 144
7.4.2 The role of soil storage characteristics for the evaporation ratio . . . . . 146
7.4.3 Offsets from the Budyko curve . . . . . 148

8 Synthesis and conclusions 153
8.1 Synthesis of key findings . . . . . 153
8.1.1 Estimation of precipitation and pot. evapotranspiration in data-scarce environment . . . . . 153
8.1.2 Similarity of Peruvian catchments and their Budyko positions . . . . . 154
8.1.3 Soil storage and other controls on mean water balance and on Budyko offsets . . . . . 156
8.2 Outlook and further research . . . . . 158

A Appendix 160
A.1 Appendix of chapter 3 . . . . . 160
A.2 Appendix of chapter 5 . . . . . 162
A.3 Appendix of chapter 6 . . . . . 164
A.4 Appendix of chapter 7 . . . . . 166

Bibliography 171

Own publications 185

Declaration 186

## ABSTRACT

Water is a vital resource to human development and ecosystems. Understanding water balances of river basins is key in water management decision-making, especially in regions facing water stress. Besides water stress stemming from dry climate and rapid demographic development, some countries of the Global South suffer at the same time from monitoring data limitations for lack of financial resources. This thesis is centered around methods to tackle challenges arising from limitations in hydrometeorological monitoring data that are required to assess water balances as well as to calibrate and run hydrological models.

In order to make predictions in ungauged basins, hydrological similarity frameworks are a way to overcome the lack of discharge data. The Budyko curve, a famous similarity framework connecting climate and runoff similarity of catchments for mean annual time scales and large-enough spatial scales, estimates a catchments' mean annual water balance ($ET_a/P$) based on its climatic dryness ($ET_p/P$). This widely tested framework seemed a useful tool in an environment of scarce and uncertain data, and is applied, tested and analyzed from different angles throughout this thesis - in particular with respect to deviations from the curve, *Budyko offsets*. While certain questions are approached in a more theoretical way, the thesis is predominantly embedded in the geographic context of catchments on the Western Flanks of the Peruvian Andes, in particular the two river basins Chillón and Lurín. The main study region presents a seasonal rainfall regime, total rainfall amounts however varying considerably along steep elevation gradients within the catchments.

As a basis for subsequent aridity and water balance assessment of the Peruvian catchments as well as for hydrological modeling, methods are developed and applied to estimate areal precipitation and potential evapotranspiration. *CovVar*, a simple and robust precipitation regionalization method for data-scarce and mountainous regions, solely based on rain gauge data, is introduced. The method exploits long-term statistical relationships between elevation and rainfall on a monthly basis and combines these monthly patterns with a weighted regionalization of the fluctuation at a nearest reference station. CovVar showed good performance metrics, also in comparison to the national PISCO rainfall product. Differences in the catchment-average rainfall became apparent at annual scales, mostly in the Lurín river basin which lacked monitoring in the most humid headwater parts. For potential evapotranspiration, the Hargreaves-Samani coefficient is calibrated for the region based on a short time series of fully equipped

weather stations and applied to historical time series. Both datasets were successfully implemented as forcing data in the hydrological model.

Making use of hydrological similarity and the Budyko curve as a water balance landmark in order to set up a hydrological model (mHM) and derive a suitable parameter set for the poorly monitored Lurín basin, a paired-catchment modeling approach is conducted. The better monitored neighboring Chillón basin served as reference and parameter donor catchment. The approach helped evaluate the quality of different meteorological forcing datasets. The datasets had a significant impact on observed and modeled water balances of the Lurín. Compared to the PISCO rainfall dataset, CovVar yielded aridity indexes and water balances in better agreement both with the presumably similar neighboring catchment and the Budyko-based estimate, suggesting more realistic estimates. The variability of the different datasets outweighed by far the influence of the different model parameter sets. The transfer of model parameters from Chillón to Lurín did however yield reasonable model runs, comparable to direct calibrations of Lurin's short discharge records.

The analysis was widened to 17 similarly-arranged catchments in the study region to explore their water balance similarity and Budyko offsets. A linear correlation analysis was conducted to investigate the influence of subscale climatic and catchment characteristics on water balances and offsets from the Budyko curve. The analysis revealed both a systematic overestimation by the Budyko curve as well as a high variability between the catchments initially presumed more similar. The individual coefficients of determination remaining expectedly low for the coarse correlation approach, it showed signals for climatic heterogeneity, snowiness and discharge seasonality as proxy for all catchment storage-related characteristics. While these influences are discussed based on physical mechanisms and literature information, the remainder of the variance as well as the systematic trend is presumed to be related to soil storage, potentially in combination with seasonal effects.

Due to the rather inconsistent picture of water balances in the study region as well as the steep Andean topography in combination with the semi-arid climate, a model-based study explores the influence of soil storage more in-depth. Its reported importance as a control on the mean water balance conflicts with the difficulty to quantify it at the catchment scale. Therefore, multiple catchments of varying aridity, from the US, Germany and Peru, were selected as realistic systems for a virtual experiment. Both storage capacity in terms of free pore space as well as capillary storage fractions were varied in the model and the resulting water balances analyzed with respect to resulting Budyko offsets. The results corroborated the important role of soil storage properties as a control on the mean annual water

balance and potential Budyko offsets. Both total storage capacity and capillary storage fraction turned out to be sensitive parameters. Through variation of total storage, the Budyko curve was reached for most cases, showing a certain degree of clustering at storage volumes of around 5-15% of mean annual precipitation -corresponding to values commonly found in nature- before the water balances level off quasi-asymptotically.

Wasser in von essentieller Bedeutung für die menschliche Entwicklung und Ökosysteme. Das Verstehen von Wasserbilanzen in Flusseinzugsgebieten ist eine Grundvoraussetzung für Entscheidungen im Wasserressourcenmanagement, insbesondere in wasserknappen Regionen. Neben der Wasserknappheit durch trockenes Klima sowie eine rasante demographische Entwicklung, erschweren eine limitierte Datenlage die Bedingungen in einigen Ländern des globalen Südens. Die vorliegende Arbeit konzentriert sich auf Methoden, die hydrometeorologische Datenlage zu verbessern, um Herausforderungen bei Wasserbilanzschätzungen sowie Modellkalibrierungen entgegenzutreten.

Um trotz des Mangels an Abflussdaten in nicht bepegelten Einzugsgebieten hydrologische Modelle zu kalibrieren, können Ähnlichkeitsansätze Abhilfe leisten. Die Budykokurve, ein verbreiteter Ähnlichkeitsansatz, der Klima- und Abflussähnlichkeit auf langen Zeitskalen miteinander verbindet, schätzt die stationäre Wasserbilanz ($ET_a/P$) als Funktion der klimatischen Aridität ($ET_p/P$). Dieser Ähnlichkeitsansatz schien ein nützliches Tool in einer datenarmen Region und wird in der vorliegenden Arbeit angewandt, getestet und analysiert- vor allem in Bezug auf Abweichungen von der Budykokurve (sog. *Budyko Offsets*). Während manche Fragen allgemeingültiger behandelt werden, liegt der geografische Schwerpunkt dieser Arbeit auf Einzugsgebieten der westperuanischen Anden, insbesondere des Chillón und Lurín. Das Untersuchungsgebiet weist ein saisonales Kima auf, mit Jahresniederschlägen, die entlang eines steilen topografischen Gradienten stark abfallen innerhalb der Einzugsgebiete.

Als Basis für Aridităts- und Wasserbilanzbetrachtungen in den peruanischen Einzugsgebieten werden Methoden entwickelt und angewandt, die Gebietsniederschlag sowie potentielle Verdunstung schätzen. *CovVar* wird eingeführt, ein simpler und robuster Ansatz zur Regionalisierung von punktuellen Niederschlagsmessungen in datenarmen Gebirgsregionen. Die Methode basiert auf statistischen Zusammenhängen zwischen Höhe und Monatsniederschlägen, in Kombination mit einer gewichteten Regionalisierung der Fluktuation an einer Bezugsstation. CovVar wies gute Performanzmetriken auf, auch im direkten Vergleich mit dem landesweiten Niederschlagsprodukt PISCO. Unterschiede zeigten sich vor allem im Bereich des Gebietsniederschlags im Lurín Einzugsgebiet, welches über kein Niederlags-Monitoring in den feuchtesten Kopfeinzugsgebieten verfügte. Um längere historische Zeitreihen für die potentielle Verdunstung zu generieren, wird der Hargreaves-Samani Koeffizient in der Region kalibriert, auf Grundlage von kurzen Zeitreihen gut ausgestat-

teter Wetterstationen. Beide Datensätze wurden erfolgreich in einem hydrologischen Modell eingesetzt.

Ausgehend von hydrologischer Ähnlichkeit und der Budykokurve als Wasserbilanz-Orientierungspunkt, wurde ein gekoppelter Einzugsgebiets -Modellieransatz angewandt, um ein hydrologisches Modell (mHM) für den Lurín aufzusetzen und einen passenden Parametersatz abzuleiten. Dabei diente das benachbarte, besser beobachtete Chillón Einzugsgebiet als Referenz und Parameter-Spender. Durch die Einzugsgebiets-Kopplung konnte die Qualität der verschiedenen Forcing-Datensätze evaluiert werden. Diese hatten einen starken Einfluss auf beobachtete und simulierte Wasserbilanzen im Lurín. Im Vergleich zum PISCO-Datensatz, lieferte CovVar Aridităts indizes und Wasserbilanzen für den Lurín, die sowohl mit dem als ähnlich angenommenen Nachbareinzugsgebiet als auch mit der Budykokurve deutlich besser übereinstimmen, was auf realistischere Schätzungen schließen lässt. Das Gewicht der Variabilität der verschiedenen Datensätze überstieg bei Weitem das der verschiedenen Modell-Parametersätze. Der Parametertransfer lieferte dennoch funktionale Parametersätze für den Lurín, die mit direkten Lurín-Kalibrierungen vergleichbar waren.

Die Analyse wurde auf 17 ähnlich angeordnete Einzugsgebiete im Untersuchungsgebiet erweitert, um deren Wasserbilanzähnlichkeit und Budyko offsets zu untersuchen. Eine lineare Korrelationsanalyse wurde durchgeführt, um den Einfluss von subskaligen klimatischen und Einzugsgebietseigenschaften auf Wasserbilanz und Budyko offset zu beleuchten. Die Analyse zeigte sowohl eine systematische Überschätzung der Budykokurve als auch eine enorm hohe Variabilität zwischen den Einzugsgebieten, für die vor der Analyse mehr Ähnlichkeit erwartet wurde. Die individuellen Bestimmtheitsmaße blieben bei diesem recht einfachen, linearen Ansatz erwartungsgemäßig niedrig, dennoch gab es Signale für klimatische Heterogenität, Schneebedeckung sowie Abflusssaisonalität als Proxy für sämtliche Speichervorgänge im Einzugsgebiet. Während diese Einflüsse im Hinblick auf physikalische Vorgänge sowie Literaturinformationen diskutiert werden, werden Gründe für Restvarianz sowie den systematischen Trend bei Einflüssen wie dem Bodenspeicher, potentiell in Kombination mit saisonalen Effekten, vermutet.

Aufgrund der inkonsistenten Wasserbilanzen in der Region sowie der steilen andinen Topographie in Kombination mit dem semiariden Klima, untersucht eine Modellstudie gezielt den Einfluss des Bodenspeichers. Der aus der Literatur bekannte Einfluss der Bodenspeicherkapazität auf die mittlere Wasserbilanz steht seiner schweren Quantifizierbarkeit auf Einzugsgebietskale gegenüber. Aus diesem Grund wurden mehrere Einzugsbebiete als realitätsnahe Systeme für ein *virtuelles Experiment* ausgewählt. Sowohl Bodenspeicher in Form von freiem Porenraum als auch ein kapillaritätsgesteuerter Anteil

wurden im Modell variiert und die resultierenden Wasserbilanzen analysiert. Die Ergebnisse bestätigen die bedeutende Rolle des Bodenspeichers für die mittlere Wasserbilanz und potentiellen Budyko Offsets. Sowohl der Gesamtbodenspeicher als auch die kapillaritätsbeeinflusste Teil erwiesen sich als sensitive Größen. Durch Variation des Bodenspeichers erreichte fast jedes System die Budykokurve, mit einem erkennbaren Clustering bei Speichergrößen von etwa 5-15% des mittleren Jahresniederschlags -was in der Natur vorkommenden Werten entspricht- bevor die Wasserbilanzen ein quasi-asymptotisches Level erreichen.

# ACKNOWLEDGMENTS

Many people have contributed to the success of this seemingly never-ending endeavor and for that I wish to express my gratitude in the following lines.

First and foremost to my professor, Dr. Erwin Zehe, who gave me the chance to join his research team at KIT and to do my PhD. Erwin is in many ways a special character, who always makes for interesting discussions, conveys an enormous amount of enthusiasm for and knowledge in his field, who is (sometimes too) full of ideas and heads the group with his humorous, liberal and personable nature. He always stands up for his employees and motivates them to go on in moments of doubt. Thank you, Erwin!

Secondly, to Dr. Jan Wienhöfer, who coordinated the TRUST project, a task that proved rather complicated and *obstaclicious*. In all those five to six years, Jan has been incredibly helpful and always available for discussions. He possesses the wonderful gift of smartly and most efficiently structuring chaos, and does so in a very pleasant manner. He has been an enriching unofficial advisor and complemented Erwin perfectly. Thank you, Jan!

Furthermore, I wish to thank all my colleagues at IWG who together created a work environment that made the 2 hours commute to Karlsruhe for more than three years seem remarkably easy. It has been a pleasure to be your colleague, discuss, share and laugh with you on a regular basis- it still is and hopefully stays that way. Thank you Alex, Franzi, Mirko, Rik, Stephanie, Ralf, Samuel, Svenja, Uwe, Sybille and Lucas! Special and more personal thanks go to the ones I have shared most with..those probably know who I mean.

To our colleagues in administration, the organizational backbone of the group, Raziye, Maria and Jutta, who almost invisibly make everything smooth and easy at the institute, thank you for that!

Many thanks also to the students who contributed to this work, Lucas Alcamo, Selin Özgür and Alcides Aybar. Guiding you, discussing results and having your input was an enriching experience, both work-wise and on a human level.

On a more personal note, I want to thank my parents whose support on many levels up until today has always been an important pillar in my life. To my two dearest friends in this world, Johannes and Philipp, who never fail to motivate me and who have accompanied me for almost 15 years. In particular, thank you Philipp for opening up your home to me once a week in three years of commuting!

To Denise, my former life partner and partner in crime when it comes to maneuvering one's ship through the stormy waters of the

PhD project. Without her by my side all those years, I would not have had the strength and resilience to arrive at the right harbor at the end.

I also wish to convey my gratitude to my new project coordinator, Dr. Ulrich Blahak, as well as my supervisor and colleague, Dr. Vanessa Fundel, of my new work group at DWD, who not only provide a very comfortable and motivating work environment but who have also been just the right amount of supportive and pushy when it comes to me finishing the PhD.

# NOMENCLATURE, ABBREVIATIONS AND ACRONYMS

## REMARKS ON BASIN VS. CATCHMENT NOMENCLATURE

Chapter 5 treats the comparison and paired modeling of the two river basins of Chillon and Lurin. However, the comparisons are done primarily on the basis of stream gauge-imposed subcatchments of the basins. For clarity, the entire river basins, which discharge into the Pacific ocean, are referred to as "basins", and their subbasins as "subcatchments" or just "catchments". While the lower subcatchments (Puente Magdalena/Antapucro) are called "main (sub)catchments" of the basins, the upper parts are referred to as "headwater catchments" (Obrajillo/Santa Rosa). The headwater catchments are part of the main catchments.

## ACRONYMS

| | |
|---|---|
| BMBF | Bundesministerium für Bildung und Forschung— German Ministry for Education and Research) |
| DEM | Digital elevation model |
| ENSO | El Nino Southern Oscillation, a global atmosphere-ocean coupling phenomenon, leading to anomalies in ocean temperature and atmospheric circulation patterns |
| GIS | Geographic Information System, here often used to refer to digital geographic datasets |
| HS | Hargreaves-Samani, method to determine potential evapotranspiration |
| INGEMMET | Instituto Geológico, Minero y Metalúrgico— Peruvian state authority for geology and mining activities |
| NSE | Nash-Sutcliffe-Efficiency, common objective function in hydrological modeling |
| ONI | Oceanic Niño Index |
| PM | Penman-Monteith, method to determine potential evapotranspiration |
| RMSE | root mean square error |

SED / SEDAPAL
: "Servicio de Agua Potable y Alcantarillado de Lima"— the drinking water supplier of Lima metropolitan area

SEN / SENAMHI
: "Servicio Nacional de Meteorología e Hidrología del Perú" — the Peruvian national weather service

TRUST
: Trinkwasserversorung in Wassermangelregionen— BMBF project, within the framework of which the studies of this thesis were carried out

## ABBREVIATIONS

BUDYKO OFFSET
: The deviation of the (mean annual) water balance (as expressed by the evaporation ratio) of a catchment from the Budyko curve

BUDYKO POSITION
: The x- (dryness index $\phi$) and y- (evaporation ratio EVR) position in the Budyko space

CHIRILU
: The three catchments of **Chi**llon, **Ri**mac and **Lu**rin

CHILU
: The two catchments of **Chi**llon and **Lu**rin

ETP-HS-CALIB
: Potential evapotranspiration on the basis of a regionally calibrated Hargreaves-Samani (HS) approach

EVAPORATION
: is used interchangeably with evapotranspiration

## RECURRING LATIN VARIABLES

$ET_a$
: actual evapotranspiration

$ET_p$
: potential evapotranspiration

$ET_o$
: FAO reference (potential) evapotranspiration

$EVR$
: evaporation ratio (mean annual actual evapotranspiration / mean annual precipitation)

$HRD$
: rel. air humidity (spanish: *humedad relativa diaria*)

$K_T$
: Hargreaves-Samani coefficient

$P$
: precipitation

$Q$
: stream flow (discharge)

| | |
|---|---|
| $R$ | Pearson correlation coefficient |
| $R^2$ | coefficient of determination |
| $R_a$ | extraterrestrial radiation |
| $R_s$ | solar radiation |
| $T_x$ | temperature, the kind depending on its subscript |
| $VVD$ | wind velocity (spanish: *velocidad del viento diaria*) |

RECURRING GREEK SYMBOLS

| | |
|---|---|
| $\phi$ | climatic dryness (aridity) index, ratio of mean annual potential evapotranspiration to precipitation |

# 1 INTRODUCTION

## 1.1 WATER AND DATA SCARCITY IN THE GLOBAL SOUTH

Water is a critical resource for ecosystems and human development. A river basin with less than 500 $m^3$ of freshwater per capita and year qualifies as *very severe water stress* according to UNESCO (2012). Water stress, resulting from the combination of scarce physical water resources and human presence and activity, is unevenly distributed in the world, with major water stress regions appearing over Northern and Eastern Africa, the Arabian Peninsula and Central Asia (UNESCO, 2012). Smaller spots are found for instance in the West of the United States, Southern Africa as well as along a thin strip of land along the West coast of South America. The latter is located in the tropics and subtropics, and is part of the countries of Chile and Peru. As a result of the massive Andes mountain range (the *Cordillera*), Peru's geography is extremely heterogeneous both in terms of water availability and demography, receiving 97.3% of its freshwater in the Amazonian part yielding 150.000 $m^3$/capita/year and 2.2% in the Pacific watersheds, which translates to 125 $m^3$/capita/year in the river basins around Lima, the latter thus suffering from *very severe water stress* (Bernex et al., 2017; Sanchez, 2016).

*Water stress & water management challenges*

A well-organized and precise management of the scarce water resource is key in a region such as West Peru, and can only result from a thorough understanding of the resource's spatiotemporal occurrence. Such understanding of hydro systems is generated through an interplay of monitoring and modeling. These two components allow for the assessment of past and present situations, and provide a basis for predicting future scenarios. Apart from advancing model approaches and techniques, observation data are thus crucial to further system understanding. Constant efforts are made to increase data availability, both by developing new measuring techniques and by increasing data coverage in formerly unobserved locations. The latter is provided through the installation of new ground-based sensors as well as by the deployment of new generations of satellites (e.g. ESA-Sentinel, NASA-GPM, EUMETSAT-MTG). Depending on the environmental variable of interest and relevant spatiotemporal scales, the types of monitoring techniques differ in the degree of reliability and precision. While satellites increasingly contribute to rainfall monitoring, for precise quantitative measurements, especially at smaller spatial scales, ground-based monitoring still remains indispensable (AghaKouchak

*Tackling the lack of observation data*

et al., 2010).

*Three challenges for the water management*

In certain countries of the so-called Global South, such as Peru, there is a particular need for a refined water management, whereas the ability to provide that remains limited. The water management in such a region is confronted with the combination of three major challenges:

- **water scarcity, (semi-)arid climate**: many parts of the Global South tend to be comparably dry, or at least face pronounced seasonal dryness which requires water storage infrastructure to bridge the dry season (notably Northern and Southern Africa, Arabian Peninsula, Western parts of South America, see global aridity index in Trabucco and Zomer (2018)).
- **rapidly evolving demographics**: rural exodus (sometimes combined with high birth rates) lead to fast-growing urban areas and surrounding industries (Borsdorf, 1978) with increasing, spatially concentrated freshwater demand.
- **data scarcity and data quality limitations**: insufficient hydrometeorological monitoring due to limited financial resources (shortcomings in monitoring network density, maintenance, data quality control).

*The TRUST Project*

This thesis started out in the framework of the TRUST project (Leon et al., 2021). The BMBF-funded joint research project engaged in the better understanding and improvement of the basis for decision-making in an exemplary river basin in Peru: the Lurín. Apart from organizational and institutional elements of the water management, a major focus of TRUST was on the quantitative understanding of the available water resources in the basin. The latter comprised of hydrometeorological monitoring and hydrological modeling, in order to characterize the spatiotemporal dynamics of relevant water fluxes as well as the water balance at the catchment scale. The objectives were centered around monthly and annual time scales that are of importance to water resource management decisions.

*The Lurín river basin*

The Lurín valley is located on the slopes of the western Andes in Peru. The headwater streams originate in the high elevation zones of the mountain range, and the catchment channels its stream waters to and through the outskirts of Lima, eventually discharging into the Pacific ocean. It is one of the three adjacent basins of Chillón, Rímac and Lurín -abbreviated as *Chirilu*- that together sustain the freshwater supply of the metropolitan area of Lima. The natural conditions, from semi-arid climate with a pronounced precipitation seasonality in medium and upper basin parts to hyper-arid climate at the coast, pose enormous challenges to the water management, especially in the

context of the rapidly growing megacity of Lima, Peru's capital. The Lurín river basin can be considered as nearly ungauged and poorly monitored in terms of meteorological data. There is only one stream gauge in the heterogeneous basin, with short data records of three to four years. In addition, the highest and presumably most humid part of the basin, lacked rainfall monitoring prior to the TRUST project.

## 1.2 HYDROLOGICAL PREDICTIONS AND ASSESSMENTS IN DATA-SCARCE ENVIRONMENTS

*Use of hydrological models*

Fundamental hydrological tasks in water management include predicting floods, assessing the frequency of flood occurrence as well as comprehending and predicting seasonal and annual water balances across a basin for water availability assessments. Hydrological models are used to accomplish these tasks. Such models are supposed to represent the behavior of the catchment system by bringing monitoring data and knowledge of hydrological processes together in a coherent picture. With models it is possible to estimate non-measured water fluxes (e.g. evapotranspiration or individual runoff components), gain information about inner-catchment heterogeneity in the hydrologic response (e.g. ungauged subcatchments) and make predictions of potential future scenarios (e.g. changing precipitation regimes, anthropogenic interventions). Common hydrological models are rainfall-runoff models which transform the meteorological forcing data, rainfall and potential evapotranspiration, into streamflow. Independent forcing or input data is thus required to run a rainfall-runoff model, and needs to be known or estimated at the catchment scale. In the case of spatially-explicit models, spatially-distributed data is gained via a regionalization approach or directly taken from remotely sensed areal products.

*Conceptual models*

There is a great number of different hydrological models and modeling approaches in hydrology, and the model type strongly depends on the specific task, purpose and available data (Blöschl et al., 2013). In operational hydrology and in general for intermediate mesoscale or larger catchments (roughly above $A_o$>500 km$^2$), conceptual hydrological models are commonly used. Depending on the model's particularities, conceptual models can account for a number of hydrological processes. While all the processes are conceptualized and parametrized, the type and degree of the representation or approximation of the fundamental physical laws governing the processes at smaller scales, varies (Berkowitz and Zehe, 2020; Beven, 1996). In such models, the hydrological behavior of a catchment is represented by a specific set of model parameters. The catchment-specific parametrization is usually derived via model calibration, an

optimization process fitting the model parameters to discharge time series measured at a stream gauge, using one or several objective functions.

*Challenges in calibrating a hydrological model*

There are model-inherent challenges that limit the ability to unambiguously derive a parameter set describing the realistic hydrological behavior of a catchment because of the equifinality problem (Beven and Binley, 1992). Equifinality implies that optimization over a varying but potentially great number of degrees of freedom (parameters) against the point-wise and aggregating discharge output, does not necessarily have one unique solution that approximates the system behavior at the outlet. The main challenge in data-scarce and ungauged basins however stems from insufficient hydrometeorological monitoring data- both of meteorological forcing (model input) and of discharge (model output), both in terms of quantity and quality. While for potential evapotranspiration and in particular precipitation, long data series are often available at point-wise weather stations or rain gauges, the challenge consists in the regionalization across the catchment domain. Shortcomings result from the monitoring network's density in relation to the spatial variability of the environmental variables in question, which introduces uncertainty in the catchment-wide estimates (Ly et al., 2013; Segond et al., 2007). Discharge data on the other hand suffers from a lack of long data records and from quality limitations because it is a high maintenance variable, requiring reference flow measurements in order to develop a rating curve. The rating curve has to be controlled and potentially updated continuously since the monitoring cross section's geometry can change over time, especially in rivers with high sediment and bed load dynamics.

*Comparative hydrology, similarity vs. catchment uniqueness*

Despite the shortcomings in data availability and quality as well as their implications for hydrological models, predictions and decision-making in terms of water management need to take place. Therefore, alternative estimation methods and modeling approaches are developed as remedies to data limitations. Comparative hydrology and its underlying assumption of hydrological similarity across catchments provides a variety of useful approaches in this context, an extensive review of which is presented by Blöschl et al. (2013). As opposed to other disciplines like meteorology, in hydrology it is feasible to study spatial units (catchments) in an isolated manner and come up with tailor-made and unique models, resulting in a very fragmented and non-wholistic vision of hydrological processes and their representation in models (Blöschl et al., 2013). While the paradigm of catchment uniqueness is not completely unjustified since no catchments in our diverse nature are perfectly equal in all possible aspects, the Darwinian perspective on landscape and catch-

ment co-evolution (Harman and Troch, 2014; Troch et al., 2015) looks at the development of catchments and at similarities that have resulted.

*Types of similarity*

Hydrological similarity in terms of similarity of hydrological processes is hard to assess due to limited knowledge and measurability (Blöschl et al., 2013). If we assume that runoff signatures result from the interplay of climatic variability and physiographic-structural catchment characteristics, the generic similarity notion can be subdivided into three types: (i) *Climate similarity* that summarizes mean meteorological conditions like mainly water and energy input (e.g. Budyko, 1974; Köppen, 1936; Lvovich, 1979; Thornthwaite, 1931 ), often described by the aridity or dryness index, or indexes at the seasonal scale, (ii) *Catchment similarity* that describes structural characteristics of the landscape such as for instance soil storage capacity, stream network density, area, or the topographic wetness index. The identification of structural similarity is in many cases limited since subsurface structures are effectively unknown (Blöschl et al., 2013), (iii) *Runoff similarity* is a signature of hydrologic functionality and processes, resulting from the combination and complex interaction of characteristics of the first two aspects. Depending on the temporal scale of interest, for example the flow duration curve or mean annual runoff coefficient can be used as similarity indexes (Patil and Stieglitz, 2012). Moreover, depending on the region, geographical proximity can be used as a proxy for all three kinds of similarity (Patil and Stieglitz, 2012), then assuming that for instance climate as well as structural aspects like geology to be similar over larger geographic extents.

*Use of similarity*

While hydrological similarity can be exploited in several ways, it usually serves the goal of obtaining hydrological model parameters for an ungauged catchment. For catchments presumed to be similar in their hydrological functioning, model parameters can be transferred from a gauged donor catchment to ungauged receptor catchment (Buytaert and Beven, 2009; Singh et al., 2014). Runoff signatures can be used to constrain model parametrizations, such as the mean annual water balance (Schaefli et al., 2011). The mean annual water balance is of particular relevance in that regard since the Budyko curve (Budyko, 1974), an aridity-based similarity framework, attempts to predict it by relating climate and runoff similarity for long-term steady-state conditions.

## 1.3 MEAN ANNUAL WATER BALANCE AND BUDYKO CURVE

Hydrological processes and dynamics occur and have different controls at a wide range of spatiotemporal scales, from point-scale soil water fluxes, dynamic small-scale overland-flow driven flood events, to annual water balance dynamics and mean annual conditions of

*Spatio-temporal scales and similarity*

larger catchments (Blöschl and Sivapalan, 1995). In consequence, also similarity characteristics are subject to scale dependence. While in nature all processes and scales are part of a coherent picture, in hydrological sciences, scales are often treated, analyzed and modeled separately. Practical reasons such as computational limitations as well as limited knowledge of small-scale structures and processes condition the simplification and scale separation in modeling.

*The Budyko curve predicts the mean annual water balance*

The mean annual water balance of a catchment is an aggregated signature of dominant hydrological processes, both in time and space. It describes the water partitioning of mean annual rainfall into mean annual evapotranspiration and runoff in a catchment, while storage effects are negligible at long-term steady-state conditions. Reliable a priori estimates of the catchment water balance based on minimum data requirements still represents the holy grail for many hydrologists (Sivapalan, 2003). Budyko (1974) postulated a framework to address this issue, based on a top-down estimate of the steady state energy and water balance of hydrological systems. By relating the normalized actual evapotranspiration to the corresponding normalized atmospheric demand, using rainfall supply for normalization, he observed a considerable degree of clustering around his empirically-derived Budyko curve. The Budyko curve presents a climate-based similarity framework that predicts the mean annual water balance of catchments as a function only of their aridity, i.e. the ratio of mean annual potential evaporation to precipitation. Ever since, the Budyko framework has been successfully used for catchment classification studies at the continental scale (Berghuijs et al., 2014b; Wagener et al., 2007), for reducing equifinality in conceptual models by constraining the catchment water balance (Gharari et al., 2014), or for verifying uncalibrated predictions of the catchment water balance using thermodynamic optimality approaches (Porada et al., 2011).

*Approaches to develop Budyko framework further*

In the quest of finding more universally applicable hydrological frameworks that are invariant over space and time (Ehret et al., 2014; Milly et al., 2008), the Budyko framework has regained attention in recent years (e.g. Berghuijs et al., 2020; Daly et al., 2019; Reaver et al., 2022; Sposito, 2017a; Yao et al., 2020). While the simple supply-demand concept of the Budyko curve is able to explain much of the observed geographic variance, there is considerable scatter around the curve, including also large offsets (Padrón et al., 2017). Offsets from the Budyko curve continue to be subject to research and can depend on various influences, from sub-annual water and energy variability as well as various landscape characteristics (Padrón et al., 2017). One research approach regarding the *Budyko offsets* introduces a supposedly catchment-specific parameter into the equation, constituting the parametric versions of the Budyko framework (e.g. Choudhury,

1999; Donohue et al., 2007; Fu, 1981; Roderick and Farquhar, 2011). It is however difficult to tie all possible influences to one parameter. Recently, Reaver et al. (2022) extensively revisited and criticized this approach in former studies, stating that such fitted relationships are underdeterminded and non-unique, and thus lack transferability.

*Budyko offsets and role of soil storage*

Due to its widely reported success, its simplicity and its theoretical underpinning (Wang et al., 2015; Westhoff et al., 2016), the Budyko curve seemed a useful tool in an environment of scarce and uncertain data like the study region of the TRUST project in West Peru. This thesis is solely based on the non-parametric, original Budyko curve by Budyko (1974) and understanding offsets from a physical point of view. Soil storage capacity, serving as a necessary buffer for water supplying the evapotranspiration process, has been identified in literature as an important control on the mean water balance (Daly et al., 2019; Gentine et al., 2012; Milly, 1994). Conflicting however with a limited ability to assess soil storage capacity at the catchment scale, the present work focuses more in-depth on understanding the role of soil storage in terms of Budyko offsets.

## 1.4 OBJECTIVES AND OUTLINE

The thesis is centered around the applicability of the Budyko curve as well as the assessment and use of similarities between catchments. While methods and approaches address issues both of more theoretical character and with a focus on specific challenges in catchments on the Western flanks of the Peruvian Andes. The present works confront the challenges in the regionalization of precipitation and potential evaporation in a data-scarce region, investigates region-specific water balances and their relationship to the Budyko curve and uses similarity in a hydrological modeling context. The particular role of soil storage controls on the mean water balance and Budyko offsets are addressed separately in a model-based approach. Methodologies are thus conceived and implemented to answer the following main research questions:

- How can we estimate precipitation and potential evapotranspiration in data-scarce and mountainous catchments?
- Can the Budyko framework and catchment similarity be useful in the evaluation of measured and modeled water balances, in reducing model uncertainty in data-scarce regions?
- Does the apparent geographic-structural similarity of catchments along the Western slopes of the Peruvian Andes result in water balance similarity? What are region-specific controls on the mean water balance and related Budyko offsets?

- How does soil water storage and the underlying controls determine offsets from the Budyko curve?

While all chapters are centered around the same goal and build on one another, the structure of the thesis remains fairly modular, providing the four content chapters with its own, more specific introduction.

*Structure and content*

Chapter 2 provides a theoretical overview of the catchment water balance and the Budyko framework and curve, the topic which the subsequent studies are embedded in. Chapter 3 describes the main study area in Peru and data from that region used in multiple chapters. Chapter 4 focuses on the estimation of areal precipitation and potential evapotranspiration, the two fluxes required to assess the catchment's aridity and Budyko estimate of the mean water balance as well as to generate forcing data for the hydrological modeling approach in chapter 5. The chapter's main part consists of the development of a robust precipitation regionalization method for data-scarce and mountainous regions such as the study region in Peru. Chapter 5 adopts a similarity-based paired-catchment modeling approach, comparing the better monitored neighboring Chillón basin to the Lurín basin. Taking into account water balances and Budyko offsets, a parameter transfer is conducted, the Chillón serving as donor catchment. In chapter 6, benefiting from the favorable topographic arrangement, the study region in Peru is widened and water balances of multiple catchments along the Western slopes of the Peruvian Andes are examined, looking also at potential explanations for offsets from the Budyko curve in the region. Chapter 7 presents a model-based study that explores the role of soil storage capacity in the deviations from the Budyko curve. To that end, multiple catchments of varying aridity, mostly from the US and Germany, serve as study catchments in the virtual experiment approach. Cross-chapter conclusions are drawn with respect to the guiding research questions in chapter 8.

# 2

# CATCHMENT WATER BALANCE AND BUDYKO FRAMEWORK

This chapter provides a brief theoretical background to the natural water and energy balance on continents, zooming in on river catchments as main spatial unit of interest (sections 2.1). Temporal scales are introduced to the water balance as well as the Budyko framework and curve, which rely on steady-state conditions and were derived for long-term catchment-averaged values (section 2.3). The third section gives an overview of the nature of deviations from the Budyko curve.

## 2.1 WATER CYCLE AND CATCHMENT WATER BALANCE

At the global scale, the land-ocean-atmosphere continuum represents the system and spatial envelope, in which the total water content remains more or less constant (Marsily, 2009). In our Earth system, the sun constitutes the primary source of energy. Its radiation serves as a driver of atmospheric and oceanic movement, triggering a cascade of complex meteorological and hydrological interaction and exchange processes over a broad range of spatiotemporal scales. The global water cycle is a mechanism where water moves within and between different storage compartments (e.g. atmosphere, oceans, rivers, soils, permeable rocks, glaciers) at varying paces and changing the state of matter (water vapor, liquid water and as ice or snow). Evaporation occurs both over the oceans and continents, and the water vapor stored and transported in the atmosphere eventually falls back onto the surface in the form of precipitation, replenishing oceanic and continental water resources. On the continents, hydrological transformation and redistribution processes ultimately lead to evapotranspiring the water back to the atmosphere or channeling it via stream flow and groundwater flow back to the ocean (see Figure 2.1).

For more detailed hydrological analyses, the global perspective and scale is generally not necessary nor appropriate (Hornberger et al., 2014). The most fundamental and common spatial unit in hydrology is a river catchment. It corresponds to an area of land that collects precipitation and drains this water towards the same river system and outlet. The outlet of a catchment can coincide with any point along the stream (for water balancing purposes, the stream gauges are important points of reference) or with the river mouth where the

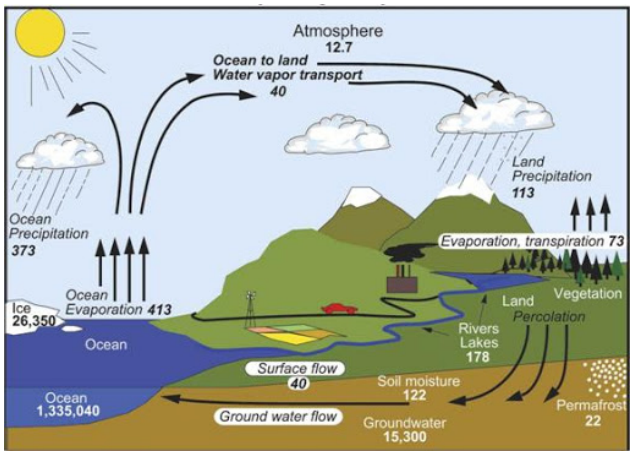


Figure 2.1: The water cycle within the land-ocean-atmosphere continuum UCL, 2021

stream discharges into a higher-order stream or into the sea.

From a system theory perspective, a catchment can be considered an open thermodynamic system (Kleidon and Schymanski, 2008), with defined physical boundaries and exchanging both energy and mass (water) with its surrounding. Complex processes govern the internal system dynamics of a catchment. Its internal structure consists of water storage compartments whose filling levels correspond to state variables (e.g. groundwater level or soil moisture). Catchment-internal fluxes represent water exchanges either within a compartment (e.g. flow in the stream channel) or between compartments (e.g. melting snow infiltrating into the soil).

### *Catchment water balance*

In terms of the water balance, the scale of interest may extend to the catchment as a whole, with catchment-averaged values for fluxes and states. The mass exchanges of the catchment with its surrounding and the integral catchment storage can be summarized as follows:

- **inflows:** Preciptiation ($P$) from the atmospheric environment reaching the ground surface of the catchment, spatially averaged to the extent of the catchment
- **outflows:**
  - Actual evapotranspiration ($ET_a$) from water bodies and land surfaces in the catchment to the atmosphere, spatially averaged to the catchment extent
  - Total runoff $Q$ (surface runoff and groundwater flow) discharging at the system outlet into higher order (Strahler) river system or the sea

- **Catchment storage**: The integral storage term ($S$) combines and spatially averages all catchment-internal water storage compartments, i.e. canopy storage and water stored within the vegetation system, root zone storage, soil water storage in the vadose zone, groundwater storage in the saturated zone, snow pack, glaciers, stream water, lakes and reservoirs. It represents the water volume stored within the system.

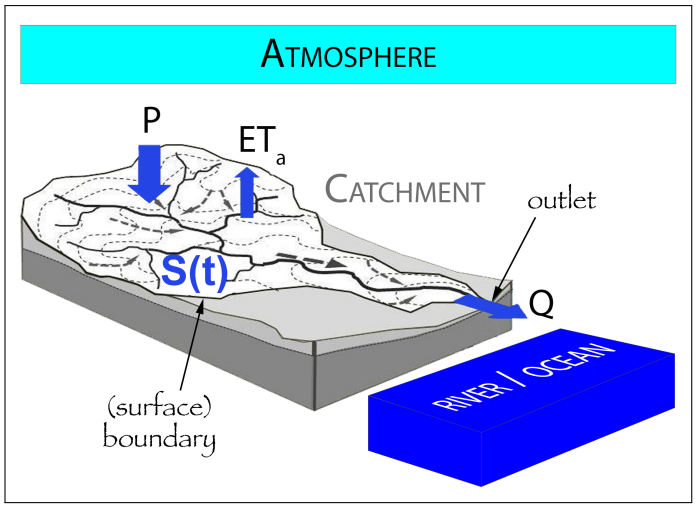


Figure 2.2: Fluxes of catchment water balance and mass exchange with catchment environment and the time-dependent integral storage term $S(t)$ (adapted from Rinaldi et al. (2015))

Figure 2.2 illustrates the water exchanges of a catchment with its surroundings. The catchment represents a contol volume that we can apply the principle of mass conservation to: over a defined period of time, catchment-internal storage changes equal the difference of inflows and outflows of the control volume, as described by Eq. 2.1.

$$\frac{dS}{dt} = I - O, \tag{2.1}$$

with the integral catchment storage S, the inflows $I$ and the outflows $O$. The catchment water balance is thus described by Eq. 2.2.

$$\frac{dS}{dt} = P - ET_a - Q. \tag{2.2}$$

Geographic catchment boundaries are delineated by the surface topography. In the headwaters, the water divides correspond to the mountain crests. The assumption, however, that surface catchment boundaries coincide with the groundwater divides and that a catchment thus represents a mass conservative system does not necessarily hold true, since impermeable hydrogeological formations can differ from surface-topographical constraints (Hornberger et al., 2014).

Such settings would allow intercatchment groundwater flows and exchanges (e.g. Eakin (1966) and Goswami and O'Connor (2010)). The assumption of equal surface and underground divides are however commonly made for lack of better knowledge of subsurface structures.

## 2.2 ENERGY BALANCE AND POTENTIAL EVAPOTRANSPIRATION

This section introduces the energy or heat balance at the surface of a landscape and how it relates to the notion of potential evapotranspiration. Note that here, the term "energy balance" of a catchment refers solely to the energy fluxes associated with and resulting from the radiation budget, and not for instance the kinetic energy of raindrops that is transferred to the catchment or its soil structure during the impact.

For convenience and simplification, we imagine as a control volume a piece of landscape surface, vertically encompassing a few millimeters of soil below it as well as the immediate surrounding air above it (Hornberger et al., 2014). The definition of a control volume allows us to consider a spatially confined sphere, in which the total energy is conserved. Unlike the water balance, the catchment boundaries are not directly relevant to the energy balance. However, they can be used to calculate the total energy intake of the catchment system at its surface.

Extraterrestrial solar radiation hitting the top of the atmosphere undergoes diverse transformation and scattering processes both within the different atmospheric layers and at the ground surface, which on land mainly consists of vegetation, bare soil or a glacial/snow cover. Figure 2.3 illustrates the different energy fluxes and processes.

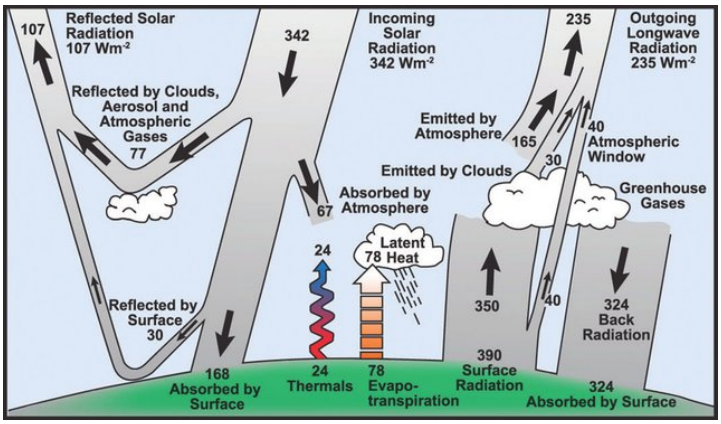


Figure 2.3: Energy balance at the Earth's surface (Follett et al., 2011)

Radiation interacting with matter usually splits into a reflected (scattered) part and an absorbed part, the proportions depending on its wavelength spectrum and the optical characteristics of the target. The radiation budget in the atmosphere-ground continuum has to be understood as a cycle of these energy exchange processes. Atmospheric components like clouds, dust and greenhouse gases absorb both direct solar radiation and outgoing longwave radiation from the Earth's surface, and re-emit the energy as longwave (thermal) radiation. Likewise, the ground surface receives direct, mainly short-wave solar radiation, a part of the scattered short-wave radiation from the atmosphere (termed 'diffuse sky radiation') as well as a fraction of the downward atmospheric longwave radiation. The heating of the soil as a result of the absorption of short-wave radiation provokes the emission of thermal radiation from the ground surface, closing the radiative cycle.

Apart from the radiative exchanges of energy, also other forms of heat transfer occur at the ground surface. A fraction of the absorbed energy is transformed to and released as sensible and latent heat from the ground surface. While sensible heat (thermals) transfers energy through convective heat transfer to the atmosphere, latent heat is stored within the elevated molecular energy state of water vapor, generated through the vaporization of liquid water at the ground surface. The latter describes the evapotranspiration process, which affects the water present in soils, vegetation, open water bodies as well as snow or glacial covers. The word evapotranspiration combines the evaporation of water from bare soils or water bodies (evaporation) and through vegetation systems (transpiration), two vaporization processes of which transpiration is additionally controlled by plant-specific behavior.

With negligible net heat transfer between ground surface and soil (soil heat flux) at daily or longer time scales (McMahon et al., 2013; Sposito, 2017b), the energy balance at the ground surface is described by Eq. 2.3.

$$R_n = \lambda_W ET_a + H, \tag{2.3}$$

with latent heat $H$, latent heat of vaporization of water $\lambda_w$ and the mass of the evaporated water, $ET$, as well as net radiation or the radiation balance $R_n$, which represents the net energy intake at the ground surface. $R_n$ results from balancing net short-wave radiation, $R_{ns}$, and long-wave radiation $R_{nl}$, as given by Eq. 2.4 - each individual term stemming from the balance of all incoming and outgoing radiation at the surface for the two respective wavelength ranges.

$$R_n = R_{ns} - R_{nl}. \tag{2.4}$$

Spatially averaging the components of the energy balance in Eq. 2.3 over the extent of a river catchment yields the energy balance of the catchment.

When all radiative terms are balanced, it becomes apparent from Eq. 2.3 that the maximum energy available to both other heat transfer processes corresponds to the energy surplus, net radiation $R_n$. The proportion between sensible and latent heat is called the *Bowen ratio* and it is primarily conditioned by available soil moisture. When regarding evapotranspiration independently of available and potentially limited soil moisture, net radiation emerges as maximum possible evapotranspiration, the energy-imposed physical upper limit to this water flux.

Apart from net radiation as maximum possible evaporation, the notion of *potential evapotranspiration* has been introduced and used in hydrology. Its definition varies however according to authors and methods (Granger, 1989; McMahon et al., 2013). $R_n$ being the major term providing energy to the evaporation process, other potential evaporation methods also account for the vapor pressure deficit between ground surface and the atmosphere (Monteith, 1965), reflecting atmospheric transport conditions, which might further reduce potential evaporation compared to net radiation $R_n$.

## 2.3 MEAN ANNUAL WATER BALANCE AND BUDYKO CURVE

### 2.3.1 *Steady state*

A catchment is an open system, across whose boundaries water and energy fluxes are exchanged. The two relevant climatic boundary conditions are precipitation as mass input and net radiation (or, as explained in section 2.2, potential evapotranspiration) as energy input to the catchment. Apart from spatially averaging over a defined control volume like a catchment, the temporal dimension of the fluxes and storages are of importance, since dynamics depend on the time scale. While the annual catchment water balance does undergo interannual fluctuations -reflecting dry year-wet year cycles-, these dynamics can be presumed to oscillate around a certain mean value which relates to the aridity of a region or catchment. Catchment storage dynamics are closely linked to these interannual variations, since wet years tend to fill the storages, whereas dry years drain them.

In system theory, the steady-state or stationary state of a system describes a state where there is no change of structure, states and net fluxes both within the system and across its borders. Applied to a catchment's water balance, this translates to zero change of storage

($dS/dt = 0$) and constant fluxes across its boundaries. At steady-state, the water balance in Eq. 2.2 would thus reduce to:

$$\frac{dS}{dt} = P - ET_a - Q \quad |dS/dt = 0 \tag{2.5}$$

$$0 = P - ET_a - Q \tag{2.6}$$

$$\Leftrightarrow P = ET_a + Q \tag{2.7}$$

The catchment energy balance at steady state is provided by Eq. 2.3, in which energy storage terms have already been neglected. As opposed to the water balance, there is no significant storage of energy in the system between the years.

The steady state of a catchment system can be conceptualized and approximated by long-term annual average conditions and time scales, where catchment storage fluctuations average out over the years and become effectively negligible compared to the fluxes. The question of how many years are required to compute such long-term average or mean water balances depends on the interannual variability of annual totals of precipitation and potential evapotranspiration in a region. For the derivation of a mean climate, it is often referred to a time span of 30 years. In equations 2.6 and 2.7, $P$, $Q$ and $ET_a$ thus represent annual average fluxes. Such a climatic characterization of a region or catchment is only valid as long as the climatic conditions, hence the mean values of the two defining variables of annual $P$ and $ET_p$, are stationary, i.e. do not evolve over time.

### 2.3.2 *Budyko hypothesis and equation*

The Budyko hypothesis is centered around the idea that the mean catchment-scale water balance can be expressed and characterized by a more generic formula including climate variables like precipitation and potential evapotranspiration. While Schreiber (1904) empirically developed a functional relationship for the dependence of mean actual evaporation on precipitation and some "empirical constant", it was Ol'dekop (1911) who rewrote the equation and explicitly introduced the aridity index $\phi = ET_p/P$ as independent variable to the function, and by that the concept of *maximum evaporation* (Andréassian et al., 2016). The works of Budyko (1974), a famous Soviet climatologist (1920-2001), underlay these preliminary works with his deep insights and knowledge of atmospheric processes and catchment systems (Sposito, 2017b), and resulted in an equation that corresponds to the geometric mean of the equations by Schreiber and Ol'Dekop. In the following, individual contributions by the authors mentioned above are not explicitly distinguished but together serve to give an overview

of the Budyko framework.

The Budyko hypothesis relies on the steady-state water and energy balance given by the equations introduced in sections 2.2 and 2.3.1,

$$P = ET_a + Q \,(water\, balance) \tag{2.8}$$
$$R_n = \lambda_W ET_a + H \,(energy\, balance) \tag{2.9}$$

It becomes apparent that the actual evaporation term $ET_a$ appears in both equations, it is the flux that links the water with the surface energy balance (Kleidon and Schymanski, 2008). Based on his collection of catchment data, Budyko introduced two limiting conditions to the steady-state water balance of a catchment,

1. $ET_a \longrightarrow ET_p$ as $P \uparrow$ (wet condition)
2. $ET_a \longrightarrow P$ as $ET_p \uparrow$ (dry condition).

Budyko concluded that for long-enough time scales, at steady-state, a functional relationship exists between the mean annual evaporative output of a catchment and its two climatic boundary conditions, $P$ and $ET_p$:

$$ET_a = f(ET_p, P). \tag{2.10}$$

Assuming that Eq. 2.10 is a homogeneous function of its argument and introducing the dryness index $\phi = ET_p/P$, Sposito (2017b) mathematically shows the equivalence and transforms the functional relationship to

$$EVR = \frac{ET_a}{P} = f(\phi), \tag{2.11}$$

with EVR introduced here as mean annual *evaporation ratio*. By doing so, Sposito (2017b) briefly demonstrated the assumption contained in the Budyko hypothesis.

The limiting conditions thus transform to:

1. $EVR = ET_a/P \longrightarrow \phi$ as $\phi \longrightarrow 0$, system is energy-limited
2. $EVR = ET_a/P \longrightarrow 1$ as $\phi \longrightarrow \infty$, system is water-limited

These two limiting conditions present physical limits and span the so-called Budyko space (Figure 2.4), which all mass-conservative catchments at long-term, steady-state conditions theoretically plot in. Catchments or their mean actual evaporation are thus either water- or energy-limited. In other words, the Budyko framework is a supply-demand concept, with the mean annual precipitation input on the supply side and the atmospheric *thirst* for evaporation on the demand

side.

Budyko proposed an explicit function for the relationship in Eq. 2.11, which corresponds to the geometric mean of the equations by Schreiber (1904) and Ol'dekop (1911):

$$EVR = \frac{ET_a}{P} = \sqrt{\phi \cdot tanh(1/\phi) \cdot (1 - e^{-\phi})} \tag{2.12}$$

Eq. 2.12 is today known as the Budyko equation or curve. Figure 2.4 shows the position of the curve within the Budyko space. Budyko used net radiation $R_n$ as energy input and termed $R_n/P$ the „radiative index of dryness", whereas today $ET_p/P$ is used as energy input and it is referred to as dryness or aridity index. If atmospheric transport provides a constant humidity deficit (vapor pressure deficit), $R_n$ is a good approximation of potential evapotranspiration. Budyko (1974) (p. 338) showed that for annual scales, $R_n$ is in good agreement with potential evaporation as calculated with the Penman-Monteith method for his selection of catchments.

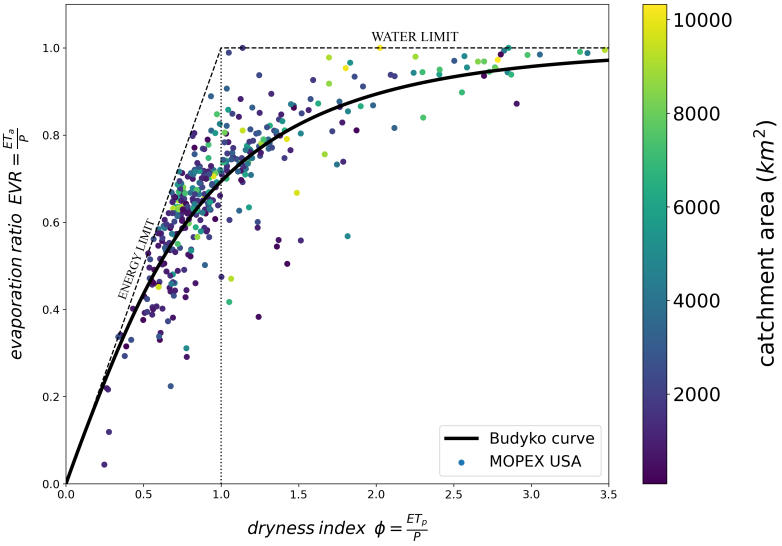


Figure 2.4: Budyko space and curve with catchments from MOPEX multi-catchment dataset

The main reasoning behind the Budyko hypothesis is that climatic dryness, or the relative availability of water and energy implied by it, is a first-order estimator of the mean annual water partitioning in a catchment. In Budyko (1974), Budyko thought in terms of geographic zonality and biomes. He argued that landscape elements such as vegetation and soils, which hydrological process-wise are relevant to evaporation, are on the one hand interdependent and on the other hand considerably conditioned by climatic dryness. In other words, landscape elements evolve, driven by climatic boundary conditions, towards a state where mean evaporation tends to approach a certain

value - in his framework this value is represented by the Budyko curve. The concept of interdependence and coevolution of catchment characteristics has been studied and analyzed multiple times and from different angles (Gentine et al., 2012; Schaefli et al., 2011; Troch et al., 2015; Westhoff et al., 2016), and the Budyko curve is often viewed as one of the few more universal trends and characterizations of hydrological systems.

The Budyko curve thus adopts a Darwinian perspective on catchments and landscapes, as opposed to Newtonian approaches (Harman and Troch, 2014). The Darwinian perspective focuses on more fundamental relationships like the conservation of mass and energy, and tries to find dominant controls that shape and condition a system (a catchment) in an evolutionary sense, which ultimately results in the fine-scale Newtonian processes describable by mechanistic equations. In terms of the Budyko hypothesis and curve, it means that there are no Newtonian constraints for catchments to fill the whole Budyko space spanned by the water and energy limit. However, we observe a clear clustering around the Budyko curve as demonstrated by a large-scale catchment dataset in the USA in Figure 2.4, indicating that climatic aridity is indeed a dominant first-order control of the mean water balances across a variety of geographic zones and landscapes.

## 2.4 DEVIATIONS FROM THE BUDYKO CURVE

While Figure 2.4 appears to corroborate the Budyko hypothesis that climatic dryness serves as dominant first-order predictor for the mean water balance, we also witness considerable spread around the Budyko curve. The variance of the mean annual water balance can be due to natural second-order controls, anthropogenic interference or to estimation errors. The following three sections briefly elaborate on these three influence mechanisms. The term "Budyko offset" here refers to the deviation of the mean annual water balance from the estimate by the Budyko curve - regardless of its causes. In the Budyko space, an offset thus describes a vertical deviation along the y or EVR-axis at the same dryness index.

### 2.4.1 *Natural second-order controls*

If the catchment's climatic dryness index is considered a first-order approximation, biogeophysical catchment characteristics as well as finer-scale spatiotemporal characteristics of the climate are considered and referred to as *second-order controls* on the mean water balance. While the first-order control explains the most geographic variability and is considered to be practically independent, second-order controls

fulfill these two criteria to a lesser extent. Figure 2.5 illustrates how a water balance-relevant second-order control would affect the Budyko position in both directions from the curve.

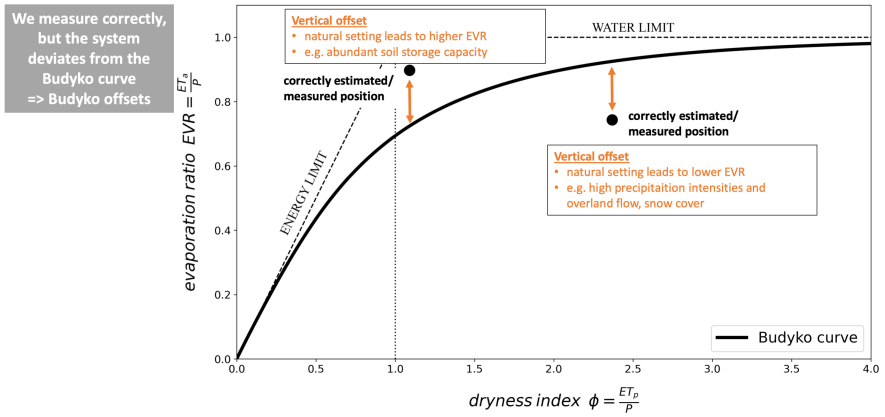


Figure 2.5: Effects of natural 2nd order controls on mean annual catchment water balance in the Budyko space

The attempt to explain in a more general manner offsets from the Budyko curve by identifying the second-order controls has been present in hydrological research for many years. A wide range of possible influences has been suggested and analyzed in studies, a broad overview of which is provided by Padrón et al. (2017). Biogeophysical characteristics include topographic controls (e.g. slope), vegetational controls (e.g. NDVI) and soil-related controls (e.g. water holding capacity). The subscale climate variability-related second-order controls comprise for example seasonality of rainfall and potential evaporation as well as the phase lag between the two (Lavenne and Andréassian, 2018), mean storm depth or snowiness.

While certain studies are based on some form of hydrological or water balance models (e.g. Milly, 1994), the approach of many others rely on parametric versions of a Budyko-type model. Such parametric Budyko frameworks introduce a supposedly catchment-specific parameter ($n$ or $w$) into the Budyko-type equation. Various similar parametric models were developed over the years by (Choudhury, 1999; Fu, 1981; Mezentsev, 1955; Tixeront, 1964; Turc, 1954). Numerous studies use these parameterized equations, relating parameter values to physiographic catchment characteristics by fitting the model to observation data (e.g. Abatzoglou and Ficklin, 2017; Bai et al., 2020; Li et al., 2018). Donohue et al. (2007) used the catchment-specific parameter to incorporate vegetation information (e.g. leaf area, photosynthetic capacity and rooting depth) in the Budyko framework in

order to explain and correct offsets from the original curve. Roderick and Farquhar (2011) used the parametrized equation to investigate changing of climate conditions and catchment characteristics.

However, physiographic catchment characteristics that affect the water balance are manifold and interrelated, and it thus appears difficult if not inappropriate to represent those by a single parameter. Recently, Reaver et al. (2022) reexamined the frameworks and underlying assumptions of parametric Budyko-type approaches. He concluded that these parametric Budyko equations are under-determined and thus non-unique, and that the parameters can change without biophysical catchment characteristics changing and thus not be transferred to other catchments. According to Reaver, such parametric frameworks lack a physical foundation and correspond rather to the results of parameter fitting in limited datasets, resulting in a lack of predictive skill.

### 2.4.2 *Anthropogenic influences*

The general, non-parametric Budyko curve and the idea behind it were developed on the basis of natural, anthropogenically unaltered and widely non-managed catchments. Human intervention in natural systems has its own logic, varies with the human intentions and interests, and thus cannot be generically captured by a framework based on water and energy availability. The following paragraphs briefly describe the different ways, the position of a catchment in the Budyko space can be altered by human activity and how they relate to the meaning of the Budyko curve.

#### *Climate change*

Firstly, the hydroclimatic boundary condition of catchments ($P/ET_p$) can be altered through changes in the global or regional climate. For instance, by releasing carbon dioxide stored in fossil fuels to the atmosphere, mankind is provoking a global warming, a positive trend in the mean atmospheric and oceanic temperature due to an altered radiation balance. This global climatic trend affects regions differently, atmospheric variables relevant both to potential evapotranspiration (e.g. temperature, rel. air humidity) as well as mean precipitation amounts and weather patterns can change (Masson-Delmotte et al., 2021). Even without anthropogenic interference, climate has always been subject to changes and variations, to which the human component is increasingly contributing (Masson-Delmotte et al., 2021). The Budyko curve can be interpreted as a more universal and constant relationship, a perspective according to which all systems are supposed to develop or strive towards the curve (e.g. Schaefli et al.,

2011). In consequence, with a changing climatic boundary condition, one of the quasi-independent drivers of catchment coevolution (Troch et al., 2015), a catchment system would evolve over time towards a new, changed state of mean hydrologic partitioning. Depending on how far-reaching the climatic change is, it might entail adaptation processes of catchment elements like soils and vegetation that take decades and centuries. Hence, in terms of the Budyko framework and of offsets from the Budyko curve, changes in the global climate due to anthropogenic influences do not violate the basic assumption of the framework, they merely alter or accelerate climatic evolution. In that sense, catchment systems can be presumed to evolve along the climatic changes in coherence with the Budyko idea.

*Changes of catchment properties*

A second way of altering the mean water balance of a catchment is by directly imposing changes on the system's elements: Changes in vegetation or land use such as deforestation, afforestation, crop cultivation and all their interactive effects on the soil and microorganisms or on the radiation balance (surface albedo changes). Furthermore, rectifying rivers alters the sediment dynamics and might for example deeply incise river beds which in turn can affect mean ground water levels and humidity (e.g. the Rhine correction). There are many human-made alterations to the natural properties of a landscape and a river that can considerably change the mean water partitioning into evaporation and runoff. The degree of change of the mean water balance logically depends on the alteration's magnitude, e.g. the surface of altered land use, and its functional significance within the complex catchment system. Such alterations of catchments usually do not entail a feedback on the regional climate (Budyko, 1974), unless perhaps vast spatial scales are affected (e.g. widespread deforestation of the Amazonian rain forest). In consequence, regarding the Budyko framework, anthropogenic interventions might alter the natural evolution of the landscape and catchment, which the framework is built on, and introduce new second-order controls on the mean water balance, as illustrated by Figure 2.6.

*Infrastructure directly altering water fluxes*

The third way how humans disturb the natural water balance is by directly altering water fluxes. This form of disturbance is caused by water management measures such as the construction of water infrastructure like dams and reservoirs as well as of artificial channels diverting and redistributing river water. Such measures are usually taken to

- provide water for agriculture (irrigation, livestock),
- provide water for industrial use,
- provide water for domestic use or
- aid in flood prevention.

In semiarid regions with a pronounced rainfall seasonality and resulting stream flow seasonality like in the basins in West Peru, storing water in reservoirs during the rainy season serves the purpose of increasing the water availability and the baseflow during the dry season. Reservoirs, either strengthened natural lagoons or fully artificial dam lakes, thus increase the storage capacity of the river basin. In the semiarid region of Peru, ancient pre-Inca water management systems were found that diverted water from headwater streams to mountain slopes with higher infiltration capacities and a better connectivity to aquifers, thus artificially increasing groundwater resources and the water yield of natural springs during the dry season (Ochoa-Tocachi et al., 2019). When water that has already ended up in the stream channels, is stored and subsequently diverted and re-released onto soils and crops (irrigation), it constitutes a re-transformation from runoff water (generated by system-internal hydrological processes) back to water available to (areal) evapotranspiration. In terms of the mean water balance and the Budyko position, it has an ET enhancing effect, thus causing a catchment to reach higher evaporation ratios in the Budyko space (Figure 2.6).

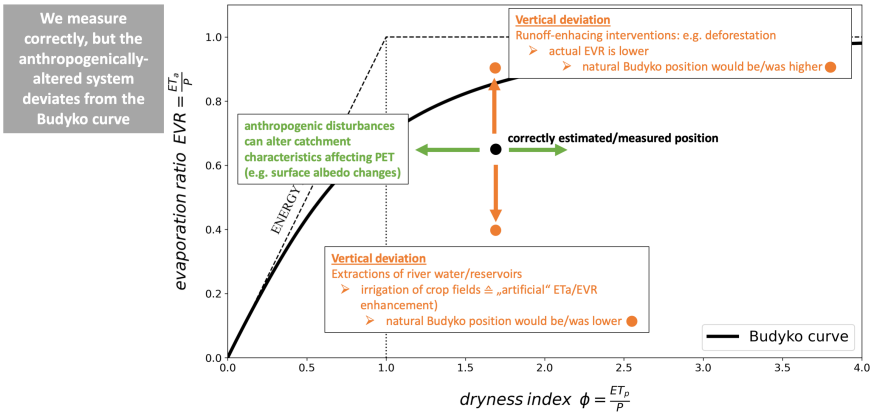


Figure 2.6: Effects of anthropogenic disturbances on the mean annual catchment water balance in the Budyko space

River water diverted to be used by households or industries, is usually re-released to the drainage network, however of lower quality, as greywater. Industries (especially mining) often require an onsite

waste water treatment system to purify it before reintroducing it to the natural system. Quantitatively speaking, it depends on how the waste water is disposed of, if it alters the catchment's water balance. If polluted or partially-treated water is reintroduced in the streams, it will still be part of and measured by the annual accumulated stream flow or the derived mean evaporation of the catchment. If the water is disposed of in evaporation ponds (Prosser et al., 2011), it will impact the mean water balance in favor of evaporation. If water is withdrawn from aquifers, on average depleting groundwater resources, it would mobilize water from the otherwise passive groundwater storage and add it to the active one, also altering the mean annual water balance - towards more stream flow if released to the drainage network, or to more evaporation if used on the fields or disposed of in evaporation ponds.

In general, storing water in open reservoirs with potentially big surfaces (for lack of depth) always entail more losses to ET than would occur by river water flowing towards and discharging into the ocean. In a semi-arid region, these losses can often not be neglected (Friedrich et al., 2018).

If water infrastructure-based alterations of the natural water balance, are to be called or included as a Budyko offset is a question of convention. The resulting water balance alteration and potentially a (more pronounced) deviation from the Budyko curve, would at least be measured as one. However, the general Budyko framework can obviously not account for such human-dependent interventions in the catchment system and water balance dynamics. Hence, if the anthropogenic influence is significant at the mean annual level, it would have to be taken into account when using or considering the Budyko estimate for a catchment.

### 2.4.3 *Effect of estimation errors and uncertainty in the Budyko space*

It is difficult to put numbers on the uncertainties associated with measurement errors. Depending on the equipment and maintenance of a region's monitoring network, combined with the challenges arising from its natural setting, the uncertainties can be considerable. However, the uncertainties have to be assessed and potentially taken into account for each region or catchment individually. Figure 2.7 illustrates schematically the effects of estimation errors for the different catchment-averaged water and energy components in the Budyko space. We assume for the Figure that the evaporation ratio is estimated based on discharge data and the catchment water balance.

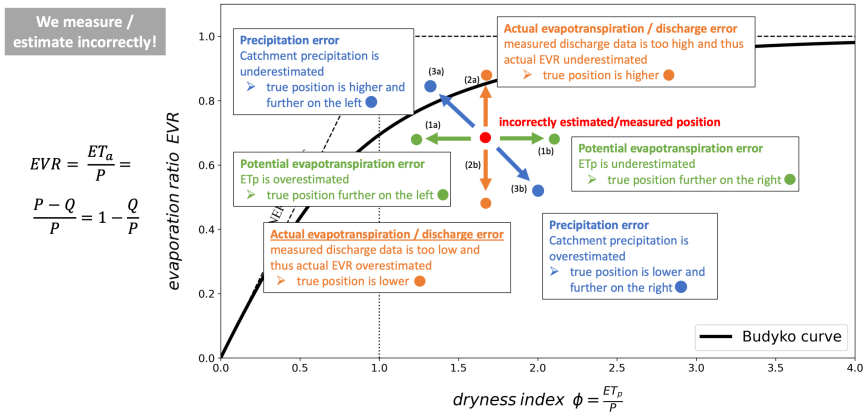


Figure 2.7: Effects of errors in estimating/measuring the catchment water balance components on mean annual catchment water balance in the Budyko space

An estimation error of a component of the catchment water and energy balance, $P$, $ET_p$ and $Q/ET_a$ that yield the Budyko space variables, aridity index $\phi$ and evaporation ratio $EVR$, result in a specific shift in the Budyko space and relative to the Budyko curve. An error in the $ET_p$ estimation produces a horizontal shift along the x-axis, towards a falsely higher aridity index when $ET_p$ is overestimated (case 1a in the figure), or vice versa (1b). An overestimation of mean discharge entails an underestimation of actual evaporation, and results thus in a vertical shift towards a falsely lower evaporation ratio $EVR$ (case 2a), or vice versa (2b). Lastly, an error in the estimation of catchment precipitation affects both Budyko space variables, the aridity as well as the evaporation ratio $EVR$. Moreover, since $ET_a$ is usually derived via the catchment water balance, $ET_a = P - Q$, an error in the precipitation estimate affects also the $ET_a$ estimate itself. Thus, an overestimated catchment precipitation leads to a falsely assumed more humid catchment (further left) and too high an evaporation ratio (case 3b). If the $ET_a$ estimate was derived otherwise and independently of discharge measurements, an overestimated precipitation would result in a lower $EVR$.

Evidently, there can be estimation errors in more than one component at the same time, which would result in the superposition of two or all three effects shown by Figure 2.7.

# 3

# STUDY AREA AND DATA

The first part of this chapter introduces the geographic region of Peru that most of the research is based upon, zooming in on the Western slopes of the Andes and the two basins of Chillón and Lurín. The second part describes hydrometeorological and biogeophysical data used in several chapters for the analyses and studies in this region. Descriptions of additional data and more in-depth catchment analyses are provided in the corresponding chapters themselves.

## 3.1 MAIN STUDY AREA: WEST PERUVIAN ANDES

### 3.1.1 *Peru's geography*

Peru is located at the western coast of the South American continent. Due to massive Andes mountain range, the *Cordillera* (Figure 3.1a,b), the country presents an interesting geographic setting. The North-South extent and arrangement of the Cordillera form a division line for climate and vegetation zones. The country's landscape can thus be subdivided into three main natural zones (Figure 3.1c): The humid east is a tropical rain forest and part of the Amazon basin, characterized by abundant vegetation (greenish zone in the figure). Proceeding East, elevation increases forming the mountain rain forest, presenting a cooler, less humid and less vegetated natural zone (brownish zone). The high mountaineous part then transitions into the increasingly dry and sparsely vegetated Western slopes of the Peruvian Andes, ending up in a coastal desert where the capital Lima is located (yellowish zone).

### 3.1.2 *Climate and meteorology*

Climate in this region is strongly related to elevation. It varies from extremely arid and semi-warm in the lower coastal parts (0-800 m) to very humid and in parts icy in the highest elevations (4800-5000 m). The aridity of the coastal region results from a quasi-permanent inversion of the lower atmosphere due to large-scale subsidence of air masses. The inversion layer effectively inhibits convection and thus rainfall in that region (Trachte et al., 2018). Precipitation on the western slopes occurs mainly in the highlands, induced by moist air masses arriving from the Amazon basin in the east (Trachte et al., 2018). Temporal precipitation patterns show a distinct annual cycle

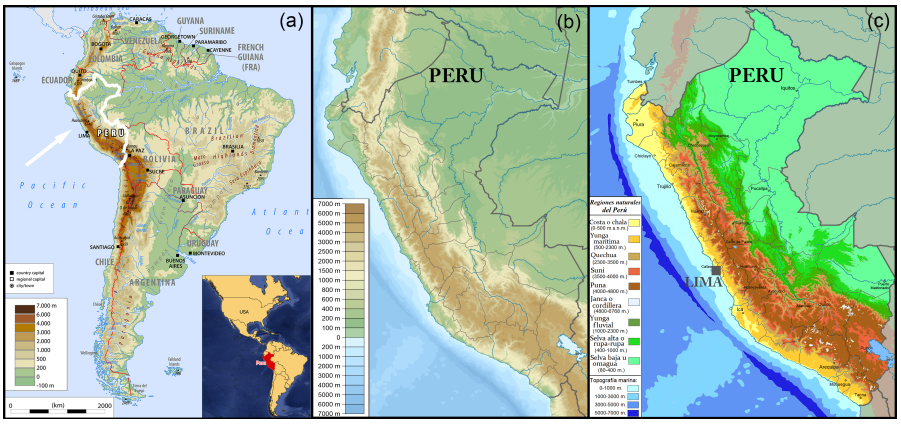


Figure 3.1: (a) South America and Andes mountain range (WorldAtlas, 2018), (b) topographic map of Peru (Wikipedia, 2021b) (c) resulting climate zones and landscape units: greenish tropical/mountain rain forest, brownish: mountain grass and scrubs, yellowish: coastal desert and scrubs (Wikipedia, 2021a)

*Precipitation and seasonality*

with a rainy season during the austral summer months (DJF) and a dry season during the austral winter (JJA). Main rainy months are from December through April, main dry months from June through September, leaving the months in between as transitional phases. The seasonality is induced by the migration of the intertropical convergence zone (ITCZ), the convergence zone of the trade winds. During the austral summer, the rainy season, the ITCZ is located south of the equator and warm moist air from the Atlantic Ocean is transported by easterly trade winds over the Amazon basin to the high central Andes (Trachte et al., 2018). However, the Andean mountains, stretching along the western coast from the north to the far south of South America, disrupt the atmospheric circulation in the region. The height (mean peak elevations above 4000 m a.s.l.) and length of the mountain range impose a strong contrast between its eastern and western slopes (Garreaud, 2009). Most of the rainfall occurs on the eastern side, as part of the tropical rainforest, while the western slopes experience a rain shadow effect (Trachte et al., 2018). Leeward, on the western slopes, precipitation decreases with lower elevations due to sinking of arriving air masses and the stronger influence of the convection-hindering inversion of the lower troposphere. During the austral winter the region experiences its main dry season. The ITCZ, now located further up north and the well-established South Pacific High, associated with a subsidence inversion, suppresses convection. In addition, during the austral winter, upper-level westerly flows reduce the westward transport of moist air from the east and thus amplify the rain-shadow effect (Trachte et al., 2018). As a result, there is little to no precipitation on the western flanks of the central Andes during the austral winter.

*Temperature*

Like precipitation, temperature is also closely linked to the elevation. In latitudes where Lima is located, daily maximum temperature in the lower elevations is about 21 °C and drops down to 10 °C in the highest parts, the seasonal fluctuations being more pronounced in the lower parts (Observatorio del Agua, 2018).

*ENSO anomalies*

In terms of interannual variability, the occurrence and influence of the El Niño Southern Oscillation (ENSO) phenomenon is relevant in the region. ENSO describes a complex coupled atmosphere-ocean mechanism, leading to anomalies in the surface temperature in the equatorial Pacific and in global atmospheric circulation patterns. Anomalies in both directions from the mean temperature (alternations between El Niño and La Niña periods as opposed to neutral situations) occur in non-regular periodicity. Across the Pacific ocean, there are different impact regions of ENSO (Sanabria, 2018) in terms of ocean temperature anomalies (Figure 3.2). While a *global* Niño is related to central Pacific temperature anomalies and causes global effects, a *Niño costero* provokes more localized anomalies (Region 1+2 in Figure 3.2, directly in front of Peru's west coast) (Ramírez and Briones, 2017; Takahashi, 2017). The impacts of ENSO dynamics on smaller regions in terms of weather patterns and rainfall events or other atmospheric variables are non-trivial. The Niño costero in 2017 is supposed to have led to heavy rainfall events and subsequent flooding in 2017 in the region (Ramírez and Briones, 2017).

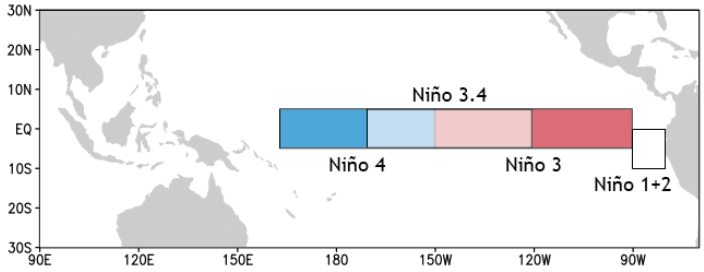


Figure 3.2: ENSO regions: Region 1+2 is adjacent to Peru's coast (Sanabria, 2018)

### 3.1.3 *Western slopes of Andes, Chillón and Lurín basin*

The wider hydrological study area is located between the Andean mountain range, the East-West water divides, and the Pacific ocean, where numerous rivers basins have formed. In this thesis, this area is referred to as *Western slopes or Western flanks of the (Peruvian) Andes*. Most basins exhibit a steep topographic gradient, with headwaters located in the Andean highlands at up to 4000-6800 m and the river mouths at sea level, over short distances of around 75-150 km (Figure

6.1).

Three of these basins, located in the wider area around Lima, supply the capital with drinking water: Chillón, Rímac and Lurín (Figure 3.3). Since runoff and water balance of the Rímac basin are altered by a trans-andean tunnel transporting water from a basin on the side of the mountain range (Alto Mantaro), more in-depth hydrological studies were conducted only for Chillón and Lurín.

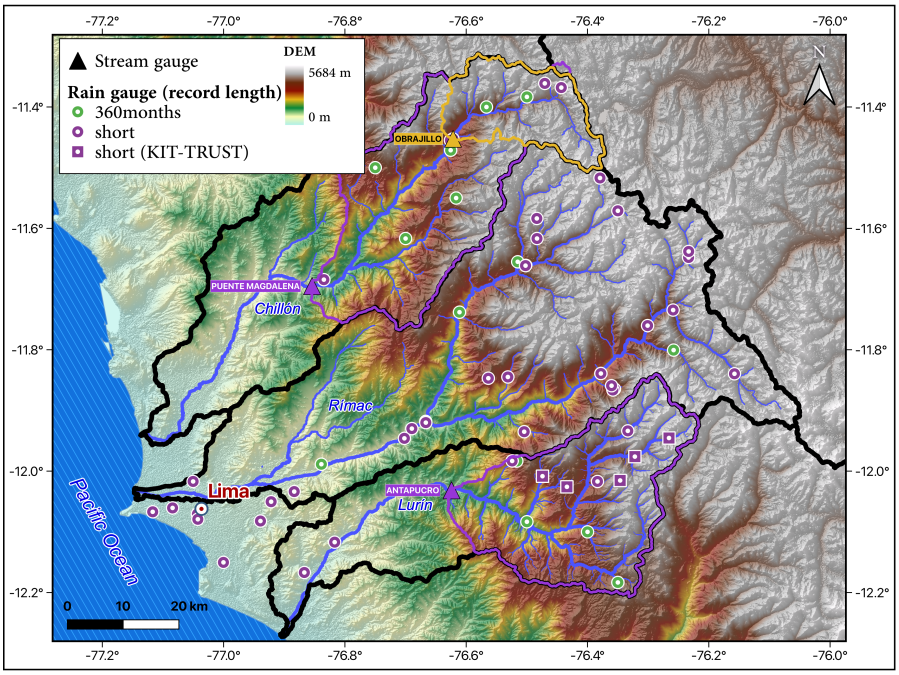


Figure 3.3: Overview map of Lima area and the adjacent Chirilu basins.

Figure 3.4 schematically presents a perceptual model of the Lurín basin and its functional sections, which is in its essence also valid for the Chillón basin. Most of the rainfall input occurs in the highest parts of the basin, transitioning into zones where runoff is increasingly concentrated. In the area below the lower stream gauges (Antapucro in the Lurín, Puente Magdelana in the Chillón), there is no more significant rainfall input. In consequence, hydrologic transformation processes, the partitioning of rainfall into evapotranspiration and runoff occurs predominantly within those gauged subcatchments. Further downstream in the basin, the river water is merely routed through the main channel, towards the coast, flowing across the increasingly urbanized areas. In addition, in the valleys' alluvial deposits in the flatter zones, which form a sedimentary aquifer along the streams, river water infiltrates into the ground and recharges the aquifer (see Figure 5.17). Both for agricultural and drinking water purposes, significant amounts of groundwater is pumped up through numerous wells in those sedimentary layers. These surface-groundwater interactions concern a different hydrologic and water management topic. Therefore, the research of

this thesis is limited to the subcatchments of Puente Magdalena and Antapucro.

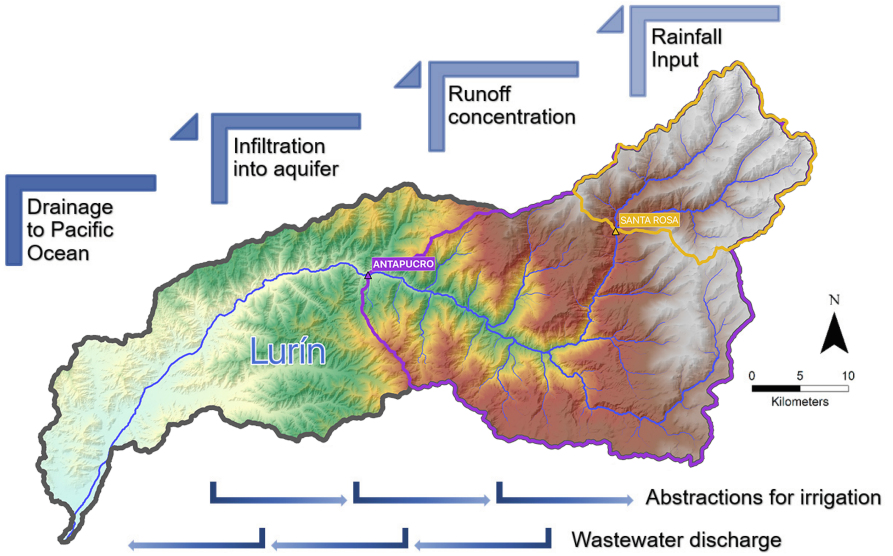


Figure 3.4: Perceptual model of water resources in the Lurín catchment, which are stem from and are replenished by the rainfall in the upper catchment. The zones are separated for illustration purposes, whereas in reality they are transitional and overlapping (adapted from Leon et al. (2021))

## 3.2 DATA

Table A.1 in appendix section A.1 provides a quick overview of all external data and datasets used for studies and analyses in Peru, that are described in the following.

### 3.2.1 *Meteorological data*

*PISCO-P, national precipitation product*

The PISCO-P dataset is a national gridded precipitation product provided by SENAMHI that covers the entire country of Peru at a spatial resolution of 0.1°. Data is available at daily and monthly resolution. The version "PISCO Prec v2p1 stable daily" (1981 to 2018) was used in the study (Aybar et al., 2020). PISCO determines precipitation based on data from three different sources: the national quality-controlled and infilled rain gauge data set, climatologies based on the TRMM data, and the Climate Hazards Group Infrared Precipitation (CHIRPS) estimates. The merging algorithm uses different deterministic interpolation methods for daily and monthly data, namely residual inverse distance weighting for daily rainfall, and residual ordinary kriging

for monthly rainfall. For further information, it is hereby referred to Aybar et al. (2020).

*PISCO-$ET_p$, national potential evapotranspiration product*

PISCO-$ET_p$ is a gridded national potential evapotranspiration product, generated in the same project and research effort as the precipitation product PISCO-P. However, this data product lacks proper documentation. According to Llauca et al. (2021), the product relies on the Hargreaves-Samani method (Samani, 2000). Given the wide spatial extent (national) of the product and the general data scarcity in the country, it seems reasonable to assume that it was generated on the basis of interpolated or satellite-inferred $T_{min}$ and $T_{max}$ surface temperature fields, as well as literature-based or otherwise derived Hargreaves-Samani coefficients.

*Rain gauges & weather stations in Chirilu basins*

Daily precipitation data from a total of 67 rain gauges at various altitudes were available (Figure 3.3). Some of the stations are additionally equipped with monitoring devices for other atmospheric variables such as temperature, wind speed, solar radiation, varying however in the composition of devices. The whole rainfall dataset covers nearly 57 years, from August 1963 until January 2020. However, due to different lengths of the time series as well as gaps, the individual records of the stations varied in the number of valid data points. 16 stations had records of at least 360 months (30 years), 50% of the remaining stations covered at least 5 years, the other half less.

Most data were provided by the Peruvian Meteorological and Hydrological National Service SENAMHI (Servicio Nacional de Meteorología e Hidrología del Perú). Other stations are operated by the power company "Enel Group Peru" or the drinking water supplier of Lima metropolitan area, SEDAPAL. In addition, as part of the TRUST project, the Karlsruhe Institute of Technology (KIT) set up five rain gauges and one well-equipped weather station in the higher parts of the Lurín basin (KIT stations represented by square symbols in Figure 3.3).

### 3.2.2 *Streamflow data*

*Multiple catchments along Western Slopes of Peruvian Andes*

For monthly streamflow data from multiple catchments along the Western slopes of the Peruvian Andes, an online database by the Columbia

university provided a collection of SENAMHI data (SENAMHI, 2020). However, the streamflow data accessed in 2020 have in the meantime been removed from the online portal.

*Chillón and Lurín*

Daily stream flow data for gauges in the Chillón and Lurín basin were taken from the SENAMHI web database (SENAMHI, 2019). In the Chillón basin, streamflow data was retrieved for the Puente Magdalena and Obrajillo as headwater gauge. From the year 2002 on, the two stream gauges have data records of around 16 years, with data coverages of around 84% and 100%, respectively (Figure 3.5).

As depicted in Figure 3.3, prior to the TRUST project there had only been one active stream gauge in the Lurín river (Antapucro). The records of the Antapucro stream gauge effectively covered only 2,5 hydrological years, since the sensor broke down during an intense flood event in March 2017. A new, contactless water level sensor was installed in June 2018 at the Antapucro bridge, complementing the discharge records with a data gap inbetween of around 15 months.

### 3.2.3 *Biogeophysical data*

Biogeophysical data used for the studies in the Peruvian region comprise a variety of different datasets, generated from satellite data, field data or their combination.

*Topography and catchment delineations*

Topographic information is derived from a global digital elevation model (DEM) of 12 m spatial resoluton for the Lurín basin (German Aerospace Center (DLR), 2016), and of 30 m resolution (NASA, 2001) for all other basins. Upon that basis, catchments were delineated and other topographic attributes (e.g. slopes) were derived.

*Vegetation and land cover*

Lastly, three kinds of vegetation and land use information were incorporated in our modeling and analysis datasets. Firstly, a national GIS map, likely derived from satellite data, illustrates vegetation zones (Figure 5.13). Secondly, NASA's remote sensing MODIS product provided gridded leaf area index (LAI) data in 8 days time steps (Myneni et al., 2015), which is a common indicator for seasonal vegetation

dynamics reflected by the variations of the vegetation cover.

*Snow cover*

The *MOD10A1* remote sensing product by NASA MODIS (Hall and Riggs, 2021) was used to detect snow cover on the Western Andean flanks. The NDSI snow cover index of that product ranges between 0 and 100, indicating the fraction of snow cover detected in a 500x500 m grid cell. It is based on the difference of visible reflectance (very high for snow cover) and shortwave infrared reflectance (very low for snow cover). 100 indicates a grid cell fully covered with snow, 0 a completely snow-free grid cell.

*Soils*

With regard to soils, two different data sets were retrieved. On the one hand, there is a national GIS map, likely originating from terrain mapping, subdiving space into rather coarse groups of presumably homogeneous soil types (Figure 5.11). On the other hand, a global database with gridded soil texture and bulk density data for different soil layers was used (Poggio et al., 2021). The soil data was generated by a machine learning-based interpolation procedure, including climate, land cover and terrain morphology as auxiliary predictors for the interpolation between measured soil profiles.

*Hydrogeology*

Information on hydrogeological units was obtained by a national hydrogeological map (ANA, Autoridad Nacional del Agua, 2017). The map was created from a geological map, which served as a basis to categorize the different geological formations with regard to their hydraulic conductivity, into groups of aquifers and aquitards as well as the basic rock type (e.g. sedimentary or volcanic) it is composed of. In addition to the hydrogeological formations, the location of groundwater sources and wells were extracted from a GIS database (ANA, Autoridad Nacional del Agua, 2017).

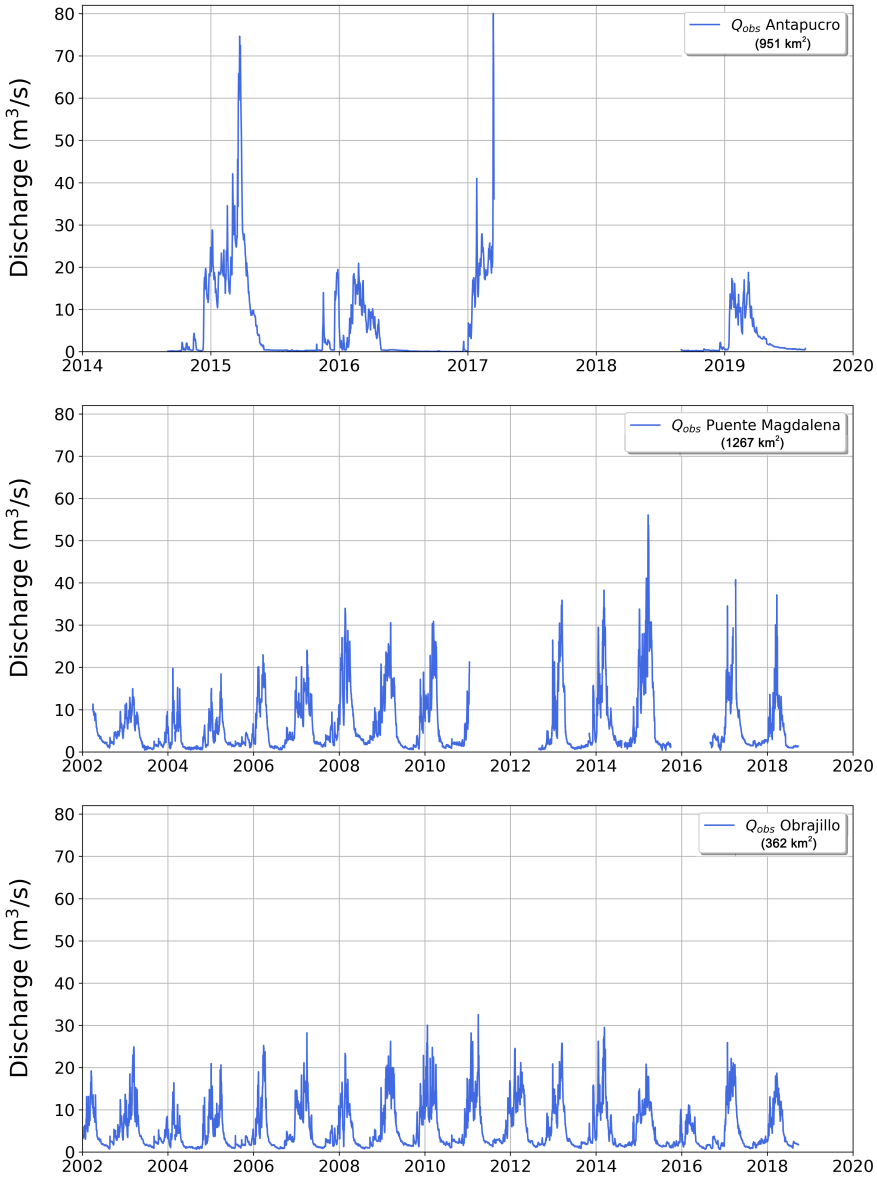


Figure 3.5: Chillón and Lurín basins: discharge records of two Chillón gauges (Puente Magdalena and Obrajillo), and one Lurín gauge (Antapucro)

# 4

# ESTIMATING CATCHMENT WATER AND ENERGY BALANCE COMPONENTS IN A DATA-SCARCE ENVIRONMENT IN THE PERUVIAN ANDES

This chapter presents methods regarding the estimation of water and energy balance components in data-scarce and mountainous regions like the Western slopes of the Peruvian Andes.

Primarily, a robust, statistical rainfall regionalization model named *CovVar model* is introduced, responding to particular challenges arising in poorly monitored regions, and subsequently applied to the two basins of Lurín and Chillón. The works related to the development and testing of the model were carried out by Alcamo (2019) in the framework of a Master thesis, embedded in the research efforts of this doctoral thesis. While the following section presents the most relevant findings and the regionalization approach itself, for more details and analyses it is hereby referred to Alcamo (2019).

For potential evapotranspiration, the Hargreaves-Samani method is applied via a regional and seasonal calibration, using short potential evapotranspiration time series based on the Penman-Monteith method from recent monitoring data to produce long historic time series. The data analysis and calibration works for this approach were conducted by Oezgür (2020) in the framework of a study project.

## 4.1 COVVAR MODEL DEVELOPMENT FOR PRECIPITATION REGIONALIZATION

Predictive skill and corresponding uncertainty of hydrological models strongly relate to the accuracy of spatially distributed precipitation input data (Arnaud et al., 2002; Das et al., 2008). In most hydrological applications, estimates of spatially distributed precipitation are based on a limited number of rain gauges spread across a river catchment or region of interest. In order to obtain spatially distributed precipitation estimates, an interpolation or regionalization of the point-wise measurements is required. In general, the choice of the interpolation method as well as its quality depend on the spatial scale, the density of the observation network, the topography of the area, and the nature of the variable to be interpolated (Herrera et al., 2019; Ly et al., 2013).

*Increasing use of remote sensing*

Satellite-based remote sensing techniques today increasingly play an in precipitation estimation, mainly due to their global coverage and availability in data-scarce regions. While such data can be used well for spatial patterns, especially in larger catchments, they come with substantial shortcomings in terms of the reliability of quantitative estimates (AghaKouchak et al., 2010). The quality of remotely sensed precipitation also depends on the geographic setting, as it tends to be more reliable in flat and humid areas (Anagnostou, 2004; Hu et al., 2019).

*Spatial covariance, deterministic vs. probabilistic interpolation approaches*

Precipitation estimates, in particular in a mountainous region like the Western slopes of the Peruvian Andes, thus still primarily rely on the regionalization of point-wise rain gauge measurements. There is a wide range of different interpolation approaches proposed in literature, which can coarsely be grouped into conventional deterministic models as well as probabilistic geostatistical methods. Basic univariate, deterministic interpolation models like Thiessen polygons use only the value of the nearest station (nearest neighbor), and an inverse-distance weighting (IDW) interpolates a value via a weighted average of several neighboring stations, the weights being higher with increasing proximity. Multiple regression interpolation models incorporate in some way auxiliary data with predictive skill on spatial trends of rainfall fields (Hu et al., 2019). However, statistical information "hiding" in the datasets, for example the spatial variance of the data (AghaKouchak et al., 2010; Zehe et al., 2005), is not exploited by deterministic interpolation methods, as opposed to geostatistical or kriging approaches. The basic Kriging interpolation procedure also relies on a weighting. The weights are however determined on the basis of a semivariogram, which describes the spatial covariance of the variable of interest (rainfall) (Arnaud et al., 2002; Matheron et al., 1962). When the underlying statistical assumptions are met, kriging offers the advantages of minimized estimation variance and prediction error estimates, but is computationally more demanding. However, if for instance the spatial covariance structure stems from different types of precipitation events -e.g. convective or frontal cyclonal- it can be difficult to obtain representative variograms (Haberlandt, 2007; Verworn and Haberlandt, 2011), plus kriging is both more challenging in data-scarce regions (Aybar et al., 2020) and not always outperforming simpler, deterministic methods (Ly et al. (2011), Dirks et al. (1998)).

*Geostatistics and and covariance structure*

*Accounting for spatial trends like the orography*

If there are spatial trends or anisotropy in the dataset, the interpolation will yield better results if accounted for in the approach. In many cases, as well as in our study region in West Peru, the orography has a significant influence on spatial rainfall patterns and statistics. This topographic information can be included with different methods, from pure regression techniques to multivariate cokriging. The linear

regression approach in the PRISM model (Daly et al., 1994) uses topographic facets with similar slope orientation, and was found to produce less statistical error in the cross-validation than geostatistical models. Buytaert et al. (2006) analyzed rainfall patterns in South Euadorian Andes and found that the impact of including correlations of rainfall patterns with topography outweighs the effects of different interpolation methods.

*Contribution and outline*

The multitude of approaches used and tested in different regions suggests that the choice of precipitation regionalization approaches should result from an analysis of region-specific hydrometeorological conditions and limitations of the monitoring network and data. The present work introduces a novel, robust alternative approach named the "CovVar" model to regionalize precipitation data in data-scarce regions where rainfall statistics correlate strongly with elevation. The approach essentially relies on the regionalization of the monthly precipitation mean in combination with the use of spatially correlated temporal precipitation fluctuations. Initially, spatiotemporal rainfall patterns and statistical relationships are analyzed. On that basis, the CovVar modeling approach is developed and applied to the main study basins, Lurín and Chillón. A model evaluation is performed by means of a cross-validation, as well as a annual rainfall totals and a qualitative evaluation of interpolated rainfall maps, comparing it to the national gridded PISCO rainfall product (Aybar et al., 2020).

### 4.1.1 *Methods*

*Data and preprocessing*

For the analysis of rainfall patterns and statistical relationships as well as for the interpolation model developed on that basis, rain gauge data from the three catchments of Chillón, Rímac and Lurín were used. For the derivation of statistical relationships, the method requires sufficiently long, point-wise rainfall measurements. A threshold of 30 years was set to derive stationary mean values, resulting in 16 stations fulfilling this criterion (see section 3.2.1 and Figure 3.3). The precipitation data were aggregated to annual and monthly rainfall totals. The national gridded precipitation product PISCO was employed in the model evaluation, as a benchmark (section 3.2.1).

The 30 m DEM was used to infer elevations 3.2.3. For the rainfall interpolation, a version aggregated to a resolution of 1000 m was employed.

*Variogram analysis*

A precondition for the applicability of kriging is a meaningful semivariogram, which essentially determines the explanatory quality of any interpolation (Aidoo et al., 2015). In order to evaluate a potential kriging approach, experimental semivariograms were computed and analyzed, based on the classical Matheron estimator (Matheron et al., 1962).

*Model validation*

In order to evaluate the performance and assess the predictive skill of the CovVar interpolation model, the method was applied and generated daily rainfall time series. By means of a *leave-one-out cross validation*, the model was evaluated quantitatively. This method is based on removing one data point from the set of $N$ data points, applying the interpolation to the reduced data set of $N-1$ data points and comparing the simulation result to the observed data at the missing point. This procedure is applied to each data point (Marcotte, 1995).

The following criteria were applied to quantify and compare the performance of the models:

- Root-Mean-Square Error (RMSE), normalized to standard deviation
- Ratio of the mean precipitation accounted for by the model
- Ratio of the variance of the observed values accounted for by the model
- Ratio of the annual peak precipitation accounted for by the model

In the case of the RMSE, a lower value indicates more reliable estimates of the respective model. For the other criteria a ratio of 1, i.e. 100%, indicates a perfect model performance for the respective criterion. As a simple measure for the representation of observed daily peak precipitations in the model, the 'annual peak precipitation", i.e., the highest observed daily precipitation value in a given year, is compared to modeled precipitation on that same day.

### 4.1.2 *Spatiotemporal rainfall patterns and statistics*

*Elevation dependence*

Annual average precipitation ranges from 0 mm/a at lower altitudes to around 700 mm/a for the highest stations (Figure 4.1a).

For elevations between 0 m and around 1500 m, the annual average precipitation totals are very small, approaching zero, and show no discernible correlation with elevation. Above an elevation threshold of approximately 1573 m, there is a near-linear increase of annual average precipitation totals with elevation. A linear model containing an automatically-derived breakpoint (Muggeo, 2003) was fitted to the data, explaining 91% of its variance.

The variance of monthly precipitation shows a trend similar to that of annual mean precipitation (Figure 4.1b). The variance in higher elevation ranges increases with elevation, while for lower elevations the variance is generally low and shows no dependence on elevation. In addition, the variances of stations at higher elevations show a larger spread than the lower ones. Again two linear functions were fitted and a breakpoint was determined at 1976 m, in order to describe the threshold-like relationship found in the elevation dependence of the monthly precipitation variance. The linear model describing the elevation-dependence of the variance in higher altitude reached an $R^2$ of 89%.

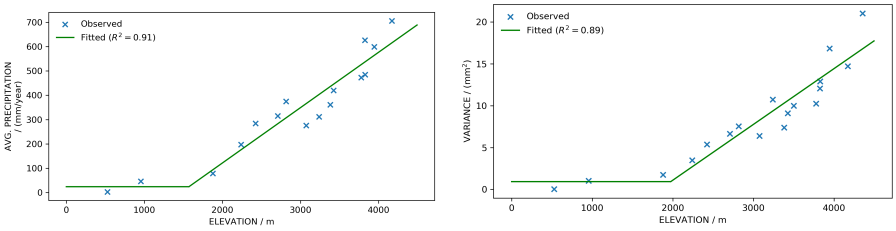


(a) Elevation-dependency of mean annual rainfall totals. Linear function fitted. 16 stations used with more than 30 years of data

(b) Elevation-dependence of monthly precipitation variance, two fitted linear functions with elevation threshold determined at 1976 m

Figure 4.1: Elevation dependence of annual mean precipitation and variance (Alcamo, 2019)

The elevation dependence of mean precipitation was also explored at the monthly scale, separately for each month of the year. There is a significant linear correlation between elevation and monthly average precipitation for rain gauges above a certain elevation threshold (Figure 4.2), similar to the trend observed for annual average precipitation (Figure 4.1a). While this trend exists throughout the whole year, the difference in magnitude between above- and below-the-threshold rainfall is considerably more pronounced during the rainy season. The elevation threshold (breakpoint) itself varies significantly throughout the year, reflecting the seasonality of the weather patterns in terms of the thickness of the inversion layer that inhibits precipitation. While the threshold is comparably low during the rainy season, ranging from 1000 m to 2000 m with its minimum of approx. 1100 m in

February and March, it rises up to around 4000 m during the dry season. The movement of the breakpoint implies also the variation in the fraction of the rainfed part of the region or the river basins. Based on Muggeo (2003), two linear functions were fitted to describe the threshold-like dependence for each month. For precipitation below the elevation threshold, in the absence of a detectable pattern, precipitation estimates were modeled as a horizontal linear function, representing a constant average throughout this elevation range. Monthly averages in the lower elevation range vary between 0 and 10-20 mm per month. Precipitation is highest and the breakpoint ist lowest during the months December until March. The months with lowest mean precipitation and highest breakpoints are go from May through September. The variances explained by the linear models for the higher elevation range are generally high, with a minimum of 74% in October and a maximum of 93% in July, February and March.

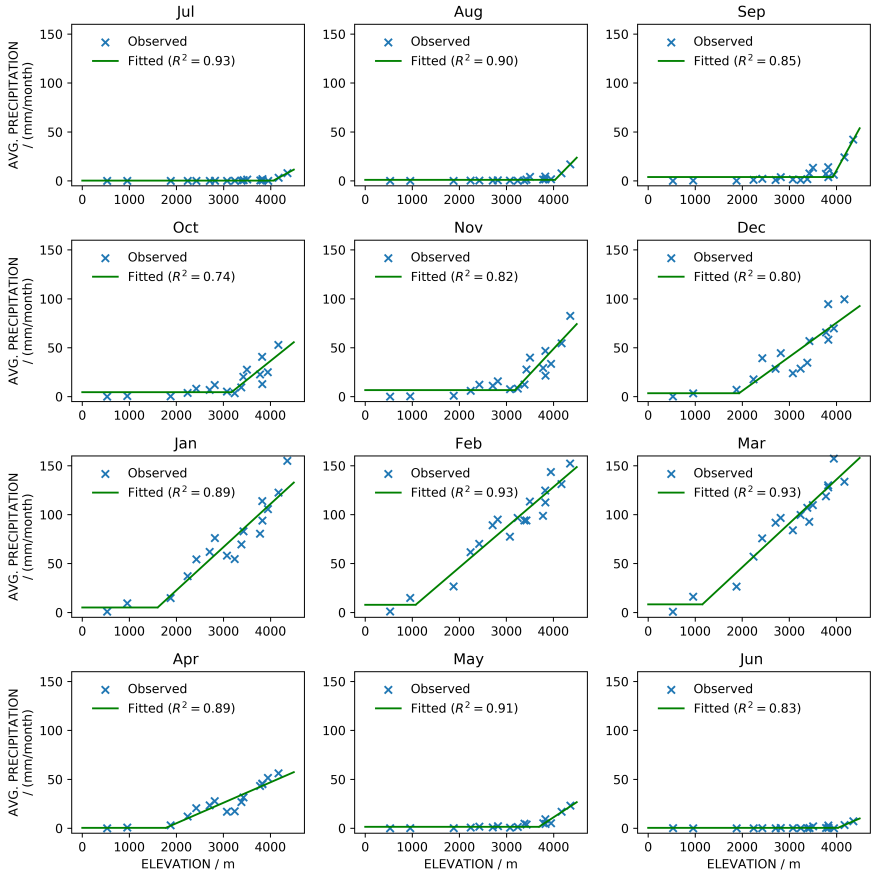


Figure 4.2: Elevation dependence of monthly rainfall totals in the study area. Linear functions fitted, only stations used with more than 30 years of data for each plot, stations with 0 mm precipitation were not considered to determine $R^2$ (Alcamo, 2019)

*Variogram analysis*

The variogram analysis based on monthly rainfall totals did not reveal consistent-enough covariance structures that would allow for a meaningful application of kriging. As shown in Figure 4.1b, there is a pronounced elevation trend in the variance of the precipitation data, violating the second-order stationarity condition for variograms and rendering a kriging-based interpolation unfeasible. An application of kriging relies on the premise that the point-wise measurements of rainfall result in a variogram in which the semivariance monotonically increases with increasing lag distance, until the range is reached and the spatial correlation fades. However, as demonstrated by four variogram examples for the month of December (Figure 4.3) -the onset of the rainy season-, there are meaningful ones (subFigures 4.3b and 4.3d), and others with an opposite, non-meaningful and non-exploitable semivariance structure (subFigures 4.3a and 4.3c).

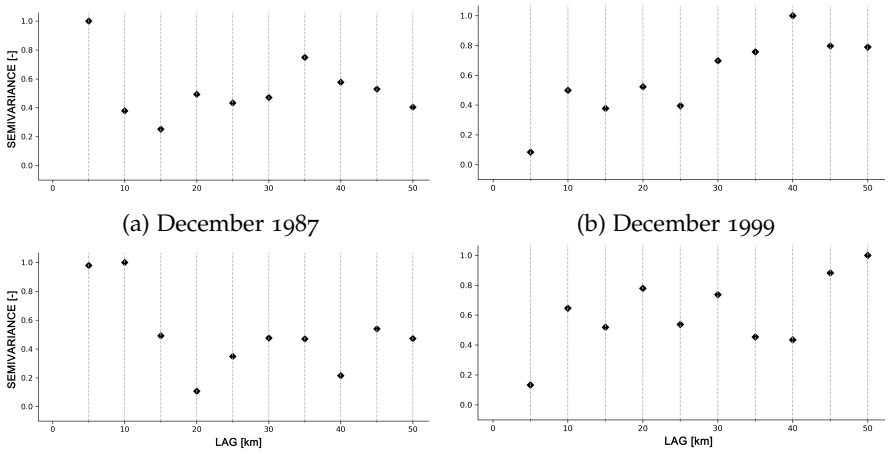


(a) December 1987 (b) December 1999

(c) December 2012 (d) December 1988

Figure 4.3: Selected variograms for monthly precipitation. Elevation-dependent trend was removed beforehand and semivariance was normalized to the respective max. Only stations above 1573 m were taken into account, since no meaningful spatial correlation was detected below that elevation threshold even at the annual scale (max. lag = 50 km, estimator="Matheron") (Alcamo, 2019)

### 4.1.3 *The CovVar model*

The basic assumption of the linear model is that precipitation at a certain point and time, $\hat{P}(\vec{r}_i, t)$, can be expressed by the sum of the elevation-dependent mean precipitation of the corresponding month, $\bar{P}(z(\vec{r}_i), m)$, and a time-dependent fluctuation, $\hat{P}'(\vec{r}_i, t)$, as described by Eq. 4.1. The approach is called Reynolds decomposition, in which the fluctuation's mean is to be zero.

$$\hat{P}(\vec{r}_i, t) = \bar{P}(z(\vec{r}_i), m) + \hat{P}'(\vec{r}_i, t), \tag{4.1}$$

where $\vec{r}_i$ is the geographic location of a point $i$ and $z(\vec{r}_i)$ its elevation, $m$ the month of the year and $t$ the time step.

The monthly elevation-dependent mean, $\bar{P}(z(\vec{r}_i), m)$, is determined using a linear regression model, exploiting the linear correlation between elevation and the average monthly precipitation total for each of the twelve months of the year. Resulting from the elevation-monthly precipitation relationship, each geographic location is assigned a monthly mean precipitation. If the model is applied at the daily scale, an elevation-dependent mean daily precipitation is derived for each day of the year, by dividing the monthly elevation-dependent mean by the number of days of the respective month. Hence, also at the daily scale the monthly statistics are decisive. To what degree this uniform disaggregation of mean monthly to mean daily rainfall depends mostly on the number of rainy days in a month.

The deviation of the precipitation at a specific location and time step (month or day) from its elevation-dependent mean is calculated using the deviation at the nearest available station (reference station) at this time step from its own elevation-dependent mean, $P'(\vec{r}_s, t)$, scaled with a factor $c$ which depends on the elevation difference between the interpolation location and the nearest station, $h$:

$$\hat{P}'(\vec{r}_i, t) = P'(\vec{r}_s, t) \cdot c(h) \tag{4.2}$$

$P'(\vec{r}_s, t)$, reflecting the precipitation fluctuation at the nearest station, is calculated by subtracting the monthly elevation-dependent mean $\bar{P}(z(\vec{r}_s), m)$ from the observed value at the respective time step. The nearest station is determined on the basis of a Voronoi diagram.

As scaling factor c for the regionalization of the precipitation fluctuation, the "CovVar coefficient" is introduced. It emerged from the criteria that it is dimensionless and takes into account that stations at higher elevations tend to have higher precipitation as well as a higher variance. The CovVar coefficient equals the covariance of two stations, normalized with the variance of one of the two. The CovVar coefficient quantifies the temporal correlation between two random variables at two different locations with elevations $z_i$ and $z_j$. The scaling factors are thus described by the matrix $C$ whose elements are defined as:

$$c_{ij}(h_{ij}) = \frac{Cov(P_{z_i}, P_{z_j})}{Var(P_{z_i})}, \tag{4.3}$$

with $P_{z_i}$ as mean monthly precipitation of a reference station at elevation $z_i$ and $P_{z_j}$ as mean monthly precipitation of an interpolation location at elevation $z_j$.

Unlike the correlation matrix, $C$ it is not symmetrical, reflecting the directional character of the elevation difference which is given as $h_{ij} = z_j - z_i$ (positive if $z_i < z_j$ and negative if $z_i > z_j$), so $h_{ij} \neq h_{ji}$. That accounts for the two possibilities that the location $\vec{r}_i$ is either higher or lower than its nearest reference station. The concept of the CovVar coefficient combines the structure of both spatial covariance and variance, both of which need to be strongly conditioned by elevation for its applicability. Furthermore, $c_{ij}$ can exceed the value 1, avoiding a smoothing of the variance which the Pearson correlation coefficient does when normalizing the covariance to the product of the two standard deviations.

The CovVar coefficients are determined from monthly precipitation totals of all available rain gauges in the area of interest. In order to derive a continuous function for the dependence of the CovVar coefficient on the elevation difference $h = h_{ij}$, a linear model for the CovVar factor $c(h)$ is fitted to the data. The linear model is confined by the condition $c(0) = 1$, so that there is zero in- or deflation of the variance if interpolation point and reference station are at the same elevation.

### 4.1.4 *Model application and validation*

This section presents the results of the precipitation interpolation obtained with the CovVar model when applied to the Chirilu study region at daily time steps. The model application is based both on the statistical relationships of rainfall shown in section 4.1.2 and on the determination and fitting of the CovVar coefficient as described in section 4.1.3.

The quantitative validation part contains on the one hand the performance of the CovVar model individually and on the other hand a comparison to the benchmark model PISCO. The quantitative evaluation comprises a point-wise cross-validation as well as a comparison of areal precipitation sums for the Lurín and Chillón catchments. The quantitative validation distinguishes the two elevation ranges: lower elevations below and higher elevations above the threshold determined at 1573 m, corresponding to the two separate linear functions of annual precipitation to elevation (Figure 4.1a) that qualitatively differ in precipitation statistics regarding an elevation dependence. The primary focuses is however on the higher elevations since those are the catchment domains where relevant precipitation amounts fall

and runoff generation processes occur.

The second and rather qualitative part of the evaluation shows an example of interpolated rainfall maps generated by the CovVar model, the PISCO model as well as by the Thiessen polygons approach.

*CovVar coefficient*

The CovVar coefficient was computed for all stations with at least 360 monthly data points as a function of their directional elevation difference. The steady increase with the directional elevation difference is approximated by a fitted linear function (Figure 4.4) that is forced to go through the point (0, 1). The linear model explains 75% of the data's variance. The spread of the CovVar coefficient is however higher for larger positive elevation differences, rendering the linear model less accurate in that range.

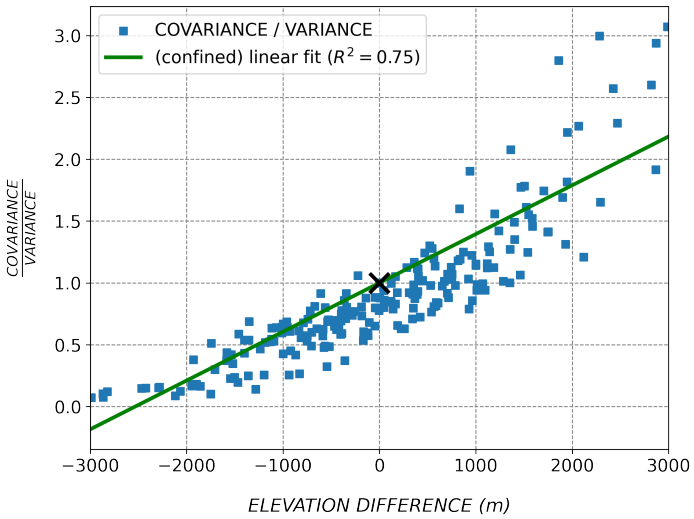


Figure 4.4: CovVar coefficient as a function of the directional elevation difference with a fitted linear function through x = 0 and y = 1. Only stations with at least 360 data pairs were taken into account.

*Cross-validation*

The lower elevation range shows both significantly higher RMSE values between 0.8 to 3.6 (mean: 1.4), and a larger spread (Figure 4.5). The normalization of RMSE with the standard deviation creates artificially high values in case of small rainfall totals and small variances at the low elevations. For higher elevations, the RMSE ranges between 0.5 and 1.3, with an average of 0.9 (table 4.1). The average long-term precipitation (ratio of simulated mean precipi-

tation) is close to 100%, with a slight overestimation of 5.3%. In contrast, the simulated variance is underestimated on average, with a small bias of 7.3 %. However, the spread of simulated variance is significant with a standard deviation of 40.0%, ranging from a minimum of 15.7% to a maximum of 189.7%. The ratio of modeled annual peak precipitation ($P_{max}$) is around 46%, thus the modeled yielded on average around half of the actual annual peak precipitation.

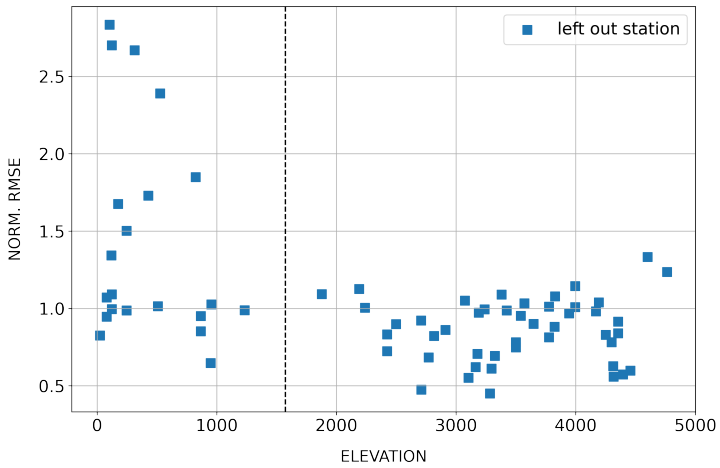


Figure 4.5: RMSE of daily precipitation values as a function of elevation based cross-validation results, the dashed line indicating the elevation threshold. The stations' data records being different, the evaluation is based on time series of potentially different length and covering different time periods

Table 4.1: Results of the cross-validation of the CovVar model for stations above 1573m. The abbreviation "% sim." indicates the ratio of e.g. the observed mean simulated by the model on average"

| | **Mean** | **Std.dev.** | **Min.** | **Max.** |
|---|---|---|---|---|
| **norm. RMSE** | 0.9 | 0.2 | 0.5 | 1.3 |
| **% sim. mean** | 105.3 | 25.3 | 65.5 | 166.7 |
| **% sim. variance** | 92.7 | 40.0 | 15.7 | 189.7 |
| **% sim. ann. $P_{max}$** | 46.3 | 15.6 | 24.4 | 80.5 |

*Interpolated maps and catchment precipitation*

Figure 4.6 shows the interpolation results as rainfall fields around the Lurín basin for three different regionalization methods, here including also a Thiessen polygon approach for the comparison. The maps

show an example day, month and year (2018-01-09), in the middle of the rainy season. Since the CovVar model was applied to a 1000m digital elevation model, its resolution is finer than the 0.1° PISCO grid. In general, the CovVar interpolation shows reasonable rainfall fields. Sharp boundaries become visible, which is due to the fact that only one station serves as reference for the weighting of the fluctuation around the mean. The sharp boundaries correspond to Thiessen polygons, as can be seen in the figure. Compared to Thiessen, traces or influences of the (smoothed) orography can be recognized in the finer distribution of precipitation in the respective polygons. The rainfall fields of the PISCO model show sightly different rainfall patterns, which may partly be due to a non-identical number of used rain gauges. The influence of one station in PISCO can be strong and produce a sharp peak in the grid, the spatial impact of such a point-wise peak appears however more limited.

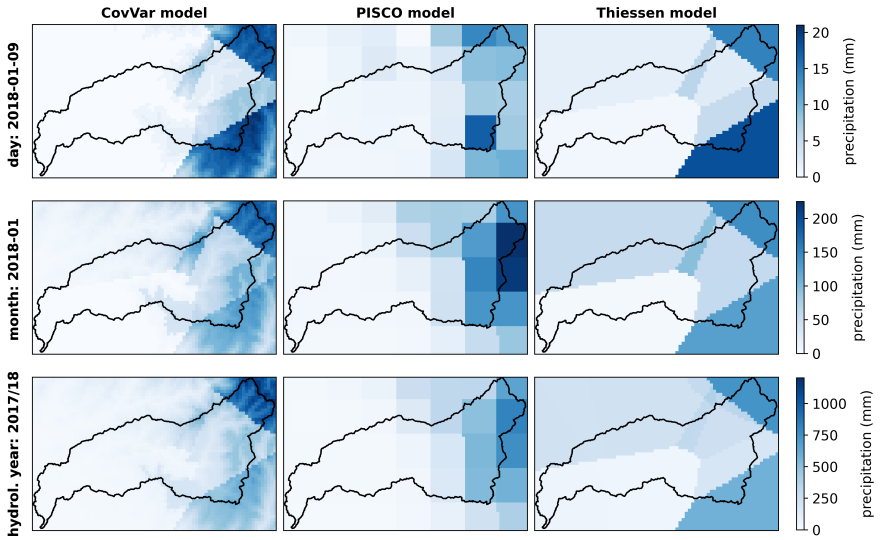


Figure 4.6: Comparison of interpolated rainfall fields of three regionalization approaches for an example date/time period in and around the Lurín basin: CovVar (left), PISCO model (center) and Thiessen polygons (right). Rainfall for three time scales: daily, (top), monthly (middle), annual (bottom).

The CovVar model simulates annual areal precipitation totals at the catchment scale comparable to the PISCO model. Figure 4.7 compares the annual precipitation volumes for two similarly sized and oriented subcatchments in the Lurín (Puente Antapucro subcatchment) and the Chillón (Puente Magdalena subcatchment), which both cover the middle and upper parts of the basins where precipitation actually occurs. In both cases, the CovVar model yields higher annual rainfall totals compared to the PISCO model in all hydrological years. The average difference between CovVar and PISCO is however more considerable

in the Lurín basin: +116 mm/a (+35 %) and +47 mm/a (+10 %) in the Lurín catchment and in the Chillón catchment, respectively, and a particular difference of +60% for the hydrological year of 2019 in the Lurín catchment.

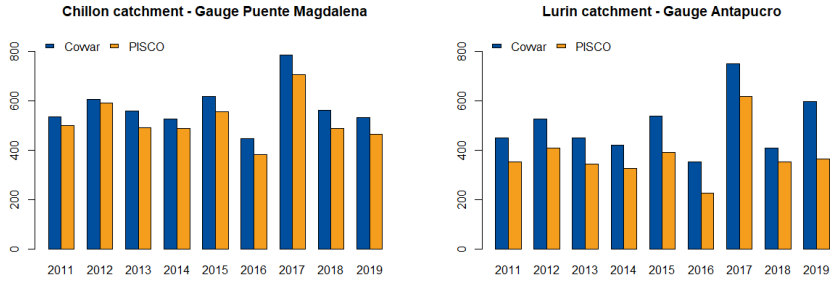


Figure 4.7: Areal annual precipitation sums for Lurín basin (Antapucro subcatchment, right) and Chillón basin (Puente Magdalena subcatchment, left)

### 4.1.5 *Discussion of model performance*

This section discusses the results and performance of the CovVar model.

#### *Cross validation*

The cross-validation yielded reasonably good performance metrics, comparable to the PISCO product (Alcamo, 2019). The validation statistics in terms of reproduced mean and variance are comparable and close to observed values (near 100%). The non-negligible standard deviation of these statistical moments indicates however that the quality of local rainfall predictions varies considerably. The coarse measure of annual peak precipitation ($P_{max}$) revealed that very high observed daily precipitation totals are poorly represented by the model. Presumably, this is due to the fact that heavy, convection-driven rainfall events (Trachte et al., 2018) are likely to be more limited in their spatial extent than other, more frequently occurring rainfall events and therefore not or poorly captured by the nearest station's fluctuation. Applied at the daily scale, the uniform disaggregation of monthly elevation-dependent mean precipitation into daily elevation-dependent mean precipitation probably also has an influence on the rainfall regionalization. The mean number of daily rainy per month turned out to be 28 during the rainy season in the study region, which puts the use of such a coarse assumption into perspective.

There is thus a difference in the model performance between mean water volume and peak events. In general, for all statistical moments of the quantitative evaluation, the standard deviation is significant, implying that the model performance varies with the validation stations ("left out ones" in the cross-validation or the independent stations in the comparative validation). Stations likely do not all have the same (statistical) importance, which is an even more relevant point in monitoring networks of low density. Depending on a station's location relative to the local station density and prevailing rainfall events or their spatial extent statistics, it provides more or less information, is more or less redundant or expendable in the interpolation than others. The observed inconsistency of variograms for the same month, with ranges or correlation lengths that are only in some cases discernible, suggests that the spatial structure of rainfall events and related weather patterns also vary between the years.

A comparison between the individual CovVar cross validation and the validation based on the independent dataset, thus with fewer available interpolation points/stations, showed that the representation of mean precipitation and variance does not change significantly. This is presumably due to the influence of the elevation-dependent monthly climatology that mainly conditions the mean water volumes and to the formulation of the CovVar coefficient that aims at preserving the variance.

*Annual catchment-averaged rainfall, water balance*

Spatial averaging of distributed rainfall in the two subcatchments of the Chillón and the Lurín river has shown that the CovVar regionalization approach has a significant effect on annual rainfall, the input of water volume to the catchment (Figure 4.7. In both cases, CovVar yields higher annual catchment-averaged rainfall than the PISCO model. The difference between the two models, however, is more pronounced in the Lurín basin, which is probably due to the elevation-imposed mean monthly rainfall that counterbalances the lack of rain gauges in the highest and most humid areas of the upper Lurín basin and generates on average more rainfall in that domain. In particular, the difference between the CovVar and PISCO model in the Lurín basin in 2019 is striking. CovVar simulates around 60% more rainfall in the catchment. The TRUST project set up new research rain gauges at high elevations in the Lurín basin, a region formerly effectively not monitored, which appears to have had an impact on mean areal rainfall. The considerably higher annual catchment rainfall in 2019 (setup of new rain gauges happened mainly at the end of 2018) in the Lurín river could indicate that this year, it was a particularly humid year in the Lurín basin or at least in the headwaters. The

high rainfall amounts were able to be measured by the newly set up rain gauges and then likely exceeded the mean elevation-dependent rainfall statistics, generating high areal rainfall.

*Rainfall fields*

The CovVar model is in principle a nearest neighbor approach, using elevation instead of euclidean distance and incorporating statistical relationships of rainfall patterns and elevation. The example rainfall fields generated by the CovVar model show the influence of the nearest neighbor approach. This imposes sharp boundaries which do obviously not correspond to actual spatial rainfall patterns, a phenomenon which is known from other commonly used methods like Thiessen polygons. Since the purpose of such regionalization methods is to assess water balances or as forcing data for hydrological models, this theoretical shortcoming is of minor importance. On the one hand, hydrological models are not per se sensitive to meteorologically or physically inconsistent rainfall structures and are on the other hand to a certain degree capable of counterbalancing spatial input data biases in the calibration process.

## 4.2 REGIONALLY CALIBRATED HARGREAVES-SAMANI APPROACH FOR POTENTIAL EVAPOTRANSPIRATION

*Methods to estimate pot. evaporation*

As described in section 2.2, potential evapotranspiration is mainly conditioned by the surface energy balance and the vapor pressure deficit in the lower atmosphere. While there are numerous methods to calculate $ET_p$, the Penman-Monteith approach (Monteith, 1965) has evolved as a standard in hydrology. Compared to the other methods, Penman-Monteith explicitly accounts for most atmospheric variables and surface resistance effects, making it the most complete but also the most data-hungry one. The FAO56-reference evapotranspiration ($ET_o$) (Allen, 1998), builds on the Penman-Monteith formula, and standardizes $ET_p$ to a short-cut green grass reference surface with fixed resistance properties. Amongst other well-known approaches such as instance Priestley-Taylor, Hargreaves-Samani or Turc (review in McMahon et al. (2013)), the Hargreaves-Samani approach stands out because of its simple and parsimonious approach, making it more applicable in data-scarce regions. Even though the short cut green grass reference surface in FAO-56 $ET_0$ might not be the ideal reference surface in semiarid regions, it still outperforms other approaches in such regions (López-Urrea et al., 2006). Moreover, amongst other methods, also Hargreaves-Samani yielded very reasonable estimates (López-Urrea et al., 2006), despite its simplicity.

*Regionalization of $ET_p$*

Regionalization of potential evapotranspiration from weather station data is achieved either by interpolating the variables required for the chosen method or by interpolating the point-wise calculated $ET_p$ itself. Potential evapotranspiration depends on controls like latitude, topography and land cover (albedo) or the resulting cloud cover and distributions of temperature and relative humidity. Throughout the year, it usually follows seasonal cycles and its interannual variability is in general smaller than that of precipitation (Koster and Suarez, 1999).

*Data-scarcity in Peru and Hargreaves-Samani approach*

In the main study region in Peru, the Chirilu basins, little data on radiation and rel. humidity was available, let alone long time series. In such data-scarce regions, the comparably simple Hargreaves-Samani (Samani, 2000) approach is often applied, since it is based only on daily minimum, maximum and average temperature. It requires however the adjustment of the Hargreaves-Samani coefficient to local conditions (Samani, 2000), ranging roughly between 0.1 and 0.25. Given the recent installation of well-equipped weather stations, these new and short data records were used to calibrate the Hargreaves-Samani coefficient (Shahidian et al., 2013) in the study region in order to produce longer historic time series that could be used as forcing in the hydrological model in chapter 5 and to estimate the catchments' aridity for determination of their position in the Budyko space.

This section first introduces the Hargreaves-Samani approach. After presenting an analysis of seasonal and spatial patterns of $ET_p$ and method-dependent differences based the short period for which full weather data sets are available, the Hargreaves-Samani coefficient is calibrated on monthly basis, by linear regression and applied to the study region via previously regionalized temperature fields.

### 4.2.1 *Hargreaves-Samani method*

The Hargreaves-Samani method only requires measurements of daily minimum, maximum and average temperature as well as the latitude for the estimation of extraterrestrial radiation. The approach is built on the idea that at least 80% of $ET_o$ variability can be explained by solar radiation and temperature. They proposed that daily incoming solar radiation can be derived from extraterrestrial radiation and the temperature difference within in the 24h-day, corrected only by a coefficient accounting for regional conditions (Eq. 4.4). The idea assumes that the heating of the ground surface and the overlying air column is heated primarily by solar radiation and not by advective transport of warm air masses.

$$R_s = K_T \cdot R_a \cdot TD^{0.5} \tag{4.4}$$

with the Hargreaves-Samani coefficient $K_T$, extraterrestrial radiation $R_s$ and the daily temperature difference $T_D = T_{max} - T_{min}$. Potential evaporation is then estimated based on equation 4.4:

$$ET_P = 0.0135 \cdot (T + 17.78) \cdot K_T \cdot R_a \cdot (T_{max} - T_{min})^{0.5} \tag{4.5}$$

### 4.2.2 *Data*

The short data records for the estimation of FAO-reference evapotranspiration $ET_0$ were based on the six weather stations spread across the Chirilu basins at different elevations (Figure 4.8). Apart from the Cullpe station that belongs to the TRUST-Project, the five other stations are part of SEDAPAL's monitoring network.

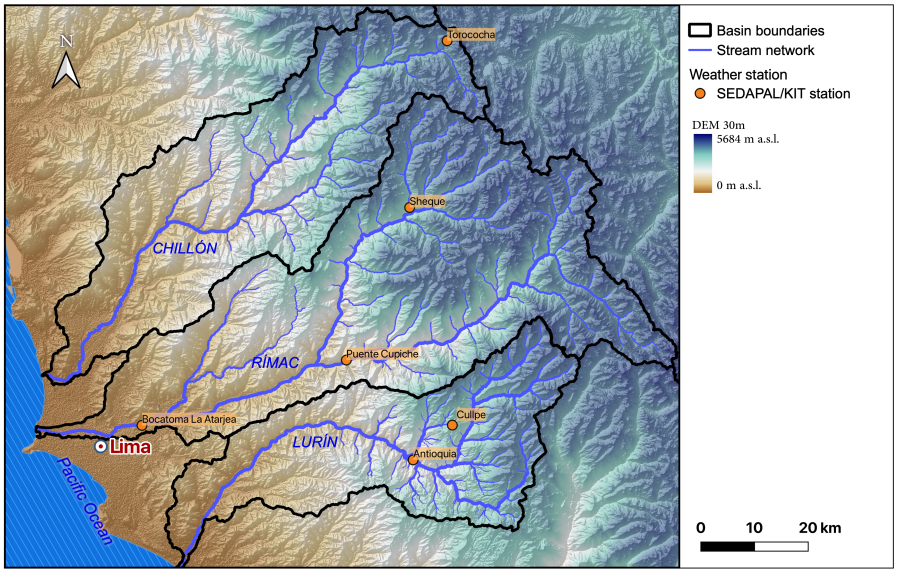


Figure 4.8: Map of new weather stations in Chirilu region, used to calibrate Hargreaves-Samani coefficient

### 4.2.3 *Spatiotemporal differences between reference evapotranspiration and Hargreaves-Samani*

The analysis of deviations of potential evapotranspiration as estimated by Hargreaves-Samani from FAO-reference evapotranspiration is based on an "uncalibrated" estimate using a fixed default HS-coefficient of $K_T = 0.17$ (Shahidian et al., 2013). The difference between FAO-$ET_0$ and Hargreaves-Samani-based estimates are related both to the season and to elevation (Figure 4.9). For stations above 1000

m, relative errors (RE) of the Hargreaves-Samani estimates decreased with increasing elevation. For all stations (except for Bocatoma La Atarjea), uncalibrated H-S estimates overestimated $ET_0$ in the rainy season, with a positive RE decreasing from 49.6% down to to 4.1% for the highest station, Torococha. For stations above 3000 m, the H-S method underestimated $ET_p$ in the dry season. For the lowest station, Bocatoma La Atarjea, the H-S estimates were also too high, however, with an inverse trend in the seasonality: while the rainy season was almost in agreement with $ET_o$, the estimates in the dry season were far too high.

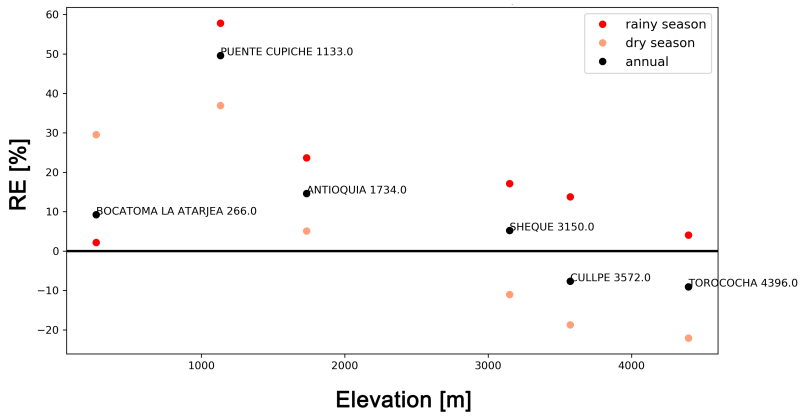


Figure 4.9: Seasonality and elevation dependence of the difference or *relative error* of Hargreaves-Samani estimates as compared to the FAO reference evapotranspiration, a positive relative error indicates an overestimation by Hargreaves-Samani and vice versa (Oezgür, 2020)

Deviations of Hargreaves-Samani $ET_p$ estimates depend both on the season and the elevation. In order to explore how atmospheric input variables used in Penman-Monteith explain the between-method differences, a correlation analysis was conducted on the basis of monthly $ET_p$ estimates. High correlations were found consistently for relative humidity ('HRD' in the figure) and solar radiation $R_s$ for all stations, with the strongest correlations for the stations at high elevations (Oezgür, 2020). Except for Cullpe, wind velocity shows lower correlation values, especially for the lower stations. The error being seasonal itself, it correlates well with all seasonally distributed variables, that are thus also interrelated and do not allow for an attribution of explained variance. There are two main sources why Hargreaves-Samani $ET_p$ is off: It does not account for ET-limitation by relative humidity, which may under humid conditions lead to an overestimation of $ET_p$ (Trajkovic, 2007). Secondly, the Hargreaves-Samani default $K_T$, that relates $R_s$ to the temperature difference (see Eq. 4.4) is not representative of the region and therefore the approach requires

a regional optimization.

### 4.2.4 *Calibration of Hargreaves-Samani coefficient*

The analysis of spatiotemporal patterns of the differences between uncalibrated Hargreaves-Samani and FAO reference evapotranspiration estimates showed a strong dependence of the performance of Hargreaves-Samani on the season and elevation. In order to improve the Hargreaves-Samani estimates and adapt the coefficent to the region, $K_T$ was optimized as a linear function of elevation, separately for each month of the year (Figure 4.11). The elevation dependence is less pronounced during the rainy months (December through March/April) than in the dry months, yielding less steep linear functions. The linear trend is thus not as pronounced in the data in the rainy season. For the six reference weather stations, the resulting seasonality of their respective optimal $K_T$ coefficients is plotted in Figure 4.10.

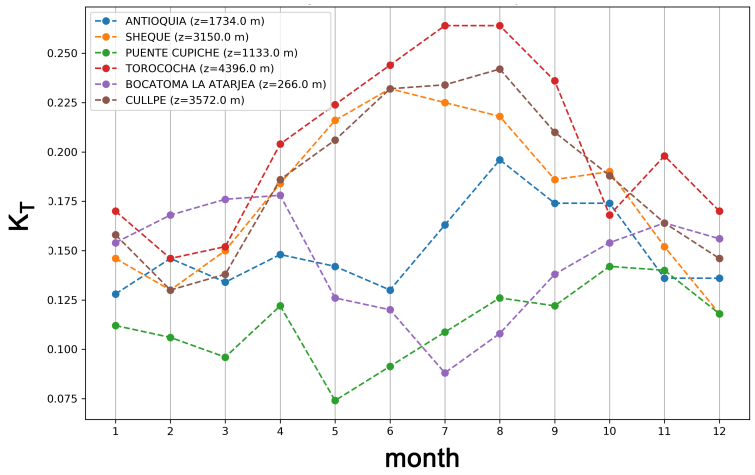


Figure 4.10: Seasonality of Hargreaves-Samani coefficients for the six hydrometeorological stations (Oezgür, 2020)

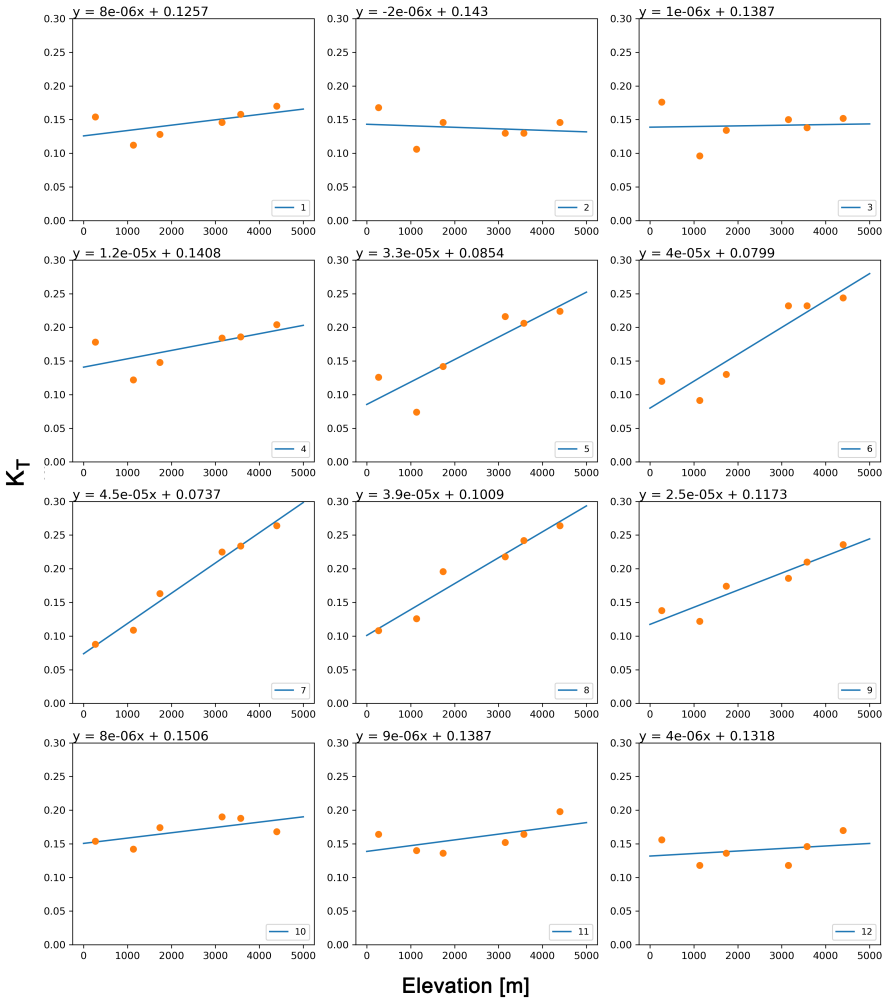


Figure 4.11: Elevation-dependent linear fits of Hargreaves-Samani coefficient for each month of the year. The month is indicated in the little legend, the fitted function equation on top of each box (Oezgür, 2020)

### 4.2.5 *Areal potential evapotranspiration*

The calibrated Hargreaves-Samani model was applied to the Lurín basin, and annual areal potential evapotranspiration time series were estimated. For the regionalization, daily maximum and minimum temperature fields were estimated from polynomial vertical atmospheric temperature profiles that were fitted based on available monitoring station data. Depending on the day, atmospheric conditions show the existence of an inversion layer in the lower atmosphere, from ground level up to around 1500m-2000m, as described by Trachte et al. (2018) (see example profiles in Figure 4.12). The choice of the polynomial fit function is supposed to account for this inversion, however without overstating the position of the station with the highest measured

temperature.

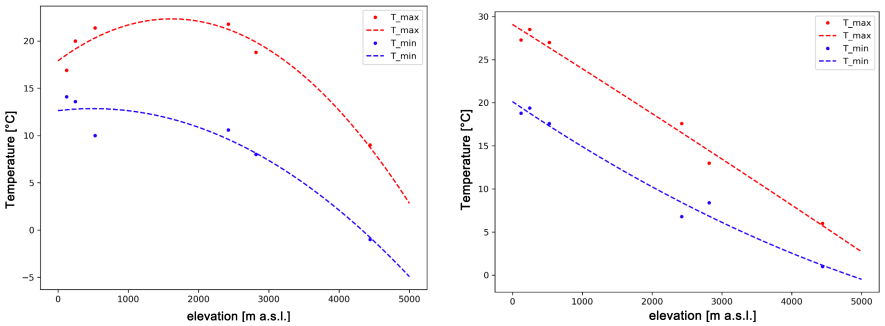


(a) Atmospheric profile showing temperature inversion (08.08.2001)

(b) Quasi-linear atmospheric temperature profile (05.04.2000)

Figure 4.12: Examples of fitted vertical atmospheric profiles of daily Tmin and Tmax temperature,

For the whole Lurín basin, mean annual $ET_p$ is 1111 mm/year and ranges between 1041 mm and 1167 mm, thus with fairly small variations as reflected by low standard deviations of 33 mm. For the upper basin part, the standard deviation of 73 mm is higher (Oezgür, 2020). Figure 4.13 shows the time series of annual potential evapotranspiration for the upper basin part. Minimum annual $ET_p$ is estimated in the upper Lurín basin at 885 mm/year. Season-wise, mean $ET_p$ in the upper basin part during the rainy season reaches 353 mm as opposed to the double of 700 mm in the dry season. For the lower basin, differences between the seasons are significantly less pronounced (488 mm and 562 mm).

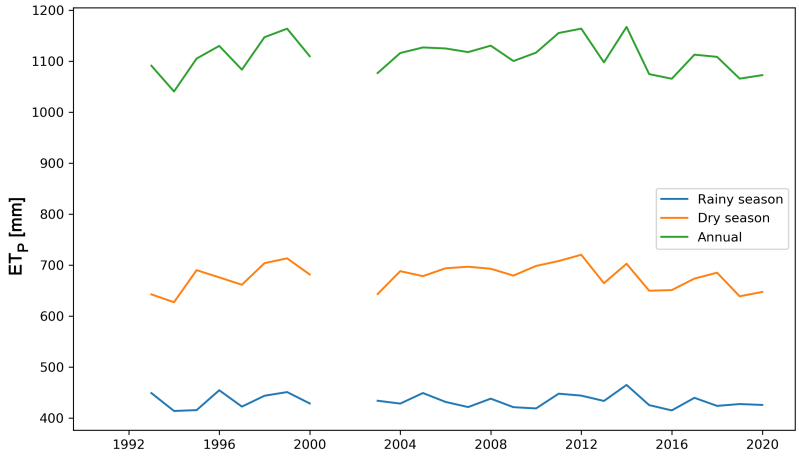


Figure 4.13: Yearly and seasonal sums of calibrated Hargreaves-Samani estimates for the upper Lurín Basin (Oezgür, 2020)

# 5

# PAIRED CATCHMENT MODELING APPROACH FOR LURÍN AND CHILLÓN RIVER

## 5.1 INTRODUCTION

*Data limitations in the Lurín basin*

The Lurín river, case study basin of the TRUST project and one the three neighboring catchments providing Lima with freshwater suffers from a lack of adequate hydrometeorological monitoring. . There is only one functioning stream gauge (Antapucro), at a lower to medium elevation (1000 m a.s.l.) in the heterogeneous basin. The short stream gauge's data records of around 3-4 years suggest a considerable interannual variability. In addition, the supposedly most humid area of the basin, the headwater catchments, are not equipped with rain gauges at all, making catchment rainfall estimates challenging. In terms of data, the basis for the setup, calibration and validation of a hydrological model is thus limited.

*Obtaining model parameter sets in ungauged basins*

Runoff predictions in ungauged basins require a catchment-characteristic model parameter set that cannot be obtained via calibration. Parameters in ungauged basins can also be derived from relationships between catchment characteristics and model parameters established through statistical regression (Blöschl et al., 2013; Samaniego et al., 2010) in gauged basins. These methods need however large amounts of calibrated catchment model data, using the same hydrological model structure and parameters (Buytaert and Beven, 2009). Alternatively, for catchments presumed to be similar in terms of hydrological processes, model parameters can be transferred from gauged (donor) to ungauged (receptor) catchments (Buytaert and Beven, 2009; Singh et al., 2014). Moreover, model parametrizations can be constrained or oriented by runoff signatures such as the flow duration curve or the mean water balance to further reduce parameter uncertainty.

*Paired catchment approach to develop model for Lurin*

In order to tackle the data limitations for the development of a hydrological model for the Lurín basin, a paired catchment modeling approach is proposed. The neighboring Chillón basin, providing a more solid basis in terms of hydrometeorological monitoring and suggesting similarity in terms of hydroclimate, size and topography to the Lurín, serves as reference and parameter donor basin. Geographic proximity of the basins should make for a comparable geological setting, which in combination with a similar climate makes soil and vegetation similarity likely (Patil and Stieglitz, 2012).

*mHM model*

The mesoscale hydrological model (mHM) (Samaniego et al., 2010) was chosen for the modeling. Parameter regionalization in mHM is based on a multiscale approach, using transfer functions (Hundecha and Bárdossy, 2004) resulting from priori defined, empirically derived functional relationships between measurable catchment characteristics and effective model parameters. According to Samaniego et al. (2010), the mHM regionalization approach makes for a higher transferability of parameters across scales and locations.

*Outline*

Firstly, mHM is set up and calibrated for the Chillón basin, taking two stream gauges into account. Multiple model configurations, varying in meteorological input datasets, calibration time periods, objective function and soil characteristics, are tested as suitable model calibrations. Three selected model parameter sets are transferred to a model of the Lurín basin. The Lurín model runs based on transferred parameters will be compared to the mHM default parameter set and to runs directly calibrated against the few years of streamflow observations in the Lurín itself. In order to improve meteorological forcing estimates in the Lurín, the datasets developed in chapter 4 are tested as alternative model input, evaluating their quality additionally by means of hydrological modeling (Heistermann and Kneis, 2011). Apart from Nash-Sutcliffe-based model evaluations, the selection of the calibrated parameter set to be transferred as well as the goodness of Lurín simulations are evaluated based on observed and simulated water balances. The latter is based both on similarity of the two basins in terms of the mean water balance and on the Budyko curve serving as a water balance landmark.

## 5.2 DATA AND PREPROCESSING

*Hydrometeorological data*

For certain meteorological variables such as precipitation and potential evapotranspriation, multiple datasets were used and tested:

**Precipitation (P)**

- **PISCO-P**: dataset described in section 3.2.1
- **CovVar interpolation of rain gauge measurements**: Spatial precipitation fields were generated by the method developed and described in chapter 4.1.

**Potential evapotranspiration (ETp)**

- **PISCO-ET$_p$** dataset described in section 3.2.1
- **Calibrated Hargreaves-Samani method** described in section 4.2

**Streamflow data**
Streamflow data used in this study is described in section 3.2.2.

**Temperature**
Daily, spatially-distributed temperature fields (daily $T_{min}$, $T_{max}$, $T_{mean}$) used both directly in the hydrological model and within in the aforementioned calibrated Hargreaves-Samani-based potential evapotranspiration, were derived from weather station datasets by SENAMHI, SEDAPAL and the TRUST project. The underlying procedure uses a fitted vertical atmospheric temperature profile, estimated on the basis of all temperature sensors in the Chirilu catchments, and regionalizes the temperature based on elevations from an aggregated 1000 m digital elevation model (see section 4.2.5).

## 5.3 METHODS

While the first part of this section provides an overview of the mHM model, the second part describes the steps of the catchment pairing approach.

### 5.3.1 *Mesoscale Hydrological Model (mHM)*

The following paragraphs present a summary of the structure, parameter regionalization and hydrological processes in mHM. For a more detailed model description it is hereby referred to Kumar (2010) and Samaniego et al. (2010), which served also as a basis to this overview.

mHM is a process-based, conceptual hydrological model, fully-distributed in space using grid cells as elementary hydrological unit. Based on parametrizations of dominant hydrological processes, mHM accounts for the following ones: canopy interception, snow accumulation and melting, vertical soil moisture dynamics, infiltration and surface runoff, evapotranspiration, subsurface storage and runoff generation, deep percolation and baseflow, as well as discharge attenuation and flood routing (Kumar, 2010). Doing justice to different spatial scales relevant to different input and state variables, mHM operates on three levels of spatial discretization:

- **Level-0**: This level is used to describe the sub-grid variability of geomorphological properties of the basin, such as sub-surface soil texture and geology classes, surface topography, leaf-area-index and land-use classes
- **Level-1 (and Level-11)**: The level used to numerically compute all hydrological processes and interactions as well as the level

at which output is generated. Level-11 describes the spatial resolution for the routing module (mRM), and is usually set to equal Level-1.

- **Level-2**: The level used to describe the variability of meteorological forcings over the basin such as precipitation, temperature and evapotranspiration.

*Multiscale Parameter Regionalization*

Parameter regionalization in mHM is achieved in two steps- a simultaneous regionalization and an upscaling step. mHM applies a simultaneous regionalization based on functional relationships called transfer functions (Samaniego et al., 2010). These a priori defined transfer functions result from empirical evidence or process understanding, and describe the relationship between basin characteristics and *effective model parameters* $\beta_i$ that are used to compute hydrological processes at the L1 level (Samaniego et al., 2010). The transfer functions themselves have parameters (degrees of freedom), constituting the *global parameters* $\gamma_i$ of the model, which are used to regionalize effective model parameters based on spatially-explicit basin characteristics, and are bound to supposedly physically meaningful parameter ranges. Instead of directly calibrating effective model parameters of each cell, in mHM's calibration procedure only global parameters are varied and optimized with respect to a defined objective criterion for the resulting model simulation based on the simultaneously regionalized effective parameters. To provide an explanatory example for soil properties: spatially distributed soil texture data and land use information (Lo level) as basin characteristics serve as input to pedo-transfer functions that compute effective model parameters like the van-Genuchten parameters for every L1 grid cell. Such a regionalization approach is computationally advantageous as it significantly reduces the parameter search space.

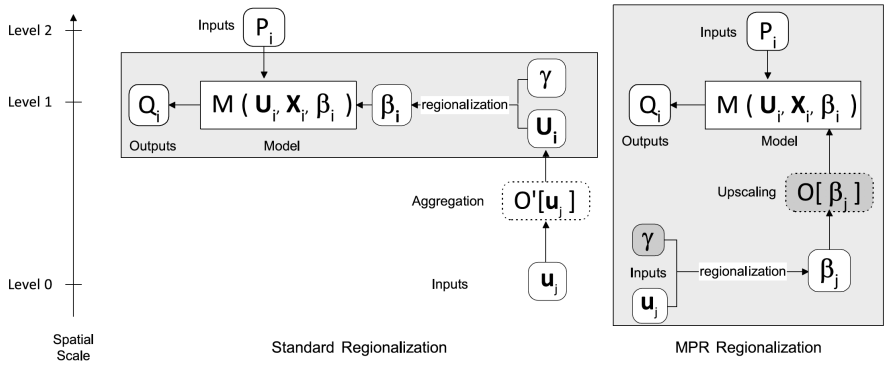


Figure 5.1: Comparison between the Multiscale Parameter Regionalization (MPR) in mHM model and Standard Regionalization (Samaniego et al., 2010)

The second step and particularity of the parameter regionalization in mHM is its multiscale approach. While standard regionalization (SR) relies on upscaling basin characteristics of higher spatial resolution (LO) to the coarser spatial resolution of the model (L1) prior to the transfer function-based regionalization, mHM performs the regionalization at the Lo-level itself and subsequently scales up the regionalized effective parameters. In order to optimize the results, the most suited upscaling operator is specifically selected for each parameter. The multiscale regionalization approach better accounts for sub-grid variability (Samaniego et al., 2010) of basin characeteristics. Figure 5.1 depicts the differences between the standard regionalization and the MPR approach.

*Model structure and hydrological processes*

This section provides a schematic overview of the hydrological processes accounted for in mHM (Figure 5.2) and is based on Kumar (2010). Descriptions of the model components shown in the Figure will be limited to the subsurfaces processes of soil moisture storage (X3), and upper and lower storage (X5, X6), as well as their associated fluxes. As the first of the three subsurface layers, the soil moisture storage layer (X3) represents the upper part of the root zone and controls the responses to rainfall and evapotranspiration. This compartment and its hydrological behavior correspond to the so-called *β-store* of the HBV model described in section 7.2.4. The soil moisture zone can be further subdivided, contingent on user preference, into an arbitrary number $l = 1, ..., l$ of horizons, with every subdivision l supplied with level depth and soil texture properties. The ratio between influx and efflux at the interface between every subdivision horizon is controlled by a simplification of the Richards equation with soil water conductivity based on the relationship from Brooks and Corey (Brooks, 1965). The governing equation is:

$$\frac{I^l(t)}{I^{l-1}(t)} = \left( \frac{x_3^l(t-1)/d^l - \theta_r^l}{\beta_6^l - \theta_r^l} \right)^{\beta_7^l(t)} \tag{5.1}$$

with $x_3^l/d^l$ denoting the relative soil water content in the $l$-th root zone horizon of any given cell and time point, $d^l$ (mm) describing the depth of this soil horizon, and $\beta_6^l$ (mm) and $\theta_r^l$ (mm) denoting the limits within which soil moisture may fluctuate. The last two respectively denote the maximum and the residual soil water content. $\beta_7$ (-) determines the relative, nonlinear contribution to runoff.

In every root zone horizon $l$, actual evapotranspiration is computed by reducing the potential rate ($ET_p$) as a result of soil water-stress, based on an ET-reduction factor, $f_{SM}$, of the Feddes equation:

$$ET^l(t) = \beta_{17}^l \cdot f_{SM}^l(t) \cdot ET_p(t), \tag{5.2}$$

with $\beta_{17}^k$ as fraction of roots in the k-th root zone layer and

$$f_{SM}^l(t) = \begin{cases} 0 & x_3^l(t-1) \leq \beta_{15}^k \\ \frac{x_3^l(t-1)-\beta_{15}^k}{\beta_{16}^k-\beta_{15}^k} & \beta_{15}^k < x_3^l(t-1) \leq \beta_{16}^k \\ 1 & otherwise \end{cases} \tag{5.3}$$

with $\beta_{15}^k$ as permanent wilting point, $\beta_{16}^k$ as soil moisture threshold above which the potential rate $ET_p$ is not limited.

In mHM, lateral flows of subsurface water from one cell to a neighboring are considered to be negligible in contrast to the magnitude of the vertical components $I$, $C$ and $K$ at scales and spatial resolutions that conceptual hydrological models usually operate at. Once water from the lowest root zone layer has percolated to the *upper storage* ($X_5$), it is no longer exposed to evapotranspiration in the model and part of the domain where runoff is generated. The total runoff from a cell, that is water that eventually reaches the stream network, is comprised of four runoff components - direct runoff ($q_1$), fast interflow ($q_2$), slow interflow ($q_3$) and baseflow ($q_4$).

Direct runoff is only generated in model cells declared *impervious* in the model setup (e.g. urban areas), where water cannot infiltrate into the soil. Fast interflow refers to the intermittent movement of water from the vadose zone to the stream channel in a given cell. This flow occurs only if the influx of water exceeds an input-data and calibration-inferred maximum holding capacity $\beta_{18}$ (mm) of the upper reservoir (Kumar, 2010). It imitates temporarily saturated upper soil conditions, producing fast surface and near-surface flow. For any moment in time $t$, the fast interflow can be calculated as:

$$q_2(t) = max\{I(t) + x_5(t-1) - \beta_{18}(z_2 - z_1), 0\} \cdot \beta_{19}, \tag{5.4}$$

with $\beta_{19}$ (1/TS) as a fast-recession constant.

The slow interflow describes the almost permanent flow of water from the unsaturated zone ($x_5$) and is estimated as the outflow from a non-linear reservoir:

$$q_3(t) = \beta_{20}(x_5(t-1))^{\beta_{21}}, \tag{5.5}$$

with $\beta_{20}$ (1/TS) as slow-recession constant and $\beta_{21}$ (-) quantifying the degree of nonlinearity of the cell response.

Groundwater recharge C (percolation rate, mm/TS) from the upper storage ($x_5$) to the lower storage (groundwater reservoir, $x_6$)) is estimated as a simple linear reservoir with:

$$C(t) = \beta_{22} x_5(t-1), \tag{5.6}$$

with the percolation coefficient $\beta_{22}$ (1/TS).

The lower storage (X6) represents the saturated groundwater zone and controls the baseflow $q_4$. This component can be conceptualized as a leaking reservoir where a gain/loss flux K determines the permanent loss (or gain) to the cell, either as a deep percolation or from a neighboring catchment as inter-catchment flow. This can be the case in karstic environments for example. The baseflow and K loss/gain equations are given respectively by:

$$q_4(t) = \beta_{23} x_6(t-1) \tag{5.7}$$

and

$$K(t) = \beta_{24} C(t), \tag{5.8}$$

with $\beta_{23}$ (1/TS) as baseflow-recession constant and $\beta_{24}$ (-) as fraction of groundwater that might be lost as deep percolation or inter-catchment groundwater flow.

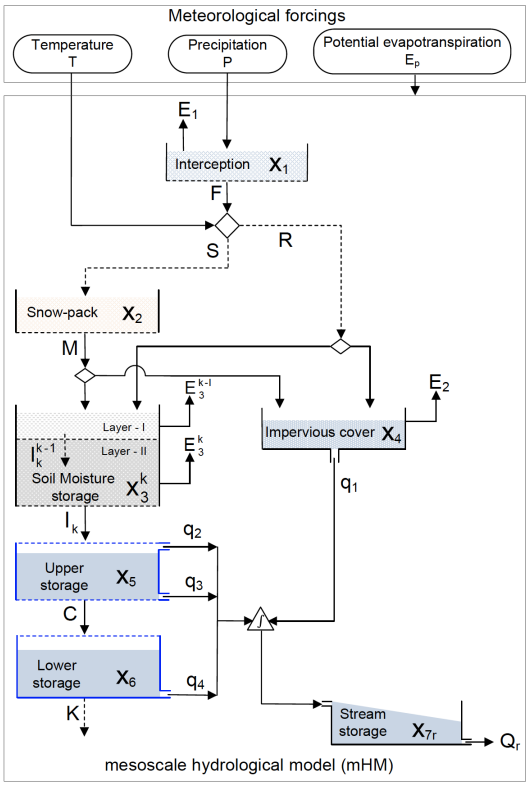


Figure 5.2: Schematic representation of different components accounted for in mHM. Where, $X$ state variable, $E$ = actual evapotranspiration, $q$ = component of runoff, $S$ = snow precipitation depth, $R$ = rain precipitation depth, F = throughfall, I = infiltration capacity, $C$ = percolation, $K$ = gain/loss flux in a leaking cell, $Q_r$ = net runoff produced at the outlet of a grid cell (Kumar, 2010)

### 5.3.2 *Modeling and parameter transfer*

The paired catchment approach, both in terms of data analysis and modeling, is spatially limited to subcatchments of the two river basins: The Puente Magdalena gauge catchment in the Chillón basin, and the Antapucro gauge catchment in the Lurín basin. Both stream gauges are located at around 1000 m a.s.l, downstream of the most relevant part of the basins in terms of runoff generation, since below these points annual precipitation approaches zero (Figure 5.6). In order to differentiate the upper parts of the basins, the headwaters, the Obrajillo catchment in the Chillón is compared to the Santa Rosa de Quilquichaca (in short 'Santa Rosa') catchment in the Lurín, a subcatchment comparable in size and functional location. While the Obrajillo headwater is actually gauged, the Santa Rosa one in the Lurín only served as a spot for the potential setup of a new gauge within the TRUST project.

The methodology consists of the following three steps, which are subsequently described in detail.

1. Comparative catchment analysis of Chillón and Lurín
2. Calibration and validation of Chillón model
3. Parameter transfer and simulations of Lurín model

*Comparative catchment analysis*

The comparisons of the two river basins of Chillón and Lurín, i.e. their respective subcatchments, are drawn on the basis of mean climatic forcing variables as well as on biogeophysical catchment characteristics. Both spatial distributions and subcatchment averages are confronted with one another. Apart a qualitative analysis based GIS maps, the aspects listed in table 5.1 are analyzed quantitatively.

Table 5.1: Climatic forcing and biogeophyiscal characteristics compared between the subcatchments of the Chillon and Lurin basin

| | **analyzed characteristic(s)** |
|---|---|
| CLIMATIC | |
| **precipitation** | spatial distribution / mean annual |
| **pot. evapotranspiration** | spatial distribution / mean annual |
| BIOGEOPHYSICAL | |
| **topography** | hypsometric curve |
| **soils** | soil types map, soil texture |
| **hydrogeological formations** | GIS map |
| **vegetation** | mean LAI dry/rainy season, GIS map |

*Calibration and validation of Chillón model*

For the Chillón catchment, 23 different calibrations were carried out with mHM. Multiple aspects were varied in order to analyze calibration differences and uncertainties as well as to obtain the most suitable parameter sets. While table 5.2 shows the different configuration options for the model calibration , table 5.3 provides an overview of all calibration runs.

As model forcing, P and $ET_p$, the two datasets described in section 3.2.1 were tested. While most of the calibrations were conducted based on both gauges in the Chillón river, assuming that such a spatially more differentiated parameter optimization would result in a better representation of the whole system's dynamics, calibrations

Table 5.2: Modeling aspects varied for the calibration of the Chillon river.

| | **configuration options** |
|---|---|
| **precipitation** | PISCO-P dataset<br>CovVar dataset |
| **pot. evapotranspiration** | PISCO-ETp dataset<br>calibrated Hargreaves-Samani (HS) dataset |
| **calibration gauges** | 2 gauges: Pte Magdalena and Obrajillo ("2")<br>only Puente Magdalena ("1_magda")<br>only Obrajillo ("1_obra") |
| **calibration period** | 09.01.2003 - 30.08.2008<br>09.01.2008 - 30.08.2017 |
| **objective function** | Nash-Sutcliffe-Efficiency (NSE)<br>NSE_mix |

against data from a single gauge were also conducted for comparison. The entire available modeling time period was subdivided into two disjoint calibration periods. Lastly, three different NSE-based objective functions were employed in the calibration- the common Nash-Sutcliffe-Efficiency (NSE) (Nash and Sutcliffe, 1970) as well as a logarithmic version of NSE ($NSE_{log}$) and the average from both ($NSE_{mix}$), in order to put less weight on high flows and the rainy season than common NSE (the latter two are described in Samaniego et al. (2019)).

Table 5.3: Overview of calibration and simulation runs for Chillón and Lurín models

| No | Precip | ETp | Calib gauges | Calib period | Objective func | Soil depth |
|---|---|---|---|---|---|---|
| **chi1** | PISCO | HS-calib | 2 | 2003-2008 | NSE | shallow |
| **chi2** | CovVar | HS-calib | 2 | 2003-2008 | NSE | shallow |
| **chi3** | PISCO | PISCO | 2 | 2003-2008 | NSE | shallow |
| **chi4** | PISCO | HS-calib | 2 | 2008-2017 | NSE | shallow |
| **chi5** | CovVar | HS-calib | 2 | 2008-2017 | NSE | shallow |
| **chi6** | PISCO | PISCO | 2 | 2008-2017 | NSE | shallow |
| **chi7** | PISCO | HS-calib | 2 | 2003-2008 | NSE_log | shallow |
| **chi8** | PISCO | HS-calib | 1_magda | 2003-2008 | NSE_log | shallow |
| **chi9** | PISCO | PISCO | 2 | 2003-2008 | NSE_log | shallow |
| **chi10** | PISCO | HS-calib | 2 | 2008-2017 | NSE_log | shallow |
| **chi11** | CovVar | HS-calib | 2 | 2008-2017 | NSE_log | shallow |
| **chi12** | PISCO | PISCO | 2 | 2008-2017 | NSE_log | shallow |
| **chi13** | PISCO | HS-calib | 1_magda | 2008-2017 | NSE | shallow |
| **chi14** | PISCO | HS-calib | 1_obra | 2008-2017 | NSE | shallow |
| **chi15** | PISCO | HS-calib | 2 | 2008-2017 | NSE | thicker |
| **chi16** | PISCO | HS-calib | 2 | 2008-2017 | NSE_log | thicker |
| **chi17** | PISCO | HS-calib | 1_obra | 2008-2017 | NSE | thicker |
| **chi18** | PISCO | HS-calib | 1_obra | 2008-2017 | NSE_log | thicker |
| **chi19** | CovVar | PISCO | 1_obra | 2003-2008 | NSE | shallow |
| **chi20** | CovVar | PISCO | 2 | 2003-2008 | NSE | shallow |
| **chi21** | CovVar | PISCO | 2 | 2003-2008 | NSE | thicker |
| **chi22** | CovVar | PISCO | 2 | 2003-2008 | NSE_log | shallow |
| **chi23** | CovVar | HS-calib | 2 | 2003-2008 | NSE_log | shallow |
| **lu1** | CovVar | PISCO | 1 | 2014-2019 | NSE | shallow |
| **lu2** | CovVar | PISCO | 1 | 2014-2019 | NSE_mix | shallow |
| **lu3** | CovVar | PISCO | 1 | 2014-2019 | NSE_log | shallow |
| **lu5** | CovVar | HS-calib | 1 | 2014-2019 | NSE | shallow |
| **lu6** | CovVar | HS-calib | 1 | 2014-2019 | NSE | thicker |
| **lu7** | CovVar | HS-calib | 1 | 2014-2019 | NSE_log | shallow |
| **lu8** | CovVar | HS-calib | 1 | 2014-2019 | NSE_log | thicker |
| **lu9** | PISCO | HS-calib | 1 | 2014-2019 | NSE | shallow |
| **lu10** | PISCO | HS-calib | 1 | 2014-2019 | NSE_log | shallow |
| **lu5_def** | CovVar | HS-calib | 1 | 2014-2019 | (no opti.) | shallow |
| **lu5_3** | CovVar | HS-calib | 1 | 2014-2019 | (transfer) | shallow |
| **lu5_21** | CovVar | HS-calib | 1 | 2014-2019 | (transfer) | shallow |
| **lu5_19** | CovVar | HS-calib | 1 | 2014-2019 | (transfer) | shallow |
| **lu11** | CovVar | HS-calib | 1 | 2014-2019 | NSE_mix | shallow |
| **lu12** | CovVar | HS-calib | 1 | 2014-2019 | NSE_mix | thicker |

The evaluation of modeling results is done on the basis of the two subcatchments, Obrajillo and Puente Magdalena. Both NSE criteria and annual as well as mean annual water balances are considered, in particular with respect to the Budyko curve estimate.

*Parameter transfer and simulations of Lurín model*

In order to find a global parameter set suited to represent the Lurín river, three calibrated parameter sets obtained for the neighboring Chillón catchment were transferred unaltered to the model of the Lurín catchment. The choice of the three parameter sets was based on a good model performance in terms of NSE, in terms of the mean water balance with respect to the Budyko curve as well as to ensure a certain variability in the parameters. For the comparisons between optimized global parameter sets, only a subset of presumably most relevant parameters were selected from the whole parameter set. The selection of the subset resulted from a combination of a first-order sensitivity analysis in the Chillón river and the findings of Höllering et al. (2018) who conducted a more in-depth parameter sensitivity study with mHM.

The Lurín simulations will be analyzed and evaluated on the basis of short discharge observations at the Antapucro gauge. The simulation results based on the parameter transfer are also compared to direct calibrations of the Lurín, as well as to a run based on the mHM default parameterization. Again, NSE-based as well water balance- and Budyko-based criteria will serve as model goodness criteria.

*Model configuration and input data*

The models set up for the Chillón and Lurín river run at the following spatial model scales: L2 - 1000m, L1/L11 - 1000m, L0 - 200m.

*Morphological data*

Stream networks were derived with the 30m DEM for the Chillón and 12m DEM for the Lurín model (section 3.2.3). There are two root zone soil layers in the model whose texture and bulk density properties were taken from the soilgrids product described in section 5.4 and shown in the map in Figure 5.12. The soil layers depth are homogeneous in all model cells, and was varied for the calibrations (see section 5.3.2), with the shallow soil encompassing 15 cm, and the thicker one 500 cm of depth. 8 geoclasses were set for the Chillón and Lurín model according to the map in Figure 5.17. In terms of land cover, all model cells were set to *pervious*, thus excluding the other two options in the model, *forest* or *impervious*.

*Forcing and streamflow data*

Meteorological forcing data was taken from all data products described in section 3.2.1. They were remapped to the respective model grids. Stream gauge data as described in section 5.4, with calibration periods as listed in section 5.3.2). The models had a spin-up phase of one year prior to the beginning of the calibration period.

*Optimization*

The optimization was performed by means of the DDS (Dynamically Dimensioned Search) algorithm with 1000 iterations.

## 5.4 COMPARATIVE CATCHMENT ANALYSIS

This section describes and compares the two basins of Chillón and Lurín, or rather their respective subcatchments. In terms of drainage area, the entire Chillón basin covers 2179 km$^2$, the Lurín 1569 km$^2$, the gauge catchments' areas are listed in table 5.4. As visible in Figure 5.3, the two delineated headwater catchments- Obrajillo, Santa Rosa- are both part of the main catchments, Puente Magdalena and Antapucro. The Santa Rosa catchment in the Lurín only served is not gauged, and serves merely as a comparable headwater catchment to Obrajillo in the Chillón.

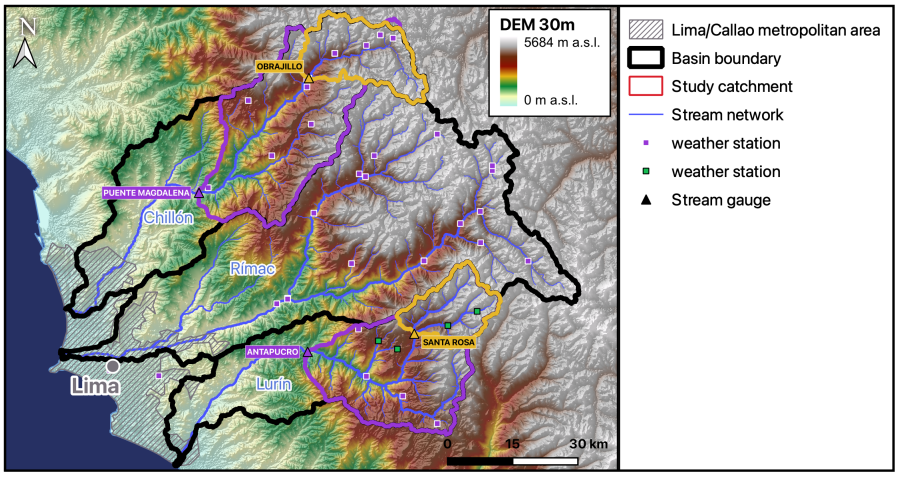


Figure 5.3: Overview, DEM and rain gauges of Chillón, Rímac and Lurín catchments ("Chirilu"). The highlighted subcatchments of the Chillón and Lurín river basins constitute the study areas

### *Catchment arrangement and topography*

The two study basins, Lurín and Chillón are separated by the Rímac catchment, thus no immediate neighbors (Figure 5.3). All three catchments extend from the Andean crest to the Pacific coast. The total Chillón basin as well as its subcatchments are slightly bigger than the

Lurín and its subcatchments. The basins are similarly oriented, i.e. their main axis is roughly perpendicular to the coast and the Andean crest- imposing a similar exposition to moist air masses flowing in from the east. The shapes of the two basins are comparable in terms of width and length ratio. The hypsometric curves in Figure 5.4 show a very similar elevation-to-area ratio for the two subcatchments Puente Magdalena and Antapucro. The peaks in both subcatchments are slightly above 5000 m, going down to the gauge elevation of around 1000 m. The Chillón subcatchment covers a bit more area in the higher elevation range of 3400-4900 m.

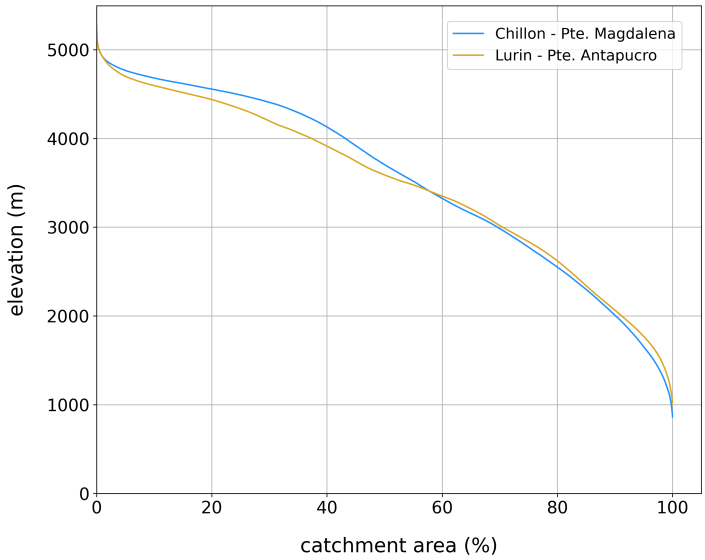


Figure 5.4: Comparison of hypsometric curves of the two subcatchments of Puente Magdalena and Antapucro

*Precipitation*

For precipitation, the two different datasets described in section 5.2 were used to assess the climatic conditions in the catchments and as meteorological forcing for the hydrological models. Being intimately linked to elevation in this region as described in section 4.1, mean annual precipitation can be expected to be similar for both catchments. Both precipitation datasets in Figures 5.5 and 5.6 show the elevation dependence across all three Chirilu catchments. In the case of the CovVar rainfall, elevation was a basic and explicit component of the regionalization method, which is reflected by a finer mean rainfall distribution following smoothed topographic structures. The range of mean annual rainfall extends from 1100 mm (PISCO) and 1560 mm (CovVar) in the highest elevation points of the Chirilu domain to 0 mm in the hyperarid coastal zone, presenting a pronounced spatial

Table 5.4: Overview of average topographic and climatic characteristics of the four subcatchments (dataset1 (ds1) indicates the PISCO-P/PISCO-ETp, and dataset2 (ds2) the CovVar/ETp-HS-calib combination)

| characteristic | **Puente Magdalena** | **Obrajillo** | **Antapucro** | **Santa Rosa** |
|---|---|---|---|---|
| **river basin** | Chillon | Chillon | Lurin | Lurin |
| **area (km2)** | 1267 | 362 | 951 | 252 |
| **elevation range (median)** | 864m -5273m (3704m) | 2702m-5273m (4539m) | 1024m-5261m (3588m) | 2986m-5261m (4472m) |
| **mean ann. P (mm/a) - PISCO** | 495 | 739 | 351 | 543 |
| **mean ann. P (mm/a) - CovVar** | 570 | 852 | 493 | 910 |
| **mean ann. ETp (mm/a) - PISCO** | 817 | 620 | 973 | 848 |
| **mean ann. ETp (mm/a) - HS-calib** | 1072 | 960 | 1087 | 967 |
| **rainfall seasonality (-) - PISCO** | 0.94 | 0.86 | 1.14 | 1.11 |
| **rainfall seasonality (-) - CovVar** | 0.81 | 0.72 | 0.8 | 0.7 |
| **dryness index $\phi$ (-) ds1** | 1.65 | 0.84 | 2.77 | 1.56 |
| **dryness index $\phi$ (-) - ds2** | 1.88 | 1.13 | 2.2 | 1.06 |

gradient in mean annual rainfall over the short distance between Andean crest and coast of about 70-100 km.

There are differences in terms of quantitative catchment-averaged precipitation between the two datasets. While the two datasets are more or less in agreement with respect to rainfall in the main catchments, there are considerable differences for the headwater catchments.

Both datasets indicate a higher mean annual rainfall in the main catchment of the Chillón (Puente Magdalena) with an IQR of around 500-600 mm/a vs. 350-420 mm/a in the Lurín based on PISCO, and the CovVar model approaching the two basins which results in an IQR of approx. 550-650 mm/a vs. 450-550 mm/a in the Lurín (Figure 5.7a). The higher mean annual rainfall in the Lurín main catchment in the

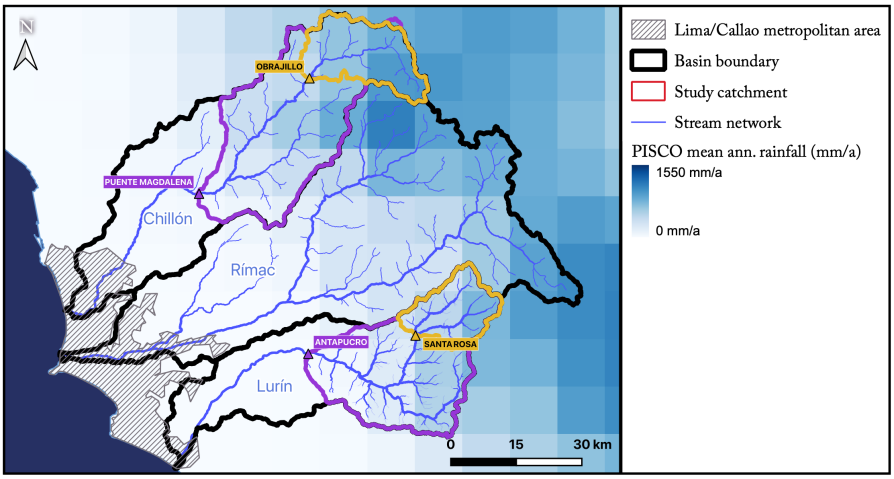


Figure 5.5: Chillón and Lurín basins: mean annual precipitation (PISCO-P dataset)

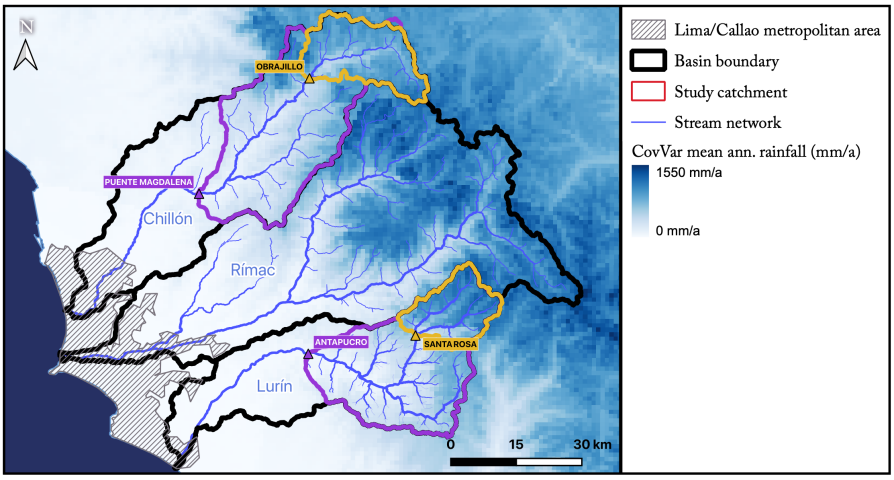


Figure 5.6: Chillón and Lurín basins: mean annual precipitation (CovVar model)

CovVar model stems from higher rainfall in its headwater catchment.

*Difference in the headwaters*

While PISCO shows higher mean annual precipitation in the Obrajillo headwater catchment of the Chillón, ranging from around 700 to 850 mm/a as opposed to 500-650 mm/a in the corresponding Santa Rosa headwater catchment in the Lurín, this trend is inverse in the CovVar dataset. CovVar predicts generally higher annual rainfall totals for both headwater catchments than PISCO, however with the mean annual rainfall in the Santa Rosa headwater catchment (910 mm/a) exceeding Obrajillo's (852 mm/a) by 60 mm/a. Rainfall in the semi-arid region of the Peruvian west coast is fairly seasonal.

*Seasonality*

Figure 5.10 illustrates the seasonality calculated on the basis of both available rainfall datasets for the main catchments and the headwater catchments separately. The main rainy season takes place from December to March, the main dry season from May to August, leaving August through November as well as April as transitional months. The monthly rainfall peak is reached in the month of March across all catchments and datasets. The difference between the datasets for the headwaters noticed for mean annual rainfall, becomes visible in the PISCO-based seasonality in the months of September until January, where PISCO indicates less seasonality in the Obrajillo headwater, i.e. higher monthly rainfall, than CovVar. This between-catchment differences disappear when looking only at CovVar-based rainfall seasonalities, which are fairly similar in the corresponding subcatchments.

*Subannual rainfall characteristics*

In terms of subannual rainfall characteristics depicted in Figure 5.7 (c) and (d), there are also noticeable differences between the two datasets. The PISCO dataset suggests significantly more rainy days for the Chillón than for the Lurín subcatchments, whereas the CovVar dataset shows a similar number of rainy days in the main catchments, and considerably more in the Lurín headwater catchment Santa Rosa. On the other hand, the rainfall depths of rainy days are lower in both Lurín subcatchments according to the CovVar dataset, whereas they are comparable in the PISCO one.

### *Potential evapotranspiration*

For potential evapotranspiration, two datasets were compared (section 5.2) and used as meteorological forcing for the hydrological model.

*Spatial distribution differs in coastal lowlands*

The spatial distribution of mean annual potential evapotranspiration of the two datasets exhibits distinct differences in the lowest basin parts (Figures 5.8 and 5.9). While the PISCO-$ET_p$ datasets peaks in the coastal lowlands, the other dataset indicates highest values in the medium-elevation zones of the basins. The lowlands are not part of

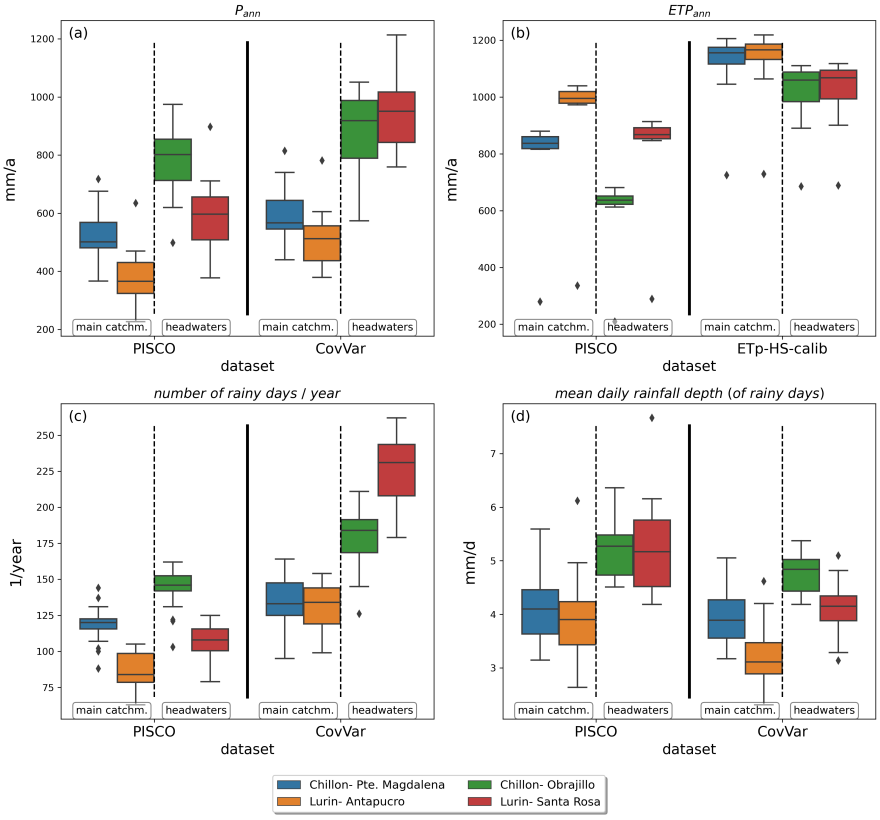


Figure 5.7: Chillón and Lurín basins - meteorological forcing characteristics of the subcatchments

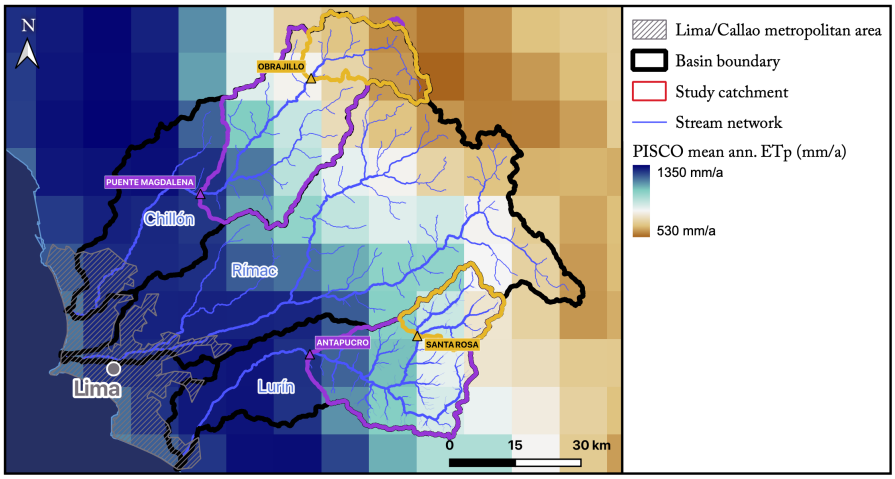


Figure 5.8: Chillón and Lurín basins: mean annual potential evapotranspiration (PISCO-$ET_p$ dataset)

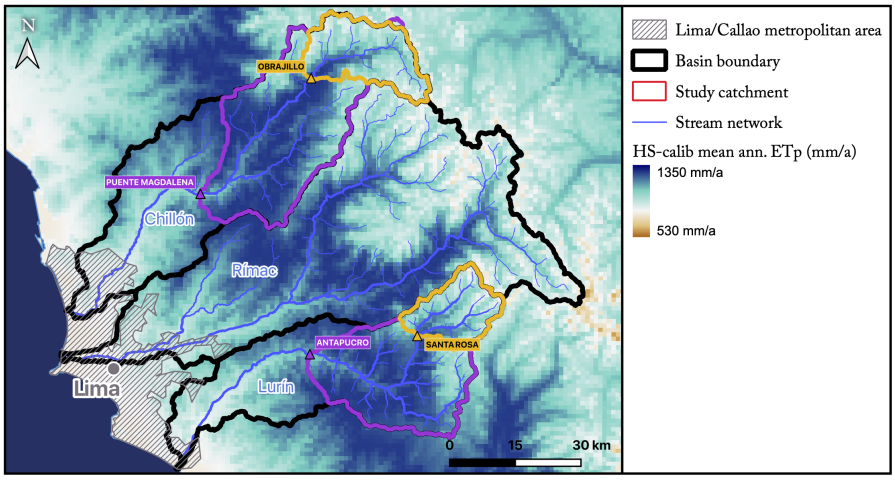


Figure 5.9: Chillón and Lurín basins: mean annual potential evapotranspiration ($ET_p$-HS-calib dataset)

the gauge catchments and thus of lesser interest to this study. For the middle and upper parts, both datasets show a mean annual potential evapotranspiration steadily decreasing with elevation, resulting in generally lower potential evapotranspiration in the headwater catchments. In the PISCO-$ET_p$ dataset, the headwater catchments in both basins are subject to 150-200 mm/a less potential evapotranspiration than the main catchments (Figure 5.7).

*Interannual variability differs*

The two datasets differ in several aspects. Firstly, total annual potential evapotranspiration in the $ET_p$-HS-calib dataset is higher for both basins and their subcatchments (Figure 5.7b). While the main catchments in the PISCO-$ET_p$ datasets reach values of around 850/1000 m for Chillón and Lurín, respectively, the other datasets predicts catchment-averaged values of 1150-1200 mm/a. In addition, the PISCO dataset shows very little interannual variability compared to $ET_p$-HS-calib, in particular concerning the headwater catchments (Figure 5.7b). Secondly, the $ET_p$-HS-calib dataset does not show significant differences between the Chillón and Lurín basins, stemming from the fact, that this $ET_p$ approach is mainly based on the (similar) topography and regionally determined vertical temperature profiles. Lastly, the seasonal potential evapotranspiration cycle of the two datasets are not comparable (Figure 5.10b). While the calibrated HS-$ET_p$ dataset exhibits a distinct seasonal cycle, with potential evapotranspiration reaching its lowest values in February and March, the other dataset is fairly uniform throughout the year, with only one slightly lower value in February.

*Seasonality is different*

*Summing up: aridity*

Summing up the data analysis in terms of precipitation and potential evapotranspiration, which together make the climatic aridity of a catchment or region, we can note a few things:

- the headwaters are more humid parts, both because of higher rainfall totals and lower potential evapotranspiration
- depending on the combination of P and $ET_p$ datasets, the corresponding dryness indexes vary (table 5.4).
- the PISCO datasets suggest significantly less agreement and thus less hydroclimatic similarity between the Chillón and Lurín basins than the other two datasets

*Soil*

According to a national soil map, there are mainly two different soil types covering the area of the main subcatchments of the Chillón and Lurín basin, with comparable spatial distributions and coverage (percentages see Figure 5.18b): In the medium to medium-high elevations, a mixing between Leptosols and sporadic bedrock outcrops (*Leptosols*

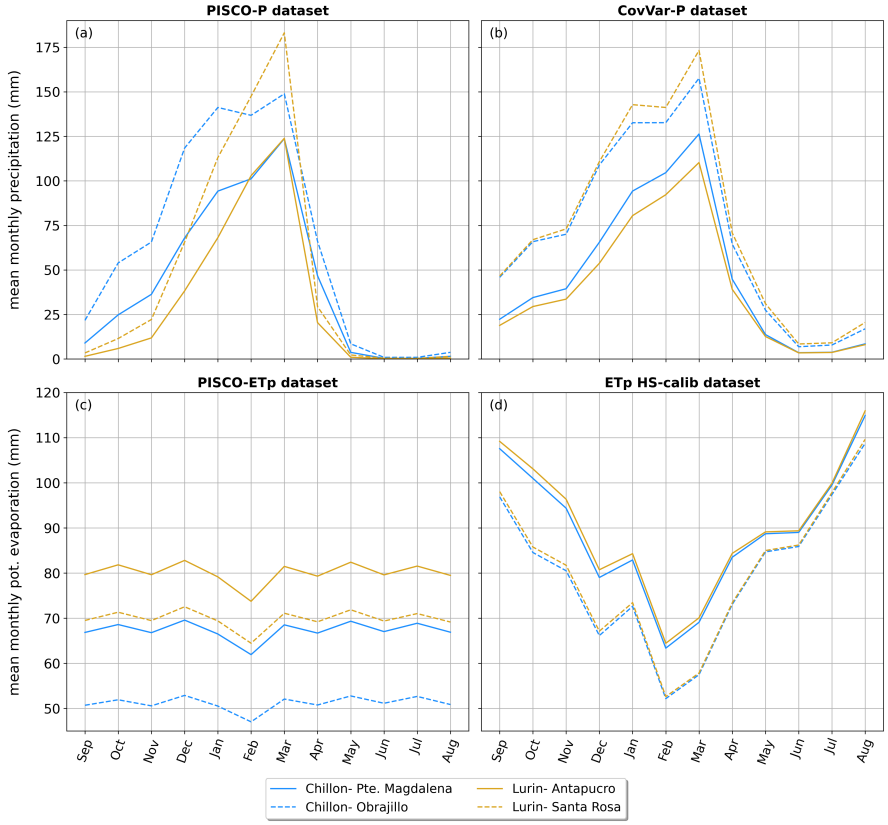


Figure 5.10: Chillón and Lurín subcatchments: rainfall and pot. evapotranspiration seasonality based on both rainfall datasets. Dashed lines show the headwater subcatchments

*districo, afloramiento litico*), and Regosols mixed with sporadic bedrock outcrops for the highest headwater parts (*Regosols districo, afloramiento litico*).

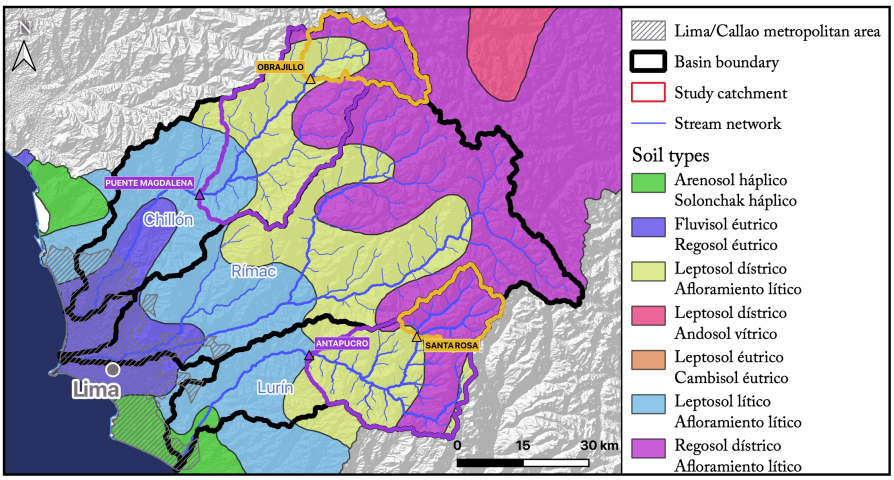


Figure 5.11: Chillón and Lurín basins: soil types (Observatorio del Agua, 2017)

As modeling input data, globally available soil texture and bulk density data were used (Poggio et al., 2021). As indicated by Figure A.1 in appendix A.2, according to this data product, there are no significant differences in mean soil properties between all four sub-catchment, with slightly more clayey soils in the Lurín and slightly higher bulk densities. In terms of spatial distribution, the soils are less sandy and more clayey in the upper parts (Figure 5.12). Bulk density is quite homogeneous in the Lurín, whereas in the Chillón there are higher bulk densities in the medium elevation zones.

Information of the thickness of the soil layers was not available. Field trips to the Lurín valley and point-wise assessments of soil depths, showed that the thickness varies locally but is generally low, ranging somewhere between 10 and 50 cm, sometimes reaching 1-1.5 m.

### *Vegetation and land cover*

Two different data sources were used to assess and compare vegetation and land cover of the Chillón and Lurín basins. The first one is a national GIS map containing a land use classification, likely derived from satellite data (Figure 5.13), and the second one a global leaf area index (LAI) satellite data product.

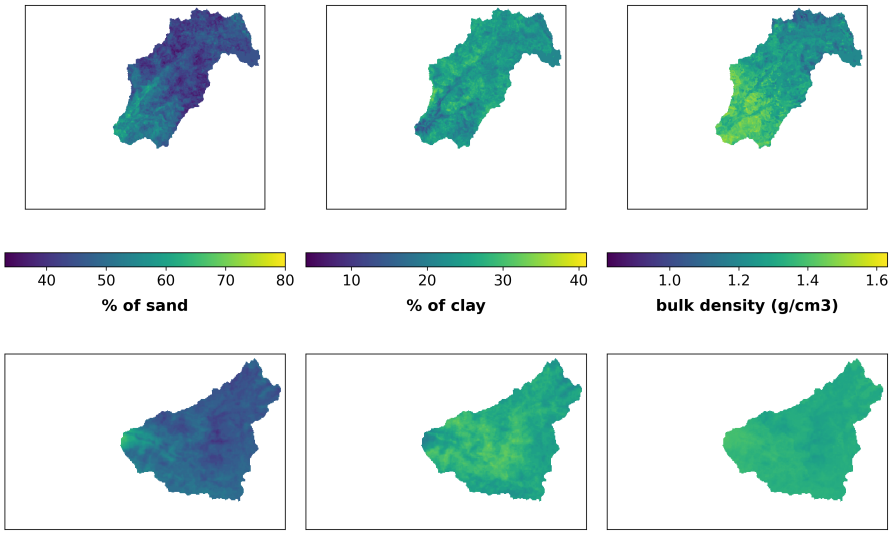


Figure 5.12: Chillón and Lurín basins: spatial distribution of soil texture of main subcatchments (soilgrids product). (top row) Chillón-Puente Magdalena (bottom row) Lurin-Antapucro

The whole national map comprises 11 land cover classes, not all of which are part of the study subcatchments' domains. The most prominent classes in the middle and upper basin parts are (in order of increasing altitud): *cardonal* (sparse arid cactaceous plants), *matorral arbustivo* (also dry but more shrubland vegetation), *pajonal andino* (dry Andean grassland) and *area altoandina con escasa o sin vegetacion* (high Andean land, scarce or no vegetation). Starting at the barren coast, the presence of vegetation cover increases with elevation in the basins. In the lowest basin parts, vegetation only occurs adjacent to the stream, resulting from agriculture fed by groundwater resources of the valley aquifer (see also next subsection on *hydrogeology*), as also shown by prominent LAI values along the stream in Figures 5.14 and 5.15. While the LAI maximum and densest vegetation cover is found at medium to medium-high elevations, it turns sparser and dryer in the very highest parts, the headwaters. The higher leaf area indexes in the medium to high parts are mainly related to agriculturally used lands, as the map overlay shows in Figures 5.14 and 5.15.

The spatial arrangement and percentage area covered by each land cover class (Figure 5.18a) are fairly similar across the study subcatchments in Chillón and Lurin. The map also shows agriculturally used lands, which in both catchments represents around 6-7% of the catchment area. There is more catchment surface covered with reservoirs and lakes in the Puente Magdalena catchment of the Chillón basin (0.3%) compared to the Antapucro catchment of the Lurín basin (0.06 %), which hints at more reservoir- and lake-based retention capacity in the basin. Glacial parts are of small and similar extent in both basins

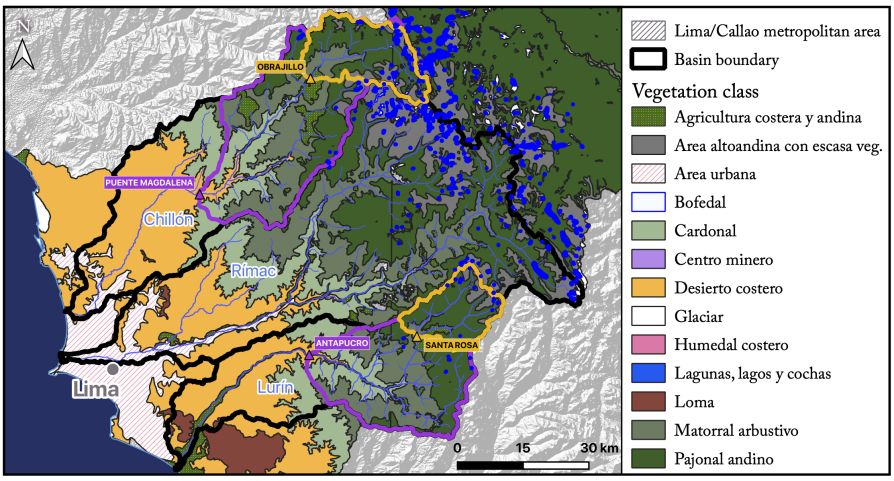


Figure 5.13: Chillón and Lurín basins: vegetation types (Observatorio del Agua, 2017)

(0.03-0.05%).

The seasonality of vegetation cover, as expressed by the mean monthly LAI in the study subcatchments (Figure 5.16), follows more or less the seasonality of rainfall. Both Chillón subcatchments show slightly higher LAI values than the Lurín catchment throughout the year.

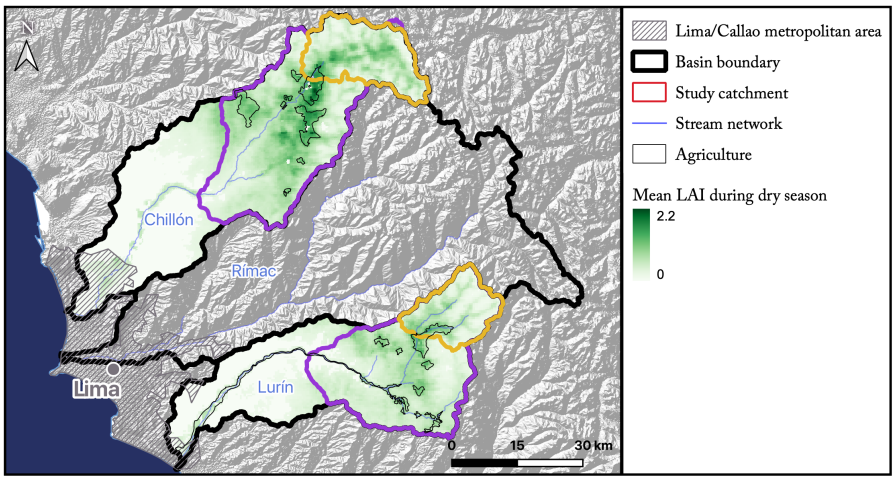


Figure 5.14: Chillón and Lurín basins: Leaf Area Index (LAI) during the rainy season. The shapes of "agriculture" were taken from the national vegetation map in 5.13

.

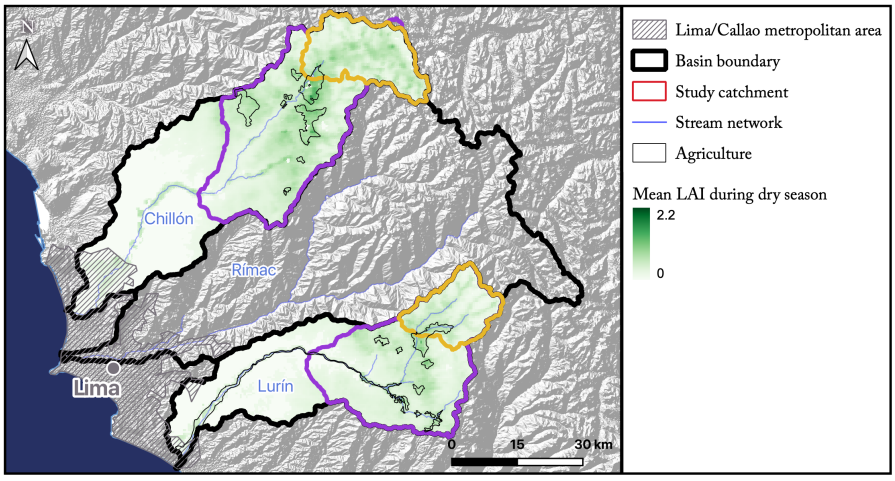


Figure 5.15: Chillón and Lurín basins: Leaf Area Index (LAI) during the dry season. The shapes of "agriculture" were taken from the national vegetation map in 5.13

.

*Hydrogeology*

For an overview of groundwater-related geological structures, a national map of "hydrogeological units" in Figure 5.17. In the map, presumably on the basis of a map of geological formations, hydrogeological units were derived and classified in terms of hydraulic conductivity (aquifer or aquitard) and the type of rock as well as the kind of aquifer (porous/fissured).

In the lowest and flat parts of the Chillón and Lurín, the alluvial valley deposits visible along the streams form a thick sedimentary

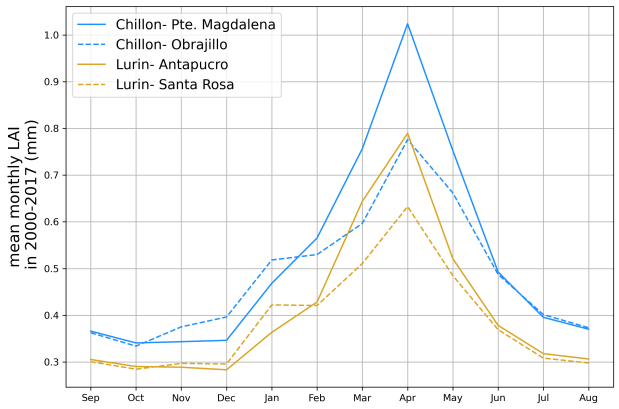


Figure 5.16: Chillón and Lurín basins: seasonality of subcatchment-averaged leaf area index (LAI)

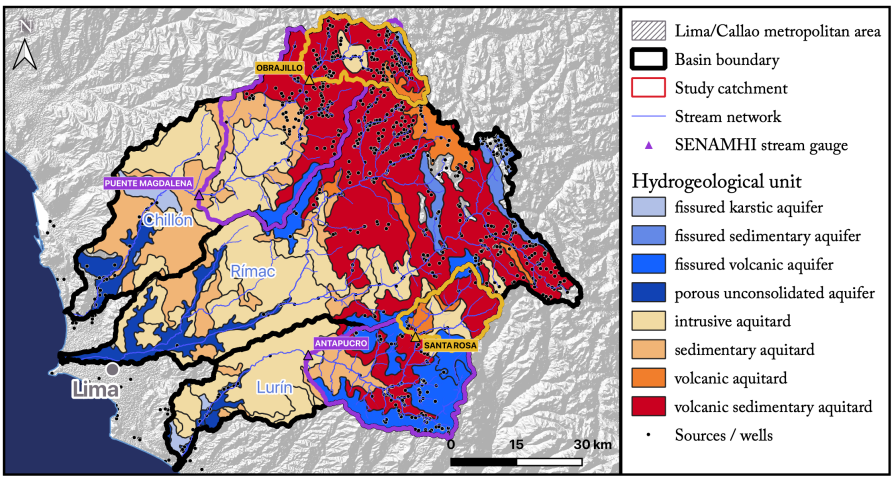


Figure 5.17: Chillón and Lurín basins: Hydrogeological units. Blue colors indicate geological formations classified as aquifers, red colors formations classifed as aquitards

stream water-fed aquifer, whose groundwater is pumped up and used for irrigation in these parts. In the middle and upper parts, larger contiguous geological structures ("volcanic sedimentary aquitard") stretch across the three basins, however to a lesser extent in the Lurín basin. The map and the percentage of coverage comparison in Figure 5.18d both suggest that the layer of "fissured volcanic aquifer" and by that aquifer formations in general are significantly more present in the Lurín basin. An aquitard is a rock formation deemed significantly less permeable than aquifers, yet still capable of storing and slowly transmitting groundwater. However, the relatively high number and density of wells and sources in the aquitard formation in the Chillón headwater shown by an overlain map of wells and sources in Figure 5.17 could be an indication that groundwater dynamics and flow in this aquitard formation is higher than suggested by the hydrogeologi-

cal map.

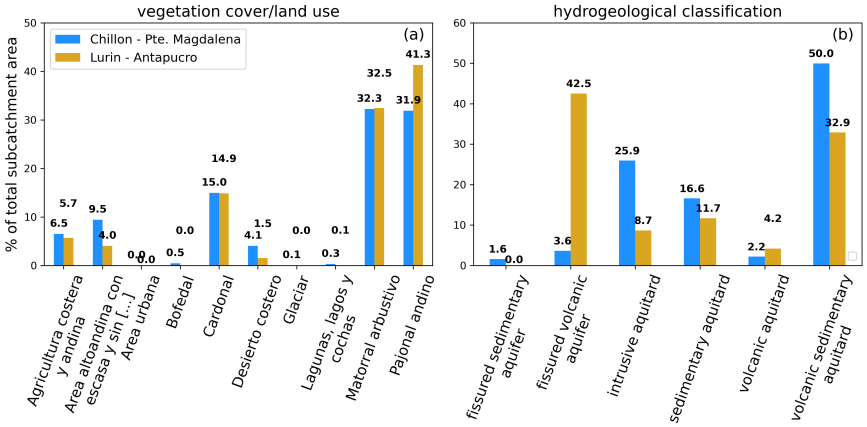


Figure 5.18: Chillón and Lurín subcatchments: comparison of spatially aggregated vegetation and hydrogeological classes, in percent of covered catchment area

*Anthropogenic activities*

Apart from the uppermost area near the mountain crests, villages and localities are spread all over both river basins, concentrated alongside streams (Figure 5.19). The density of localities is comparable in the two basins. In the Chillón, there appears to be more mineral deposits and mining activities. The map also shows five hydropower plants in the Chillón basin, whereas there are none in the Lurín valley. However, many of those are placed (or georeferenced) quite far off › the streams and there is no indication of adjacent reservoirs which are normally found upstream of hydropower plants.

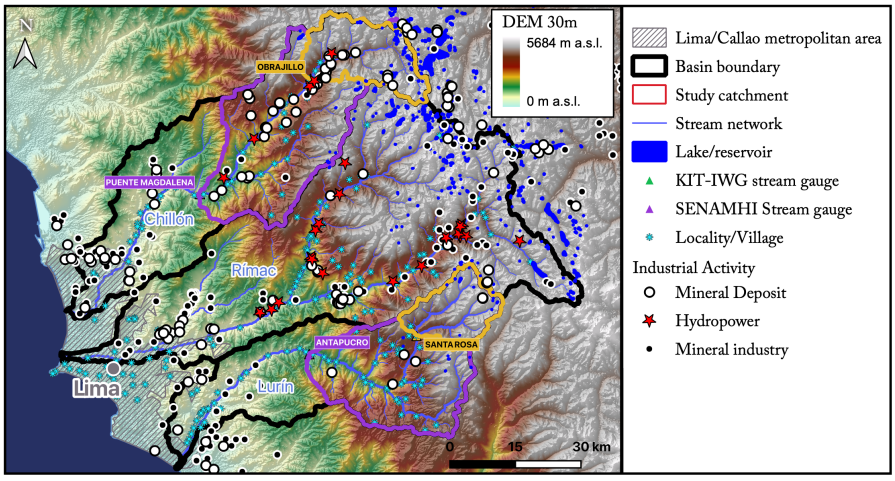


Figure 5.19: Chillón and Lurín basins: Anthropogenic activities

## 5.5 RESULTS

### 5.5.1 *Calibration and validation of Chillón river model*

*Model performance of calibrations*

23 different calibrations were conducted for the Chillón model, varying in forcing datasets, objective function, time period and calibration gauges. The resulting model performances are summarized in Figure 5.20, which shows NSE and water balance errors for the main (Puente Magdalena) and headwater (Obrajillo) catchment. Since one of the $ET_p$ products only provides data until end of 2016, the calculation of performance metrics for all runs was limited to that time period, to ensure a fair comparison. This had a significant impact on the general model performance in the main catchment since hydrological year 2016/17 presented an unusually high model error, e.g. with an NSE dropping to -3.8 for the chi10 run for the main catchment Puente Magdalena because of heavily overestimated observed stream flow (see Figure 5.22a).

We observe that both in terms of NSE and water balance error, the performances of the calibration runs vary for both subcatchments, however to a considerably higher degree for the main catchment. NSE for the headwater ranges between 0.55 and 0.88, whereas it spans a range from -0.29 to 0.83 for the main catchment (counting both calibration and validation values). While for the headwater catchment, the calibration and validation time period perform similarly, for the main catchment the two time periods can differ greatly (e.g. runs chi6-chi8). The modeled water balances show biases in opposite directions for main catchment and headwater (Figure 5.20 -bottom). While for the main catchment, the model systematically overestimates the discharge at the stream gauge between approx. 15 and 70% (mean: 36%), the headwater stream flow data is underestimated by 5-30% (mean: 19%). The performance according to NSE and to the water balance error for the whole time periods are well correlated for the main catchment ($R^2$ = 0.75) and moderately correlated for the headwater ($R^2$ = 0.57).

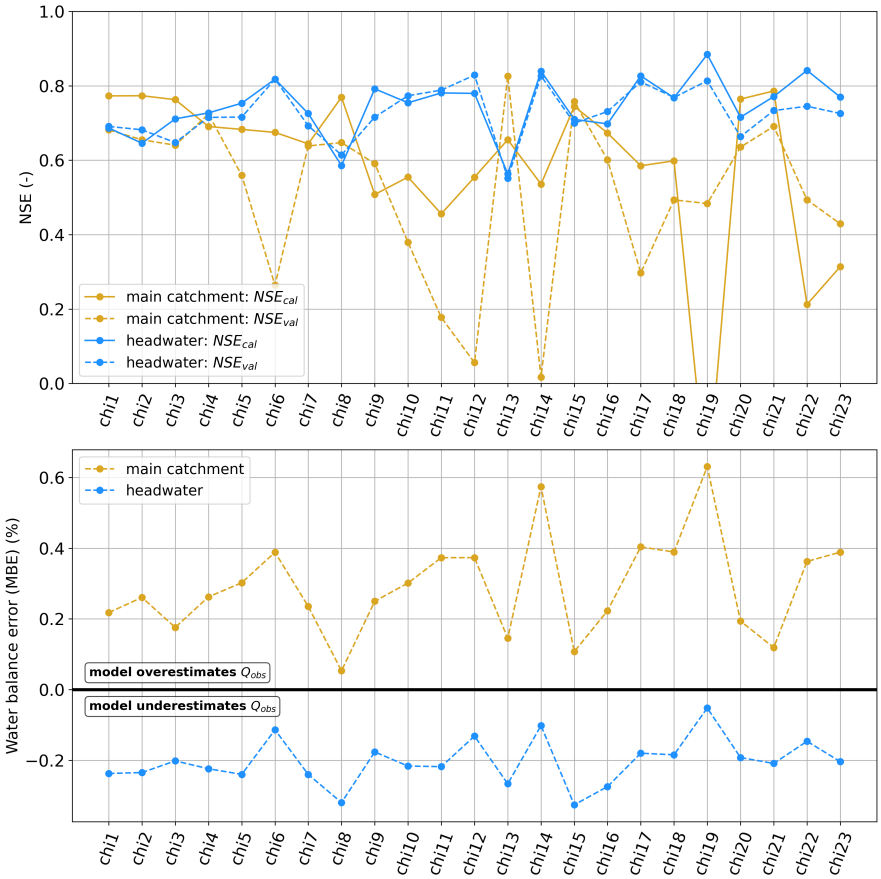


Figure 5.20: mHM calibration results Chillón- Comparison of all calibration runs. (top) Nash-Sutcliffe-efficiency (NSE), separately for each gauge catchment and distingiushing calibrationa and valiation time periods. (bottom) MBE mean biased annual water balance error throughout full simulation time period

The best model runs in terms of a compromise between the two stream gauges are 3, 4, 13, 15, 20, 21. The simulations producing the poorest model performances for the Puente Magdalena catchment are 11, 12, 14, 19, 22, 23. The poorest performances for the main catchment stem from calibrations based on the $NSE_{log}$ objective function and against stream flow data of only the headwater gauge, Obrajillo (see table 5.3). Inversely, calibration only against stream flow data of the main catchment, Puente Magdalena, also results in the poorest performances for the headwater, however to a significantly lesser extent, still producing NSE values around 0.6 for the headwater in these cases. The intra-annual comparison of the model runs revealed that the poor performances for the main catchment primarily stem from 3-4 particular years during which the simulations fail to reproduce the measured stream flow at the Puente Magdalena gauge: 2003/04, 2005/06, 2006/07, 2008/09 (and especially 2016/17 as aforementioned, which was however excluded from the averaged model performances in Figure 5.20 analyzed here), as illustrated by Figure 5.21. In compar-

ison, the headwater Obrajillo shows a far more stable performance throughout the years, reaching its lowest values in the first two modeled years (2003/04 and 2004/05). The performance at Obrajillo gauge also suggests a somewhat periodic behavior, with longer lasting, multi-annual periods of better and worse performance, as shown by the position of the performance envelope of the headwater in Figure 5.21. For lack of stream flow data for the main catchment Puente Magdalena between 2009/10 and 2012/13 as well as the very poor performance in the years mentioned, such trends in the fluctuation cannot readily be discerned for that gauge. Towards the end of the modeling period, starting around 2013/14, the water balance errors seem to shift and the simulation biases are inverted, with Puente Magdalena beginning to underestimate and Obrajillo to overestimate the observed stream flows.

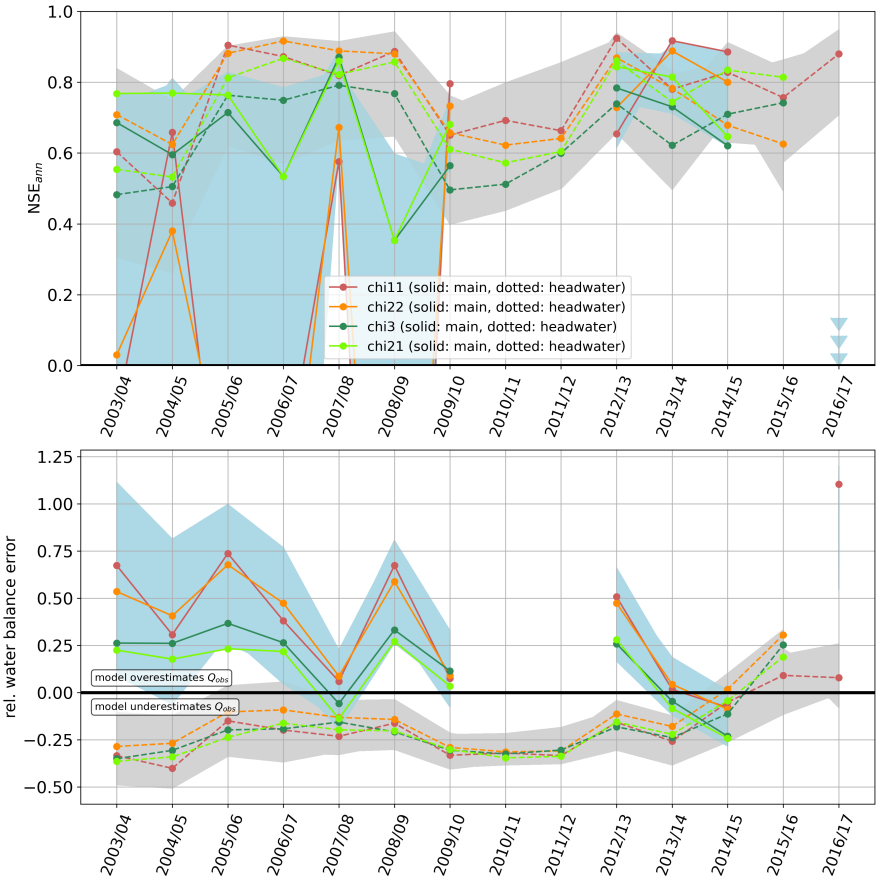


Figure 5.21: mHM calibration results Chillón- Interannual performances, selection of two well (chi3, chi21, greenish colors) and two poorly (chi11, chi22, reddish colors) performing runs. The colored envelopes in the background show the full set of runs, in grey the headwater performance and in the blue the main catchment

The precipitation-discharge time series of two well and two poorly performing examples are visualized in Figure 5.22 for the two subcatchments respectively (reddish colors indicates poor performance, greenish colors good performance). The rainfall seasonality that translates also to a pronounced stream flow seasonality is generally captured by the model for both subcatchments. However, the model reproduces the baseflow during the dry season more accurately for the headwater, while it tends to significantly overestimate it for the main catchment in most years and for all four simulations shown. Only in the first two hydrological years, the main catchment's dry season flow corresponds well to the model simulation, possibly stemming from initial conditions and spin-up effects in the storages. The runs with lower model performance (11, 22) were optimized based on the $NSE_{log}$ criterion (see section 5.3.2), which does not overstate the high flows as much, and leads to a better representation of the dry season flow. The defining criteria for the model performance are however the high flows during the rainy season, since they are dominant both for the NSE and the water balance error. In all the poorly modeled years for the main catchment, the high flows are heavily overestimated, explaining the low NSE and considerable water balance errors in Figure 5.21. The same influence of high flows can be seen for the headwater simulations, where the model performance drops between 2010 and 2013 because of clearly underestimated peaks.

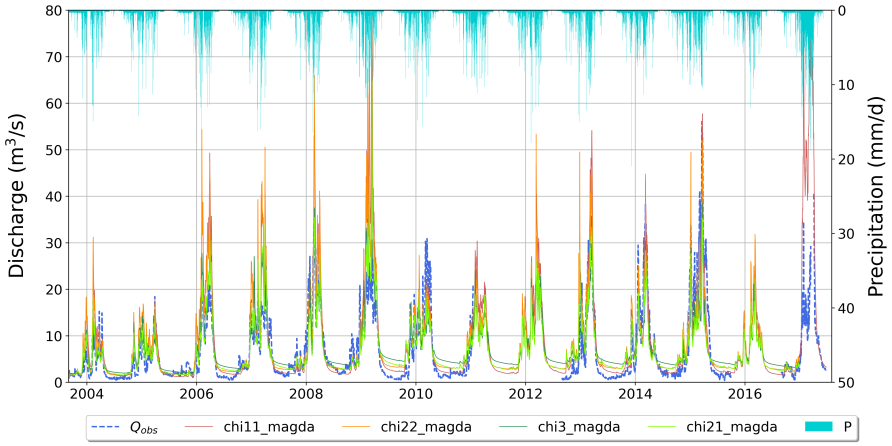


(a) mHM simulation results- Time series comparison of selected runs for main catchment (Puente Magdalena)

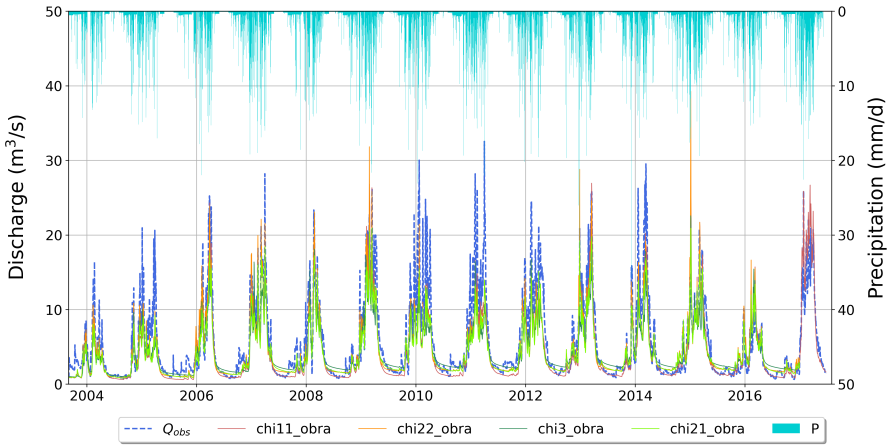


(b) mHM simulation results- Time series comparison of selected runs for headwater (Obrajillo)

Figure 5.22: mHM simulation results for Chillón catchment- Time series of selected runs. Runs with poor model performance have reddish, the good ones greenish colors. Mind that the precipitation shown on the upper y-axis corresponds only to one of the two rainfall datasets (here: CovVar), whereas the four runs differ in the forcing dataset

*Water balances and Budyko positions*

The mean annual water balances, both measured and modeled, remain in general below the estimate by the Budyko curve (Figure 5.23). The Budyko curve thus overestimates the evaporation ratios of the Chillón basin, in both its subcatchments. The headwater expectedly plots on the more humid section of the Budyko space. The four possible combinations of available meteorological forcing datasets (see section 5.2) result in four distinct aridity indexes, covering a relatively wide range of 0.6 in dryness. The forcing combination P-CovVar and $ET_P$-PISCO yields the most humid scenario and the evaporation ratios closest to the Budyko curve. The order of forcing combinations for

both subcatchments in Figure 5.23 from humid (left) to dry (right) is: P-CovVar & $ET_p$-PISCO / P-PISCO & $ET_p$-PISCO / P-CovVar & $ET_p$-HS-calib / P-CovVar & $ET_p$-HS-calib.
The differently calibrated models span EVR ranges between around 0.02 and 0.12, and runs chi21 and chi22 produce water balances closest the Budyko curve for both subcatchments. Simulated mean water balances from the different forcing combinations with different dryness indexes, do not follow the trend that higher dryness results in higher evaporation ratios as suggested by the Budyko curve.

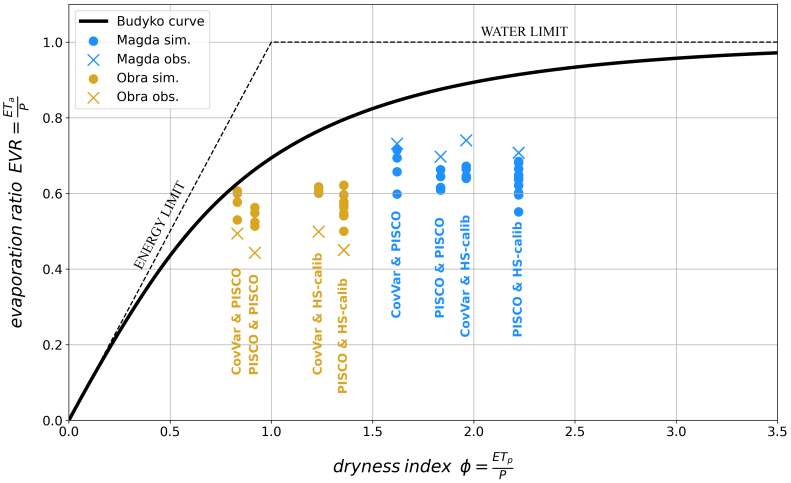


Figure 5.23: mHM simulation results Chillón- mean annual water balances of all model runs in Budyko space, the four possible combinations of forcing datasets yield four distinct aridity indexes, confronted with the measured water balance

For the headwater Obrajillo, the runs closest to the Budyko curve are however furthest away from the observed water balance s since the model underestimates the measured runoff and thus overestimates actual evaporation (the Budyko positions based on observations vary due to different rainfall datasets, since $ET_a$-observed is determined by P-Q). The combination of forcing datasets thus has a significant impact on the position of the catchment along the dryness axis and on the Budyko offset, both observed and simulated water balances. That is most relevant for the more humid headwater catchment, which plots in the vicinity of the steeper section of the Budyko curve. It approaches the Budyko curve in the case of observed data and practically reaches the curve in the case of simulation chi21 and chi22.

In terms of interannual variability of the simulated water balances and their corresponding Budyko positions, we observe in parts a considerable spread around the mean annual values, along both axes of the Budyko space (Figure 5.24). Differences in the spread between model runs are mainly related to the combination of meteorological

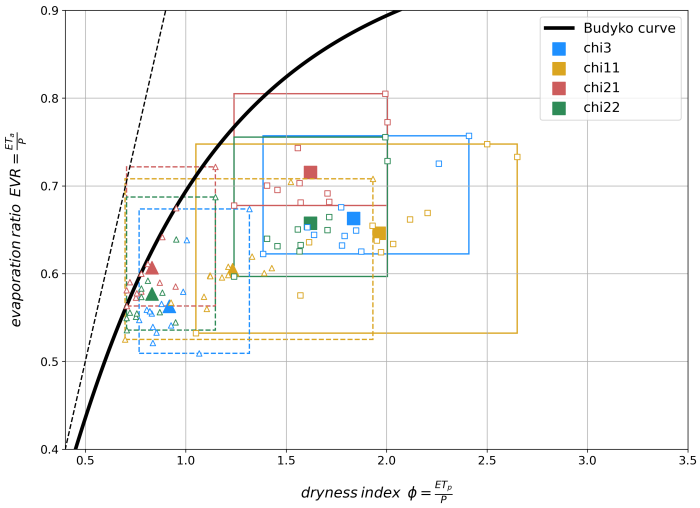


Figure 5.24: mHM simulation results- annual water balances of four selected model runs (best compromise between gauges) in Budyko space. Big symbols correspond to mean annual, little symbols to annual water balances. Square symbol and solid lines for main catchment (Pte. Magdalena), triangles and dashed lines for headwater (Obrajillo)

forcing datasets, which on the other hand is conditioned by the time period covered. When the dataset includes the outlier year of 2016/17, the spread increases significantly, both in terms of dryness and evaporation ratio (only the case for chi11). For three out of the four runs shown, the headwater's (Obrajillo) annual water balance plots on or in immediate proximity to the Budyko curve for chi3, chi21, chi22.

When comparing the simulated and measured annual water balances, it becomes visible that for runoff-favoring years (i.e. lower observed EVRs), the spread of simulated EVR increases (Figure 5.25), i.e. the two are less correlated. While the model -neglecting here the general bias found in the mean water balances of the model (visible also in the Figure on the two sides of the y=x diagonal)- does simulate higher evaporation ratios for higher observed ones, it deviates from that behavior for the runoff-favoring years, especially for the main catchment Puente Magdalena: below an $EVR_{obs}$ of around 0.7, the correlation between modeled and observed EVR changes, as indicated by the fitted lines in Figure 5.25. Only the hydrological year 2016/17 stands out in run chi11 (the other runs do not cover that ). For the headwater Obrajillo, a similar trend is somewhat visible (the threshold being somewhere around 0.5), however less clear and with a larger spread, precluding the drawing of such trend lines.

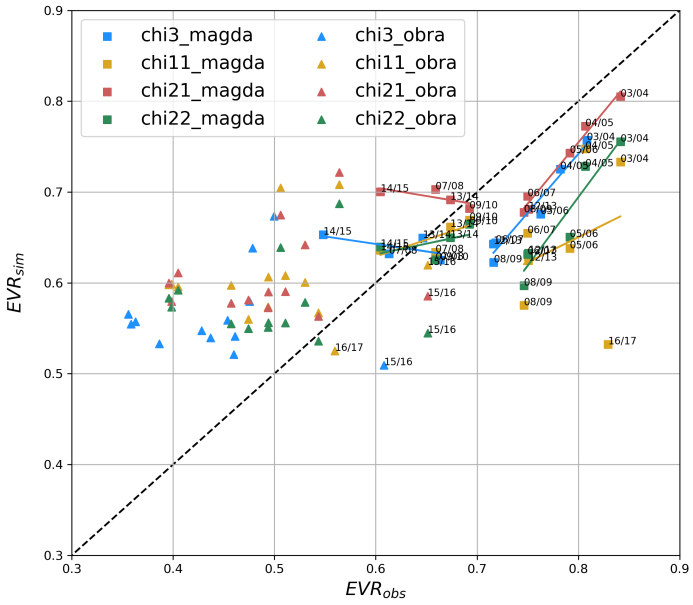


Figure 5.25: mHM simulation results- sim. vs. obs. annual water balances of four selected model runs (best compromise between gauges). Squares for main catchment (Pte. Magdalena), triangles for headwater (Obrajillo)

### 5.5.2 *Parameter transfer and modeling of Lurín river*

*Selection of transferable parameter sets*

The global parameter set from three calibrated runs of the Chillón model were chosen to be transferred to the Lurín model, to be tested for runoff and water balance prediction in the neighboring Lurín basin: chi3, chi21, chi19. The selection resulted from a compromise of several criteria: The first two were picked because of their good performance at both stream gauges in the Chillón river and because they differ in the parametrization with regard to a selection of the most sensitive parameter based on Höllering et al. (2018) and a sensitivity analysis conducted for the Chillón model. In addition, chi21 presents the run closest to the Budyko curve. The third one, chi19, was chosen because of its good performance in the headwater due to the calibration based solely on that one gauge. The headwater is likely to be under less anthropogenic influence and produces in general more robust and coherent modeling results.

*Performance of transferred parametrizations and calibrated reference runs*

The validation of model simulations in the Antapucro subcatchment of the Lurín river revealed significant differences between the few hydrological years for which stream flow data exist, both in terms of

observations and in resulting model performances. Given that two of the forcing datasets, PISCO-P and PISCO-$ET_p$, were only available until 2018-06 and 2016-12, respectively, the model runs' performances are validated only inter-annually, since a temporally aggregated performance metric would not be comparable with varying simulation periods and with such interannual variability. The validation will thus be on focused on selected and not the entire set of calibrated model runs that serve as reference runs to the runs based on parameter transfer. Furthermore, in the hydrological year 2016/17, the measured streamflow data stops near the end of the rainy season on March 17th 2017 (section 3.5), and thus does not cover a full hydrological year.

While the first two hydrological years modeled, 2014/15 and 2015/16, show a comparably stable performance with an NSE ranging from about 0.35 to 0.75, for the third year the NSE jumps between below 0 and 0.8 (Figure 5.26). The model either reaches a compromise between the first two and the third year (lu6, lu5_19), or favors the performance of one of the two periods to the disadvantage of the other. Annual water balance errors fluctuate less, going from an underestimation of measured streamflow in 2014/15 of around -18 to -50% to a clear overestimation in 2016/17 ranging from 17 to 125%, and 2015/16 plotting in between. This trend is independent of the model parametrization. The fourth hydrological year with available stream flow data, 2018/19, the discharge could not be reproduced by the model at all. For that year, the NSE drops considerably below 0, producing values between -1.5 and -12, and a water balance overestimation of about 180-250%. The color code in Figure 5.26 as well as the run nomenclature (table 5.3 distinguishes the different ways the model parametrization was obtained. The mHM-default parameters (lu5_def_anta) produces better results in the first hydrological year than the calibrated run. The performance drops however for the second and even more for the third year. The transferred parameter sets (greenish colors) show performances comparable to the calibrated runs, with lu5_21 yielding the best performance in 2016/17 and lu5_19 the best compromise across the years.

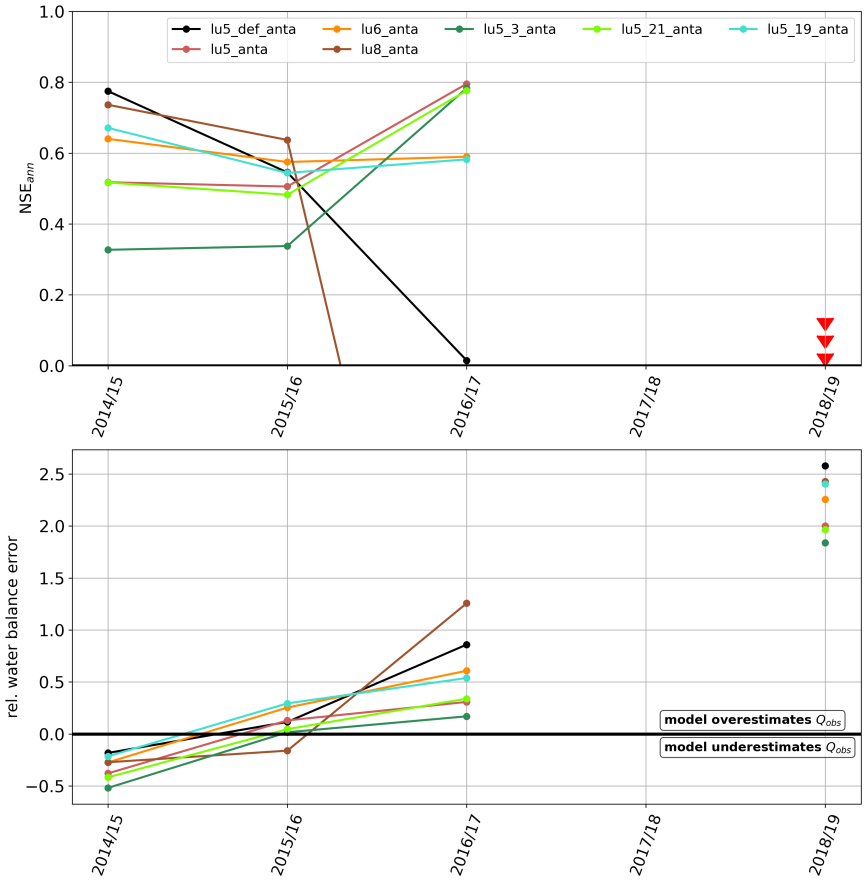


Figure 5.26: mHM simulation results Lurín- Interannual comparison of all simulation runs. Color code: black: default mHM parameters, reddish: Lurín direct calibration, greenish: parameters transferred from Chillón model. (top) Nash-Sutcliffe-efficiency (NSE), red arrows indicate NSE values below zero (values vary between -1.5 and -12) / (bottom) MBE mean biased annual water balance error

The monitoring data at Antapucro gauge show a similar seasonal streamflow pattern as in the Chillón basin, however suggesting even lower dry period flows that approach o $m^3/s$. Most of the model runs simulate however a significantly higher dry season runoff, a slower recession after the rainy season than the observation data. All three transferred model runs were initially obtained by optimizing NSE as well as two of the reference Lurín calibrations, putting put more weight on the high flows. That translates to an overestimated dry period flow in the Lurín. The same goes for the default mHM parameter run which seems to expect a slower baseflow recession. Out of the visualized runs, only lu8, stemming from an optimization of $NSE_{log}$ generates a quick recession and near-zero flow during the dry season. That is also the case of other, not visualized runs optimizing the $NSE_{log}$ criterion.

While for the dry season runoff, the monitoring data and the model error show similar behavior throughout the 3-4 hydrological years, the rainy season flows expose considerable differences that make for the variable performances between the years in Figure 5.26. In general, all runs systematically underestimate the first 2-3 months of the rainy season in 2014/15. The lu8 run, $NSE_{log}$-optimized and having more soil storage capacity, produces a more dynamic runoff response, with faster rising and sharper peaks, coming closest to the measured peaks. Even if not as striking, the behavior is fairly similar in 2015/16, whereas it is different in 2016/17. In the third year, the initial increase of streamflow at the onset of the rainy season is reproduced by most model runs. However, the peaks then are overestimated. The three Lurín model runs with parameters transferred from the Chillón basin produce peak flows that are lower than the calibrated runs in the Lurín and the mHM default run. For the first two hydrological years, this worsens the underestimation. In the third year, when rainfall-runoff proportions are different, the transfer runs are in better agreement with the peak flows.

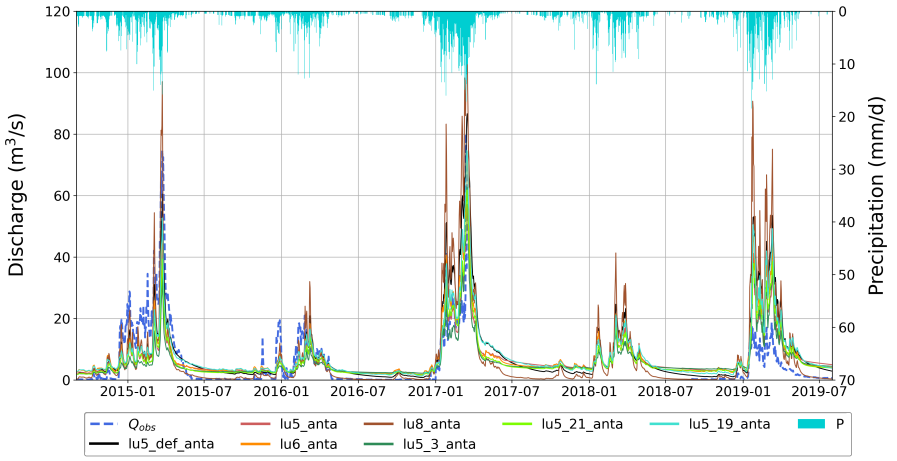


Figure 5.27: mHM simulation results Lurín- Comparison of all simulation runs. (top) Nash-Sutcliffe-efficiency (NSE), (bottom) MBE mean biased annual water balance error throughout full simulation time period

*Water balances in Budyko space*

The mean annual water balances of the Lurin-Antapucro catchment are overestimated by the Budyko curve for all simulations (Figure 5.28). There is likewise a strong dependence on the meteorological forcing dataset that impacts both the estimated dryness as well as measured and simulated EVR. In the case of the Lurín, there was however only one $ET_p$ dataset that was used, since $ET_p$-PISCO was available until 2016-12, covering only the first two hydrological years. Variations in dryness and EVR thus can stem from the rainfall dataset itself

and from the time period covered by it: the PISCO-P rainfall dataset only provides data until 2018-06, which does not contain the fourth hydrological year, and given the short time period in general, one year or data point can impact the average significantly. In addition, the hydrological 2016/17 was excluded for the Budyko plot, since streamflow data was available only until 03/2017.

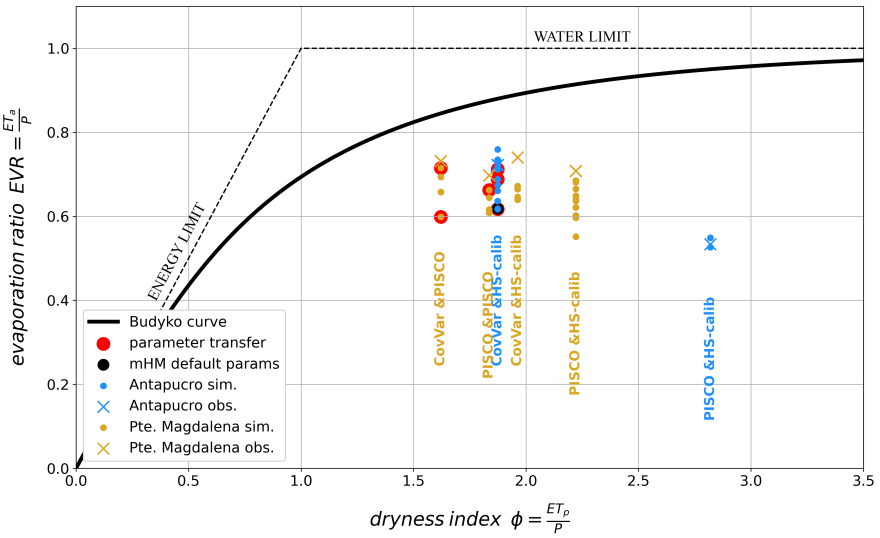


Figure 5.28: mHM simulation results Lurin- mean annual water balances of all model runs in Budyko space, the four possible combinations of forcing datasets yield four distinct aridity indexes, confronted with the measured water balance

The main influence stems from the CovVar rainfall dataset itself, which produces significantly more rainfall for the Lurín catchment (see section 4.1.4) and entails a diagonal shift in the Budyko space for the observations (see section 2.4.3). The fourth hydrological year, 2018/19, having the highest simulated runoff coefficient and the lowest observed one (together with 2016/17) and being included only in the CovVar dataset, additionally shifts the mean observed EVR towards the Budyko curve, and the simulations further away from it 5.29. Besides the proximity to the Budyko curve, the CovVar rainfall dataset also produces a mean water balance for the Lurín that is quite comparable to the one of the Chillón river. On the other hand, the PISCO dataset yields water balances and dryness indexes far off the Budyko curve and the Chillón basin. The three transferred parameter sets lead to simulated water balances in the Lurín similar to their corresponding model runs in the Chillón, and amongst the closest ones to the Budyko curve. The most comparable Chillón runs use however a different $ET_p$ dataset (PISCO-$ET_p$), partially influencing the lower dryness index (more humid).

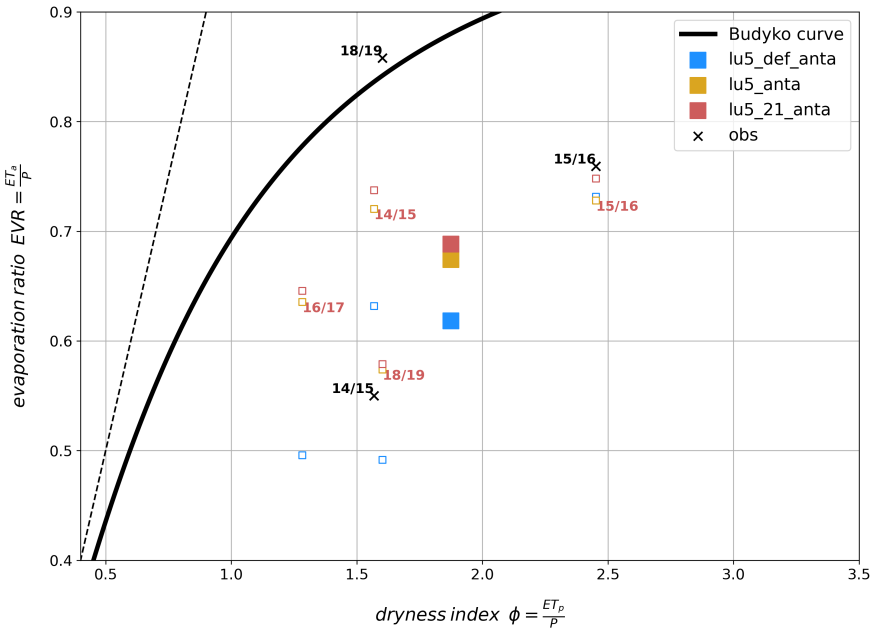


Figure 5.29: mHM simulation results Lurín and Chillon- mean annual water balances of all model runs in Budyko space, the four possible combinations of forcing datasets yield four distinct aridity indexes, confronted with the measured water balance

## 5.6 DISCUSSION

This chapter discusses relevant results obtained for the models set up for the Chillón and Lurín basin. It discusses the ability of the model to reproduce the rainfall-runoff dynamics, reflects on the initial similarity assumption for the two basins and the related parameter transfer, as well as evaluates observed and simulated water balances, their positions relative to the Budyko curve and if the Budyko curve is useful in evaluating the model performances.

### 5.6.1 *Relation between headwater and main catchment streamflow in the Chillón basin*

*Stream flow data of the two gauges appears inconsistent*

The hydrological model, mHM, was able to reproduce the general discharge dynamics in the Chillón basin, validated on the basis of two stream gauges, one placed in a headwater (Chillon-Obrajillo) and the other further downstream, effectively encompassing the whole part of the basin where significant rainfall occurs (Chillon-Puente Magdalena). The model struggled however to simulate water balances for both gauges simultaneously since their discharge data appears to be partially inconsistent. In some hydrological years, monthly and annual discharge volumes measured at the headwater gauge exceed the ones at the lower main gauge, suggesting water losses along the river path. As depicted by Figure 5.30, which visualizes the difference between

monthly discharge at Obrajillo and Puente Magdalena according to A. the observed (solid line) and B. the modeled discharge (dashed line) for two very different hydrological years. In 2004/05, the headwater flow is constantly higher during the rainy season (Figure 5.30-left), while it is the other way around in 2007/08 (Figure 5.30-right). Given the catchment sizes -Puente Magdalena 1260 km$^2$ and Obrajillo 365 km$^2$ -and the fact that there is significant rainfall occurring outside the headwater (Figure 5.5), it is unlikely that there is no contribution to the discharge, as the model demonstrates when it brings all the input data together.

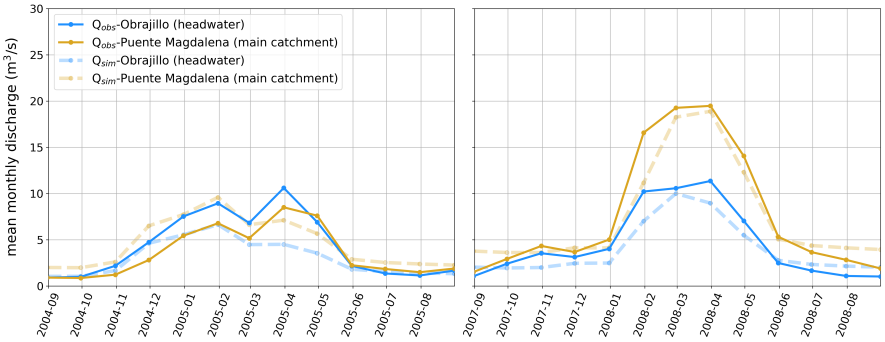


Figure 5.30: Inconsistencies of observed streamflow at the two gauges in the Chillón basin, based on chi3 run, dashed lines in the background show the model simulations: (left) year with implausible streamflow data, (right) year with plausible data

The model, when calibrated simultaneously against both stream gauge datasets, has to find a compromise between the two and thus overestimates the lower gauge while it underestimates the headwater one (Figure 5.20). The question why the two streamflow datasets do not yield a more coherent picture is probably due to a combination of the following two reasons: anthropogenic interventions and/or measurement uncertainties. Uncertainties and errors in discharge monitoring are in general hard to assess, especially if there is no information on the part of the institution conducting the measurements and developing the rating curve. Such measurement uncertainties are more likely in challenging terrains as well as in a region of limited resources for environmental monitoring and maintenance such as the study area. Geometry changes in the gauge control section are more likely in a region suffering flood events with heavy bed and sediment load (*huaycos*, local name for mudslides (Pareja Dominguez et al., 2022)).

In terms of anthropogenic interference with the natural discharge dynamics, extractions of stream water between the two gauges or artificial retention in reservoirs in the non-headwater part of the catchment could explain part of the flow differences- both are measures to

*Anthropogenic effects?*

stock or use water during the rainy season for agricultural, industrial or domestic purposes. The main flow difference occurring during the rainy months (Figure 5.30-left) would support that since the difference during the dry season is zero or switches back to the expected proportion. During the dry season, stream flow is sustained by baseflow stemming from sources and reservoir release. In the Chillón basin, most reservoirs are situated in the headwater (Figure 5.13), while sources are also found below (Figure 5.17). In the Chillón, there are mining activities, mainly silver and gold (INRENA, 2004), many of which are found between the gauges as illustrated by the map in Figure 5.19. Such water-consumptive industrial activities could explain water diversions and losses between the gauges. The same goes for agricultural activity, which in the middle and upper parts almost exclusively occurs outside the headwater (Figure 5.15) and usually represents the most important human water consumption. In accordance with agricultural activity, Andean villages are also found mainly below the headwater gauge (Figure 5.19). The total water demand for the dry season of the *Lurín* was estimated by the TRUST project at around 13 $Mm^3$, mainly for agriculture. A difference of approx. 2.5 $m^3/s$ between the gauges of Obrajillo and Puente Magdalena (Figure 5.30-left) during the rainy season would correspond to a volume stocked for the dry season of 32.4 $Mm^3$, or more since the flow difference between the gauges, under unaltered natural conditions, is supposed to go the other way. However, as a rough estimate and knowing that the Chillón has more industrial activities (Sanchez, 2016) as well as more storage capacity in reservoirs than the Lurín (Observatorio del Agua, 2019), withdrawals during the rainy season can play a role in the two streamflow measurements. The mHM model at its current state, without explicitly developed extensions or modules (the model is constantly under development), cannot and thus does not account for anthropogenic interference with the natural hydrological processes.

*Inconsistent flows depend on year*

While it is difficult to quantitatively tell the two influences mentioned apart, they presumably both play a role to some degree. The fact that the inconsistencies between the two stream gauges are highly variable throughout the years, could also be related to both influences. While measurement uncertainties could be more prominent in years with or after heavy flood events, inconsistencies across the years could also indicate differences in the management of the stream water extractions and reservoir management. It might vary depending on remaining reservoir fillings, wetness of previous and current year, changes in the consumption or its prioritization with respect to conflicts with downstream Lima metropolitan area.

### 5.6.2 *Mean annual water balance and relation to the Budyko curve of Chillón and Lurín basin*

Before starting to discuss mean annual water balances, it shall be reminded that for the Lurín, only three to four years of streamflow data was available, violating the steady-state condition the Budyko curve is designed for (section 2.3), and thus limiting the representativeness of a derived mean annual water balance as in the Figure since storage effects play a role at this short time range. The mean water balance derived on the basis of three to four years is however used here as a coarse estimate and comparison to the Chillón, rather for plausibility than for exact quantitative assessment.

*Budyko curve overestimates all subcatchments water balances*

All subcatchments of Chillón and Lurín have measured evaporation ratios lower than estimated by the Budyko curve. The Budyko positions and offsets vary however considerably as a function of the meteorological forcing dataset used to make simulations, to estimate observed $ET_a$ ($P\text{-}Q_{obs}$) as well as to determine the dryness index. There is a multitude of possible reasons for the systematic overestimation by the Budyko curve. In literature, studies have found a more general trend of regions with pronounced rainfall seasonality to generate lower evaporation ratios (Fu and Wang, 2019; Lavenne and Andréassian, 2018). Lavenne and Andréassian (2018) argue however that rainfall seasonality leads to significantly lower EVR only in combination with a relative phase lag of potential evaporation. Other influences, potentially interacting with the seasonal aspects, can contribute to the offsets as well. In chapter 6, which takes a closer look at multiple catchments along the western slopes of the Peruvian Andes, all exposed to similarly seasonal climate, a systematic however very variable overestimation by the Budyko curve is observed for all those catchments. Chapter 7 investigates the role of soil storage in Budyko offsets by means of a model-based virtual experiment. Soil storage capacities as well a capillary storage fraction therein appear to be of crucial importance in the lower soil storage capacity ranges, thus potentially explaining a part of the trend to be overestimated by the Budyko curve. In field campaigns, soil depth in the Lurín basin proved to be variable yet often very limited within the range of 10-20cm.

*CovVar rainfall approaches the two basins, and suggests more proximity to Budyko*

The CovVar rainfall dataset developed in section 4.1 proved to yield more plausible water balances for the Lurín basin. The plausibility here is based on a greater similarity to the neighboring Chillón basin, on a smaller offset to the Budyko curve as well as on a better agreement between observed and modeled water balances (Figure 5.28). Use of the CovVar rainfall model supports the initial hypothesis of similarity between Chillón and Lurín. Hydrological models can

be used to evaluate the performances of different rainfall datasets (Kneis and Heistermann, 2009). The similarity also depends on the meteorological datasets used for the Chillón, however to a significantly lesser degree in terms of the rainfall dataset. The two datasets yield comparable Budyko positions for Chillón's main catchment Puente Magdalena. For the Lurín, only one $ET_p$ dataset is shown in the Budyko plot in Figure 5.28 since the other one (PISCO-$ET_p$) only covers two hydrological years.

*Transferred parameter sets yield useful model runs*

The transfer of model (global) parameters simulates evaporation ratios in the Lurin-Antapucro catchment that are fairly similar to the water balances of the corresponding calibrations of the donor catchment (Figure 5.28). It thus serves as a valid way of obtaining a functional model parameter set for the ungauged target catchment. The run with parameters transferred from a calibration only against the Chillón headwater (Obrajillo, chi19, lowest EVR dot in Figure 5.28) also clearly underestimates the water balance in the main catchment of Lurín, indicating similar differences between headwater and residual catchment in the Lurín. However, the variability of the meteorological input datasets has a far greater impact on the observed and simulated water balances than the model parametrization itself. The model run based on mHM's default parameter setting produces a mean water balance in the Lurín furthest away both from observation and the Budyko curve, however still in some proximity to the other runs as opposed to the runs based on the other rainfall dataset.

*Differences between headwater and residual catchments' water partitioning*

The water balances resulting from both stream gauges of the Chillón basin do not appear to be coherent, as explained in the previous section. When both gauges condition the model calibration, the model behavior results in a compromise between the gauges, and thus in the two subcatchments approaching one another in terms of $EVR_{sim}$. While the model does follow the general tendency to generate more runoff in more humid catchments -as described by the Budyko curve-, it does not suggest such a big difference in the mean water partitioning (EVR) between the headwater and the rest of the main catchment. If it is not solely related to discharge data quality issues, catchment characteristics would have to differ more strikingly between head and main catchment in order for the model to generate a more different mean hydrological response. Soil characteristics, whose importance for the mean water partitioning was shown in chapter 7, are not very different between the two subdomains based on the soil texture data used in the model (Figures 5.12 and A.1 in appendix A.2) homogeneously distributed, for lack of more detailed information at the catchment scale (section 5.4). Effective model parameters like conceptualized field capacity and hydraulic conductivity based on soil textural input data in the calibration procedure, could theoretically result in different

drainage mechanisms in different areas of the model domain - in the morphological input data provides such spatial variability.

### 5.6.3 *Interannual variability of the water balance of Chillón and Lurin*

The high interannual variability in terms of observed annual runoff coefficients for both the Chillón and Lurín basin, made it difficult for the model to reproduce the hydrographs and water balances. The variability concerns all subcatchments of both basins in theory, the discrepancies between modeled and simulated water balance is however not as striking in the Obrajillo headwater of the Chillón basin. Figure 5.25 showed that the relation between modeled and observed annual water balance depends mainly on the value of the observed annual runoff coefficient itself, the model not being able to adequately represent two different runoff coefficient scenarios for the basin.

While for the two Chillón subcatchments, the systematic water balance errors of the model were found practically in all hydrological years, this was strongly conditioned by flow volume inconsistencies between the two stream gauge datasets, as discussed above in section 5.6.1. However, certain hydrological years, in particular 2008/09 and 2016/17 in the Chillón and to a lesser extent 2018/19 in the Lurín), stand out from the mean water balance error by the model heavily overestimating stream flow at the lower gauge. The question arises if this pronounced variation of the annual runoff coefficient is due to natural processes or to shortcomings in measurement and estimation of discharge and areal rainfall. Anthropogenic influences are not likely to play an important role at volume differences of that order of magnitude. Figure 5.31 reveals that the observed runoff coefficient tends to be quite low in very wet years in 2008/09 and 2016/17 for the main catchment of the Chillón. While the rainfall amount in those years is also high in the headwater alone, in comparison to the other years they do not stand out as much as the rainfall amounts in the main catchment - suggesting a particularly rainy year in the residual catchment. Similar issues are observable in 2018/19 for the Lurín (Antapucro), even though rainfall-wise the year, while indicating a comparably wet year, the annual total is not that high. For 2016/17, with partial streamflow data only until 03/2017, a statement on the annual total difference between model and observation cannot readily be determined, the first half of the year hinting at a volume error, however probably not as striking. If taking the Budyko curve as an orientation, such low runoff coefficients as in 2016/17 correspond better to the expected water balance - bearing in mind however that the Budyko framework is representative at multiannual scales.

Interannual dry-wet cycles and catchment memory in terms of storage could be relevant at the interannual level. The antecedent years to 2016/17 (and to 2008/09 in the Chillón) were significantly drier, and resulting comparably empty subsurface and reservoir storages may have caused lower runoff coefficients than other years. If this aspect had a significant impact on the resulting model error, actual catchment storage dynamics would not be adequately represented by the model.

Furthermore, the year 2016/17 raises attention in terms of the ENSO anomaly, since that year a coastal, more localized *El Niño* anomaly in ENSO-region 1+2 (see Figure 3.2) was detected that also lead to extreme flood events in Peru (Son et al., 2020). One supposedly *El Nino*-driven event in March destroyed the water level sensor Antapucro in the Lurin. The influence of ENSO anomalies on rainfall patterns in the region not being straightforwad -e.g. higher annual precipitation total in Perus north, lower ones in the south (Rome-Gaspaldy and Ronchail, 1998; Tapley and Waylen, 1990). If at a subdaily scale, higher intensity rainfall events occurred with preference at *El Niño* conditions, making Hortonian overland flow more probable, mHM's model structure running at daily forcing time steps, would not be able to model that process. Such a shortcoming would result in underestimated simulated runoff coefficients, the opposite is the case however, rendering an El Niño based reasoning unfounded. For 2008/09, the ENSO indexes indicated *La Niña* conditions.

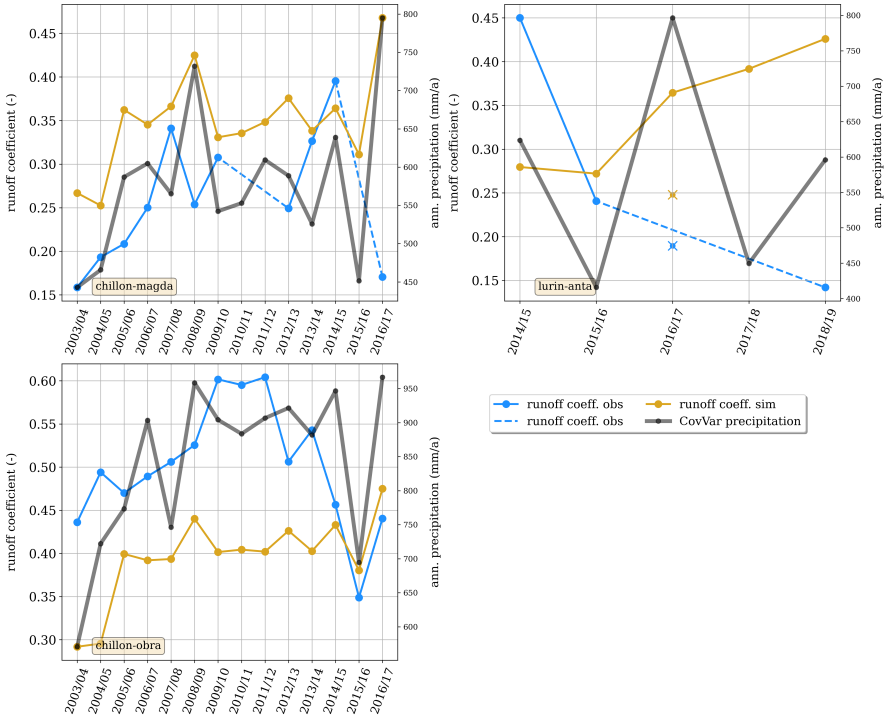


Figure 5.31: ChiLu interannual variability of runoff coefficients and CovVar precipitation, one illustrative example model run per basin (chi11, lu5), dashed lines without dots indicate years without enough $Q_{obs}$ data (and no interpolation), crosses indicate the partial hydrological year 2016/17 with the runoff coefficient evaluated only until 2017-03-17

Upon analysis of the outlier nature of the years mentioned, comparison of Luríns' observed annual double mass curves with the ones from the Chillón, it seems that rather a year like 2014/15 with higher runoff coefficients is out of range when compared to all Chillón-Pte. Magdalena years (Figure 5.32a), while 2016/17 and 2018/19 are within this range. Looking at the Budyko curve, those low runoff coefficients are also in better agreement with the Budyko-expected water balance. Given however the high interannual variability and the small number of years taken into account, a derived mean annual water balance is however not at steady-state and barely representative for the catchment. With such variability and data uncertainty, conclusions on more or less plausible water balances remain difficult.

### 5.6.4 *Similarity in intra-annual dynamics and seasonality of Chillón and Lurin*

When zooming in on intra-annual dynamics, high flows during rainy season and low baseflow during the dry season, differences between both between the basins and between model parametrizations become

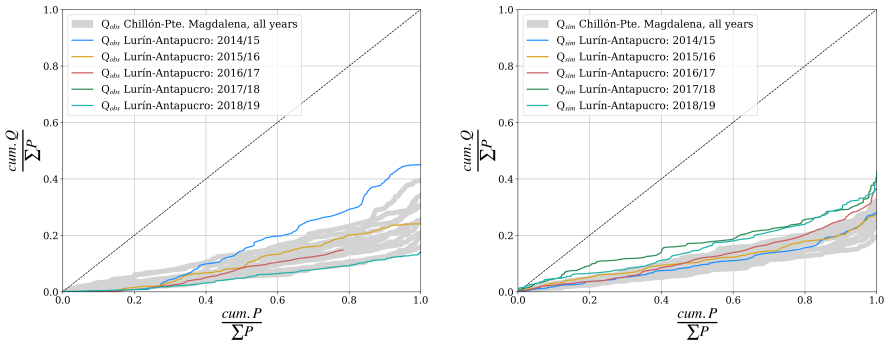


(a) based on observed runoff (b) based on simulated runoff

Figure 5.32: Annual double mass curves of observed and simulated runoff for Chillón-Pte. Magdalena and Lurín-Antapucro, Lurín curves in color, Chillón curves in grey

apparent. Given the pronounced rainfall seasonality, all models reproduce in general the resulting seasonal pattern of the streamflow. However, with respect to the representation of peak flows of flood events and the baseflow recession and sustainment after the rainy season, the models can deviate considerably from the observed behavior. The model behavior in this regard is related to runoff generation types and their calibrated recession constants. mHM distinguishes four types of runoff: direct runoff over impervious areas $Q_D$ (of which there are none in the Chillón and Lurín model setups), fast interflow $Q_{If}$, slow interflow $Q_{Is}$ and baseflow $Q_B$ (section 5.3.1). The proportions between the three runoff components are conditioned by the parametrization and are sensitive to the objective criteria which weight high and low flows differently, which in such a seasonal setting is of particular importance.

*High flows in rainy season*

The Lurín model runs based on transferred parameters produces plausible simulations of flood events, however with even greater underestimations in the first two hydrological years than the calibrated reference runs and the mHM default parameter settings 5.26. In the third year, 2016/17, with high rainfall and a low runoff coefficient, the peaks of the transfer runs are closer to the observations. The transfer run parametrizations partition the runoff quite equally between baseflow $Q_B$ and slow interflow $Q_{Is}$ (Figure 5.33), with the parametrization from the Chillón headwater slightly preferring slow interflow in comparison. Lu8 with a deeper soil layer and calibrated against $NSE_{log}$ generates almost 90% of the runoff via slow interflow, resulting in a more jumpy and dynamic hydrograph. Relating the behavior to global model parameters is not straightforward, it results rather from the interplay of multiple global parameters that in combination with the morphological input shape the regionalized effective

model parameters ($\beta_i$).

The observed stream flow at Antapucro contains two major peaks, around 75 $m^3/s$ in 2015 and 80 $m^3/s$ in 2017, the latter resulting from the local El Niño event that destroyed the water level sensor in March 2017. Those flood events occurring in this short time period of four years are higher than any measured event in the Chillón-Puente Magdalena catchment over the extent of a significantly longer time period and despite the approx. 315 $km^2$ larger catchment area ($Q_{obs}$) in Figure 3.5).

*Smaller Lurín catchment exhibits higher peak flows?*

Apart from the possibility of discharge measurement errors for the highest peaks as a result of rating curve extrapolation uncertainty, other natural and anthropogenic reasons might explain the differences between the basins. It may be indicative of a higher dynamic retention capacity in the Chillón. According to Observatorio del Agua (2019), there is significantly more natural and artificial reservoirs/lakes in the Chillón upper basin part than in the Lurín, that is not only relevant at longer term storage but can also play a role in flood mitigation, if managed accordingly (see also the GIS map in Figure 5.13).

The mHM model does however capture that difference. It simulates such high discharges for the two major flood events in the Lurín, even overestimates them in some model scenarios, but never reaches comparably high streamflows in the Chillón. Hence, certain hydrological ingredients of the flood events must be included in the model, mainly continuous rainfall over days, antecedent and increasing soil moisture as well as an additional fast interflow generated by the model as a result. As visualized in Figure 5.7, the daily input data suggests on average more rainy days yet of less daily totals in the Lurín. More frequent rainfall can also result in higher average soil moisture and lead to more proneness to generate saturation-excess overland flow, a potential difference between the basins.

For the fourth hydrological year, 2018/19, all model runs clearly overestimate the rainy season streamflow. Despite the differences between the model configurations and their parametrization, the interannual variability suggested by the observation data and the related model deficiencies clearly outweigh the importance of the parametrization.

*Dry season flow*

The dry season streamflow also presents significant differences between the model parametrizations and the two basins. All three transferred parameter sets resulted in an overestimated dry season runoff compared to the near-zero observations in the Lurín-Antapucro catchment (Figure 5.27). The corresponding original Chillón-Puente Magdalena runs also generated too high dry reason flow in some

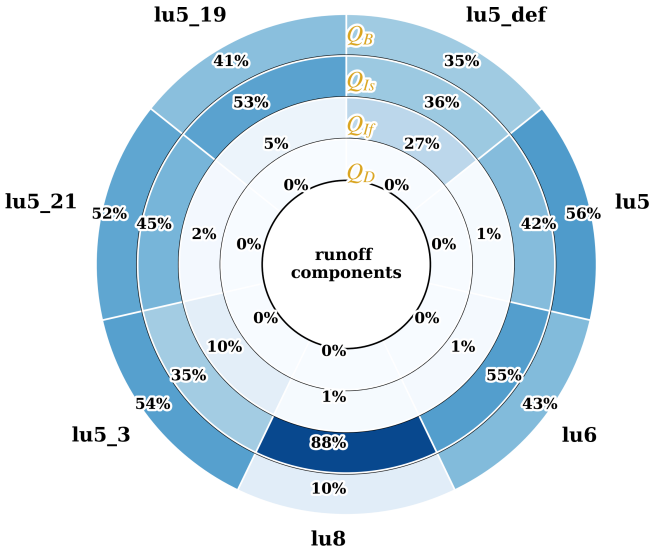


Figure 5.33: Runoff components by model run, in percent of total runoff

*Differences in water retention capacity, anthropogenic and natural*

years, in others however it was in agreement. In general, the dry season flow in the Lurín main catchment is significantly lower than at the corresponding position in the Chillón river, with almost 0 $m^3/s$ in the Lurín vs. 2-2.5 $m^3/s$ in the Chillón. As aforementioned, the Chillón appears to have more surface water storage capacity in the form of lakes and reservoirs (Observatorio del Agua, 2019), which is probably a crucial difference for the dry season's baseflow. Moreover, the higher amount of industrial mining activity (Sanchez, 2016), a stronger management of the resources in the dry season is likely to produce targeted infrastructure that increases storage. Besides anthropogenic retention of rainy season stream water, also geological differences might sustain more runoff during the dry period. There is a higher number of sources in the Chillón, especially in the highest basin parts (map in Figure 5.17). The map shows numerous sources in a hydrological layer classified as aquitard, rendering this classification questionable. Differences in hydrogeological characteristics could thus also explain a higher dry season runoff, sustained by groundwater sources. In addition, the measured dry period flows at the lower gauges do probably not correspond to the actual baseflow from groundwater and reservoirs in the upper basin, since withdrawals and diversions occur for water uses like industry, agriculture and households. Those measured streamflow-reducing influences occur however in both basins, even if to different degrees. Works within the TRUST project estimated around 16 $Mm^3$ of agricultural water demand (mostly irrigation) for the basin part above Antapucro in the Lurín, of which around 83% percent fall within the dry part of the

year. If all that water was withdrawn from the stream during the dry season only, 0.73 $m^3/s$ would be missing in the baseflow. With the overestimated simulated dry season runoff of 3-4 $m^3/s$, anthropogenic interventions cannot by itself explain that discrepancy. Plus, water consumed in the dry season is likely to be stored to a large extent in reservoirs during the rainy season. In consequence, the overestimated dry season runoff in the model must stem from model shortcomings. Model runs in the Lurín that were calibrated based on $NSE_{log}$, like for example lu8, were able to reproduce such quick recessions after the rainy season and near-zero dry season flows. Lu8 controls most of the runoff via the slow interflow reservoir (Figure 5.33), which is drained faster, leaving little water to be drained via the slower baseflow after wards. The trade-off in the lu8 calibration however presents itself in the overestimation of high flow peaks in the rainy season.

# 6

# WATER BALANCE SIMILARITY AND BUDYKO OFFSETS OF CATCHMENTS ON THE WESTERN SLOPES OF THE PERUVIAN ANDES

Offsets from the Budyko curve, with their climatic and physiographic controls, are continuously subject to research (see section 2.4). Padrón et al. (2017) complied catchment water balances of 2733 catchments from around the globe in a systematic literature review, and attempted to identify dominant controls on the water partitioning into runoff and evapotranspiration. Padrón et al. (2017) found that the controls vary with the region and climate. In their study, Padrón et al. (2017) gathered and considered numerous potential controls. He concluded that, besides climatic dryness, other climatic characteristics like snow and phase shifts between rainfall and potential evapotranspiration as well as topographic properties like slope outweigh the often overestimated influence of land cover and anthropogenic influences.

The rather inconsistent picture in terms of observed and modeled water balances of the Chillón and Lurín river in chapter 5, and their overestimation by the Budyko curve, served as a motivation to broaden the picture of water balances in the study region. Thanks to the orographic arrangement, with the Andes following parallelly the coastline, there are many similarly arranged catchments located between mountain crest and Pacific Ocean. While they stretch over a north-south range of approx. 1000 km and are presumed to have different climates and landscapes, they are all part of the tropics, cover tropical highlands and are exposed to seasonal, semi-arid climate.

In order to explore the water balance similarity and the applicability of the Budyko curve in the region, a brief data and correlation analysis is conducted for the catchments along the western slopes of the Peruvian Andes. To that end, data for catchment precipitation, potential evapotranspiration and streamflow were retrieved to estimate dryness and water balances. Globally available topographic and physiographic datasets were used to quantify catchment characteristics. The characteristics were translated to one-dimensional indexes and linearly correlated to offsets from the Budyko curve.

## 6.1 METHODS

The study presents a purely data-based analysis, assessing the mean annual water balances and analyzing detected offsets from the Budyko curve by means of a linear correlation analysis. The multi-catchment analysis consists of the following steps, whose methodologies will be described subsequently.

1. Data retrieval and preprocessing
2. Selection of eligible catchments
3. Derive climatic and biogeophysical properties in the form of one-dimensional indexes for selected catchments
4. Correlation analysis between Budyko offsets and catchment indexes

### *Data retrieval and preprocessing*

Datasets used in the study are described and referenced in chapter 3. For rainfall and potential evaporation, the national gridded PISCO products were used. Monthly streamflow measurements were retrieved from a database. For biogeophysical data, multiple remote sensing data products were used to determine catchment characteristics, the references and methods of which are described in table 6.2. All spatially distributed data were averaged to the extent of each catchment.

### *Selection of eligible catchments*

The study is based on gauge catchments whose downstream boundary or outlet is represented by a stream gauge. The topographic delineation of catchments was conducted on the basis of a 30m resolution global digital elevation model (NASA, 2001). The eligibility of a catchment for the study depended on two criteria:

- **location consistency**: the availability of geographic coordinates of a stream gauge permitting to unambiguously assign it to a specific stream
- **record length**: the availability of sufficient stream flow data for the gauge to calculate mean annual water balances. In general, the more hydrological years the records cover, the more robust is the mean annual estimate. For climatological time scales, 30 years are often indicated as sufficiently long to cover enough interannual variability. Given the rather data-scarce region in Peru, the threshold was lowered to 14 hydrological years in order

to assess more catchments, also allowing the hydrological years to be non-consecutive. The number of hydrological years with valid stream flow data per catchments are listed in table 6.1.

Moreover, visual inspection of the streamflow data ensured that it looked like reasonable hydrographs.

Table 6.1: Valid hydrological years of each gauge stream flow record, between at 1982 and 2016

| | **no. of valid years** |
|---|---|
| **BATAN** | 22 |
| **CONDORCERRO** | 39 |
| **MALVADOS** | 17 |
| **QUIRIHUAC** | 37 |
| **SALINAR** | 32 |
| **SOCSI** | 29 |
| **YANAPAMPA** | 31 |
| **SANTO DOMINGO** | 31 |
| **LA CAPILLA** | 29 |
| **CONTA** | 31 |
| **PUENTE JAQUI** | 25 |
| **PUENTE MAGDALENA_2** | 24 |
| **YONAN_2** | 31 |
| **HUACAPONGO_2** | 30 |
| **LETRAYOC_2** | 31 |
| **LA ACHIRANA_2** | 21 |
| **PUENTE OCOÑA** | 14 |

A total of 119 gauge positions were retrieved for catchments stretching from around 6.5° S to 17.0°S latitude along the western slopes of the Andes. However, given the data limitations mainly stemming from insufficient or unavailable stream flow data, only 17 gauges from separate river basins were found suitable for the analysis. Many stream gauges only measured for short time periods or there were too many gaps in the dataset. The location of the stream gauges as well as the corresponding catchments are visualized in Figure 6.1.

The Rímac basin in the surrounding of Lima was excluded from the analysis since transandine tunnels transport water from the eastern side of the Andes, from the (Alto) Mantaro basin (a headwater of the Ucayali and later the Amazon river) through tunnels to the other side of the basin - significantly altering the water balance of the Rímac

basin itself.

*Climatic and biogeophysical characteristics and indexes for selected catchments*

A number of different climatic and biogeophysical (sometimes also referred to as physiographic) catchment characteristics or indexes were derived for each of the selected catchments. Spatially distributed data, mostly remotely sensed data such as the MODIS snow cover index, were spatially averaged to the extent of the gauge catchment. Table 6.2 lists all the indexes that were included in the analysis and indicates the method or reference of how it was determined. For evident reasons, the list of indexes cannot be exhaustive. It is rather conditioned and limited by available data. In particular soil-related data, whose importance was shown and elaborated in chapter 7, is hardly available at the catchment scale, even more so in a data-scarce region like Peru.

Table 6.2: Indexes of climatic, biogeophysical and proxy catchment characteristics used to analyze the Budyko offsets. Proxy here refers to an index used to derive other, not measured characteristics.

| Category | Characteristic/Index | Index abbrev. | Method |
|---|---|---|---|
| Climatic | | | |
| | precipitation seasonality | seas. P | seasonality index (Walsh and Lawler, 1981) |
| | ETp seasonality | seas. Etp | seasonality index (Walsh and Lawler, 1981) |
| | phase lag P-Etp | phase lag P-Etp | Correlation between monthly P and ETp |
| | | | time lag between peaks of P and ETp (months) |
| | climate heterogeneity | Z diff. | elevation difference |
| | | Z diff. norm. | difference normalized by catchment area |
| | | std. dev. Z | standard deviation of elevation |
| | no. of rainy days | rainy days/year | count of days where daily precipitation >1mm |
| | mean rainfall depth | mean rainfall depth | mean amount of precipitation only on rainy days |
| | mean snow/ice cover | mean snow cov. | MODIS NDSI snow cover, catchment-averaged |
| | interannual variability of precipitation | int.-ann. var. P | |
| Biogeophysical | | | |
| **Topography** | mean elevation | mean Z | derived from DEM30m |
| | mean slope | mean slope | derived from DEM30m |
| **Catchment geometry** | Catchment area | area | Polygon area (km2) |
| **Vegetation** | mean LAI | mean LAI | MODIS LAI, catchment-averaged |
| | LAI seasonality | seas. LAI | seasonality index (Walsh and Lawler, 1981) |
| **Atmospheric transport** | mean air humidity during rainy season | mean rH | mean rel. air humidity measured |
| | | | by stations in catchment |
| Proxy | | | |
| **Stream flow** | Stream flow seasonality | seas. Q | seasonality index (Walsh and Lawler, 1981) |
| | Dry period volume relative | Q_dry period perc | ratio Q_dry/Q_total |

*Correlation analysis between Budyko offsets and catchment indexes*

A linear correlation analysis was performed to analyze potential controls on the Budyko offsets in the catchments of the study area. For each index listed in table 6.2, the Pearson correlation coefficient $R$ and the coefficient of determination $R^2$ were computed.

The results, i.e. discernible trends, are discussed by relating the findings to literature and by a hypothesis-based reasoning as to how physical mechanisms in the catchment might explain deviations from the Budyko curve. A correlation matrix between the indexes themselves was computed to check for potential collinearity of the predictors.

Finally, a multiple linear regression analysis was conducted to test how much of the variance of the Budyko offset can be explained by a limited number of the most significant indexes emerging from the univariate approach. To that end, all two-part, three-part and four-part combinations of indexes with coefficients of determination above 0.2 were used as predictors for the Budyko offsets.

## 6.2 RESULTS

### 6.2.1 *Characteristics of selected catchments*

For 17 catchments, sufficient stream flow data was available and their gauge coordinates were unambiguously attributable to streams in the catchment delineation process. The gauge catchment and data of Puente Huamba was dropped as improbable outlier with an evaporation ratio of 0.08, far off all the other catchments and suggesting that more than 90% of incoming precipitation leaves the catchment as runoff at an aridity index of almost 3. The geographic positions and shapes of the selected gauge catchments are visible in Figure 6.1. Figure 6.2 provides an overview of all catchment-related climatic and physiographic characteristics.

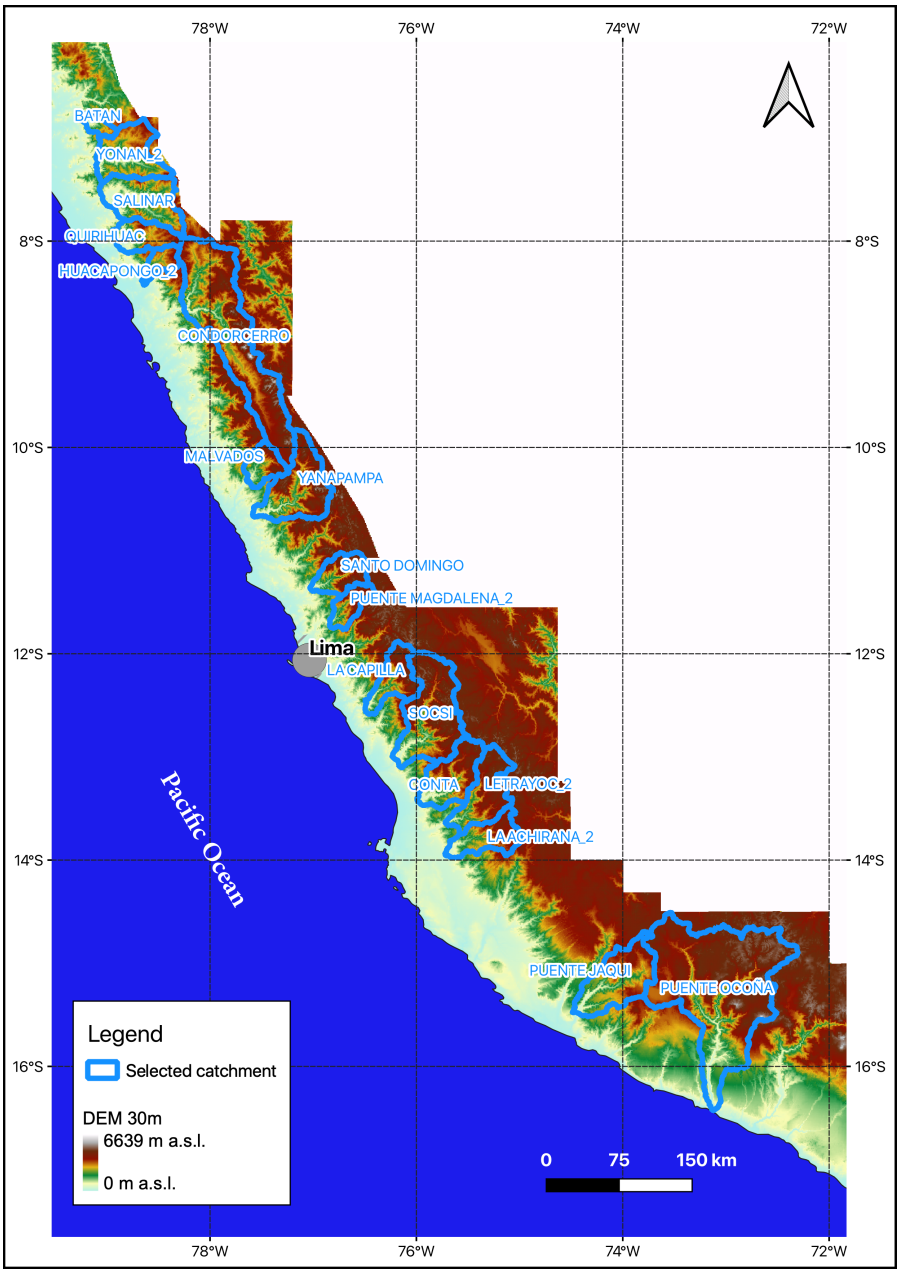


Figure 6.1: Map of selected catchments along western slopes of Peruvian Andes for Budyko offsets analysis (white space: the DEM tiles were retrieved only for the area west of the Andes mountain range, where the catchments are located)

The selected catchments extend over a wide latitude range, between 6.5° and 15.5° S, roughly 1000 km. Most of them are similarly arranged between the Andean main ridge and the Pacific Ocean and have somewhat comparable shapes, with the exception of Condorcerro which stretches over around 270 km parallel to the coast line. In general, the catchment area varies from 621 km² to 10405 km² with a median 2620 km². The dryness index range spanned by the selected dataset goes from 1.55 to 4.49, thus covering a large spread which is

mainly due to variations of mean annual precipitation while mean annual potential evapotranspiration shows little variability.

The gauges of the catchments are all located below 1000 m a.s.l., between 250 m a.s.l. and 930 m a.s.l, indicating that all of them include a significant degree of inner-catchment climatic heterogeneity in the form of a dryness gradient going from semi-humid to humid near the Andean crest to arid in the regions closer to the coast. The heterogeneity is accounted for by the elevation difference normalized by the catchment area. Vegetation-related leaf area indexes are distributed fairly homogeneously across the catchments. Only the catchment of Batan stands out with a higher mean leaf area index. In terms of snow and ice cover in the catchments, there are noticeable differences between the catchments, with Condorcerro and Cahua showing the highest mean snow cover.

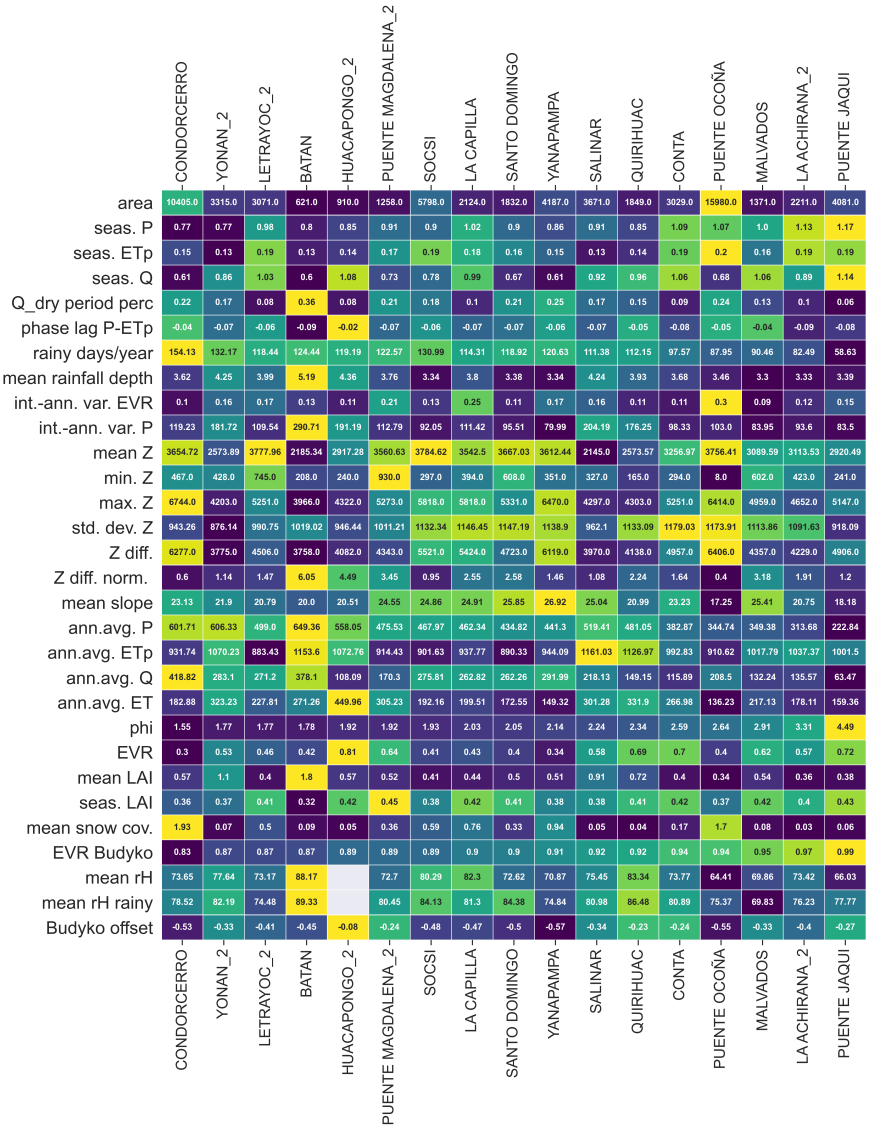


Figure 6.2: Overview of catchment and climate characteristics of selected catchments of Western Andes slopes (sorted by ascending dryness index). Color scale: yellow indicates high values, blue indicates low values, normalized to the range of each variable

### 6.2.2 *Budyko offsets and correlation analysis*

The entire set of selected catchments along the western slopes of the Andes exhibit mean evaporation ratios (EVR) significantly below the Budyko curve (Figure 6.3), meaning that mean annual evaporation is overestimated by the Budyko curve. While one catchment (Huacapongo) nearly reaches the curve (offset of -0.1), the rest of the catchments show offsets between -0.23 and -0.57, with corresponding evaporation ratios of 0.65 to 0.3 (see also Figure 6.4). Most of the catchments, which are encompassed by a dryness index range of 1.5 to 2.5, show a high degree of dataset-internal variability in the

evaporation ratio.

The Puente Jacqui catchment appears to be considerably drier than the other catchments, with a dryness index of 4.5, however within the same EVR range.

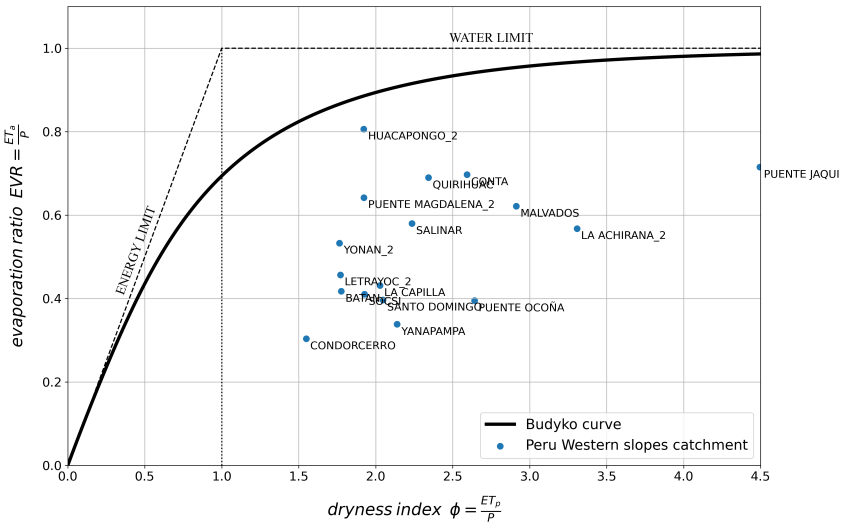


Figure 6.3: Budyko positions of all selected catchments on the western slopes of the Peruvian Andes

A first-order linear correlation analysis looked at correlations between climatic or physiographic catchment characteristics and the Budyko offsets. It yielded coefficients of determination ($R^2$) generally smaller than 0.65, for most characteristics below 0.3 (Figure 6.5) and for more than half of the indexes tested, it remained smaller than 0.1.

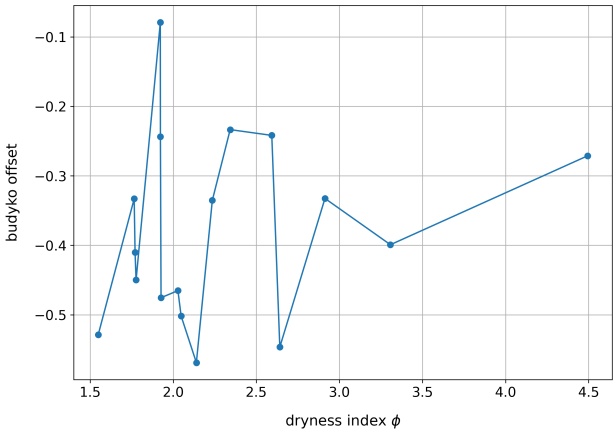


Figure 6.4: Budyko offsets of all selected catchments on the western slopes of the Peruvian Andes

The correlation analysis suggests that increasing catchment area is slightly related to a higher Budyko offset in our dataset. The $R^2$ of 0.27 is however mainly driven by the two catchments of Condorcerro and Puente Ocona, the two largest catchments, while for the rest of the catchments a considerable spread becomes visible. Correlations with topographic indexes were found for mean elevation ($R^2$=0.22) as well as for maximum elevation ($R^2$=0.42) and elevation difference ($R^2$=0.41), of which the latter two are highly collinear with an $R^2$ of 0.9 (Figure A.3 in appendix A.3). The higher the maximum elevation or the elevation difference is, the larger are the Budyko offsets. Mean snow cover reaches an $R^2$ of 0.45, with snowier or more glacial catchments showing higher Budyko offsets.

Seasonality of certain indexes stood out as well. Budyko offsets were

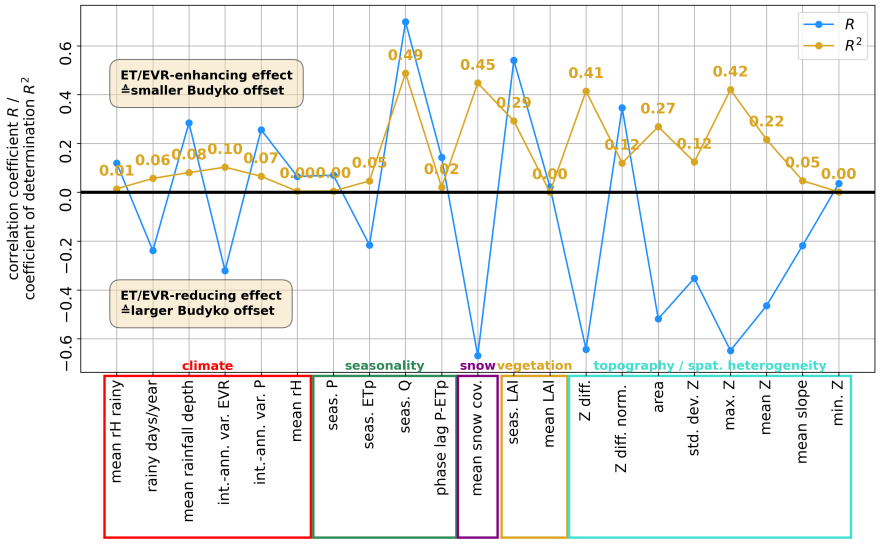


Figure 6.5: Correlation coefficients $R$ and coefficients of determination $R^2$ for each index and the Budyko offsets. The color frames categorize the indexes, note however that some cannot be assigned unambiguously to one category

lower for catchments with higher stream flow seasonality ("seas. Q"), represented by a coefficient of determination of 0.49. LAI seasonality reached an $R^2$ of 0.29.

Indexes related to relative humidity and to average LAI showed coefficients of determination near zero, thus not indicating any linear correlation with the Budyko offsets.

The multivariate regression was performed for combinations of 2, 3 and 4 different predictors, chosen out the most prominent indexes that arose during the first-order correlations: area, seas. Q, max. Z, mean snow cov., seas. LAI. The results are visualized by Figure 6.6. The

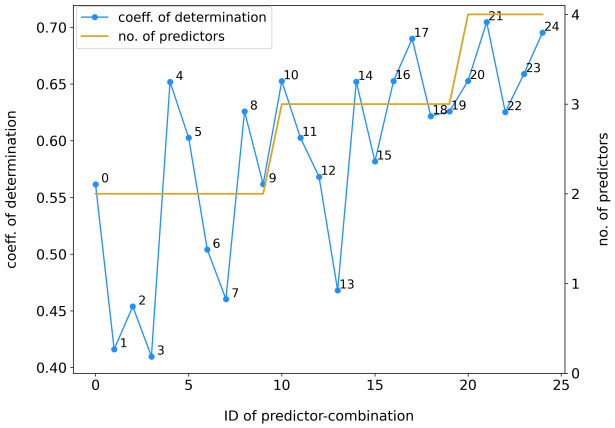


Figure 6.6: Coefficients of determination of multivariate regression, numbers in the Figure indicate the combination ID in table A.2

combinations of two, three or four predictors resulted in a maximum explained variance of 0.65, 0.69 and 0.70, respectively (table A.2 in appendix A.3). The three most prominent predictors of the univariate regression ($R^2$>0.4) explain 0.65 of the variance. Combined with LAI seasonality 0.70 of explained variance is reached.

## 6.3 DISCUSSION

The results of the data analysis showed a clear and systematic trend of the Peruvian catchments to produce mean water balances, i.e. evaporation ratios, below the estimate by the Budyko curve. In other words, the Budyko curve systematically overestimates the evaporation ratios of the study catchments, and thus -assuming the catchment sample to be representative to a certain degree- likely of all comparable catchments of that particular geographic region along the Western slopes of the Peruvian Andes. Figure 6.7 compares the mean water balances of the Peruvian study catchments with an extensive compilation of 2700 catchment water balances by Padrón et al. (2017). The Figure illustrates well that the Peruvian catchments are all located in a very sparsely populated domain within the Budyko space. That being said, there is a monitoring bias in favor of moderate climates in the US and Europe to be acknowledged, meaning that semi-arid and arid catchments often located in the Global South tend to be underrepresented in global studies.

*Peruvian study catchments have very low evaporation ratios in global context*

Note that the analysis is limited to the dataset itself and its internal variability in the Budyko offsets. While the dataset-internal variability is considerable and thus allows the analysis of controls on the mean water balance, it cannot discern influences that are present in the entire sample of catchments. For instance, all catchments are exposed to a

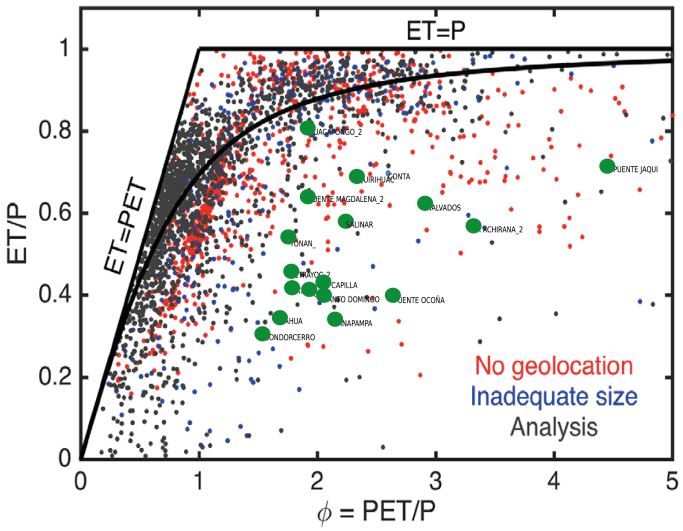


Figure 6.7: Comparison of Peruvian study catchments with extensive compilation of over 2700 catchment water balances by Padrón et al. (2017). Green dots represent our Peruvian catchments that were graphically inserted in the original Figure by Padrón et al. (2017). The blue catchments were dismissed from Padrón's analysis because they were either smaller than 12 km$^2$ or larger than 12.000 km$^2$. The red ones without known geolocation were also dismissed from Padrón's analysis, their water balances however remain valid.

relatively high precipitation seasonality. The point of dataset-external controls potentially affecting all catchments is addressed at the end of the discussion.

There is a high degree of dataset-internal variability in the mean annual water balances and the resulting Budyko offsets, varying from -0.1 to -0.55 and not showing any correlation with the dryness index itself (Figure 6.4). The correlation analysis conducted aims at relating the offsets to climatic and biogeophysical catchment characteristics. Since influences on the mean water balance are known to be interdependent (e.g. Gentine et al., 2012; Schaefli et al., 2011) and possibly non-linear, a linear correlation analysis is only a rough means to assess such relationships. However, the correlation analysis did reveal trends of characteristics affecting the mean water balance. The subsections below discuss the relationships found with respect to their interpretation in terms of underlying physical mechanisms, focusing only on coefficients of determination $R^2$>0.4. The analysis revealed correlations both for climatic heterogeneity as expressed by the elevation difference ($R^2 = 0.44$) and for mean snow cover (NDSI) with an $R^2$ of 0.48. The two indexes themselves are however somewhat collinear, with an $R^2$ of 0.8, since both correlations are partially driven by snowier catchments like Condorcerro and Yanapampas. Having a higher mean snow cover obviously translates to a non-negligible

fraction in high elevation ranges (which is why snow cover is likewise correlated to $Z_{max}$, Figure 6.5), making for a steeper climatic gradient. These two indexes are both strongly related to higher elevations. However, the heterogeneity aspect is not limited to higher elevations and can be relevant without the effect of snow cover. Two paragraphs discuss how spatial heterogeneity, and in particular snow cover can affect the Budyko position and offset. In addition to that, a correlation was found for streamflow seasonality. Treated as a proxy for catchment retention and storage capacity, potential influences of different natural and anthropogenic storages on the mean water balance are discussed.

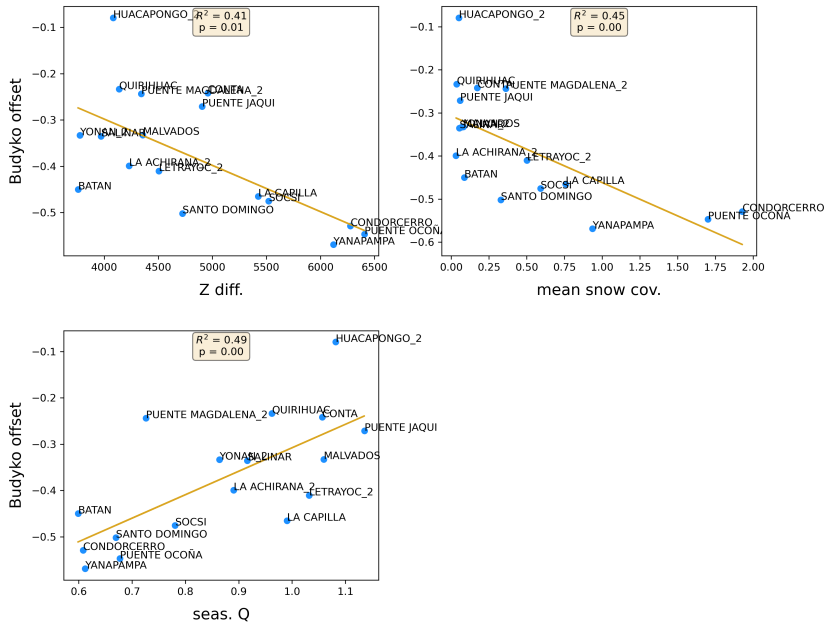


Figure 6.8: Correlations of the most prominent features in the linear correlation analysis, with an $R^2$ above 0.4

### 6.3.1 *Spatial heterogeneity and scale*

Given the strong dependence of the climate (precipitation as well as potential evaporation) on elevation (see Figures 5.5 and 5.8 for examples catchments Chillón and Lurín), the elevation difference within the catchment was used as proxy index for spatial heterogeneity in climate. We observe that with increasing spatial climatic heterogeneity, the Budyko offset increases ($R^2 = 0.44$). In literature, catchments with pronounced climate gradients tend to be excluded from studies applying the Budyko framework (Gentine et al., 2012). The Budyko framework relies on the dryness index, $\phi = P/ET_P$, as a catchment-

*Average $\phi$ less representative of heterogeneous catchment*

characterizing property and as dominant control on the mean water partitioning. Having various climate zones within a catchment -with greatly differing dryness indexes between the zones- a singular, spatially averaged dryness index $\phi$ is not able to describe or capture the whole system's behavior, ultimately also because of the nonlinearity of the Budyko curve itself. Thus, even if all different climatic subzones within a catchment were conditioned by their respective dryness index and corresponded perfectly to the Budyko curve, spatial averaging of $\phi$ would result in an offset from the curve. As depicted by the 2nd numerical derivative of the Budyko curve in Figure 6.9, the nonlinearity is greatest for aridity ranges between 0.25 and 1.5, which includes the headwater part of the Peruvian catchments, as visible in the example shown in Figure 6.10.

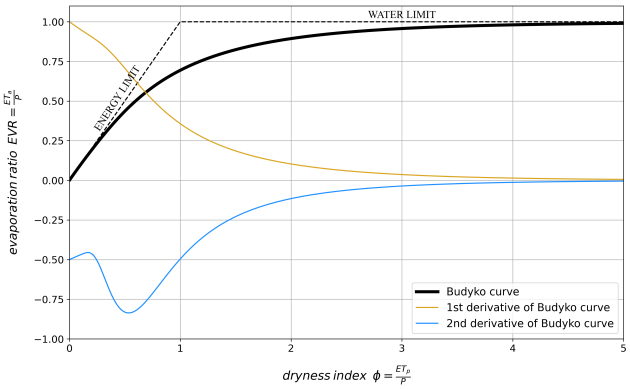


Figure 6.9: 1st and 2nd numerical derivative of Budyko curve

Evidently, the degree of heterogeneity will determine the relevance to the expectable deviation from the Budyko curve. In order to illustrate that, Figure 6.10 shows the movement of a catchment's water balance through the Budyko space, from the headwater ($A_o$ = 80 km$^2$) down to the river mouth at the coast ($A_o$ = 2150 km$^2$). The dryness indexes and water balances in the Figure were extracted from the distributed hydrological model developed and calibrated for the Chillón river in section 5.5.1, one of the Peruvian study catchments also used for the present analysis. It shows that due to the pronounced climatic gradient within a comparably small catchment of roughly 2000 km$^2$, the evaporation ratio covers a wide range of from 0.4 to 0.6. The position of the water balance point, i.e. the stream gauge, is thus relevant to the determination of the Budyko position of the catchment. Approaching lower elevations and the coast, the catchments transform into arid to hyper arid landscapes, with no precipitation input and thus zero hydrological partitioning processes but with rising mean aridity. Most of the Peruvian study catchments encompass a significant degree of climatic heterogeneity. However, even if the EVR range in Figure 6.10 is significant and may account for a portion of the

Budyko offset, it does not on its own explain the systematic deviation of the catchments from the Budyko curve, as it does not reach the vicinity of the Budyko estimate despite the wide range covered in the example in Figure 6.10.

The point of spatial heterogeneity also relates to the question of the applicability of the Budyko curve across different spatial scales. Is the spatial scale of the Peruvian catchments appropriate? The point has been addressed in literature, also originally by Budyko himself (Budyko, 1974). In general, the Budyko model is assumed to be increasingly valid at larger scales, Budyko (1974) mentioned catchments with an area above 10.000 $km^2$ to produce very little deviations from his curve. It is reasonable to assume that at very small scales (below for example 10 $km^2$), local influences such as for instance topography, soil structure or local weather patterns dominate the behavior in terms of runoff generation, and that macroclimatic descriptions like the dryness index have little significance. However, determining a fixed threshold for the transition of the applicability of the Budyko curve seems inappropriate as well. It results rather from the struggle between the spatial variability and influence of physiographic controls and that of the climate. Perhaps this issue can be described by an interplay of *coupling* and *competition*. While the Budyko curve approach relies on the idea that the influence of water and energy availability (macroclimate) predominantly shapes water balance-relevant landscape elements like soil and vegetation, it is not the only driver. As described by Troch et al. (2015), geology in terms of tectonics and bedrock weatherability which influence topographical gradients and soil formation and by that also vegetation, is a driver whose spatial distribution is independent from the climate. It thus depends on the spatial correlation between climate on the one hand and soil and vegetation on the other (coupling), as well as on the kind and degree of control of such landscape elements on the water balance or rather the Budyko offsets (competition). If climate is the dominant driver, predominantly shaping the landscape elements over time (climate and landscape well correlated spatially) and/or overlaying a spatially random pattern of other influences within the domain, there should not be any significant offset from the Budyko curve. If however the other controls follow spatial trends against the climate and are water-balance relevant, they will cause the mean water balance to deviate from the Budyko curve. The same holds true for subscale climatic influences such as for instance mean rainfall intensity, if they are not well correlated with the macroclimatic dryness index.

*At which scale is Budyko a reasonable framework?*

*Correlation of climate and catchment characteristics*

Usually, gradients in the macroclimate extend over larger spatial scales and therefore tend to be a good descriptor for water balances of larger catchments. At such scales, the climate becomes dominant while

the catchment-internal variability of physiographic characteristics or the relevance of small-scale extreme weather events start averaging out spatially, in comparison.

*Controls of steep hillslopes and climate in Peruvian catchments*

Our study catchments in West Peru cover a pronounced climatic or aridity gradient - a product of the markedly sharp topographic gradient, along which the distinguishable vegetation zones have formed. In addition to the general topographic gradient, tectonic and geological activity has produced a landscape of fairly steep hillslopes in the region, to be found everywhere from high elevations almost down to coast level. The question arises in what way and to what degree climate and soil and vegetation resulting from the steep topography are correlated at smaller scales. Satellite images indicate that while sometimes the plateau-like hilltops are green during the rainy season, many hillslopes often show little to no vegetation cover - suggesting that this effect is not due to elevation or the climate but to topography-related mechanisms. In comparison to the tropical Andes, mountains in the Alps in Europe show significantly more vegetation cover on their hillslopes, up until the climate-imposed tree line interrupts it, underlining the correlation of climate and vegetation. The steeper the hillslopes, the smaller is the potential for soil formation and vegetation growth due to the proneness to overland flow and soil erosion. As a result, as demonstrated also by the model study in chapter 7, mean evapotranspiration decreases when soil storage is limited and an overestimation by the Budyko curve is more likely. The present correlation analysis used mean slope as an indicator for steep topography, without showing any signal towards Budyko offsets. The lack of a direct influence could be related to the limited dataset-internal variability of mean slope. It is a characteristic shared by practically all catchments in the region, and can thus have an ET-reducing effect on all of them which contributes to the general trend of the detected Budyko offsets.

### 6.3.2 *Snowiness*

Mean snow cover has a correlation coefficient of 0.45 and 0.78 of collinearity to elevation difference, thus also being related to the point of a steep climatic gradient in the catchments. The higher the snow cover fraction in the catchment, the lower is the mean evaporation ratio, likely responsible for the lowest evaporation ratios of the dataset by the catchments Condorcerro, Cahua and Yanapampas. An influence of snowiness of catchments on mean water balances overestimated by the Budyko curve, have also been suggested by Milly (1994), Berghuijs et al. (2014b), Berghuijs et al. (2014a) and Padrón et al. (2017). The following paragraphs discuss how Budyko offsets relate to the

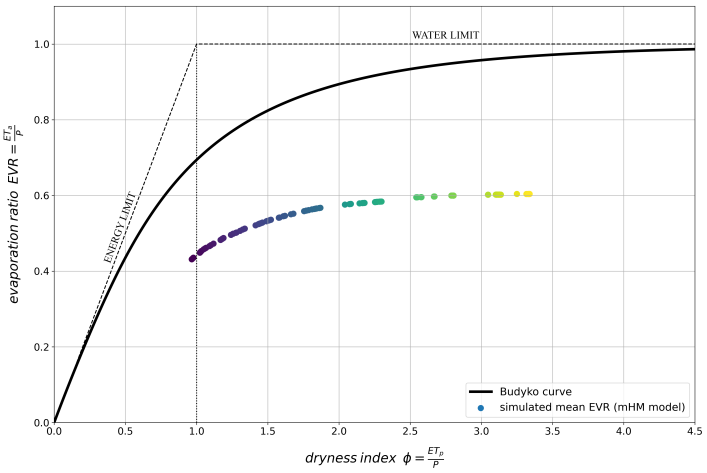


Figure 6.10: Budyko position as a function of the relative stream gauge position and thus the upstream climatic heterogeneity. Extracted from a calibrated mHM model of the Chillón basin, going from a catchment area of around 100 km$^2$ (blue) to 2200 km$^2$ (yellow)

estimation of potential evapotranspiration in cold and snowy regions, and how snowpacks and glaciers can affect the mean water balance by favoring runoff and streamflow over evaporation.

*Calculation of potential evaporation in snowy regions*

Precipitation falling down as snow accumulates above the soil, forming a snowpack. In the case of a positive snow mass balance, it leads to glaciation and the presence of an ice layer over time. The snowpack or ice layer, contingent on atmospheric conditions, is exposed to the evaporative demand and melting. From an energy perspective, the sublimation process (phase transition from solid/ice to gaseous state/water vapor) requires more energy intake than the evaporation from a free water surface or the soil domain. Moreover, the surface albedo of snow and ice are higher than that of vegetated surfaces, resulting in higher surface reflectivity and a lower net radiation- common $ET_p$ calculation methods however assume a reference crop with a fixed albedo of 0.23 (Allen, 1998). Therefore, Meira Neto et al., 2020 argues that the estimate of potential evaporation and the resulting true aridity of a catchment would have to be adjusted in the presence of snow cover, something which usually is not accounted for. According to Meira Neto et al., 2020, in global studies on water resources, snow-covered regions tend to be neglected in general, which does not remedy the incomplete description of potential evaporation in such regions. In consequence, the potential evaporation estimates used in the present Budyko study cannot adequately represent the actual energy-based upper limit to the evaporation for snowier catchments. An overestimation of potential evaporation in catchments with non-negligible influence of snowfall and snow accumulation leads to an overestimated aridity in the Budyko space (shift on x-axis). A

correction towards a more humid system would reduce the actual deviation from the Budyko curve.

*Runoff processes in the presence of snowpacks*

Secondly, physical mechanisms related to accumulation of frozen water and snowmelt can result in an increased streamflow. While Berghuijs et al. (2014a) present empirical observations in 420 US catchments that the fraction of precipitation falling as snow has a streamflow-enhancing effect on the mean water balance, they do not investigate any underlying physical processes. The effect can be due to a combination of interacting processes and influences. For instance, the potentially rapid release of melting, accumulated precipitation (Williams et al., 2012)- in comparison to the same amount of liquid precipitation falling down on snow-free surfaces will likely increase streamflow compared to evaporation. In combination with saturated and/or frozen soils having very low hydraulic conductivity and infiltration capacity, mobilized water from snowpacks is likely to run off rather than to infiltrate and evaporate. In addition, in the case of glaciers having a constant ice layer, melting would not lead to infiltration and sustain a soil water-based evaporation process at all. If water infiltrates the soil beneath the ice, it would feed groundwater resources and contribute to baseflow or run off close to the surface.

### 6.3.3 *Catchment storage and anthropogenic influences*

Natural catchment storage comprehends several compartments: subsurface storage including soil, alluvial deposits, regolith and permeable bedrock, lakes as well as snowpacks and glaciers. In the case of subsurface storage capacity, the individual components are not easy to distinguish and present in nature rather a continuum than fully separate domains as often conceptualized in hydrological models for simplification. In addition to naturally available storages, human-made reservoirs can increase the water retention capacity of river basins. The release of stream water is intimately linked to the catchment's storage dynamics, unless stream flow is predominantly precipitation-driven, which may become more relevant at smaller scales and high-intensity rainfall events (Blöschl and Sivapalan, 1995). Since catchment storage capacities are hard to measure and assess directly, the resulting stream flow signatures can be used to reversely derive certain characteristics (Kirchner, 2009). Stream flow can be viewed as the system's integrated response to a variety of properties and interactions.

With an $R^2 = 0.5$, the correlation analysis showed that there is some relationship between effects leading to more seasonal discharge and the Budyko offsets. The higher the discharge seasonality, the lower

is the Budyko offset, i.e. the higher is in general the evaporation ratio. In some cases, the seasonality index of discharge surpasses the one of rainfall (Yonan, Letrayoc, Huacapongo, Salinar, Quirihuac, Malvados). If the variability of discharge seasonality is not related to rainfall events during the dry season and thus the variability of rainfall seasonality itself (collinearity only of $R^2 = 0.3$), there are two reasons why discharge seasonality is more or less pronounced (sharp) in some catchments: It can be related to the initial filling or refilling of catchment storages at the onset of the rainy season or to the prolonged release of stream flow (base flow) after the rainy season.

*Storage effects at the onset of the rainy season*

After the onset of the rainy season, it can take a while until the seasonal stream flow sets in, i.e. that the runoff-to-rainfall ratio increases significantly. That becomes visible in the selected double mass curves in Figure 6.11, where catchments like Huacapongo and Conta with high discharge seasonalities only show higher runoff coefficients from February/March on, while the others start a month earlier (note that it is based on monthly discharge data, thus of coarse temporal resolution). That delay shortens and thus sharpens runoff seasonality. It likely stems from the initial refilling of and retention by certain catchment storages, both natural and anthropogenic ones: soils, groundwater, lakes and artificial reservoirs, although the individual contributions to storage cannot be discerned here. After a while, soils are more saturated which triggers more runoff, the delayed groundwater response sets in and reservoir intake slows down or even stops. After that point, storing and retaining of water seems to occur at a lower rate. For snowier catchments, snow is likely accumulating throughout the rainy season, without reaching a sort of "filling" threshold where the storage amount itself would trigger a stronger runoff response in the middle of the rainy season. While the delayed increase of the runoff coefficient is visible in almost all catchments, showing a certain storage capacity, it varies however, which points to differences between the catchments' storage capacities and dynamics.

*Release of stored water in dry season*

The second relevant characteristic of the discharge regime is the potential release of water after the rainy season, which attenuates discharge seasonality. An extension of stream flow towards the dry season without significant dry season rainfall events, corresponds to the release of water from certain storage compartments. The relative amount of stream flow after the rainy season corresponds to the increase along the y-axis past the red dot of month May in Figure 6.11. The percentag of dry season runoff to total annual runoff is listed in Figure 6.2 under *Q_dry period perc*, it includes however also the transitional month of October, when some rainfall events already set in. The percentages vary from 6% to 25%, thus potentially relevant to annual water balances. In this regard, apart from groundwater

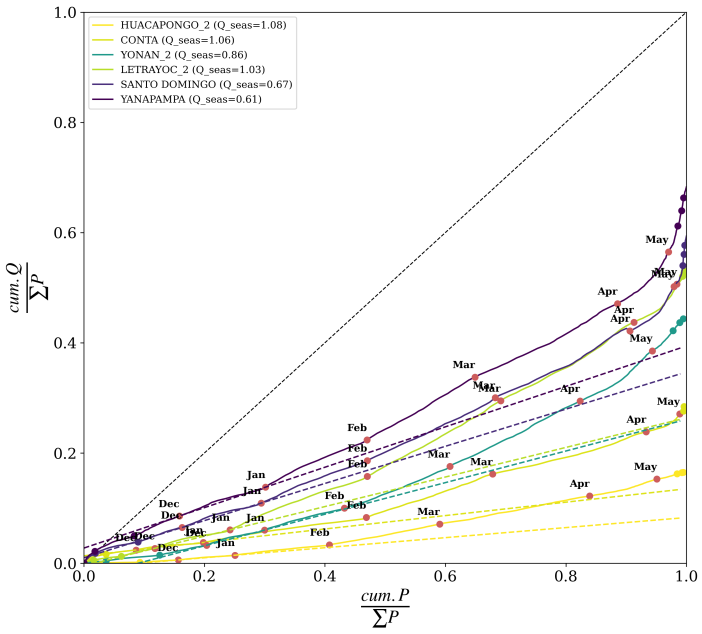


Figure 6.11: Mean double mass curves for selected catchments. Gradual colors correspond to the discharge seasonality index, as do the values in parentheses in the legend. Dashed straight lines follow the slope of the double mass curve between December 1st and January 1st, the first significant month of the rainy season. Dots indicate the first day of a month, red dots delineate the rainy season from beginning of December until end of April

base flow and reservoir water release, also snow melt can play a role. Soils are less important here since root zones would rather retain the moisture and only be drained by evaporation than sustain runoff after the rainy season.

*Anthropogenic alterations*

The important question is why some catchments have a higher water yield during the dry season than others. If the water balance is measured correctly and this is strictly due to natural catchment dynamics, it would mean that there is no or significantly less catchment storage capable of sustaining the stream flow after the rainy season (no gradual groundwater recession). As explained more theoretically in section 2.4.2, especially given the low position of the stream gauges, it is likely that a considerable portion of the stream or reservoir water is diverted and used for irrigation, livestock, industrial and domestic activities above the stream gauge. In that case the measured water balances do not only result from naturally occurring hydrological processes. The withdrawal and use of stream water probably happens throughout the entire rainy season as well, which on the other hand cannot be disentangled from between-catchment differences in dry season stream flow. It is to be expected, however, that with the onset of the dry season the withdrawals generally increase since any rainfed

agricultural activities stop. Differences in the mean water balance and intensified resulting Budyko offsets can thus be partially due to anthropogenic withdrawals, which end up as evaporation one way or another (section 2.4.2). In addition, artificial reservoirs also enhance evaporation. This is of particular relevance in a semiarid tropical region like West Peru, with dry air during the dry season and high solar radiation. Catchments in West Peru are often strongly influenced by anthropogenic activities and measures (Lavado Casimiro et al., 2012).

### 6.3.4 *Dataset-external controls: seasonality*

There is a tendency of catchments of the same aridity but with markedly seasonal rainfall to result in higher runoff coefficients (i.e. lower evaporation ratios), as demonstrated by Fu and Wang (2019). Lavenne and Andréassian (2018) argued that -for their collection of French catchments- seasonal rainfall only lead to lower mean annual EVR when there was also a phase shift between P and ETp.

Figure 6.12 compares the Peruvian catchments to the MOPEX catchments above a rainfall seasonality index of 0.8. While the trend to be overestimated by the Budyko curve is noticeable in the MOPEX catchments, it is negligible compared to the offsets of the Peruvian catchments - showing that other influences, potentially interacting with seasonal aspects, dominate the considerable offsets.

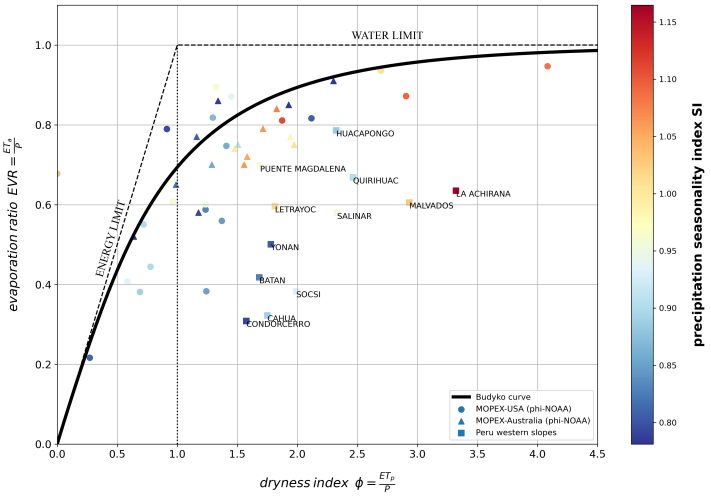


Figure 6.12: Budyko offset and precipitation seasonality in comparison to MOPEX dataset containing both US American and Australian seasonal catchments with seasonality index SI $\geq$ 0.8. Labeled, square symbols show Peruvian catchments (Budyko positions and catchment selection differ slightly from the dataset and Figures shown in section 6.2, it is based on an older version of data preprocessing)

# 7

# EXPLORING THE ROLE OF SOIL STORAGE CAPACITY FOR EXPLAINING DEVIATIONS FROM THE BUDYKO CURVE USING A SIMPLE WATER BALANCE MODEL

This chapter is based on the HESS preprint by Bondy et al. (2021).

## 7.1 INTRODUCTION

*Water limitation and storage supply, and competing process velocities*

While the Budyko curve (Budyko, 1974) has regained attention in recent years, understaning deviations from it continue to be subject to research efforts (e.g. Berghuijs et al., 2020; Daly et al., 2019; Reaver et al., 2022; Sposito, 2017a; Yao et al., 2020). While both climatic and physiographic factors control the steady-state water balance, evaporation itself is commonly conceptualized as either energy- or water- limited. Water limitation of evaporation, however, strongly relates to root zone storage supply and thus root zone storage capacity, because evaporation is two or three orders of magnitude slower than surface runoff. Root zone storage capacity determines the amount of plant-available water and can be characterized by its total storage volume as well as capillarity-related properties like the storage at field capacity held against gravity. While free soil water above field capacity feeds groundwater and ultimately streamflow, the water content between field capacity and wilting point (effective field capacity) sustains evaporation. These catchment properties controlling root zone storage and recharge capacities are co-evolutionary fingerprints of climate and the geology setting (Gentine et al., 2012; Troch et al., 2015).

*Soil storage and other second-order controls on mean water balance*

The climate controlling the mean annual water balance to first-order, there is broad agreement that second-order controls and potentially resulting offsets from the Budyko curve are caused by both subscale climate variability and physiographic characteristics of the catchment (examples are cited in section 2.4.1). In line with the above-mentioned explanation of physical processes making soil storage capacity controls relevant to mean evaporation, it was identified as an important control in other studies. Milly (1993) and Milly (1994) explored the influence of soil water storage on the annual average water balance, using a 1d vertical soil water balance model with a stochastic meteorological forcing. While Milly's approach was simplified with respect to variability of the forcing, it nevertheless explained 85% of the variance in water balances in the contiguous USA east of the Rocky

Mountains. Milly identified the dryness index, ratio of plant-available water holding capacity to annual average precipitation and number of precipitation events per year as main controls. Daly et al. (2019) present an approach to introduce a new characteristic hydrological space in the form of a storage limitation by combining the physical storage capacity with the temporal variability of $ET_p$ and P. They conclude that soil storage is a key parameter in terms of the Budyko offsets. Gentine et al. (2012) also investigated the relationship between the Budyko curve and -amongst other- soil storage, trying to reversely infer Budyko-optimized soil storage capacities for MOPEX catchments, neglecting however capillarity-based influences.

*Our approach to explore soil storage capacity influences*

The need to better understand second-order controls on the long-term water balance and their relationship to the original, non-parametric Budyko curve remains. The main objective of this work to explore the role of specific soil characteristics in the steady-state water balance and, building on other studies and ET-related physical mechanisms, operate on the hypothesis that root zone storage is an important physiographic control of offsets from the Budyko curve. Instead of using a parameterized version of the Budyko framework based on a lumped parameter, a model-based virtual experiment approach is proposed. The approach targets specific model parameters that are more relatable to physiographic characteristics of a catchment. The study being based on a limited number of catchments, that via calibration are supposed to represent realistic hydrological systems, uses the hbv model and the beta store (Lindström et al., 1997) as a learning tool to understand the role of total soil storage capacity and a capillary storage fraction in the mean water balance and resulting Budko offsets. The focus is on mesoscale catchments, the scale at which physiographic catchment characteristics are likely to be more relevant controls that at larger scales where the climate can be expected to dominate.

To that end, 16 catchments covering a wide range of climate and landscape settings were selected for the virtual experiment. For each catchment, a simple hydrological model was calibrated based on 30 years of water balance observations. The calibrated models were subsequently used to investigate how variations in total soil storage and a capillary storage fraction affect offsets from the Budyko curve, and to look for similarities in terms of the storage configurations that match the Budyko curve.

Table 7.1: Datasets used and references

| Region | Data used | Dataset |
|---|---|---|
| **Southwest Germany** | Precipitation | DWD-REGNIE |
| **Baden-Württemberg ("BaWue")** | Pot. evapotranspiration | DWD-ETp |
| | Stream flow | LUBW |
| **Continental USA ("MOPEX")** | Precipitation | MOPEX |
| | min./max. daily temperature | MOPEX |
| | Stream flow | MOPEX |
| **Peru, Western Andes ("Peru")** | Precipitation | PISCO-P |
| | min./max. daily temperature | station data |
| | Stream flow | Stream gauge data |

## 7.2 METHODS, DATA AND MODEL

### 7.2.1 *Selection of study catchments*

In order to represent a broad range of climate settings, the study is based on several publicly available datasets from around the globe. The choice was also conditioned by the type of available data (precipitation, potential evapotranspiration and streamflow), a minimum time series length of 30 years and the degree of preprocessing (especially spatial aggregation to catchment area) to allow for a multi-catchment approach. Finally, 16 study catchments were selected from the three datasets listed in table 7.1.

The goal was not to include as many catchments as possible, but to conduct a multi-catchment study focusing on 16 distinctly different catchments. Those were selected from the three datasets using the following criteria:

- **A wide range of climatic dryness indices:** In order to integrate catchments covering a large climatic gradient, catchments spreading over a dryness index between $\phi = 0.3$ to $\phi = 2$ were selected. For extremer dryness values such as in desert regions or in extremely humid or cold regions (e.g., polar regions), rainfall partitioning into runoff and evaporation is not expected to relate to soil water storage characteristics. In the case of the MOPEX

dataset, where several catchments at similar or same dryness indices are available, a random subset of catchments was picked.

- **Catchment area:** The selection was limited to lower mesoscale catchments ranging from around 50 to 1.000 $km^2$. Larger catchments potentially contain climate gradients and need to be represented by more complex distributed models. This hinders identification of clear causal relations.
- **Minimum anthropogenic influence:** In line with the Budyko framework that was developed on the basis of pristine catchments, catchments with significant anthropogenic disturbance were excluded from the study. The MOPEX dataset claims that its catchments are of little anthropogenic disturbance. The BaWue catchments were drawn from a preselection where anthropogenic influences in the form of extractions or inlets were excluded. The selected headwater catchment in the Peruvian Andes is sparsely populated due to its elevation and only has a few smaller reservoirs not expected to alter the annual catchment water balance significantly.
- **A closed water balance:** Catchments with a closed long-term water balance (within 5% error) were preferred, because this is a pre-condition to apply the Budyko framework and it facilitates water balance modeling.
- **No significant snow/ice dynamics:** Catchments with significant snow and ice storage were not selected in order to to ensure that water limitation is mainly controlled by storage in the root zone.

### 7.2.2 *Data and preprocessing*

The Budyko framework was derived empirically, and is applicable at steady state, climatological timescales at which inter-annual storage changes in the catchment become negligible. In terms of modeling input (meteorological forcing) and output (stream flow) for the study, daily data for 30 consecutive years were retrieved for each catchment to fulfil that premise. The following paragraphs briefly outline the necessary preprocessing steps to prepare the different data sets for modelling.

#### *Preparation of the BaWue dataset*

The German Meteorological Service (DWD) provides 1x1 km Germany-wide raster datasets for several climatological meteorological variables, stemming for example from the interpolation of point-wise monitoring

data (e.g., from rainfall gauges) or from the processing in the framework of the spatially distributed agrometeorological AMBAV-model. For the BaWue dataset, catchment averages of daily precipitation (DWD, 2020b) and potential evapotranspiration (DWD, 2020a) were derived from the corresponding raster datasets. The potential evapotranspiration estimates are essentially based on the Penman-Monteith method. Stream flow data were obtained from the environmental agency of the State of Baden-Württemberg (LUBW, 2020).

*Preparation of the MOPEX dataset (USA)*

The MOPEX dataset (Duan et al., 2006) provides complete, catchment-averaged time series of precipitation, minimum/maximum daily temperature, NOAA climatological pan evaporation as well as stream flow data for a total of 438 catchments. Since NOAA climatological pan evaporation is based on seasonal averages with the same values recurring every year, it was considered to be less suited as forcing data for a hydrological model. Instead, potential evapotranspiration was estimated based on daily minimum and maximum temperature (Samani, 2000).

*Preparation of the Peruvian data set*

For the Peruvian catchment, the national 0.1° gridded PISCO dataset was used (section 3.2.1). The gridded PISCO data was used to calculate catchment average precipitation for the Obrajillo (P-1) catchment. Station data from the SENAMHI station "Canta" as well as a regionally calibrated Hargreaves-Samani model (section 4.2) was used to estimate potential evapotranspiration. For the purpose of gap filling and obtaining catchment averages from the point-wise measurements, linear correlations to nearby stations as well as elevation-dependency of the temperature were made use of. Streamflow data for the Obrajillo catchment was provided by SENAMHI. For this catchment, streamflow data was available only for roughly 19 out of the 30 years of meteorological data used to compute long-term water balances.

### 7.2.3 *Characteristics of selected catchments*

In the end, 16 catchments were selected for the study, seven from Germany (IDs: "B-x"), eight from the US (IDs: "M-x") and one from Peru ("P-1"). For the sake of readability, the original catchment/stream gauge IDs from the datasets were modified. Table A.3 in appendix A.4 links the original catchment IDs to the newly assigned IDs used in this study. Figures A.4, A.5 and A.6 in appendix A.4 show the geographic locations of the catchments. Figure 7.1 provides an overview over catchment and climate characteristics spanned by the selected catchments. The catchments cover areas between 50 and 1000 $km^2$.

The catchments in Baden-Württemberg in Germany cover the most humid climate settings with dryness indexes of from 0.31 to 0.77, while some of the drier MOPEX catchments, mostly due to significantly higher potential evaporation, range between 1.05 and 1.55. In all catchments, annual total precipitation exceeds 750 mm/year. The most humid catchments in Germany reach annual totals of up to 1600 mm/year. The variation of the dryness index largely stems from the higher variations in energy supply. This is reflected in the spreading of the annual potential evapotranspiration between 500 mm/year and 1350 mm/year. Potential evapotranspiration is quite evenly distributed among the catchments in Germany, whereas precipitation is more heterogenous. Figure 7.1 also provides the number of rainy rays per year (a rainy day is defined as P > 1 mm/d). For most catchments, the number of rainy days correlates with mean annual precipitation. However, in the Peruvian catchment (P-1) 150 rainy days occur per year, a frequency similar to the far more humid catchments in Germany. In the more arid MOPEX catchments, the number of wet days per year is generally lower ranging between 80 and 100. Catchment M-7, however, has the lowest number of rainy days, despite a total annual precipitation of 1075 mm.
Rainfall seasonality was calculated according to Walsh and Lawler (1981):

$$SI_i = \frac{1}{P_i} \sum_{j=1}^{12} \left| P_{ij} - \frac{P_i}{12} \right|, \tag{7.1}$$

where $P_i$ is annual precipitation for year $i$ and $P_{ij}$ is monthly precipitation for month $j$ in year $i$. For the multiannual timescale the annual seasonality indexes were averaged. Rainfall seasonality is higher in the drier catchments, in particular in catchments P-1 and M-7 (7.1).

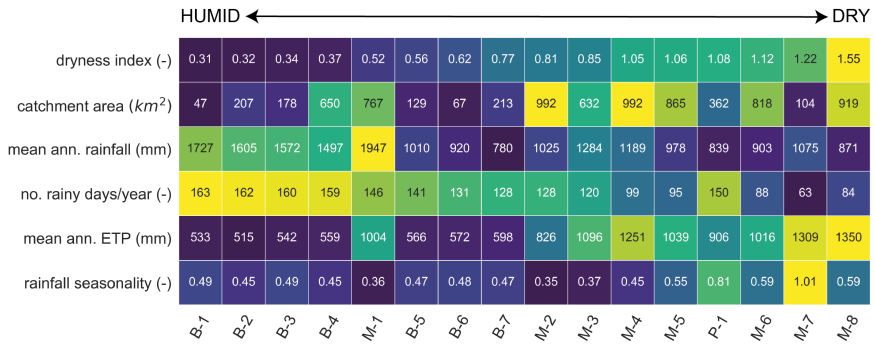


Figure 7.1: Overview over catchment and climate characteristics of the selected catchments (sorted by ascending dryness index). Color scale: yellow indicates high values, blue indicates low values, normalized to the range of each variable.

### 7.2.4 *Hydrological modeling*

The conceptual hydrological model used for this study is a simplified version of the HBV model (Lindström et al., 1997). HBV is a widely-used hydrological model, capable of reproducing catchment dynamics across numerous hydrological settings (e.g. Booij, 2005; Osuch, 2015; Uhlenbrook et al., 1999). The following section explains our slightly altered and simplified derivative.

*Conceptual model structure*

The modeling approach for the water balance is fully lumped and thus based on catchment-scale averaged values, with daily precipitation and potential evapotranspiration as meteorological forcing. The model consists of the HBV soil store to model runoff generation and actual evapotranspiration, and a single linear reservoir for daily streamflow (Figure 7.2).

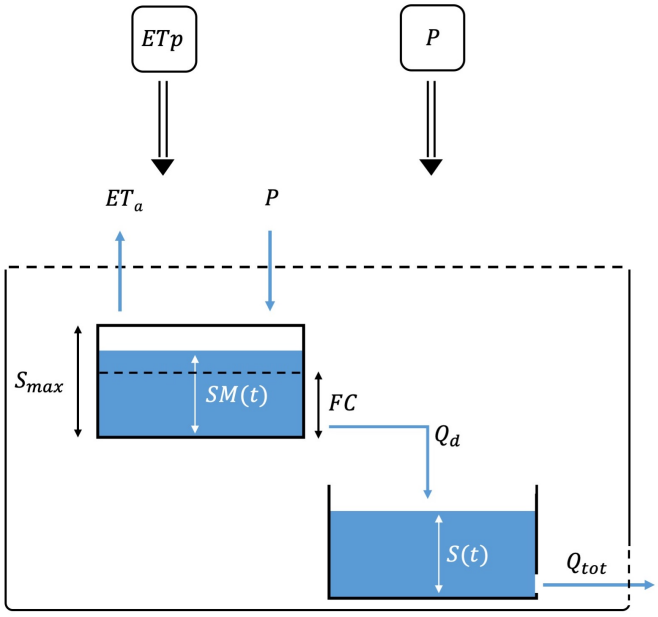


Figure 7.2: Setup of hydrological model. Abbreviations used for states and fluxes are explained in section 7.2.4

The soil store is characterized by the total storage volume $S_{max}$, its field capacity $FC$, and $\beta$-parameter. $S_{max}$ corresponds to the product of effective porosity and soil depth, while $FC$ describes the threshold below which actual evapotranspiration drops below the potential one. The water balance of the water balance of the soil bucket is:

$$\frac{dSM}{dt} = P - ET_a - Q_d, \tag{7.2}$$

with soil water storage $SM$ (mm), precipitation $P$ (mm/d), actual evapotranspiration $ET_a$ (mm/d) and direct runoff $Q_d$ (mm/d). Direct runoff per time is calculated based on the relative saturation using a power law with $\beta$ as parameter (Eq. 7.3). The remaining water infiltrates, and feeds evapotranspiration, while direct runoff goes to the linear reservoir:

$$Q_d = \left(\frac{SM}{S_{max}}\right)^{\beta} \cdot P \tag{7.3}$$

Actual evapotranspiration is a linear function of soil moisture $SM$ below $FC$ as given by Eq. 7.4 and 7.5:

$$ET_a = \frac{SM}{FC} \cdot ET_p \qquad f.SM < FC \tag{7.4}$$

$$ET_a = ET_p \qquad f.SM \geq FC \tag{7.5}$$

Contrary to the usual reservoir series used in the original HBV model, this model version uses a single linear reservoir to simulate streamflow. It is characterized by a recession constant $k_{res}$ (1/d) and its reservoir storage S(t), as described by Eq. 7.6:

$$Q_{tot} = k_{res} \cdot S \tag{7.6}$$

This model is rather simple, but fits the purpose of annual water balance simulations (Uhlenbrook et al., 2010) and a multi-catchment approach. Here, the focus is on two qualitatively different types of storage. The model accounts for the capillarity-bound storage fraction $SM < FC$ and corresponding water limitation of evaporation, while for $SM > FC$ evaporation is not water limited. Runoff production increases nonlinearly with $SM$ until $S_{max}$. In order to characterize the relative portion of both storage fractions, the capillary storage fraction $FC_{frac}$ is defined as $FC_{frac} = FC/S_{max}$.

*Model calibration and objective functions*

In order to reproduce the catchment water balance, the hydrological model's parameters had to be calibrated. Meteorological forcing data (P, $ET_p$) and discharge data described in section 7.2.2 were used to optimize the model parameters. Due to the simple fully lumped model structure and the objective to reproduce the annual water balance, the model parameters were optimized for monthly discharge values using the Kling-Gupta-efficiency (KGE) (Gupta et al., 2009) as objective function. An acceptable simulation of the water balance at the monthly scale was deemed acceptable for exploring the partitioning of rainfall into runoff and evapotranspiration at the annual and inter-

Table 7.2: Model parameter ranges for calibration

| Parameter | Unit | Parameter limits |
|---|---|---|
| $\beta$ | - | 0.05 – 5 |
| $S_{max}$ | mm | 50 – 800 |
| $FC_{frac}$ | - | 0.1 – 0.9 |
| $k_{res}$ | 1/d | 0.05 – 0.9 |

annual scales. The calibration was performed on the entire datasets covering 30 consecutive years, excluding the first year as model spin-up phase. In order to make a final catchment selection based on model performance, not only monthly KGE but also the resulting mean biased water balance error (MBE) was taken into account. The MBE was calculated as given by Eq. 7.7, with annually aggregated streamflows, $Q_i$, respectively for the i-th hydrological year:

$$MBE = \frac{1}{N} \sum_{i=1}^{N} \frac{(Q_{sim,i} - Q_{obs,i})}{Q_{obs,i}} \tag{7.7}$$

While for the monthly KGE a threshold of 0.7 was set for acceptable model performance, a water balance error of MBE $\leq$ 15% was considered sufficiently small.

Four parameters were varied within defined limits (table 7.2) using the shuffled complex evolution SCE-UA (Duan et al., 1994) uniform sampling scheme. The parameter ranges were defined in close accordance with other studies (Beck et al., 2016; Osuch, 2015; Piotrowski et al., 2017; Wang and Solomatine, 2018).

*Sensitivity of the water balance to soil storage parameters*

The behavior of mean annual water balances across a wide range of catchments with different soil water storage properties was investigated. Therefore, the calibrated models with their optimized parameter sets were used to vary the two parameters characterizing soil water storage, $S_{max}$ and $FC_{frac}$ in the following within three different variation schemes:

(i) Variation of $S_{max}$ between 1 and 2000 mm in increments of $\Delta S_{max}$ = 20 mm, while the other optimized parameters ($k_{res}$, $\beta$ and $FC_{frac}$) were kept constant

(ii) Variation of $FC_{frac}$ between 0.1 and 0.9 in increments of $\Delta FC_{frac}$ = 0.05, while the other optimized parameters ($k_{res}$, $\beta$ and $S_{max}$) were kept constant

(iii) Combined variation of both soil storage parameters: all possible parameter combinations of $S_{max}$ and $FC_{frac}$, given the same boundaries and increments as in (i) and (ii)

For each parameter combination resulting from the iterative variation process, a long-term simulation (30 years at a daily timestep) was run and the mean annual evaporation ratio (EVR) calculated. Observed EVR were estimated based on the assumption that at multiannual timescales, catchment storage changes are negligible and that mean actual evaporation thus equals the difference between mean annual precipitation and mean annual observed discharge ($ET_a = P - Q$).

## 7.3 RESULTS

### 7.3.1 *Water balance simulations*

The model performed acceptably for the selected study catchments, with monthly KGE > 0.8 and a water balance MBE within ±15% (Figure 7.3). While for catchments with lower dryness indexes, the MBE is does not exceed 5%, it is noticeably higher for the more arid ones, reaching errors close to +15% indicating slight overestimations of the mean annual discharge.

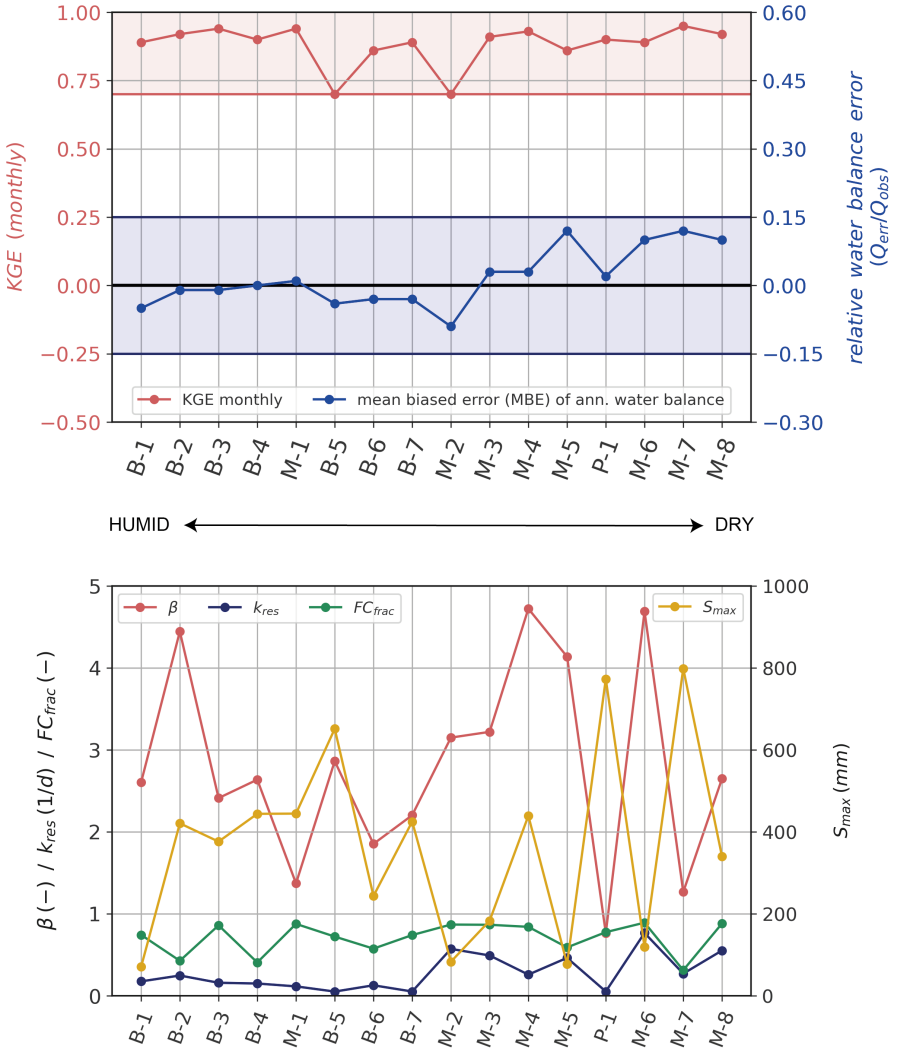


Figure 7.3: (top) KGE of monthly streamflow simulations and mean biased (MBE) water balance error of the calibrated models, catchments are sorted by ascending dryness. + overestimation, - underestimation. Highlighted areas: value ranges for KGE (red) and water balance (blue) with acceptable model performance. (bottom) Model parametrizations resulting from calibration of each catchment, catchments sorted by ascending dryness

The calibrated model parameters cover their predefined parameter ranges, without reaching the boundaries (Figure 7.3 and table A.4 in appendix A.4). The calibrated $\beta$ parameters varies between 0.8 and 4.7, indicating a large spread between strong to moderate growth of area contributing to runoff with relative saturation. $S_{max}$ ranges between 70 mm and 800 mm. Assuming a porosity of e.g. 0.4, this corresponds to an average root zone depth between 0.175 and 2 m. Field capacity ranges between 40 and 90 % of total root zone storage, suggesting either a rather small or strong influence of capillarity on

root zone storage. The $k_{res}$ parameter is quite uniformly distributed for the more humid catchments with values around 0.1-0.2, whereas it shows greater variability throughout the drier catchments with values between 0.26 and 0.77.

### 7.3.2 *Variation of total storage volume $S_{max}$*

The selected catchments spread across a dryness range from 0.30 to 1.55, while simulated evaporation ratios (EVR$_s im$), caused by the incremental variation of $S_{max}$, range between 0.05 and 0.92 (Figure 7.4). Generally, a higher total storage volume $S_{max}$ corresponds a larger evaporative fraction, as visualized by the color code of the plots. At the minimal total storage volume of $S_{max}$ = 1 mm, the catchments' evaporation ratios are around 0.1, almost independent of the dryness, as nearly 90% of the precipitation would run off. An increase in $S_{max}$ by only 20 mm causes EVR to jump from 0.25 to 0.4. The total range of the EVR varies for the different catchments, with smaller ranges for the more humid systems, which tend to approach the energy limit at a certain point. MOPEX catchment M-7 shows the largest EVR range.

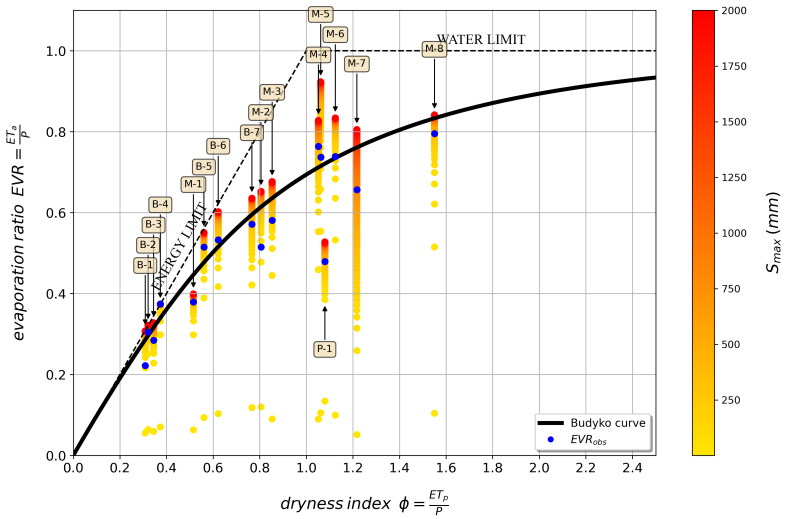


Figure 7.4: Variation of $S_{max}$ in Budyko space: the simulated mean evaporation ratios (EVR) of each variation step are shown as dots. Catchment IDs indicated by arrows

The offset from the Budyko curve is a nonlinear function of total storage volume, normalized with annual precipitation, for most study catchments (Figure 7.5 left). The reduction of the initially negative offsets with increasing storage shows a steep decline at small normalized storage volumes which flattens to an almost asymptotic curve at larger normalized storage volumes. This appears plausible, as the

EVR is bound by the energy limit as an asymptote. When the latter is reached, the curve becomes horizontal as can be seen for the humid catchments reaching the energy limit. Exceptionally, catchment M-7 is characterized by a gradual and steady increase in EVR, with a quasilinear development up to a $S_{max}/P_{ann-avg}$ ratio of about 0.5, never really reaching this asymptotic tendency.

The EVR offset of most catchments is zero at a distinct normalized total storage volume. A comparison of these distinct total storage volumes revealed a clustering at 5-15% of the annual rainfall (Figure 7.5 (right)). Exceptions are the Peruvian catchment P-1 as well as the U.S. catchment M-1, which do not reach the Budyko curve at all. It is also important to note that the catchment with the highest dryness index, M-8, meets the Budyko curve at a normalized total storage volume of 1.2.

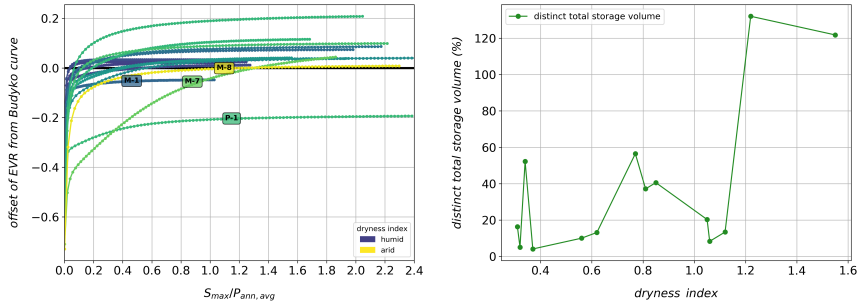


Figure 7.5: (left) Variation of $S_{max}$: offsets from Budyko curve as a function of normalized total storage. Color scale is relative to the catchments' dryness. positive values: simulated EVR higher / negative values: simulated EVR lower than Budyko curve / zero line: $EVR_{sim}$ matches Budyo curve. Labeled catchments are specifically addressed in the discussion. (right) distinct normalized total storage at which the catchments reach the Budyko curve as a function of the dryness index (catchments M-1 and P-1 remain below Budyko curve throughout variation of $S_{max}$ and are thus not plotted here)

### 7.3.3 *Variation of the capillary storage fraction $FC_{frac}$*

In the second variation scheme, the $FC_{frac}$ model parameter was varied in [0.1, 0.9] by increments of $\Delta FC_{frac}$ = 0.05, while keeping $S_{max}$ constantly at the calibrated value. The lower the $FC_{frac}$ parameter, the more water evaporates -being subject to water limitation in the soil- which implies higher evaporation ratios in the Budyko space (Figure 7.6). The total spreading of EVR is generally smaller, when compared to the variation of the total storage volume. The min-max extent of simulated EVR varies throughout the catchments, the majority of which generate EVR ranges scattering in a narrow envelope around

the Budyko curve. Simulated evaporation ratios of the M-7 catchment, however, are all below the Budyko curve, while EVR for catchment M-4 remains solely above the Budyko curve. The lowest $FC_{frac}$ values cause comparably high evaporation ratios. For humid catchments, many of those are located close to the energy limit. Catchments with dryness indices above one also reach high evaporation ratios. For instance, catchments M-8 and M-4 show simulated EVR values of around 0.9-0.95 at their lowest $FC_{frac}$ values, which is close to the water limit.

For most catchments, the gradual increase of capillary storage fraction $FC_{frac}$ causes a decrease in simulated EVR, which is initially quite slow at low $FC_{frac}$ values, indicating little sensitivity in this parameter range (Figure 7.7). At higher $FC_{frac}$ values of around 0.4-0.6 the reduction becomes steeper. Note that 50% of the catchments, mostly humid ones, reach the Budyko curve at distinct capillary storage fractions clustering between 0.6 and 0.75. For another group of four catchments this distinct capillary storage fraction cluster at 0.9, which corresponds to the maximum. For two other catchments, the Peruvian P-1 and the German B-1, the distinct capillary storage fractions are around 0.2. Both show a quasilinear dependency of the evaporation ratio on $FC_{frac}$. The M-7 catchment, as in the previous exercise, does not reach the Budyko curve.

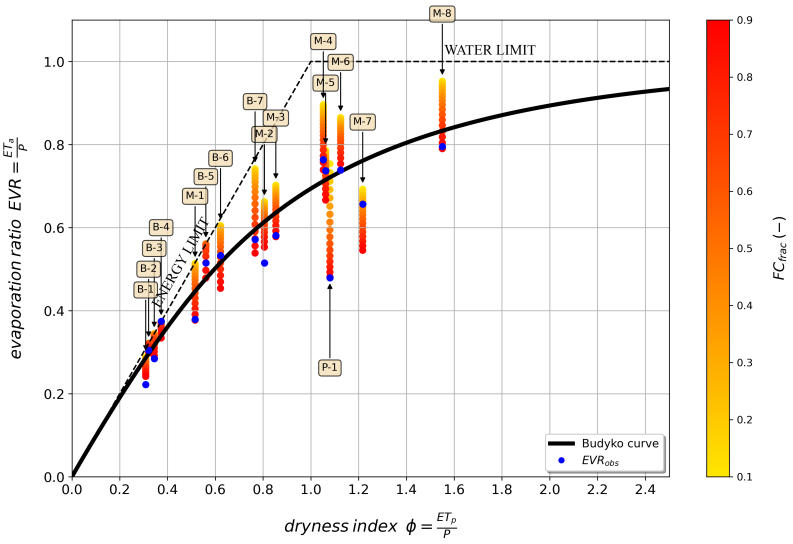


Figure 7.6: $FC_{frac}$ variation in Budyko space. For each catchment the simulated mean evaporation ratios (EVR) of each variation step are visualized as one dot. Catchment IDs indicated by arrows

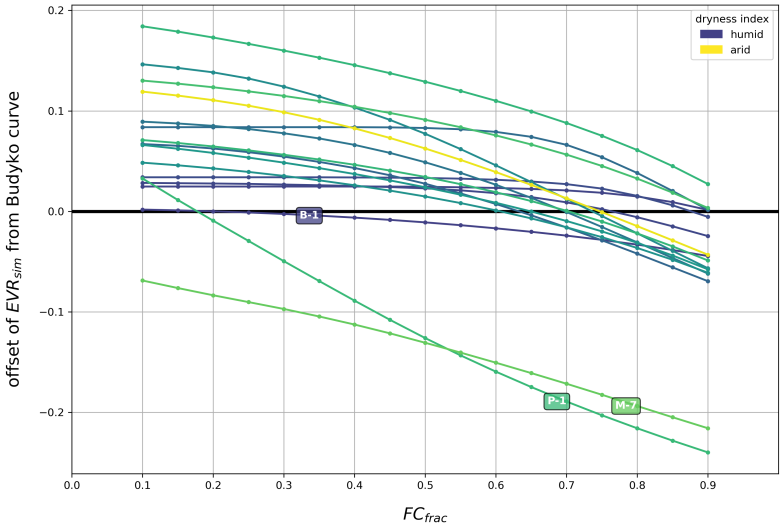


Figure 7.7: $FC_{frac}$ variation, offsets from Budyko curve. Color scale is relative to the catchments' dryness indexes. positive values: simulated EVR higher / negative values: simulated EVR lower than Budyko curve / zero line: $EVR_{sim}$ meets Budyko curve. Labeled catchments are specifically addressed in the discussion

### 7.3.4 *Simultaneous parameter variation*

The simultaneous variation of the total storage volume and capillary storage fraction revealed three main types of 2-dimensional Budyko offset and EVR sensitivity pattern. Each type is visualized using representative catchments in Figure 7.8.

- **Type 1: humid, close to energy limit**. Almost all parameter combinations result in an evaporation ratio close to the Budyko curve with the exception of the minimum $S_{max}$ value of 1mm).
- **Type 2: intermediate dryness, little seasonality**. There is a parameter domain whose combinations result in an evaporation ratio close to the Budyko curve (hereinafter referred to as "Budyko domain", with EVR offsets within $\pm$0.05 from Budyko curve). At low $FC_{frac}$ values, the Budyko domain is very sensitive to an increase of $S_{max}$, while at higher $FC_{frac}$ values, this sensitivity is inverted. In between the two extremes, there is a transition zone with intermediate sensitivity of the Budyko domain to both sort of parameter changes. In this example, this transition zone extends from roughly 15-50% of normalized total storage volumes and capillar storage fractions between 0.55-0.8 (see yellow square in Figure 7.8).
- **Type 3: dry ($\phi$ >1) catchments with pronounced seasonality**. The two catchments with stronly seasonal climate M-7 and P-1 revealed similar EVR patterns. The Budyko domain is reached

for normalized total storage volumes of more than 60% and even 90% of annual rainfall, respectively, at comparably low capillary storage fractions comprised between 0.1-0.4.

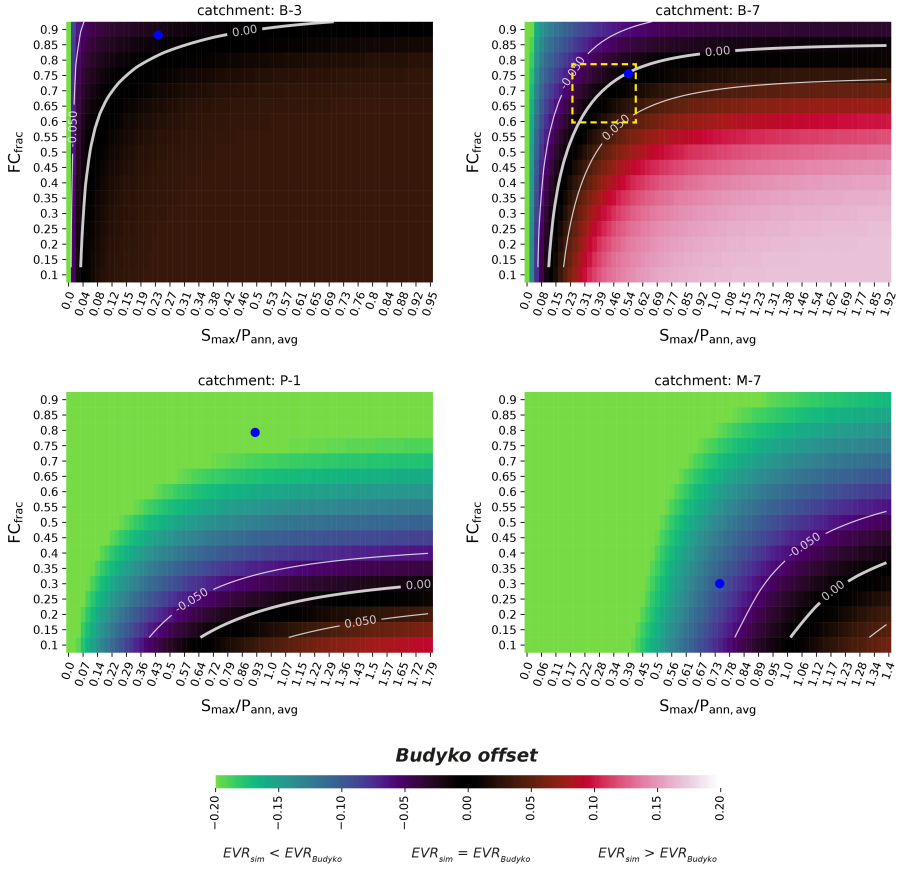


Figure 7.8: Simultaneous parameter variation. Simulated EVR is visualized in terms of its offset from the Budyko curve (only offsets ΔEVR $< \pm$ 0.2 are sensitive to color scale). Contour lines delineate parameter combinations causing mean EVR within ±0.05 range around Budyko curve ("Budyko domain"). Blue dots: calibrated parameter combination. Yellow square: highlights a parameter subspace where catchment could evolve inside the Budyko domain with both parameters changing only moderately. Three catchment groups with distinguishable patterns emerged: (1) upper left: quite humid, close to energy limit / (2) upper right: intermediate dryness, no seasonality / (3) lower two: drier catchments with pronounced seasonality.

## 7.4 DISCUSSION

In this study, a conceptual hydrological model was used to conduct a systematic variation of two soil storage-related parameters ($S_{max}$, $FC_{frac}$) for selected catchments across a variety of climate and landscape settings. The main goal was to investigate their role as second-order controls on the steady-state catchment water balance

and in particular their suitability to explain offsets from the Budyko curve.

The discussion starts with the performance of the water balance modeling, the calibrated parameterizations, and the implications of the approach taken for the presented results. Secondly, the sensitivity of the water balance to soil storage variations and the related findings for different groups of catchments are reflected upon. Thirdly, the relative offsets from the Budyko curve and the clustering found in the distinct soil characteristics for matching the Budyko curve are discussed. Finally, the results are interpreted in terms of catchment coevolution in the Budyko framework, concentrating on patterns that emerged during the simultaneous parameter variations.

### 7.4.1 *Water balance modeling*

*Model performance and hydrologic processes representation*

The hydrological model, despite its simplicity, proved capable of reproducing monthly discharge dynamics as well as the catchments' annual and interannual water balance in the 30 years of simulation period. The usefulness of similar HBV model versions for simulating discharge and water balance dynamics has been shown throughout numerous studies at comparable spatio-temporal scales (e.g. Lindström et al., 1997; Osuch et al., 2015; Seibert, 1999; Uhlenbrook et al., 2010). The performance of the model was slightly inferior for more arid catchments, perhaps due to more interannual variability in the annual water balances (and potentially also the rainfall-runoff mechanisms), which is more likely in drier climates (Koster and Suarez, 1999).

*Effects of not explicitly modeled processes compensating*

The hydrological model conceptualizes and simplifies hydrological processes. The chosen modeling approach is primarily focused on catchments where soil water storage plays a crucial role in the partitioning of rainfall into runoff and evapotranspiration, which includes a large number of catchments around the globe. For other settings, e.g., with considerable impact of snow cover or Hortonian overland flow, the dominant processes would not be well represented by the model used for this study. On the other hand, the soil storage-based reasoning of this study is not as relevant for these types of catchments, since the water partitioning is conditioned by influences not related to soil storage volumes. Other processes that are not explicitly modelled include soil moisture redistribution due to percolation and capillary rise, and the effective cutting of evapotranspiration below the permanent wilting point. The effects of these processes on the water balance, however, are potentially compensating, depending on the

individual conditions in a catchment. While percolation into deeper layers and the introduction of a permanent wilting point are likely to reduce evapotranspiration, capillary rise would rather increase evapotranspiration. The successful calibration suggests that the model yields robust estimates of mean annual water partitioning, the lack of process detail notwithstanding. The simple hydrological model used thus seemed adequate for the main purpose of the study.

*Catchment parametrizations and parameter interrelations*

The hydrological setting of the study catchments is represented by their calibrated parameter combinations. There was notable variability in the calibrated parameterizations not only between the three global regions, but also among the catchments within one region, for example in the geographically limited region of Baden-Württemberg in Germany (B-x). The catchments thus cover a range of relevant conditions, while the limited number made it possible to keep track of more detailed characteristics of each catchment. The systematic selection helped explore the influence of storage volume-related parameters on mean hydrologic partitioning and their relationship to the Budyko curve for different hydroclimates and catchments in a more direct way than it would have been possible in a statistical analysis of an unsystematic collection including as many catchments as possible. Nonetheless, the selection of catchments is limited, and does not cover all possible meteorological forcings and hydrologic responses. For instance, the drier regimes used in this study have climates with high potential evapotranspiration. The datasets and the selection process did not yield any catchments in the dry regime with low annual precipitation (cf. section 7.2.3). Including such catchments in future studies would show if additional variability in the calibrated parameterizations would also increase the sensitivity to the subsequent parameter variation conducted on that basis.

*Limits of catchment selection*

In this regard, the issue of parameter correlation needs to be addressed. The calibration results show strongly contrasted $\beta$ and $S_{max}$ values for the drier catchments included in the study, suggesting that the interplay of the two parameters affects the monthly (monthly KGE calibration) and thus likely also the annual water balances. Evidently, also total root zone storage capacity and its field capacity are closely related, as both increase with increasing fraction of silt and clay in the soil. This naturally implies that the model parameters $S_{max}$ and $FC_{frac}$ are interrelated as well and interact with respect to the sensitivity to EVR (Figure 7.8). The separate variation of both parameters yields, nevertheless, information about their relative importance in controlling EVR. The significantly larger EVR ranges in the results showed that total storage capacity dominated against the subdivision of the total

*$S_{max}$ and $FC_{frac}$ are not independent*

storage volume in free and capillarity-controlled fractions. The simultaneous variation of both parameters provides a better understanding of the interactions and helps to infer distinct combinations that match the Budyko curve and find behavioral parameter sets (Schaefli et al., 2011).

### 7.4.2 *The role of soil storage characteristics for the evaporation ratio*

*Variation of the total storage volume*

Soil water storage hydrologically acts as a control for direct runoff generation and it buffers water to feed the much slower evapotranspiration process from intermittent rainfall. When storage capacity increases, the soil is less likely to be water-saturated, leading to a higher saturation deficit and thus infiltration potential $(1 - (SM/S_{max})^{\beta})$ during rainfall events. This causes an increased water stock in the root zone which feeds evapotranspiration. In the extreme case of zero soil storage capacity, corresponding to impervious soil surface, nearly all precipitation would run off as overland flow, and the EVR would tend to zero. This is also shown by the low evaporation ratios in the corresponding simulations with the lowest $S_{max}$ value of 1 mm. When $S_{max}$ was increased from the minimum to small and moderate values, water partitioning was very sensitive to changes in total soil storage capacity, with evaporation ratio ranges ΔEVR from 0.1 to 0.3 for most catchments. The observed variations in sensitivities among the catchments, however, suggests additional controls on the EVR resulting from the interplay of the meteorological forcing and the parametrization.

*Influence of number of rainy days*

A correlation analysis revealed that the number of rainy days per year explains 93% of the variability in the total EVR ranges (beyond minimal $S_{max}$ = 1 mm) that occurred during the variation of total storage volumes (Figure 7.9). Interestingly, the catchment M-7 with the highest EVR range of ΔEVR = 0.6, is characterized by a comparably small number of rainy days, which indicates, given the total rainfall amount, rather intense rainfall events (catchment characteristics in Figure 7.1). This is in line with Milly (1994), who found that the number of rainy days is a sensitive variable in terms of the role of soil storage and for the mean annual water balance. The number of rainy days did not act as a proxy for a different characteristic such as mean annual precipitation or dryness itself, as the correlation plots in Figure A.7 in appendix A.4 show by explaining considerably less variance of the EVR range than the number of rainy days. For a given amount of total annual rainfall, the number of rainfall days relates to the mean depth of rainfall events as well as to the average interstorm period. The time between rainfall events influences the

soil depletion ($ET_a$ resulting from $ET_p$ and rel. soil saturation) and thus the mean antecedent soil moisture state prior to rainfall events. More storage capacity leads to less saturated soils on average which in turn enhances infiltration and the amount of water available for evapotranspiration.

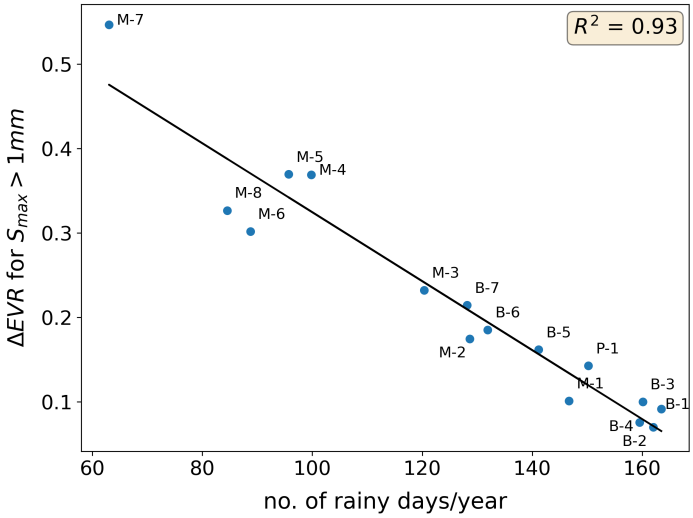


Figure 7.9: Linear correlation between the no. of rainfall days/year and the evaporation range (ΔEVR) spanned by the variation of $S_{max}$ (excluding its minimum value of $S_{max}$=1 mm)

*Quasi-asymptotic behavior above certain storage capacity $S_{max}$*

For almost all catchments, the sensitivity to further increase of storage capacity vanished beyond a critical normalized total storage volume, with negligible to no changes in mean evaporation (see Figure 7.5). For humid, energy-limited systems, a further increase of total soil storage cannot increase evapotranspiration anymore, once the energy limit is reached. The other systems reach this quasi-asymptotic behavior when two competing soil moisture influences are balanced in the model. On the one hand, a further increase of $S_{max}$ leads to a lower relative saturation, causing a higher infiltration potential and thus providing more water for subsequent evaporation. On the other hand, this decrease of relative soil moisture leads to an increasing reduction of the evaporation flux (imitating capillary forces), which in turn retains moisture longer in the soil and limits further decrease of soil moisture. The critical $S_{max}$ value for reaching this behavior depends on forcing characteristics and parametrization. Catchment M-7, characterized by an exceptionally low number of rainy days per year, does not reach this near-asymptotic behavior within the bounds of the $S_{max}$ variation, again underlining the aforementioned influence of rainfall frequency on the importance of total water storage volume regarding mean annual partitioning. This finding is again in line with Milly (1994), who found a maximum value of water-

holding capacity, beyond which mean evapotranspiration does no longer increase significantly.

*Variation of the capillary storage fraction in soil*

The mean annual water balance was also sensitive to changes of the capillary storage fraction of the soil, $FC_{frac}$, spanning EVR ranges of around ΔEVR=0.3 and ΔEVR=0.5 and with notable between-catchment variability reflecting different hydrologic behaviors. In general, higher $FC_{frac}$ caused lower mean evapotranspiration ratios, because $FC_{frac}$ determines the onset of water-limited evapotranspiration. This reflects in a simplified and linearized manner the decrease in capillary matric potential and reduction of capillary supply of upper soil layers losing water to sustain evapotranspiration. The conceptual soil water balance models used by Milly (1994) and Potter et al. (2005) neglect this effect. For the most humid systems in particular, the decline in mean evaporation ratio occurs at capillary storage fractions $\geq$ 0.6. In these humid climate regimes, relative soil moisture tends to be high and in combination with lower capillary storage fractions, evapotranspiration occurs mostly without water limitation. With increasing $FC_{frac}$ values, evapotranspiration is more likely to fall below the threshold to reduce evaporation, the soil retains more soil moisture and in turn enhances direct runoff production during rainfall. For other catchments, the sensitivity of mean EVR remains nearly uniform within the variation range of $FC_{frac}$, in particular for the two seasonal catchments (P-1 and M-7). This may be due to the fact that these drier, seasonal catchments tend to have relative soil moistures even below lower $FC_{frac}$ values, making their mean water balance sensitive to $FC_{frac}$ across the whole variation range.

### 7.4.3 *Offsets from the Budyko curve*

*Soil storage characteristics matching the Budyko curve*

For most study catchments, the modelled EVR ranges intersect the Budyko curve at distinct values of $S_{max}$ and $FC_{frac}$, respectively. The distinct storage parameters that made the systems reach the evaporation ratio predicted by the Budyko curve showed a clustering, and can be interpreted hydropedologically. For most of the systems, in particular for the humid catchments, the distinct normalized total storage that matches the Budyko curve is between 5-15% of the mean annual precipitation. In case of a uniform annual rainfall regime this corresponds roughly to the monthly precipitation amount and to an $S_{max}$ = 60-180 mm given a mean annual precipitation of P=1200 mm/a. When recalling that $S_{max}$ equals the product of soil depth and porosity, and assuming porosity values of around 0.3-0.5, this suggests soil

*$S_{max}$ matching Budyko curve partially cluster at 5-15 % of the mean ann. P*

depths ranging between 120-540 mm. This is in the range of the root zone depths found in vegetated systems (Gentine et al., 2012). The distinct capillary storage fractions for matching the Budyko curve scattered between 0.18 and 0.90 of the total storage volume, which is the range to be expected for sandy and clayey soils, respectively. For half of the catchments, the distinct $FC_{frac}$ ranged between 0.6 – 0.8, equivalent to loamy soils. There was, however, no clear trend of distinct capillary storage fractions with dryness index.

From the findings, it can be concluded that soil storage characteristics are important controls on the mean annual water balance, which can help explain observed offsets of catchments from the Budyko curve. The fact that some catchments did not reach the Budyko curve through independent variation of the soil storage parameters, however, also underlines that other second-order controls such as for example temporal variability and seasonality of the forcing, or their interplay with soil storage, can play an important role for hydrologic partitioning. Among the study catchments, the two drier and in particular seasonal catchments, P-1 and M-7, stand out in this respect. While Fu and Wang (2019) show that seasonality can indeed have a significant influence on the position in the Budyko space, Potter et al. (2005) pointed out in his study on Australian catchments, that seasonality by itself was not able to explain the inter-catchment variance in the observed mean evaporation ratio. Lavenne and Andréassian (2018) pointed out the importance of the phasing of P and $ET_P$ in seasonal climate regimes in France. In consequence, while seasonality-related aspects appear to play a role, its interaction with other characteristics such as soil storage cannot readily be discerned. Another possibility is that a catchment's evapotranspiration can be transport-limited when the vapor pressure gradient in the lower boundary layer is low and the air is moisture-saturated. Strongly seasonal environments could present a more favorable setting for transport limitation, since the atmosphere is more likely to be moisture-saturated when the entire annual precipitation occurs within a limited number of months during the rainy season. A straightforward supplement analysis of relative humidity data of stations in the vicinity of the study catchments revealed that mean relative humidity during the rainy season for the Peruvian catchment was around 85%, and higher than the year-round average for all other catchments. Assuming that most of the annual evapotranspiration in the Peruvian catchment occurs during the period of abundant soil moisture storage in the rainy season, the mean evaporation flux could. This reasoning, however, does not apply to the other seasonal catchment (M-7).

*Seasonal catchments stand out*

*Atmospheric transport limitation*

*Interpretation in terms of catchment coevolution and behavioral model parameterization*

*Parameter variations regarded as two weathering mechanisms*

The findings fit well into the perspective that a catchment's form and functioning are co-evolutionary (Troch et al., 2015), which also implies that the development of total storage volume and of capillary storage fraction are not independent of each other. The successive variation of the two soil storage parameters sheds light on the role of the soil formation process resulting from two weathering mechanisms. While the first one ($S_{max}$) represents the generation of soil storage volume, i.e., porosity, the second one ($FC_{frac}$) relates to the transformation of coarse to increasingly fine-grained material with higher capillary forces. In a chronosequence study on proglacial moraines, Hartmann et al. (2020) show such a soil development over time at scales of centuries and millennia, both in terms of soil storage and retention characteristics (i.e. porosity and the fraction of silt and clay increasing). They detected a similar soil evolution for two different parent materials, however occurring at different rates. While this type of soil evolution is an example for discussing the parameter variation and hypothesized related weathering processes in this study, in other hydro-pedogenetic contexts (e.g. highly erosive terrains) the storage development can differ.

The parameter variations corresponding to these two mechanisms resulted in opposite effects on the mean evaporation ratio. This could imply that catchments with their related soil formation processes converge towards an optimal state with regard to hydrologic partitioning. While in early stages of a catchment's evolution –probably starting out far off Budyko– the development of total storage $S_{max}$ is likely to dominate the evolution, at later stages both parameters could continue to evolve simultaneously within the Budyko domain, thus keeping the water balance in a steady-state in accordance with Budyko.

*Underlying organizing principles that explain clustering around Budyko curve?*

The idea of finding underlying organizing principles for the steady-state hydrologic partitioning described by the Budyko curve has been addressed by multiple studies in the past (cf. Berghuijs et al., 2020). Westhoff et al. (2016) showed in a backward approach that the Budyko curve can be derived using the Maximum Power principle as a constraint. Porada et al. (2011) simulated the water balance of the 35 largest basins on Earth using the SIMBA model and inferred parameters controlling root water uptake by maximizing entropy production. Simulations were in line with the Budyko framework. Milly (1994), referring also to similar conclusions by Milly and Dunne (1994), stated that simulated threshold values of water-holding capacities, beyond which evaporation does not change significantly anymore, were in proximity to the observed ones, which lead him to hypothesize that ecosystems strive to maximize evapotranspiration. The Budyko curve

could thus also represent the strategy to maximize evapotranspiration by approaching the supply and demand limit, yet not reaching them due to limiting factors such as climate variability (Berghuijs et al., 2020). If catchments were in fact to coevolve towards an optimal state of hydrologic partitioning, it would still remain difficult to infer which stage of coevolution a catchment actually is in. The plots shown in Figure 7.8 can be helpful in this respect, as they connect a wide range of total storage volumes and capillary storage fractions to the resulting offsets of simulated EVR from the Budyko curve. This space represents all possible system configurations with respect to these two soil storage-related parameters, and thus which soil states a catchment might potentially go through.

*Catchment groups in terms of Budyko "domain" emerged in simultanous parameter vairation*

Groups of catchments emerging in terms of the "Budyko domain" were identified, which clustered with respect to their climate setting and their parameter combinations in a close range of $\Delta$EVR = $\pm$0.05 around the Budyko curve. The most humid catchments are bound by a tight energy limit, and hence proximity to the Budyko curve is easier to achieve, also at lower $S_{max}$ values. For catchments of intermediate humidity, a Budyko domain stretching throughout the parameter space is observable, with the sensitivity of one parameter to the mean water balance being strongly conditioned by the other parameter. The domain highlighted by the yellow square in Figure 7.8-upper right represents a parameter subspace where both parameters could develop whilst remaining within the Budyko domain. A catchment in that subset could evolve at "moderate pace" in terms of soil storage, while the water balance partitioning in terms of the Budyko framework would roughly remain constant.

*Hydrologic aging different in seasonal environments?*

In the drier range of catchments, the two seasonal ones (P-1, M-7) are of particular interest. In both cases, the Budyko evaporation ratio is only reached at high $S_{max}$ and low $FC_{frac}$ values. According to observed discharge and precipitation data, both are currently not inside the Budyko domain. Troch et al. (2015) introduced catchment forming factors, as quasi-independent drivers of catchment coevolution: climate, bedrock weatherability, tectonics and time, and the concept of hydrologic age as the result of their combined effect. The latter is related to the amount of energy that has flown through the catchment and to the amount of physical work expended thereby. In this context one might speculate that catchments' hydrologic aging in a highly seasonal climate is slower than in humid settings. The two dryness-defining variables (P, $ET_p$) and their corresponding mediators –water and energy– are interacting simultaneously only during 4-6 months during the rainy season, which could lead to a slower evolution towards the Budyko state in these catchments. Catchments with seasonal climates are known to produce lower evaporation ratios than non-seasonal ones of the same aridity (Fu and Wang, 2019; Lavenne

and Andréassian, 2018) and tend to be overestimated by the Budyko curve (cf. Figure 6.12), which supports this point of view.

# 8

# SYNTHESIS AND CONCLUSIONS

The main goals of this thesis were to assess catchment water balances in a data-scarce and mountainous environment on the Western flanks of the Peruvian Andes, as well as to explore in what way the Budyko curve can serve as a water balance landmark for hydrological modeling in that region. To that end, methods were developed to estimate catchment-wide precipitation and potential evaporation in the region based on minimum data, and subsequently used to estimate catchments' aridity and as model forcing. A paired modeling approach between two climatic-structurally similar catchments was conducted, with the better monitored Chillón catchment serving as reference and parameter donor catchment to overcome data shortcomings in the target basin, the Lurín. The focus was on annual and mean annual water balances, with the Budyko curve as orientation. In a second step, due to the favorable topography, the water balance and Budyko offset analysis was widened to multiple similarly arranged catchments along the Western flanks of the Andes. A rather inconsistent picture of water balances prompted a more in-depth exploration of the role of soil storage capacity since -despite its importance- it is hardly quantifiable at the catchment scale. A virtual, model-based experiment was carried out to analyze the sensitivity to the mean water balance and the relationship to the Budyko curve of two soil storage-related properties.

In the following sections, the key findings are summarized and put in relation across the individual chapters.

## 8.1 SYNTHESIS OF KEY FINDINGS

### 8.1.1 *Estimation of precipitation and pot. evapotranspiration in data-scarce environment*

A robust approach for the interpolation of rainfall over mountainous catchments, named CovVar, was introduced and applied to two study catchments in West Peru, Chillón and Lurín. Based solely on rain gauge data, it establishes and incorporates long-term statistical relationships between monthly rainfall totals and elevation as well as elevation-dependent structures of the variance and the covariance. The regionalization involves a nearest neighbor approach, using elevation difference instead of the euclidean distance and weighting the fluctuation around an elevation-dependent, long-term average rainfall.

Showing reasonable performance metrics, also in comparison to the national gridded PISCO rainfall product. Differences between the two datasets in catchment-average rainfall became apparent at annual scales, with CovVar yielding higher annual rainfall - both as a result of the CovVar method exploiting the statistical patterns and of the newly installed rain gauges in the high elevation headwater zones of the Lurín basin. The CovVar model was successfully implemented as forcing data in the distributed hydrological model (mHM) for the Chillón and Lurín basin, proving valuable in the estimation of the water balance.

### 8.1.2 *Similarity of Peruvian catchments and their Budyko positions*

*Paired catchment modeling approach*

The paired-catchment approach, using the Budyko space and curve as a tool and water balance landmark, helped evaluating the quality of different meteorological forcing datasets. The datasets had a significant impact on observed and modeled water balances, not only for the Lurín but also for the better monitored Chillón basin. The Lurín, keeping in mind that the observed and modeled time period covers only 3-4 years, showed water balances far off the Budyko curve and far off the presumably similar neighboring catchment without use of the newly developed CovVar rainfall dataset, both in terms of dryness and of the evaporation ratio. The CovVar method thus seemed to simulate more plausible catchment rainfall totals. In conclusion, with the right datasets, the initial similarity assumption seemed more reasonable and a parameter transfer possible. The parameter transfer from Chillón to Lurín yielded useful parameter sets for the Lurín which performed similarly to direct calibrations of the Lurin. However, both the effect of different forcing datasets and model errors dominated by interannual water balance variability in four years of discharge records in the Lurín outweighed the influence of the model parametrization.

*New datasets present more plausible scenarios*

Not only the similarity but also dissimilar aspects between the two basins became apparent, regarding for example the water release during the dry season. Besides differences in hydrogeological conditions, in this context questions of anthropogenic alterations might be relevant. Lack of more detailed knowledge about management of reservoirs and of water extractions, limited the ability to explain differences between the two stream gauges in the Chillón and differences between the two basins in terms of dry season stream flow. In conclusion, the two basins did expose a considerable degree of similarity in aridity and mean water balance as well as in their seasonal flow regime, however with notable differences at shorter

*Limited knowledge of differences in water management*

timescales, whose explanations could only be hypothesized.

*Water balance similarity and Budyko offsets of multiple catchments in West Peru*

There were two findings regarding the water balances in the wider geographic context of the Western slopes of the Peruvian Andes. On the one hand, there is a marked systematic trend of the 17 catchments' mean water balances to be overestimated by the Budyko curve. On the other hand, a pronounced between-catchment variability in the mean annual water balance and thus also of the Budyko offsets distinguished the catchments.

*3 $R^2$ signals for Budyko offsets*

A linear correlation analysis was conducted in order to relate the different water balances to subscale climatic or physiographic catchment characteristics. While the individual coefficients of determination remained expectedly low for the coarse correlation approach, it did show signals (here, $R^2 > 0.4$) for elevation difference as a proxy for inner-catchment climatic heterogeneity, partially related snowiness and discharge seasonality serving as proxy for all catchment storage-related characteristics. Hypothesis- and literature-based reasoning offered possible explanations as to how these characteristics might lead to the offsets from the Budyko curve.

*Macroscale vs. microscale similarity*

The remaining variance is due to other influences that were not accessed or accessible, or their interrelations. The similarity notion is limited by what is known or measurable, and has to distinguish macroscale and microscale similarity. While e.g. macroscale climatic similarity in terms of mean precipitation and potential evaporation may be provided to a certain degree, microscale soil properties, resulting from other, not climate-related influences like rock weatherability, are relevant to the evapotranspiration process and might cause such differences. Anthropogenic influences may also play a role, given however the magnitude of Budyko offsets, such influences are of minor importance.

*Soil storage and seasonal influences*

The systematic trend of the water balance with respect to the estimate by the Budyko curve must also be due to characteristics that differentiate those catchments from the numerous other catchments around the world that are in better agreement with the Budyko curve. Characteristics affecting all of the Peruvian study catchments to some degree, are not detectable in an internal correlation analysis. The importance of soil storage capacity that was demonstrated by means of the virtual experiment in chapter 7 and the fact that semi-arid climate combined with the steep slopes of the Andean topography present favorable conditions to soil storage deficits, make soil storage deficits

likely to explain a part of the general water balance trend. Effects related to the seasonal climate likewise affects all catchments and might contribute to the shift in the Budyko space as well.

### 8.1.3 *Soil storage and other controls on mean water balance and on Budyko offsets*

*Soil storage capacity is a dominant control*

Soil storage capacity had already been identified as a dominant control on mean annual water balance and on potential Budyko offsets in literature. Process velocity-wise, soil storage is required to buffer the slower evapotranspiration process that competes with runoff. However, soil storage is notoriously hard to assess and thus quantitatively effectively unknown at the catchment scale, resulting in a conflict between importance and data availability. In the geographic context of the West Peruvian catchments, limited soil storage capacity is likely in the semi-arid region with fairly steep topography. In consequence, soil storage could one the one hand contribute to the general water balance bias found for all Peruvian catchments compared to the Budyko estimate as well as to the between-catchment variability.

A model-based virtual experiment was conducted to explore the role more in detail, built on catchment observation data (P, $ET_p$, Q) in order to represent realistic systems. The fully-lumped and simple hydrological model, similar to the widely used HBV model, proved to be an effective and efficient tool to simulate multiple catchment water balances at scales between 50-1000 $km^2$. The study singles out specific root zone characteristics, namely total soil storage volume and the capillary storage fraction, two physically interpretable parameters.

*Both soil storage properties are important & observable clustering in terms of Budyko optimum*

The results corroborated the important role of soil storage as a control on the mean annual water balance and potential offsets from the water balance predicted by the Budyko curve. In most cases, the parameter variations generated evaporation ratio envelopes enclosing the Budyko curve. A clustering was observed in terms of normalized soil storage required to match the Budyko curve at around 5-15% of mean annual precipitation which reasonably corresponds to soil storage capacities commonly found in nature. Similarly, also the second parameter (capillary storage fraction) clustered in a range that agrees well with hydropedological interpretation. As a result of the study, and given the indispensable buffering role between runoff and evapotranspiration processes, and in line with the proposition of a hydrological space related to soil storage combined with water and energy availability by Daly et al. (2019), soil storage could also be

ranked a first-order control.

When making model-based predictions or when assessing the water balance in ungauged basins, the Budyko curve can be used as a landmark for long-term simulations. If taking potential deviations due to soil storage volume into account, model parameterizations could be oriented and constrained based on the behavior of the "Budyko domains" identified in section 7.3 for different climate types. Doing that, one could take into consideration that in catchments with high soil storage capacity, the actual water balance might exceed the evaporation ratio given by Budyko, or vice versa for catchments with little soil storage capacity (below 5-10% of mean annual precipitation in humid climates).

*Role of seasonal climate*

Climate seasonality-related aspects appear to play a role in mean annual water balances and Budyko offsets. Such catchments stood out in the model-based soil storage study and such a reasoning comes to mind when considering the systematic and in parts considerable bias of evaporation ratios lower than the Budyko estimate for such aridity indexes (chapter 6). Comparison to seasonal catchments in the US (MOPEX dataset) showed that seasonality by itself cannot explain such offsets. In literature, the tendency of catchments markedly seasonal rainfall to result in higher runoff coefficients (i.e. lower evaporation ratios) was also found to act in combination with other characteristics. Seasonal rainfall only lead to lower mean annual EVR when there was also a phase lag between P and $ET_p$ or in combination with soil storage capacity limitations (Daly et al., 2019). Moreover, atmospheric transport limitation might play a role in markedly rainy seasons, where air saturation and slow transport conditions of the moisture might impede the evaporation flux. The pronounced between-catchment variability shown in the multi catchment analysis of water balances also suggests an interplay of the seasonal climate with other system properties.

While the general reasoning is based on the lack of temporal co-occurrence of incoming energy and available soil moisture as a result of available rainfall, and the more out of phase they are, the less evaporation is likely to occur -always compared to a uniformly distributed climate, P and ETp. In that sense, mean annual dryness might not be ideal in characterizing the system in terms of water- or energy-limitation. Like the issue of spatial heterogeneity addressed in section 6.3.1, which might result in an effective catchment area for the mean water partitioning, also in a temporal sense there could be a hydrologically effective part of the year, related to the maximum co-availability of water and energy and similar to the phase lag issue by Lavenne and Andréassian (2018). Hence, while as an annual aggregate the catch-

*Seasonality challenges the water-limitation assumption of the annual aggregate*

ment system appears to be water-limited, this does not necessarily apply to the rainy season where most of the annual water partitioning into P and $ET_a$ however occurs. The characterization of the systems thus depends on the season and might undergo a phase change from water-limited to neutral or even energy-limited. Taking this reasoning a bit further, from a landscape evolutionary perspective, seasonal provision of water and energy, often not in phase, might affect the rate of catchment evolution (soil and vegetation), since the amount of energy flown through a and applied to a catchment is inferior or more slowly in such a setting.

*Water balance estimation errors*

When applying the Budyko curve (calculating aridity) or when assessing observed catchment water balances as in chapter 6, estimation errors potentially affect the analysis. If all components of the Budyko framework are affected, aridity in terms of catchment rainfall and potential evaporation as well as actual evaporation estimated via streamflow measurements, it remains difficult to get a realistic picture. Discharge measurements can be a major source of uncertainty in such a region. However, the bias found for all catchments in West Peru that clearly points in one direction regarding the offset from the Budyko curve, indicates a systematic shift due to physical mechanisms governing the water balance of the catchments, and not due to random estimation errors. In addition, a certain degree of reliability of discharge data was backed up for instance by redundant and consistent stream flow data available for some catchments due to two gauges positioned in proximity in the same stream (e.g. Yanapampas), or by the fact that the runoff-favoring influence of snowiness or glaciers on catchment water balances known in literature is well captured in the Peruvian dataset since it affects the correct catchments (Yanapampas, Condorcerro).

## 8.2 OUTLOOK AND FURTHER RESEARCH

CovVar could be developed further, e.g. use more than one reference station for calculation and weighting of the fluctuation from the elevation-dependent mean. Such an approach could be implemented by inverse-distance-weighting the fluctuations of multiple neighboring stations. Additionally, an evaluation of the performance of this simple regionalization algorithm in comparable regions would be of interest.

More in-depth research as to the systematic deviation of catchment water balances in West Peru from the Budyko curve as well as their considerably high variability despite the similar geography, which in thesis was carried out only on the basis of linear correlations with a limited number of predictors.

With model- and multiple catchment data-based studies on the role of soil storage capacity on Budyko offsets conducted, including the virtual experiment of this thesis, it would be helpful in the future to focus on catchments where soil storage properties can be estimated more precisely on the basis of comparably abundant soil data, both in terms of texture and depth, and analyze Budyko positions and offsets.

# A

# APPENDIX

## A.1 APPENDIX OF CHAPTER 3

*Overview of hydrometeorological data*

Table A.1: Overview of data used for catchment analyses and hydrological modeling in chapter 5 and 6

| Data group | Data type | Dataset | Spatiotemporal resolution (spatial extent) | Source |
|---|---|---|---|---|
| Hydrometeorological Data | | | | |
| **Precipitation** | gridded precipitation | PISCO product | daily, 0.1° (Peru) | SENAMHI |
| | point-wise precipitation | rain gauges | daily (Peru) | SENAMHI |
| **Pot. evaporation** | gridded ETp | PISCO product | daily, 0.1° (Peru) | SENAMHI |
| **Atmospheric variables** | T, rH, Rn, Patm | weather stations | daily, hourly | SEN, SED, TRUST |
| **Hydrological data** | Stream flow | | daily | SENAMHI |
| **Snow** | Snow cover | Snow cover (NDSI) index | 8days (global) | NASA-MODIS |
| Biogeophysical data | | | | |
| **Topography** | DEM | | 12m (global) | Tandem-X (DLR) |
| | | | 30m (global) | NASA-ASTER |
| **Vegetation/land use** | Vegetation zones | National vegetation map | (Peru) | SENAMHI |
| | Vegetation cover | Leaf area index (LAI) | 500m (global) | NASA-MODIS |
| **Soils** | Soil type | National vegetation map | (Peru) | |
| | Soil texture | Soil profiles and interpolated, gridded soil data | 250m (global) | ISRIC, soilgrids.org |
| **Geology** | Hydrogeological units | National GIS map | (Peru) | INGEMMET |
| | Wells / sources | National GIS map | (Peru) | INGEMMET |

## A.2 APPENDIX OF CHAPTER 5

*Soil grids data*

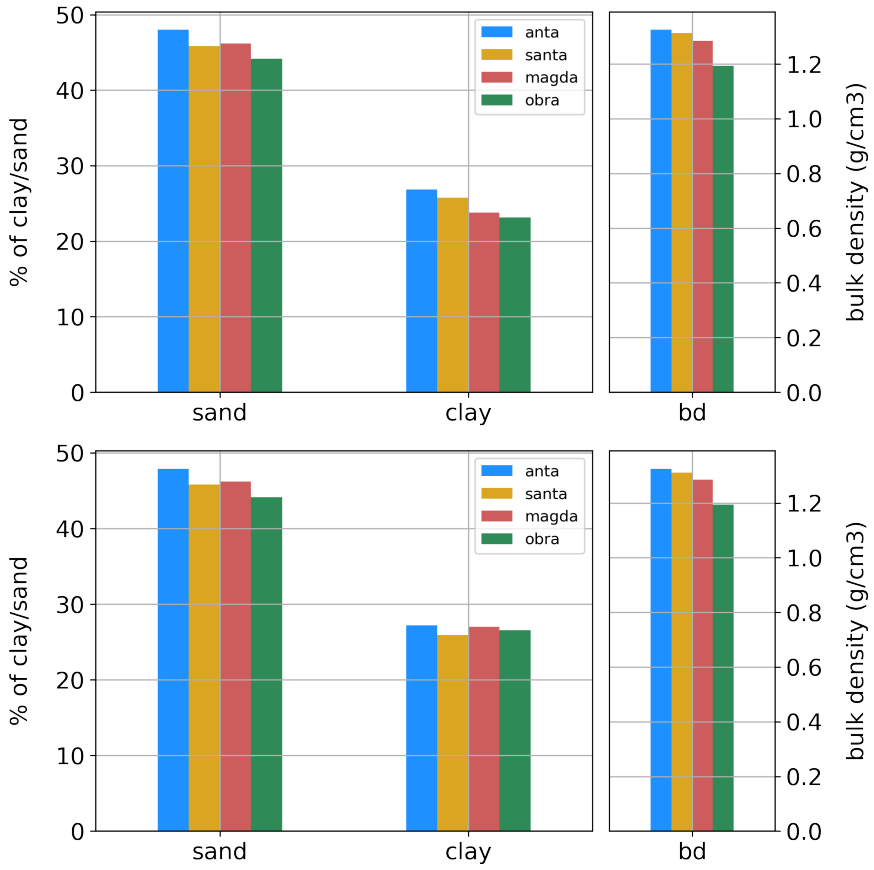


Figure A.1: Chillón and Lurín basins: mean soil texture of subcatchments (soilgrids product)

*Parameters of mHM modeling*

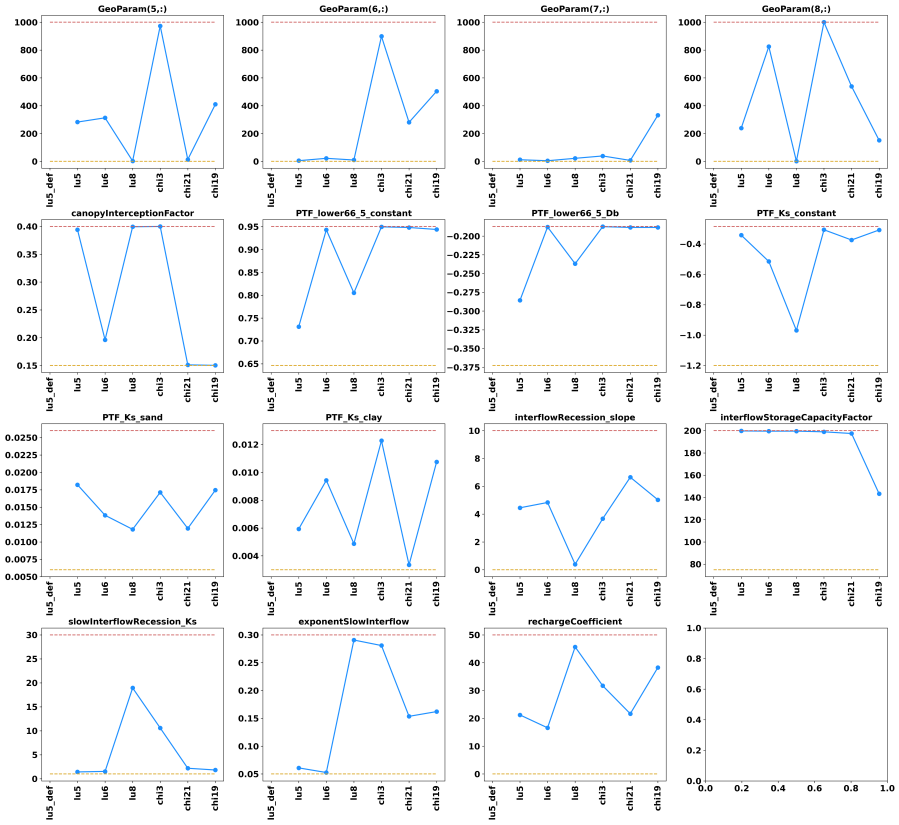


Figure A.2: mHM global parameters of transferred Chillón runs, mHM default parameter settings and calibrated Lurín reference runs

## A.3 APPENDIX OF CHAPTER 6

*Correlation matrix of all climatic and physiographic catchment characteristics and indexes*

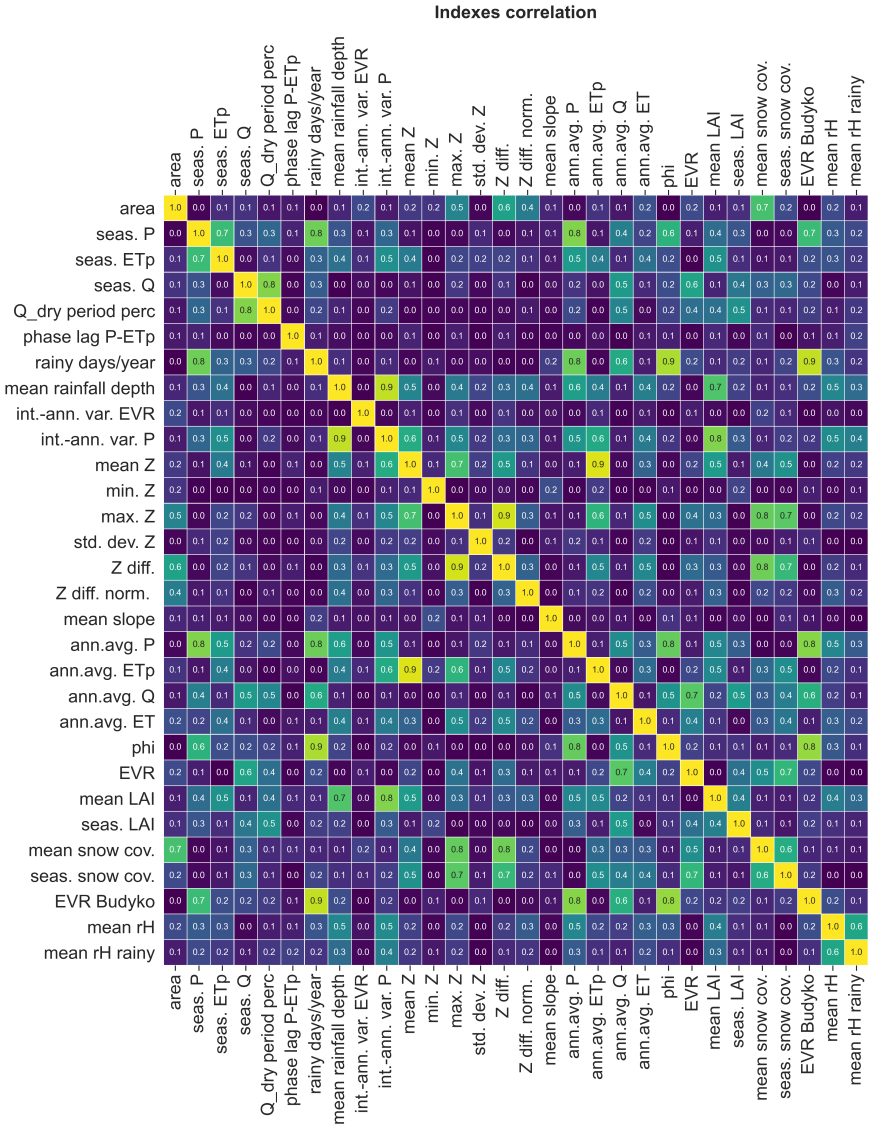


Figure A.3: Correlation matrix of all climatic and physiographic catchment characteristics and indexes

*Multivariate regression*

Table A.2: Results of multivariate regression analysis, sorted by no. of predictors and ascending explained variance

| combi_ID | no. of predictors | coeff. of determination | indexes/predictors |
|---|---|---|---|
| **3** | 2 | 0.41 | area, seas. LAI |
| **1** | 2 | 0.42 | area, Z diff. |
| **2** | 2 | 0.45 | area, mean snow cov. |
| **7** | 2 | 0.46 | Z diff., mean snow cov. |
| **6** | 2 | 0.50 | seas. Q, seas. LAI |
| **0** | 2 | 0.56 | area, seas. Q |
| **9** | 2 | 0.56 | mean snow cov., seas. LAI |
| **5** | 2 | 0.60 | seas. Q, mean snow cov. |
| **8** | 2 | 0.63 | Z diff., seas. LAI |
| **4** | 2 | 0.65 | seas. Q, Z diff. |
| **13** | 3 | 0.47 | area, Z diff., mean snow cov. |
| **12** | 3 | 0.57 | area, seas. Q, seas. LAI |
| **15** | 3 | 0.58 | area, mean snow cov., seas. LAI |
| **11** | 3 | 0.60 | area, seas. Q, mean snow cov. |
| **18** | 3 | 0.62 | seas. Q, mean snow cov., seas. LAI |
| **19** | 3 | 0.63 | Z diff., mean snow cov., seas. LAI |
| **14** | 3 | 0.65 | area, Z diff., seas. LAI |
| **10** | 3 | 0.65 | area, seas. Q, Z diff. |
| **16** | 3 | 0.65 | seas. Q, Z diff., mean snow cov. |
| **17** | 3 | 0.69 | seas. Q, Z diff., seas. LAI |
| **22** | 4 | 0.63 | area, seas. Q, mean snow cov., seas. LAI |
| **20** | 4 | 0.65 | area, seas. Q, Z diff., mean snow cov. |
| **23** | 4 | 0.66 | area, Z diff., mean snow cov., seas. LAI |
| **24** | 4 | 0.70 | seas. Q, Z diff., mean snow cov., seas. LAI |
| **21** | 4 | 0.70 | area, seas. Q, Z diff., seas. LAI |

## A.4 APPENDIX OF CHAPTER 7

*Catchment/Stream gauge IDs*

Table A.3: Reference to orginal stream gauge IDs

| Original catchment/stream gauge ID | Catchment ID used in this thesis |
|---|---|
| **3303** | B-1 |
| **3304** | B-2 |
| **3302** | B-3 |
| **2340** | B-4 |
| **3443000** | M-1 |
| **177** | B-5 |
| **3314** | B-6 |
| **478** | B-7 |
| **1534000** | M-2 |
| **3438000** | M-3 |
| **7346050** | M-4 |
| **6914000** | M-5 |
| **Obrajillo** | P-1 |
| **6888500** | M-6 |
| **11160000** | M-7 |
| **8171000** | M-8 |

*Catchment locations*

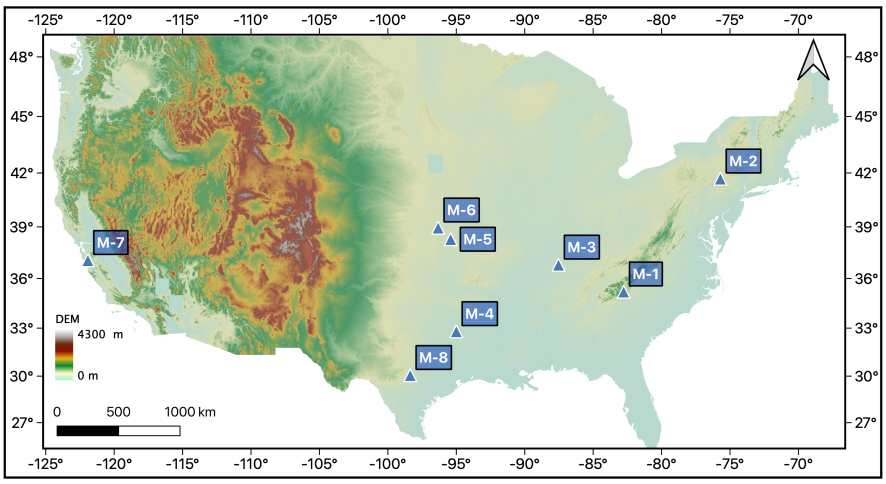


Figure A.4: Location of MOPEX catchments in the USA

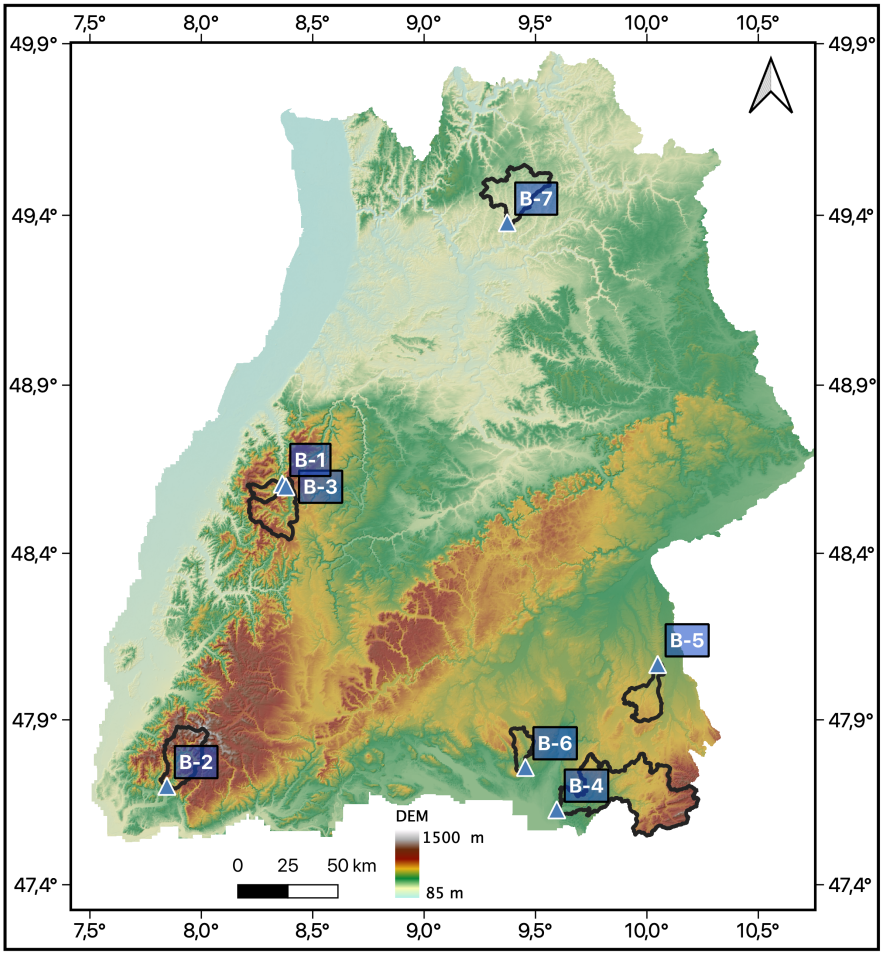


Figure A.5: Location of BaWue catchments in Germany

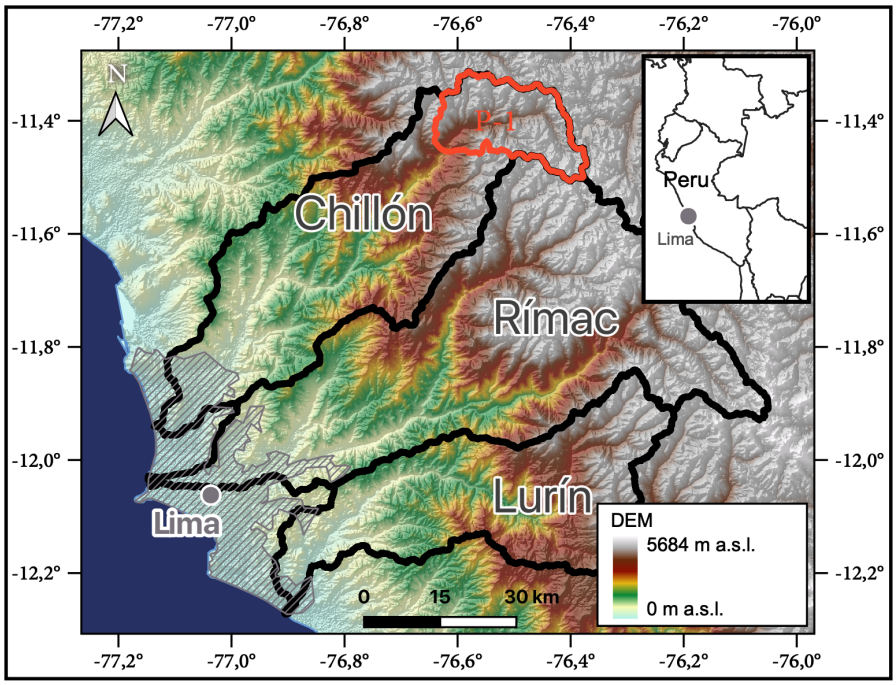


Figure A.6: Location of Peruvan catchment

*Water balance modeling with HBV*

Table A.4: Calibrated parameters and loss functions

| catchment | $\beta$ | $k_{res}$ | $FC_{frac}$ | $S_{max}$ | $KGE_{mon}$ | $MBE$ |
|---|---|---|---|---|---|---|
| **B-1** | 2.60 | 0.18 | 0.74 | 70.60 | 0.89 | -0.05 |
| **B-2** | 4.45 | 0.25 | 0.43 | 420.80 | 0.92 | -0.01 |
| **B-3** | 2.41 | 0.16 | 0.86 | 376.20 | 0.94 | -0.01 |
| **B-4** | 2.64 | 0.15 | 0.41 | 444.00 | 0.90 | 0.00 |
| **M-1** | 1.37 | 0.11 | 0.88 | 444.50 | 0.94 | 0.01 |
| **B-5** | 2.86 | 0.05 | 0.72 | 651.50 | 0.70 | -0.04 |
| **B-6** | 1.85 | 0.13 | 0.57 | 243.40 | 0.86 | -0.03 |
| **B-7** | 2.20 | 0.05 | 0.74 | 425.00 | 0.89 | -0.03 |
| **M-2** | 3.15 | 0.57 | 0.87 | 83.06 | 0.70 | -0.09 |
| **M-3** | 3.22 | 0.49 | 0.87 | 183.10 | 0.91 | 0.03 |
| **M-4** | 4.72 | 0.26 | 0.84 | 439.20 | 0.93 | 0.03 |
| **M-5** | 4.14 | 0.46 | 0.59 | 77.70 | 0.86 | 0.12 |
| **P-1** | 0.76 | 0.05 | 0.78 | 773.00 | 0.90 | 0.02 |
| **M-6** | 4.69 | 0.77 | 0.89 | 118.75 | 0.89 | 0.10 |
| **M-7** | 1.27 | 0.27 | 0.31 | 798.50 | 0.95 | 0.12 |
| **M-8** | 2.65 | 0.55 | 0.88 | 340.20 | 0.92 | 0.10 |

*Linear correlations of EVR range to other influences*

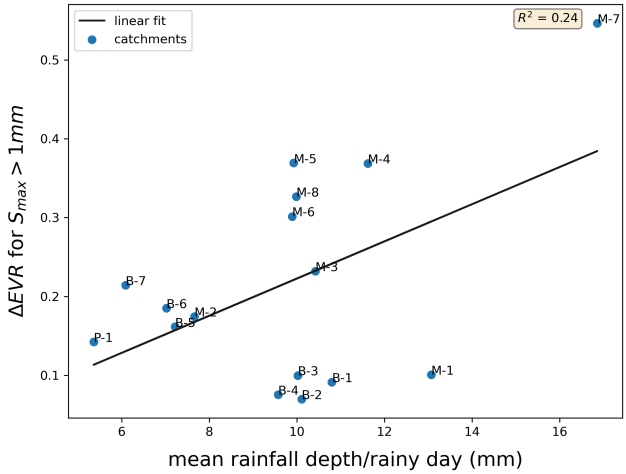


(a) correlation between mean rainfall depth and EVR range

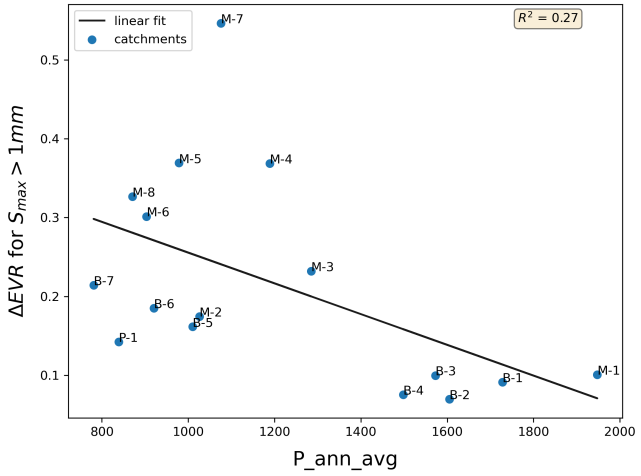


(b) correlation between mean annual rainfall and EVR range

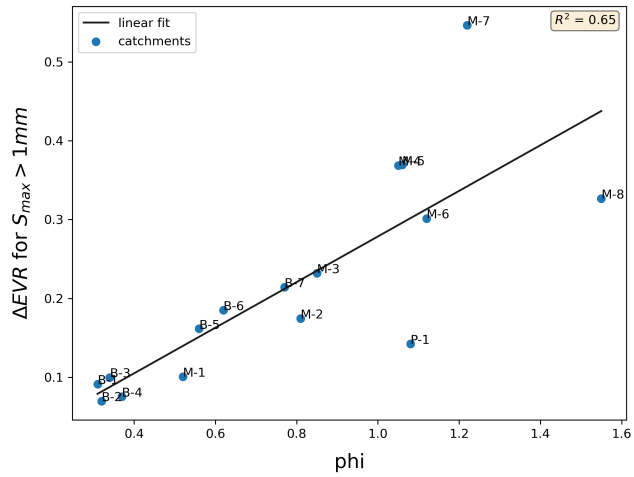


(c) correlation between dryness index $\phi$ and EVR range

Figure A.7: correlations between EVR range and other influences

# BIBLIOGRAPHY


ANA, Autoridad Nacional del Agua (2017). *National GIS Database*.

Abatzoglou, John T. and Darren L. Ficklin (2017). "Climatic and physiographic controls of spatial variability in surface water balance over the contiguous United States using the Budyko relationship." en. In: *Water Resources Research* 53.9, pp. 7630–7643. DOI: https://doi.org/10.1002/2017WR020843.

AghaKouchak, Amir, András Bárdossy, and Emad Habib (June 2010). "Conditional simulation of remotely sensed rainfall data using a non-Gaussian v-transformed copula." en. In: *Advances in Water Resources* 33.6, pp. 624–634. DOI: 10.1016/j.advwatres.2010.02.010.

Alcamo, Lucas (2019). "Regionalization of Precipitation in the Sparsely Gauged Western Slopes of the Peruvian Andes." MA thesis. Institute KIT-IWG (Chair of Hydrology): Karlsruhe Institute of Technology (KIT).

Allen, R. G., ed. (1998). *Crop evapotranspiration: guidelines for computing crop water requirements*. en. FAO irrigation and drainage paper 56. Rome: Food and Agriculture Organization of the United Nations.

Anagnostou, Emmanouil N. (Nov. 2004). "Overview of Overland Satellite Rainfall Estimation for Hydro-Meteorological Applications." en. In: *Surveys in Geophysics* 25.5, pp. 511–537. DOI: 10.1007/s10712-004-5724-6.

Andréassian, Vazken, Ülo Mander, and Taavi Pae (Apr. 2016). "The Budyko hypothesis before Budyko: The hydrological legacy of Evald Oldekop." en. In: *Journal of Hydrology* 535, pp. 386–391. DOI: 10.1016/j.jhydrol.2016.02.002.

Arnaud, Patrick et al. (Mar. 2002). "Influence of rainfall spatial variability on flood prediction." en. In: *Journal of Hydrology* 260.1, pp. 216–230. DOI: 10.1016/S0022-1694(01)00611-4.

Aybar, Cesar et al. (Apr. 2020). "Construction of a high-resolution gridded rainfall dataset for Peru from 1981 to the present day." In: *Hydrological Sciences Journal* 65.5. Publisher: Taylor & Francis _eprint: https://doi.org/10.1080/02626667.2019.1649411, pp. 770–785. DOI: 10.1080/02626667.2019.1649411.

Bai, Peng et al. (2020). "Estimation of the Budyko model parameter for small basins in China." en. In: *Hydrological Processes* 34.1, pp. 125–138. DOI: https://doi.org/10.1002/hyp.13577.

Beck, Hylke E. et al. (2016). "Global-scale regionalization of hydrologic model parameters." en. In: *Water Resources Research* 52.5, pp. 3599–3622. DOI: https://doi.org/10.1002/2015WR018247.

Berghuijs, W. R., R. A. Woods, and M. Hrachowitz (July 2014a). "A precipitation shift from snow towards rain leads to a decrease in streamflow." en. In: *Nature Climate Change* 4.7. Number: 7 Publisher: Nature Publishing Group, pp. 583–586. DOI: 10.1038/nclimate2246.

Berghuijs, Wouter R., Sebastian J. Gnann, and Ross A. Woods (2020). "Unanswered questions on the Budyko framework." en. In: *Hydrological Processes* 34.26, pp. 5699–5703. DOI: 10.1002/hyp.13958.

Berghuijs, Wouter R. et al. (2014b). "Patterns of similarity of seasonal water balances: A window into streamflow variability over a range of time scales." en. In: *Water Resources Research* 50.7, pp. 5638–5661. DOI: https://doi.org/10.1002/2014WR015692.

Berkowitz, Brian and Erwin Zehe (Apr. 2020). "Surface water and groundwater: unifying conceptualization and quantification of the two "water worlds"." English. In: *Hydrology and Earth System Sciences* 24.4. Publisher: Copernicus GmbH, pp. 1831–1858. DOI: 10.5194/hess-24-1831-2020.

Bernex, N., J. Apaéstegui, and P. Fluquer (2017). *El Agua en el Perú: Situación y Perspectivas*. Tech. rep.

Beven, Keith (Apr. 1996). "The limits of splitting: Hydrology." en. In: *Science of The Total Environment*. Modelling in Environmental Studies 183.1, pp. 89–97. DOI: 10.1016/0048-9697(95)04964-9.

Beven, Keith and Andrew Binley (1992). "The future of distributed models: Model calibration and uncertainty prediction." en. In: *Hydrological Processes* 6.3, pp. 279–298. DOI: 10.1002/hyp.3360060305.

Blöschl, G. and M. Sivapalan (1995). "Scale issues in hydrological modelling: A review." en. In: *Hydrological Processes* 9.3-4. _eprint: https://onlinelibrary.wiley.com/doi/pdf/10.1002/hyp.3360090305, pp. 251–290. DOI: 10.1002/hyp.3360090305.

Blöschl, Günter et al., eds. (2013). *Runoff Prediction in Ungauged Basins: Synthesis across Processes, Places and Scales*. Cambridge: Cambridge University Press. DOI: 10.1017/CBO9781139235761.

Bondy, Jan et al. (Mar. 2021). "Exploring the role of soil storage capacity for explaining deviations from the Budyko curve using a simple water balance model." English. In: *Hydrology and Earth System Sciences Discussions*, pp. 1–24. DOI: 10.5194/hess-2021-174.

Booij, M. J. (Mar. 2005). "Impact of climate change on river flooding assessed with different spatial model resolutions." en. In: *Journal of Hydrology* 303.1, pp. 176–198. DOI: 10.1016/j.jhydrol.2004.07.013.

Borsdorf, Axel (Jan. 1978). "Population growth and urbanization in Latin America." en. In: *GeoJournal* 2.1, pp. 47–60. DOI: 10.1007/BF00212577.

Brooks, Royal Harvard (1965). "Hydraulic Properties of Porous Media." Englisch. ISBN: 9781084094253. Ph.D. Ann Arbor, United States.

Budyko, M. I. (1974). *Climate and Life*. en. Accepted: 2019-02-14T10:36:35Z. Academic Press, Inc.

Buytaert, Wouter and Keith Beven (2009). "Regionalization as a learning process." en. In: *Water Resources Research* 45.11. _eprint: https://onlinelibrary.wiley.com/doi/pdf/10.1029/2008WR007359. DOI: 10.1029/2008WR007359.

Buytaert, Wouter et al. (Oct. 2006). "Spatial and temporal rainfall variability in mountainous areas: A case study from the south Ecuadorian Andes." en. In: *Journal of Hydrology* 329.3, pp. 413–421. DOI: 10.1016/j.jhydrol.2006.02.031.

Choudhury, BhaskarJ. (Mar. 1999). "Evaluation of an empirical equation for annual evaporation using field observations and results from a biophysical model." en. In: *Journal of Hydrology* 216.1, pp. 99–110. DOI: 10.1016/S0022-1694(98)00293-5.

DWD (Mar. 2020a). "DWD Climate Data Center (CDC), REGNIE-Raster der täglichen Niederschlagshöhe für Deutschland." In.

DWD (Mar. 2020b). "DWD Climate Data Center (CDC): Tägliche Raster der potentiellen Evapotranspiration über Gras, Version 0.x." In.

Daly, Christopher, Ronald P. Neilson, and Donald L. Phillips (Feb. 1994). "A Statistical-Topographic Model for Mapping Climatological Precipitation over Mountainous Terrain." EN. In: *Journal of Applied Meteorology and Climatology* 33.2. Publisher: American Meteorological Society Section: Journal of Applied Meteorology and Climatology, pp. 140–158. DOI: 10.1175/1520-0450(1994)033<0140:ASTMFM>2.0.CO;2.

Daly, Edoardo et al. (2019). "Hydrological Spaces of Long-Term Catchment Water Balance." en. In: *Water Resources Research* 55.12, pp. 10747–10764. DOI: https://doi.org/10.1029/2019WR025952.

Das, Tapash et al. (July 2008). "Comparison of conceptual model performance using different representations of spatial variability." en. In: *Journal of Hydrology* 356.1, pp. 106–118. DOI: 10.1016/j.jhydrol.2008.04.008.

Dirks, K. N. et al. (July 1998). "High-resolution studies of rainfall on Norfolk Island. Part II: Interpolation of rainfall data." In: *Journal of Hydrology* 208. ADS Bibcode: 1998JHyd..208..187D, pp. 187–193. DOI: 10.1016/S0022-1694(98)00155-3.

Donohue, Randall, Michael Roderick, and Tim R. McVicar (2007). "On the importance of including vegetation dynamics in Budyko's hydrological model." en. In: *Hydrology and Earth System Sciences*. Accepted: 2015-12-10T21:56:23Z Last Modified: 2020-05-19 Publisher: Copernicus GmbH.

Duan, Q. et al. (Mar. 2006). "Model Parameter Estimation Experiment (MOPEX): An overview of science strategy and major results from the second and third workshops." en. In: *Journal of Hydrology*. The model parameter estimation experiment 320.1, pp. 3–17. DOI: 10.1016/j.jhydrol.2005.07.031.

Duan, Qingyun, Soroosh Sorooshian, and Vijai K. Gupta (June 1994). "Optimal use of the SCE-UA global optimization method for calibrating watershed models." en. In: *Journal of Hydrology* 158.3, pp. 265–284. DOI: 10.1016/0022-1694(94)90057-4.

Eakin, Thomas E. (1966). "A regional interbasin groundwater system in the White River Area, southeastern Nevada." en. In: *Water Resources Research* 2.2, pp. 251–271. DOI: https://doi.org/10.1029/WR002i002p00251.

Ehret, U. et al. (2014). "Advancing catchment hydrology to deal with predictions under change." In: *Hydrology and Earth System Sciences* 18.2. Publisher: European Geosciences Union, pp. 649–671. DOI: 10.5194/hess-18-649-2014.

Follett, Ronald et al. (Jan. 2011). *Carbon sequestration and greenhouse gas fluxes in agriculture: challenges and opportunities*.

Friedrich, Katja et al. (Jan. 2018). "Reservoir Evaporation in the Western United States: Current Science, Challenges, and Future Needs." EN. In: *Bulletin of the American Meteorological Society* 99.1. Publisher: American Meteorological Society Section: Bulletin of the American Meteorological Society, pp. 167–187. DOI: 10.1175/BAMS-D-15-00224.1.

Fu, Baopu (1981). "On the calculation of the evaporation from land surface." In: *Atmos. Sin.* 5, pp. 23–31.

Fu, Jianyu and Weiguang Wang (Mar. 2019). "On the lower bound of Budyko curve: The influence of precipitation seasonality." en. In: *Journal of Hydrology* 570, pp. 292–303. DOI: 10.1016/j.jhydrol.2018.12.062.

Garreaud, R. D. (Oct. 2009). "The Andes climate and weather." English. In: *Advances in Geosciences*. Vol. 22. ISSN: 1680-7340. Copernicus GmbH, pp. 3–11. DOI: 10.5194/adgeo-22-3-2009.

Gentine, Pierre et al. (2012). "Interdependence of climate, soil, and vegetation as constrained by the Budyko curve." en. In: *Geophysical Research Letters* 39.19. DOI: 10.1029/2012GL053492.

German Aerospace Center (DLR) (2016). *TanDEM-X - Digital Elevation Model (DEM) - Global, 12m*.

Gharari, S. et al. (Dec. 2014). "Using expert knowledge to increase realism in environmental system models can dramatically reduce the need for calibration." en. In: *Hydrology and Earth System Sciences* 18.12, pp. 4839–4859. DOI: 10.5194/hess-18-4839-2014.

Goswami, Monomoy and Kieran M. O'Connor (Aug. 2010). "A "monster" that made the SMAR conceptual model "right for the wrong reasons"." In: *Hydrological Sciences Journal* 55.6. Publisher: Taylor & Francis _eprint: https://doi.org/10.1080/02626667.2010.505170, pp. 913–927. DOI: 10.1080/02626667.2010.505170.

Granger, R. J. (Jan. 1989). "An examination of the concept of potential evaporation." en. In: *Journal of Hydrology* 111.1, pp. 9–19. DOI: 10.1016/0022-1694(89)90248-5.

Gupta, Hoshin V. et al. (Oct. 2009). "Decomposition of the mean squared error and NSE performance criteria: Implications for improving hydrological modelling." en. In: *Journal of Hydrology* 377.1, pp. 80–91. DOI: 10.1016/j.jhydrol.2009.08.003.

Haberlandt, Uwe (Jan. 2007). "Geostatistical interpolation of hourly precipitation from rain gauges and radar for a large-scale extreme rainfall event." en. In: *Journal of Hydrology* 332.1, pp. 144–157. DOI: 10.1016/j.jhydrol.2006.06.028.

Hall, D. K. and G. A. Riggs (2021). *MODIS/Aqua Snow Cover Daily L3 Global 500m Grid, Version 61*. Type: dataset. DOI: 10.5067/MODIS/MOD10A1.061.

Harman, C. and P. A. Troch (Feb. 2014). "What makes Darwinian hydrology "Darwinian"? Asking a different kind of question about landscapes." en. In: *Hydrology and Earth System Sciences* 18.2, pp. 417–433. DOI: 10.5194/hess-18-417-2014.

Hartmann, Anne, Markus Weiler, and Theresa Blume (Dec. 2020). "The impact of landscape evolution on soil physics: evolution of soil physical and hydraulic properties along two chronosequences of proglacial moraines." English. In: *Earth System Science Data* 12.4. Publisher: Copernicus GmbH, pp. 3189–3204. DOI: https://doi.org/10.5194/essd-12-3189-2020.

Heistermann, Maik and David Kneis (2011). "Benchmarking quantitative precipitation estimation by conceptual rainfall-runoff modeling." en. In: *Water Resources Research* 47.6. DOI: 10.1029/2010WR009153.

Herrera, Sixto et al. (2019). "Uncertainty in gridded precipitation products: Influence of station density, interpolation method and grid resolution." en. In: *International Journal of Climatology* 39.9. _eprint: https://onlinelibrary.wiley.com/doi/pdf/10.1002/joc.5878, pp. 3717–3729. DOI: 10.1002/joc.5878.

Hornberger, George M. et al. (Aug. 2014). *Elements of Physical Hydrology*. en. Google-Books-ID: gnoZBQAAQBAJ. JHU Press.

Hu, Qingfang et al. (Mar. 2019). "Rainfall Spatial Estimations: A Review from Spatial Interpolation to Multi-Source Data Merging." en. In: *Water* 11.3. Number: 3 Publisher: Multidisciplinary Digital Publishing Institute, p. 579. DOI: 10.3390/w11030579.

Hundecha, Yeshewatesfa and András Bárdossy (June 2004). "Modeling of the effect of land use changes on the runoff generation of a river basin through parameter regionalization of a watershed model." en. In: *Journal of Hydrology* 292.1, pp. 281–295. DOI: 10.1016/j.jhydrol.2004.01.002.

Höllering, Simon et al. (Jan. 2018). "Regional analysis of parameter sensitivity for simulation of streamflow and hydrological fingerprints." English. In: *Hydrology and Earth System Sciences* 22.1. Publisher: Copernicus GmbH, pp. 203–220. DOI: 10.5194/hess-22-203-2018.

INRENA (Aug. 2004). "Estudio hidrológico de la cuenca del río Lurín: Informe final." spa. In: *Autoridad Nacional del Agua*. Accepted: 2017-11-22T04:59:04Z Publisher: INRENA.

Kirchner, James W. (2009). "Catchments as simple dynamical systems: Catchment characterization, rainfall-runoff modeling, and doing hydrology backward." en. In: *Water Resources Research* 45.2. _eprint: https://onlinelibrary.wiley.com/doi/pdf/10.1029/2008WR006912. DOI: 10.1029/2008WR006912.

Kleidon, A. and S. Schymanski (2008). "Thermodynamics and optimality of the water budget on land: A review." en. In: *Geophysical Research Letters* 35.20. DOI: https://doi.org/10.1029/2008GL035393.

Kneis, David and Maik Heistermann (Jan. 2009). "Bewertung der Güte einer Radar-basierten Niederschlagsschätzung am Beispiel eines kleinen Einzugsgebiets." In: *Hydrologie und Wasserbewirtschaftung* 53. Jahrgang, Heft 3, pp. 160–171.

Koster, Randal D. and Max J. Suarez (July 1999). "A Simple Framework for Examining the Interannual Variability of Land Surface Moisture Fluxes." en. In: *Journal of Climate* 12.7. Publisher: American Meteorological Society, pp. 1911–1917. DOI: 10.1175/1520-0442(1999)012<1911:ASFFET>2.0.CO;2.

Kumar, Rohini (2010). "Distributed hydrologic model parameterization: application in a mesoscale river basin." PhD thesis. Helmholtz-Zentrum für Umweltforschung GmbH-UFZ.

Köppen, W (1936). "Das geographische System der Klimate." de. In: p. 44.

LUBW (2020). *Pegel-und Datendienst*.

Lavado Casimiro, Waldo Sven et al. (May 2012). "Basin-scale analysis of rainfall and runoff in Peru (1969–2004): Pacific, Titicaca and Amazonas drainages." In: *Hydrological Sciences Journal* 57.4, pp. 625–642. DOI: 10.1080/02626667.2012.672985.

Lavenne, Alban de and Vazken Andréassian (Mar. 2018). "Impact of climate seasonality on catchment yield: A parameterization for commonly-used water balance formulas." en. In: *Journal of Hydrology* 558, pp. 266–274. DOI: 10.1016/j.jhydrol.2018.01.009.

Leon, Christian D. et al. (2021). *Integrated water management solutions in the Lurín Catchment, Lima, Peru : supporting United Nations' Sustainable Development Goal 6 : final report of the joint project TRUST*. en. report. Accepted: 2021-04-06T16:19:24Z ISBN: 9783000684982. DOI: 10.18419/opus-11390.

Li, Changbin et al. (Apr. 2018). "An analytical approach to separate climate and human contributions to basin streamflow variability." en. In: *Journal of Hydrology* 559, pp. 30–42. DOI: 10.1016/j.jhydrol.2018.02.019.

Lindström, Göran et al. (Dec. 1997). "Development and test of the distributed HBV-96 hydrological model." en. In: *Journal of Hydrology* 201.1-4, pp. 272–288. DOI: 10.1016/S0022-1694(97)00041-3.

Llauca, Harold et al. (Jan. 2021). "PISCO_HyM_GR2M: A Model of Monthly Water Balance in Peru (1981–2020)." en. In: *Water* 13.8. Number: 8 Publisher: Multidisciplinary Digital Publishing Institute, p. 1048. DOI: 10.3390/w13081048.

Lvovich, M. I. (Sept. 1979). "World water resources, present and future." en. In: *GeoJournal* 3.5, pp. 423–433. DOI: 10.1007/BF00455981.

Ly, S., C. Charles, and A. Degré (July 2011). "Geostatistical interpolation of daily rainfall at catchment scale: the use of several variogram models in the Ourthe and Ambleve catchments, Belgium." English. In: *Hydrology and Earth System Sciences* 15.7, pp. 2259–2274. DOI: 10.5194/hess-15-2259-2011.

Ly, Sarann, Catherine Charles, and Aurore Degré (2013). "Different methods for spatial interpolation of rainfall data for operational hydrology and hydrological modeling at watershed scale: a review." en. In: *Biotechnologie, Agronomie, Société et Environnement* 17.2. Publisher: Presses Agronomiques de Gembloux.

López-Urrea, R. et al. (Sept. 2006). "Testing evapotranspiration equations using lysimeter observations in a semiarid climate." en. In: *Agricultural Water Management* 85.1, pp. 15–26. DOI: 10.1016/j.agwat.2006.03.014.

Marcotte, Denis (July 1995). "Generalized cross-validation for covariance model selection." en. In: *Mathematical Geology* 27.5, pp. 659–672. DOI: 10.1007/BF02093906.

Marsily, Ghislain de (2009). *L'eau, un tresor en partage*. fr. Dunod Paris.

Masson-Delmotte, V. et al. (2021). *Climate Change 2021: The Physical Science Basis. Contribution of Working Group I to the Sixth Assessment Report of the Intergovernmental Panel on Climate Change*. Tech. rep. Cambridge University Press: IPCC.

Matheron, Georges, Fernand Blondel, and Bureau de recherches géologiques et minières (France) (1962). *Traité de géostatistique appliquée. Tome I*. French. OCLC: 491866302. Paris: Technip.

McMahon, T. A. et al. (Apr. 2013). "Estimating actual, potential, reference crop and pan evaporation using standard meteorological data: a pragmatic synthesis." English. In: *Hydrology and Earth System Sciences* 17.4. Publisher: Copernicus GmbH, pp. 1331–1363. DOI: 10.5194/hess-17-1331-2013.

Meira Neto, Antônio Alves et al. (Dec. 2020). "Interactions between snow cover and evaporation lead to higher sensitivity of streamflow to temperature." en. In: *Communications Earth & Environment* 1.1. Bandiera_abtest: a Cc_license_type: cc_by Cg_type: Nature Research Journals Number: 1 Primary_atype: Research Publisher: Nature Publishing Group Subject_term: Envi-

ronmental sciences;Hydrology Subject_term_id: environmental-sciences;hydrology, pp. 1–7. DOI: 10.1038/s43247-020-00056-9.

Mezentsev, V. (1955). "Back to the computation of total evaporation." In: *Meteorologia i Gidrologia – Meneopokoubz b Ublpokoubz* 5,

Milly, P. C. D. (1993). "An analytic solution of the stochastic storage problem applicable to soil water." en. In: *Water Resources Research* 29.11, pp. 3755–3758. DOI: 10.1029/93WR01934.

Milly, P. C. D. (1994). "Climate, soil water storage, and the average annual water balance." en. In: *Water Resources Research* 30.7, pp. 2143–2156. DOI: 10.1029/94WR00586.

Milly, P. C. D. and K. A. Dunne (Apr. 1994). "Sensitivity of the Global Water Cycle to the Water-Holding Capacity of Land." EN. In: *Journal of Climate* 7.4. Publisher: American Meteorological Society Section: Journal of Climate, pp. 506–526. DOI: 10.1175/1520-0442(1994)007<0506:SOTGWC>2.0.CO;2.

Milly, P. C. D. et al. (Feb. 2008). "Stationarity Is Dead: Whither Water Management?" en. In: *Science* 319.5863, pp. 573–574. DOI: 10.1126/science.1151915.

Monteith, J L (Jan. 1965). "Evaporation and environment." eng. In: *Symposia of the Society for Experimental Biology* 19, pp. 205–234.

Muggeo, Vito M. R. (2003). "Estimating regression models with unknown break-points." en. In: *Statistics in Medicine* 22.19, pp. 3055–3071. DOI: 10.1002/sim.1545.

Myneni, Ranga, Yuri Knyazikhin, and Taejin Park (2015). *MOD15A2H MODIS/Terra Leaf Area Index/FPAR 8-Day L4 Global 500m SIN Grid V006*. Type: dataset. DOI: 10.5067/MODIS/MOD15A2H.006.

NASA (2001). "ASTER DEM Product." In: *2001* NASA/METI/AIST/-Japan Spacesystems and U.S./Japan ASTER Science Team.distributed by NASA EOSDIS Land Processes DAAC.

Nash, J. E. and J. V. Sutcliffe (Apr. 1970). "River flow forecasting through conceptual models part I — A discussion of principles." en. In: *Journal of Hydrology* 10.3, pp. 282–290. DOI: 10.1016/0022-1694(70)90255-6.

Observatorio del Agua (2017). *GIS data collection*. (various contributing state authorities).

Observatorio del Agua (Sept. 2018). *Estado situacional de los recursos hídricos en las cuencas Chillón, Rímac y Lurín 2016/2017*. spa. Tech. rep. Accepted: 2019-06-01T16:05:55Z Publisher: Autoridad Nacional del Agua.

Observatorio del Agua (2019). *Diagnóstico inicial para el Plan de gestión de recursos hídricos en el ámbito de las cuencas Chillón, Rímac, Lurín y Chilca*. spa. Tech. rep. Accepted: 2020-02-29T21:50:11Z Publisher: Autoridad Nacional del Agua.

Ochoa-Tocachi, Boris F. et al. (July 2019). "Potential contributions of pre-Inca infiltration infrastructure to Andean water security." en.

In: *Nature Sustainability* 2.7, pp. 584–593. DOI: 10.1038/s41893-019-0307-1.

Oezgür, Selin (2020). "Comparison of performance/applicability of potential evapotranspiration models in semi-arid Peruvian Andes." Study project. Institute KIT-IWG (Chair of Hydrology): Karlsruhe Institute of Technology (KIT).

Ol'dekop, E.M. (1911). "On Evaporation From the Surface of River Basins." (in Russian). In: *Lur'evskogo Univ., Tartu, Estonia* Collection of the Works of Students of the Meteorological Observatory.

Osuch, Marzena (2015). "Sensitivity and Uncertainty Analysis of Precipitation-Runoff Models for the Middle Vistula Basin." en. In: *Stochastic Flood Forecasting System: The Middle River Vistula Case Study*. Ed. by Renata J. Romanowicz and Marzena Osuch. GeoPlanet: Earth and Planetary Sciences. Cham: Springer International Publishing, pp. 61–81. DOI: 10.1007/978-3-319-18854-6_5.

Osuch, Marzena, Renata J. Romanowicz, and Martijn J. Booij (Aug. 2015). "The influence of parametric uncertainty on the relationships between HBV model parameters and climatic characteristics." In: *Hydrological Sciences Journal* 60.7-8. Publisher: Taylor & Francis _eprint: https://doi.org/10.1080/02626667.2014.967694, pp. 1299–1316. DOI: 10.1080/02626667.2014.967694.

Padrón, Ryan S. et al. (2017). "Large-Scale Controls of the Surface Water Balance Over Land: Insights From a Systematic Review and Meta-Analysis." en. In: *Water Resources Research* 53.11, pp. 9659–9678. DOI: https://doi.org/10.1002/2017WR021215.

Pareja Dominguez, Marco Antonio, Henry Douglas Pascual Figueroa, and Marisa Rosana Silva Dávila (2022). "Evaluation of the Effectiveness of Flexible Debris Flow Barriers for Control of Huaycos Using Satellite Images and GIS, in the Basin of Rímac River, Perú." en. In: *Geohazard Mitigation*. Ed. by Basanta Raj Adhikari and Sreevalsa Kolathayar. Lecture Notes in Civil Engineering. Singapore: Springer, pp. 29–41. DOI: 10.1007/978-981-16-6140-2_4.

Patil, S. and M. Stieglitz (Feb. 2012). "Controls on hydrologic similarity: role of nearby gauged catchments for prediction at an ungauged catchment." English. In: *Hydrology and Earth System Sciences* 16.2. Publisher: Copernicus GmbH, pp. 551–562. DOI: 10.5194/hess-16-551-2012.

Piotrowski, Adam P. et al. (Mar. 2017). "Are modern metaheuristics successful in calibrating simple conceptual rainfall–runoff models?" In: *Hydrological Sciences Journal* 62.4, pp. 606–625. DOI: 10.1080/02626667.2016.1234712.

Poggio, Laura et al. (June 2021). "SoilGrids 2.0: producing soil information for the globe with quantified spatial uncertainty." en. In: *SOIL* 7.1, pp. 217–240. DOI: 10.5194/soil-7-217-2021.

Porada, P., A. Kleidon, and S. J. Schymanski (Sept. 2011). "Entropy production of soil hydrological processes and its maximisation."

English. In: *Earth System Dynamics* 2.2. Publisher: Copernicus GmbH, pp. 179–190. DOI: https://doi.org/10.5194/esd-2-179-2011.

Potter, N. J. et al. (2005). "Effects of rainfall seasonality and soil moisture capacity on mean annual water balance for Australian catchments." en. In: *Water Resources Research* 41.6. DOI: https://doi.org/10.1029/2004WR003697.

Prosser, Ian, Leif Wolf, and Anna Littleboy (2011). "Water in mining and industry." en. In: *CSIRO Publishing* Chapter 10, p. 12.

Ramírez, Ivan J. and Fernando Briones (Dec. 2017). "Understanding the El Niño Costero of 2017: The Definition Problem and Challenges of Climate Forecasting and Disaster Responses." en. In: *International Journal of Disaster Risk Science* 8.4, pp. 489–492. DOI: 10.1007/s13753-017-0151-8.

Reaver, Nathan G. F. et al. (Mar. 2022). "Theoretical and empirical evidence against the Budyko catchment trajectory conjecture." English. In: *Hydrology and Earth System Sciences* 26.5. Publisher: Copernicus GmbH, pp. 1507–1525. DOI: 10.5194/hess-26-1507-2022.

Rinaldi, Massimo et al. (Oct. 2015). *Thematic Annexes on monitoring indicators and models, Deliverable 6.2, Part 2, of REFORM (REstoring rivers FOR effective catchment Management), a Collaborative project (large-scale integrating project) funded by the European Commission within the 7th Framework Programme under Grant Agreement 282656*.

Roderick, Michael L. and Graham D. Farquhar (2011). "A simple framework for relating variations in runoff to variations in climatic conditions and catchment properties." en. In: *Water Resources Research* 47.12. DOI: 10.1029/2010WR009826.

Rome-Gaspaldy, Sandra and Josyane Ronchail (1998). "La pluviométrie au Pérou pendant les phases ENSO et LNSO." In: *Bulletin de l'Institut français d'études andines*.

SENAMHI (2019). *Datos hidrometeorológicos*.

SENAMHI (2020). *SENAMHI HSR PISCO Streamflow v1 stable*.

Samani, Zohrab (July 2000). "Estimating Solar Radiation and Evapotranspiration Using Minimum Climatological Data." EN. In: *Journal of Irrigation and Drainage Engineering* 126.4. Publisher: American Society of Civil Engineers, pp. 265–267. DOI: 10.1061/(ASCE)0733-9437(2000)126:4(265).

Samaniego, Luis, Rohini Kumar, and Sabine Attinger (2010). "Multiscale parameter regionalization of a grid-based hydrologic model at the mesoscale." en. In: *Water Resources Research* 46.5. _eprint: https://onlinelibrary.wiley.com/doi/pdf/10.1029/2008WR007327. DOI: 10.1029/2008WR007327.

Samaniego, Luis et al. (2019). *The mesoscale Hydrological Model (mHM) Documentation v5.10*. Tech. rep. https://git.ufz.de/mhm/mhm: Centre for Environmental Research (UFZ).

Sanabria, Janeet Margarita (Apr. 2018). "Interannual variability of the rainfall regime and strong ENSO events along the Peruvian Pacific Basin : large-scale control mechanisms." en. PhD thesis. Université Paul Sabatier - Toulouse III.

Sanchez, Daves (Nov. 2016). *AquaFondo - Estudio de riesgos hídricos y vulnerabilidad del sector privado en Lima Metropolitana y Callao en un contexto de Cambio Climático*. es.

Schaefli, B. et al. (Feb. 2011). "HESS Opinions: Hydrologic predictions in a changing environment: behavioral modeling." English. In: *Hydrology and Earth System Sciences* 15.2. Publisher: Copernicus GmbH, pp. 635–646. DOI: https://doi.org/10.5194/hess-15-635-2011.

Schreiber, P. (1904). "Über die Beziehungen zwischen dem Niederschlag und der Wasserführung der Flüsse in Mitteleuropa." In: *Z. Meterol.* 21.10, pp. 441–452.

Segond, Marie-Laure, Howard S. Wheater, and Christian Onof (Dec. 2007). "The significance of spatial rainfall representation for flood runoff estimation: A numerical evaluation based on the Lee catchment, UK." en. In: *Journal of Hydrology* 347.1, pp. 116–131. DOI: 10.1016/j.jhydrol.2007.09.040.

Seibert, Jan (Dec. 1999). "Regionalisation of parameters for a conceptual rainfall-runoff model." en. In: *Agricultural and Forest Meteorology* 98-99, pp. 279–293. DOI: 10.1016/S0168-1923(99)00105-7.

Shahidian, S. et al. (2013). "Parametric calibration of the Hargreaves–Samani equation for use at new locations." en. In: *Hydrological Processes* 27.4, pp. 605–616. DOI: 10.1002/hyp.9277.

Singh, R., S. A. Archfield, and T. Wagener (Sept. 2014). "Identifying dominant controls on hydrologic parameter transfer from gauged to ungauged catchments – A comparative hydrology approach." en. In: *Journal of Hydrology* 517, pp. 985–996. DOI: 10.1016/j.jhydrol.2014.06.030.

Sivapalan, Murugesu (2003). "Prediction in ungauged basins: a grand challenge for theoretical hydrology." en. In: *Hydrological Processes* 17.15, pp. 3163–3170. DOI: https://doi.org/10.1002/hyp.5155.

Son, Rackhun et al. (Jan. 2020). "Climate diagnostics of the extreme floods in Peru during early 2017." en. In: *Climate Dynamics* 54.1, pp. 935–945. DOI: 10.1007/s00382-019-05038-y.

Sposito, Garrison (Sept. 2017a). "Incorporating the Vadose Zone into the Budyko Framework." en. In: *Water* 9.9. Number: 9 Publisher: Multidisciplinary Digital Publishing Institute, p. 698. DOI: 10.3390/w9090698.

Sposito, Garrison (Apr. 2017b). "Understanding the Budyko Equation." en. In: *Water* 9.4. Number: 4 Publisher: Multidisciplinary Digital Publishing Institute, p. 236. DOI: 10.3390/w9040236.

Takahashi, Ken (Apr. 2017). "Fenómeno El Niño: "Global" vs "Costero"." spa. In: Accepted: 2022-02-21T10:18:54Z Publisher: Instituto Geofísico del Perú.

Tapley, Thomas D. and Peter R. Waylen (Aug. 1990). "Spatial variability of annual precipitation and ENSO events in western Peru." In: *Hydrological Sciences Journal* 35.4. Publisher: Taylor & Francis _eprint: https://doi.org/10.1080/02626669009492444, pp. 429–446. DOI: 10.1080/02626669009492444.

Thornthwaite, C. Warren (1931). "The Climates of North America: According to a New Classification." In: *Geographical Review* 21.4. Publisher: [American Geographical Society, Wiley], pp. 633–655. DOI: 10.2307/209372.

Tixeront, J. (1964). "Prévision des apports des cours d'eau (Streamflow prediction)." In: *IAHS publication n°63: General Assembly of Berkeley*.

Trabucco, Antonio and Robert J Zomer (Nov. 2018). *Global Aridity Index and Potential Evapo-Transpiration (ETo) Climate Database v2*. en. Tech. rep. Published online, available from the CGIAR-CSI GeoPortal: CGIAR Consortium for Spatial Information (CGIAR-CSI), p. 10.

Trachte, Katja et al. (Mar. 2018). "Cross-Scale Precipitation Variability in a Semiarid Catchment Area on the Western Slopes of the Central Andes." EN. In: *Journal of Applied Meteorology and Climatology* 57.3. Publisher: American Meteorological Society Section: Journal of Applied Meteorology and Climatology, pp. 675–694. DOI: 10.1175/JAMC-D-17-0207.1.

Trajkovic, Slavisa (Feb. 2007). "Hargreaves versus Penman-Monteith under Humid Conditions." EN. In: *Journal of Irrigation and Drainage Engineering* 133.1. Publisher: American Society of Civil Engineers, pp. 38–42. DOI: 10.1061/(ASCE)0733-9437(2007)133:1(38).

Troch, Peter A. et al. (2015). "Catchment coevolution: A useful framework for improving predictions of hydrological change?" en. In: *Water Resources Research* 51.7, pp. 4903–4922. DOI: 10.1002/2015WR017032.

Turc, L. (1954). "The water balance of soils: relationship between precipitations, evaporation and flow (Le bilan d'eau des sols: relation entre les précipitations, l'évaporation et l'écoulement)." In: *Annales Agronomiques* Série A (5), 491–595.

UCL (2021). *Introduction to climate dynamics and climate modelling - The hydrological cycle*.

UNESCO (2012). "Managing water under uncertainty and risk: World Water Development report, 4 (WWDR4)." In: Accepted: 2019-04-05T04:08:21Z Publisher: UNESCO.

Uhlenbrook, S., Y. Mohamed, and A. S. Gragne (Oct. 2010). "Analyzing catchment behavior through catchment modeling in the Gilgel Abay, Upper Blue Nile River Basin, Ethiopia." English. In: *Hydrology and Earth System Sciences* 14.10. Publisher: Copernicus

GmbH, pp. 2153–2165. DOI: https://doi.org/10.5194/hess-14-2153-2010.

Uhlenbrook, Stefan et al. (Oct. 1999). "Prediction uncertainty of conceptual rainfall-runoff models caused by problems in identifying model parameters and structure." In: *Hydrological Sciences Journal* 44.5, pp. 779–797. DOI: 10.1080/02626669909492273.

Verworn, A. and U. Haberlandt (Feb. 2011). "Spatial interpolation of hourly rainfall – effect of additional information, variogram inference and storm properties." English. In: *Hydrology and Earth System Sciences* 15.2. Publisher: Copernicus GmbH, pp. 569–584. DOI: 10.5194/hess-15-569-2011.

Wagener, Thorsten et al. (2007). "Catchment Classification and Hydrologic Similarity." en. In: *Geography Compass* 1.4, pp. 901–931. DOI: 10.1111/j.1749-8198.2007.00039.x.

Walsh, R. P. D. and D. M. Lawler (1981). "Rainfall Seasonality: Description, Spatial Patterns and Change Through Time." en. In: *Weather* 36.7, pp. 201–208. DOI: 10.1002/j.1477-8696.1981.tb05400.x.

Wang, Anqi and Dimitri P. Solomatine (Feb. 2018). "Practical experience and framework for sensitivity analysis of hydrological models: six methods, three models, three criteria." English. In: *Hydrology and Earth System Sciences Discussions*. Publisher: Copernicus GmbH, pp. 1–34. DOI: https://doi.org/10.5194/hess-2018-78.

Wang, Dingbao et al. (2015). "A thermodynamic interpretation of Budyko and L'vovich formulations of annual water balance: Proportionality Hypothesis and maximum entropy production." en. In: *Water Resources Research* 51.4, pp. 3007–3016. DOI: https://doi.org/10.1002/2014WR016857.

Westhoff, M. et al. (Jan. 2016). "Does the Budyko curve reflect a maximum-power state of hydrological systems? A backward analysis." English. In: *Hydrology and Earth System Sciences* 20.1. Publisher: Copernicus GmbH, pp. 479–486. DOI: https://doi.org/10.5194/hess-20-479-2016.

Wikipedia (2021a). *Archivo: Peru physical map*.

Wikipedia (2021b). *Archivo: Regiones naturales del Perú*.

Williams, Christopher A. et al. (2012). "Climate and vegetation controls on the surface water balance: Synthesis of evapotranspiration measured across a global network of flux towers." en. In: *Water Resources Research* 48.6. DOI: 10.1029/2011WR011586.

WorldAtlas (Apr. 2018). *Maps of South America*. en.

Yao, Lili et al. (2020). "The Roles of Climate Forcing and Its Variability on Streamflow at Daily, Monthly, Annual, and Long-Term Scales." en. In: *Water Resources Research* 56.7. _eprint: https://onlinelibrary.wiley.com/doi/pdf/10.1029/2020WR027111, e2020WR027111. DOI: 10.1029/2020WR027111.

Zehe, Erwin et al. (Dec. 2005). "Uncertainty of simulated catchment runoff response in the presence of threshold processes: Role of

initial soil moisture and precipitation." en. In: *Journal of Hydrology* 315.1, pp. 183–202. DOI: 10.1016/j.jhydrol.2005.03.038.

# OWN PUBLICATIONS

## FIRST AUTHOR; PEER-REVIEWED INTERNATIONAL PUBLICATIONS

**Bondy, J.**, J. Wienhöfer, L. Pfister, E. Zehe (2021), "Exploring the role of soil storage capacity for explaining deviations from the Budyko curve using a simple water balance model." In: *Hydrology and Earth System Sciences Discussion [preprint]*, https://doi.org/10.5194/hess-2021-174.

## CONFERENCE CONTRIBUTIONS (POSTER)

**Bondy, J.**, S. Schroers, J. Wienhöfer (2018), "TRUST - Sustainable water supply and management in water-scarce regions - the case study of the Lurín River in Lima, Perú", Geophysical Research Abstracts, Vol. 20, EGU2018-16633, Vienna, Austria.

**Bondy, J.**, S. Schroers, J. Wienhöfer (2018), "Hydrological modeling as a basis for water management in semi-arid regions - the case study of the Lurín River in Lima, Perú", Integrated Hydrosystem Modelling Conference, Tübingen, Germany

**Bondy, J.**, S. Schroers, J. Wienhöfer (2018), "Hydrologische Modellierung in semiariden peruanischen Anden mittels Betrachtung hydrologischer Ähnlichkeit benachbarter Einzugsgebiete", Tag der Hydrologie 2019, Karlsruhe, Germany

# DECLARATION

Eidesstattliche Versicherung gemäß §13 Abs. 2 Satz 1 Ziff. 4 der Promotionsordnung des Karlsruher Instituts für Technologie für die Fakultät für Bauingenieur-, Geo- und Umweltwissenschaften:

1. Bei der eingereichten Dissertation zu dem Thema *Catchment water balance in data-scarce environments– what insights does the Budyko framework provide?* handelt es sich um meine eigenständig erbrachte Leistung.
2. Ich habe nur die angegebenen Quellen und Hilfsmittel benutzt und mich keiner unzulässigen Hilfe Dritter bedient. Insbesondere habe ich wörtlich oder sinngemäß aus anderen Werken übernommene Inhalte als solche kenntlich gemacht.
3. Die Arbeit oder Teile davon habe ich bislang nicht an einer Hochschule des In- oder Auslands als Bestandteil einer Prüfungs- oder Qualifikationsleistung vorgelegt.
4. Die Richtigkeit der vorstehenden Erklärungen bestätige ich.
5. Die Bedeutung der eidesstattlichen Versicherung und die strafrechtlichen Folgen einer unrichtigen oder unvollständigen eidesstattlichen Versicherung sind mir bekannt.

Ich versichere an Eides statt, dass ich nach bestem Wissen die reine Wahrheit erklärt und nichts verschwiegen habe.

*Karlsruhe, 2023*

Jan Bondy

## COLOPHON

This document was typeset using the typographical look-and-feel `classicthesis` developed by André Miede. The style was inspired by Robert Bringhurst's seminal book on typography "*The Elements of Typographic Style*". `classicthesis` is available for both LaTeX and LyX:

https://bitbucket.org/amiede/classicthesis/

Happy users of `classicthesis` usually send a real postcard to the author, a collection of postcards received so far is featured here:

http://postcards.miede.de/

*Final Version* as of July 23, 2023 (classicthesis v4.6).